Exploration and Optimization of Tellurium-Based Thermoelectrics

Property enhancements through heavy p-block inclusions and complex bonding

by

Bryan Kuropatwa

A thesis

presented to the University of Waterloo

in fulfillment of the

thesis requirement for the degree of

Doctor of Philosophy

in

Chemistry

Waterloo, Ontario, Canada, 2012

Author's Declaration

I hereby declare that I am the sole author of this thesis. This is a true copy of the thesis, including any required final revisions, as accepted by my examiners.

I understand that my thesis may be made electronically available to the public.

Abstract

Thermoelectric materials are the only known materials capable of direct conversion of a heat gradient into electricity (Seebeck effect) or vice-versa (Peltier effect). Thermoelectric (TE) devices are comprised of solid-state *p*-type and *n*-type semiconductors paired in an electrical circuit and exposed to a temperature gradient. The effectiveness of the materials is evaluated based on the mathematical term $ZT = T \cdot S^2\sigma/\kappa$: S represents the Seebeck coefficient; σ represents the electrical conductivity; κ is the thermal conductivity; and T is the average of the coldest and hottest regions of the applied gradient. This ZT term is larger for better materials; most modern devices in use to-date display ZT values on the order of one. A large temperature gradient combined with a large Z term will lead to a high-performance TE material that involves no waste, no side product, and no requirement for moving parts.

Discovery and optimization of new thermoelectric materials is a critical component of current thermoelectric research. As such, researchers are constantly searching for a new material that has the following properties: the ability to withstand higher temperatures, thus maximizing the T term; exhibit a large Seebeck coefficient and electrical conductivity through doping techniques; and present minimal thermal conductivity, κ. In recent years, research attention has moved from $S^2\sigma$ to κ, which can be optimized through a variety of techniques including complex crystal structure, heavy element inclusion, and introduction of structural defects such as nanodomains/nanostructuring. Due to their tendency to form complex crystal structures and bonding, Te-based materials have become popular targets for TE research and optimization. Compounds with Te anions that also include other heavy elements such as alkali (*A*) metals, alkaline earth (*R*) elements, or heavy p-block elements including the triels (*Tr*), tetrels (*Tt*), or pnictogens (*Pn*) have become a principal source of new and ground-breaking thermoelectric materials. Likewise, optimization of existing TE materials with these aforementioned compositions has led to ZT values twice those of the materials' original reports.

Of the known TE materials, Bi_2Te_3 is one of the staples in the field. It shows narrow band-gap semiconducting properties that can be tuned to *p*- or *n*-type values based on the impurities introduced, and its κ values are inherently low due to the presence of heavy elements and their structural layering motifs. A series of compounds, $(SnTe)_x(Bi_2Te_3)_y$, based on this idea can be produced via the alteration of *x*:*y*. In this work, several of these compounds are introduced and studied as potentially useful thermoelectric materials: $SnBi_2Te_4$, $SnBi_4Te_7$, and $SnBi_6Te_{10}$ are the major targets because of their systematic layering motifs and complex structures. Phase range studies, crystal structure (Rietveld)

refinements, and synthesis optimizations were commenced to ensure that the materials were well-characterized and produced phase-pure before the attempted ZT improvements. By altering the quantity of active charge carriers in these systems, changes in ZT can be observed – this is achieved through doping with, primarily, heavy *Tr* elements Ga, In, and Tl. Thusly, the physical properties are measured and compared for a number of series: $[Tr]_xSn_{1-x}Bi_2Te_4$, $[Tr]_xSnBi_{2-x}Te_4$, $[Tr]_xSn_{1-x}Bi_4Te_7$, $[Tr]_xSnBi_{4-x}Te_7$, $[Tr]_xSn_{1-x}Bi_6Te_{10}$, and $[Tr]_xSnBi_{6-x}Te_{10}$.

Of the triels, Tl is the largest useful element in the group and is known for showing both Tl^+ and Tl^{3+} cationic states and, in thermoelectric applications, for possessing uniquely low κ values. Thallium telluride compounds such as Tl_5Te_3 are therefore quite relevant to this field. The family of compounds includes Tl_9BiTe_6 – one of the better materials with ZT = 1.2 (500 K) using a hot-pressed pellet. Herein, the system is expanded to include $Tl_{10-x}Sn_xTe_6$ which shows good TE potential with $ZT(Tl_{7.8}Sn_{2.2}Te_6)$ = 0.6 (617 K) with a cold-pressed pellet. The incorporation of tetrel elements is investigated through measurements on $Tl_{10-x-y}Sn_xBi_yTe_6$ and also applies to the lesser-studied Tl_9SbTe_6 compound via research on the systems $Tl_9Sn_xSb_{1-x}Te_6$ and $Tl_9Pb_xSb_{1-x}Te_6$. Tl is studied in three concentrations with $Tl_{10-x-y}Sn_xBi_yTe_6$: $Tl_{9...}$, $Tl_{8.67...}$, and $Tl_{8.33...}$, with varying Sn : Bi at each increment. *Tt* elements are systematically added to the $Tl_9[Tt]_xSb_{1-x}Te_6$ structure with $0.0 \leq x \leq 0.7$. Crystallographic studies, electronic structure calculations, and physical properties are explored for each series.

Due to Te's ability to form complex Te–Te interactions in certain environments, the combination of alkaline earth metals, namely *R* = Ba, with the coinage metals (*Cg* = Cu, Ag), chalcogenides (*Q* = S, Se), and Te, form a plethora of previously unknown crystal structures. Many of these are Zintl-phase narrow-band gap semiconductors with complex *Cg*–*Cg* and *Q*–*Q* bonding schemes – combined with their heavy element incorporation, the family is of great interest to the thermoelectrics community. Within this thesis, three new crystal systems are presented: $Ba_3Cu_{17-x}(Se,Te)_{11}$; $Ba_3Cu_{17-x}(S,Te)_{11}$ and $Ba_3Cu_{17-x}(S,Te)_{11.5}$; and $Ba_2Cu_{7-x}Te_6$. All structures show Cu-deficiencies in their crystal structures with d^{10}–d^{10} interactions and 3-dimensional networks of the *Cg* metal. The chalcogenide elements in the structures display unique *Q*–*Q* or Te–Te bonding of varying dimensionality. The electronic structures and bonding calculations are reported for each compound, as are the single crystal studies. The first two of the aforementioned compounds are narrow-band gap semiconductors, whereas the latter two display metallic behaviour.

Acknowledgements

To begin, I would like to extend heartfelt thanks to my supervisor, Prof. Holger Kleinke, for his friendship, guidance, and invaluable advice throughout my time in his research group. Whether he was educating me in crystallography and inorganic chemistry, discussing recent research and potential career options, or going for one of our many group runs, he was always there to provide genuine advice and a helpful push! I would consider it an impressive feat to attain even half of his knowledge on solid-state and crystal chemistry during my career as a scientist.

My friends and colleagues Dr. Jalil Assoud, the department crystallographer, and Dr. Raj Sankar: Their combined knowledge in the fields of crystallography and physics has been invaluable! Our daily discussions and experimental collaborations have been an outstanding experience, and I am indebted to them both. The hundreds of litres of coffee we consumed together will not be forgotten. Likewise, my lab-mates Katja Kleinke, Maya Ootil, Quansheng Guo, Nader Farahi, Susan Jeung, Nagaraj Nandihalli, Savitree Bangarigadu-Sanasy, and Abdul Alhadhrami have each made my time in this research group educational and enjoyable. Thanks to past group members including, but not limited to, Dr. Christian Graf, Tingting Mu, Dr. Yajie Cui, and Dr. Hong Xu – each of whom has helped me reach this point.

For our useful dialogues and helpful insights regarding thermal conductivity, I thank Prof. Robert Hill from the University of Waterloo. Likewise the added contributions and insights regarding TEM microscopy from Prof. Gianluigi Botton and David Rossouw are much appreciated, as was the In-Situ X-ray support from Prof. Mario Gieringer and Shahid Shafi. I am particularly grateful for discussions with Dr. J.R. Salvador, Dr. J. Yang, and Dr. G. P. Meisner from the General Motors R & D Center, Warren, MI.

To my parents John and Joan Kuropatwa and my fiancée Samantha Brown I owe a debt of gratitude. Their support, love, and patience (and groceries) over the years I have spent working on this thesis have meant a great deal to me! I know it occasionally felt like an eternity, but I made it in one piece! Thanks to all my friends and family for the support and confidence, games of squash, and the beer; I raise a glass to them as well.

I would like to thank my Ph.D. committee members Prof. Eric Prouzet, Prof. Pavle Radovanovic, Prof. Dmitriy Soldatov, and briefly Prof. Kathryn Preuss. Over the years, you have provided many encouraging comments. I value each of their useful discussions and unique insights into my research.

Financial support from NSERC, General Motors of Canada, the Waterloo Institution for Nanotechnology, and the University of Waterloo is appreciated.

“Poets say science takes away from the beauty of the stars – mere globs of gas atoms. I, too, can see the stars on a desert night, and feel them. But do I see less or more?”

~Richard P. Feynman~

For my lovely fiancée Samantha
at the beginning of our life together

Table of Contents

SECTION III – LAYERED Bi_2Te_3 COMPOUNDS

List of Figures

List of Equations

List of Tables

.....

List of Abbreviations

Abbreviation	Meaning
Å	Angstrom ($1 \cdot 10^{-10}$ meters)
a, b, c	Crystallographic axes
a, b*, c**	Crystallographic axes in reciprocal space
at-%	Atomic percent
cif	crystallographic information file
Cg	Coinage metals Cu, Ag, or Au
COHP	Crystal orbital Hamilton population
C_p	Specific heat capacity
DOS	Density of states
DSC	Differential scanning calorimetry
EDX	Energy dispersive X-ray (spectroscopy)
E_a	Activation energy
E_F	Fermi energy
κ_{el}	Thermal conductivity – electronic contribution
κ_{ph}	Thermal conductivity – phonon contribution
LMTO	Linear muffin-tin orbital (approximation)
PGEC	Phonon Glass Electron Crystal
Pn	Pnictogens N, P, As, Sb, or Bi
Q	Chalcogenides O, S, Se, or Te
S	Seebeck coefficient
SOC	Spin-orbit coupling
σ	Electrical conductivity
TE	Thermoelectric
TG	Thermogravimetry
Tr	Triels B, Al, Ga, In, or Tl
Tt	Tetrels C, Si, Ge, Sn, or Pb
U_{eq}	Equivalent isotropic displacement parameter
$\propto$	Proportional to
Z	Atomic number

Section I: Fundamentals

Background material and motivation corresponding to thermoelectric materials, crystallography, and the solid state sciences.

Chapter 1. Introduction to Thermoelectric Materials

The world is at a crossroads. Fossil fuels are quickly drying up, global warming and environmental pollution are now a cause for worldwide concern, and industries are under pressure to make old products less damaging and new products "green", clean, and efficient. Wind, solar, hydrogen and other forms of clean energy are being installed wherever possible, including roofs of buildings (aka *green roofs*),[1] factories, locomotives and, of course, automobiles. Politicians and scientists alike are beginning to understand (and explore) the need for alternative automotive fuel sources and ways to conserve energy that prolong and effectively utilize diminishing fossil fuels. Thermoelectric (TE) materials are the only known solids in existence that are capable of direct conversion of heat into electricity,[2] which is achieved via a temperature gradient across the material. These solid-state devices have the added advantage that they can be used alongside any other power generation material, such as combustion engines, to further improve the energy yield from said device; any lost heat recycled into electricity, is energy the device would have otherwise never recovered! Take, for example, automotive designs for hybrid, electric or even conventional starter batteries: their internal chemistry is optimized to a certain temperature range which needs to be maintained in order to sustain a long battery life. Thermoelectric materials can regulate very hot or very cold batteries and even optimize them; a lead-acid battery at 294 K generates 13.5 V, but the same battery at 266 K generates 14.5 V.[3] In short, they are complementary materials that make green technology (e.g. batteries) even greener!

When an *n*-type and a *p*-type thermoelectric material are paired together, attached to a circuit, and electrical current is moved through the device, a temperature gradient is created at both ends of said device; a system capable of removing heat from one end and depositing it on the other is the result. Known as the Peltier Effect (Figure 1.1 (a)), it is typically thought of as *thermoelectric cooling*.[4]

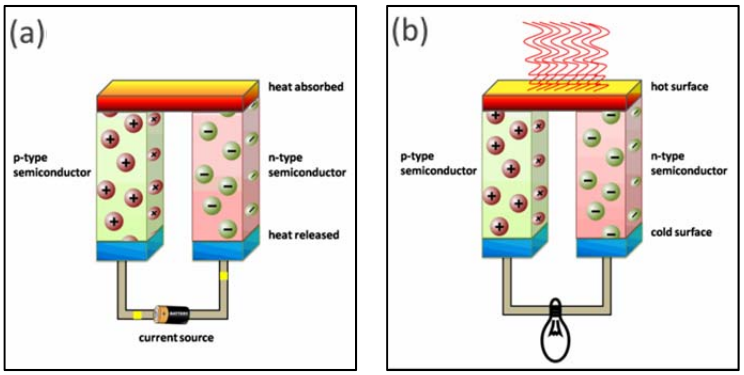

Figure 1.1 (a) Peltier Effect (b) Seebeck Effect

Opposing the Peltier Effect is the Seebeck Effect or *thermoelectric power generation*, also shown above (Figure 1.1 (b)). To observe the Seebeck Effect, one side of the thermoelectric device must be cooled while the opposite side is simultaneously heated. The resulting temperature gradient causes the dominant charge carrier (*n*-type = electrons; *p*-type = holes, not positrons) to migrate from regions of high-density (i.e. the hot side of the material) to regions of low-density (cold side).[4] Due to the pairing of both types of semiconductors, migrations appear opposite to each other, or in other words, constituting a complete electrical circuit – the generation of electricity from heat! For the purposes of the work contained in this document however, we are concerned only with the latter of the two effects: power generation.

1.1. History of Thermoelectrics

The beginnings of this field of study can be traced back as early as 1821 when German physicist Thomas Johann Seebeck (Figure 1.2 (a)) discovered that the formation of a circuit with two non-identical bismuth and copper wires, each with a different temperature, would deflect the needle of a compass.[5] Eventually he also discovered that intensifying the temperature gradient would cause a greater deflection in the compass needle. This deflection was eventually found to have originated from an electric field as opposed to Seebeck's original hypothesis – the "thermomagnetism" phenomenon.[5, 6] The ratio of the voltage difference produced between the dissimilar wires, ΔV, to the temperature gradient, ΔT, became the thermoelectric coefficient, $S = \frac{\Delta V}{\Delta T}$. After Thomas Seebeck's passing, the phenomenon was coined "the Seebeck Effect".

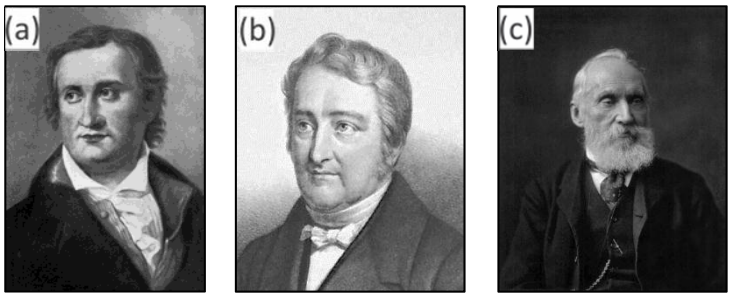

Figure 1.2 (a) T.J. Seebeck (1770 – 1831) (b) J.C.A. Peltier (1785 – 1845) (c) W. Thompson (Lord Kelvin) (1824 – 1907)

Merely 13 years later in France, a meteorologist and physicist Jean Charles Athanase Peltier (Figure 1.2 (b)) encountered a temperature difference at the junctions of two different conductors as an electrical current was moving through.[7] Experimentally, Peltier was able to show the freezing of water at one junction, and upon reversal of the current flow, the melting of the ice. Despite the knowledge of the thermoelectric effect, the relationship between these discoveries remained elusive until Russian

scientist Heinrich Emil Lenz (1804 – 1865) demonstrated that Peltier's temperature difference could be reversed if the current were reversed. The Peltier coefficient (Π) thusly describes the ratio of heat flow, Q, to current applied, I, in the form $\Pi = \frac{Q}{I}$. Following the discovery of the Seebeck and Peltier Effects, William Thompson (Figure 1.2 (c)) or Lord Kelvin, in 1852 succeeded in proving the existence of a relationship between Seebeck's and Peltier's phenomena. That is, $S = \frac{\Pi}{T}$.[8] This demonstrates that the properties discovered separately are in fact united as a single concept of thermoelectric effects.

While the effects were known and in part studied for the purpose of research, the field remained relatively dormant until the 1930s evolved Strutt's electron band theory of crystals[9] and a keen interest by William Ioffe lead to proof that a semiconductor-based thermoelectric generator could achieve an efficiency (η) of approximately 4 %.[10] In the 1950s and 1960s, the study of the key materials PbS and PbTe and their thermal conductivity[11] kept the field active. The next major discovery in thermoelectrics was work by Glen Slack in the late 1970s regarding thermal conductivity of non-metallic crystals and the concept of materials reaching a thermal conductivity minimum at some temperature[12] (i.e. reduction of all thermal transport except lattice vibrations). This work lead to performance limits and eventually evolved into an idealized notion of a material with the thermal conductivity of a glass and the electrical conductivity of a crystal – phonon glass electron crystal (PGEC).[13]

1.2. Efficiency and the Thermoelectric Figure of Merit

Thermoelectric materials are evaluated in the field based on their dimensionless figure of merit, or ZT. It allows researchers to quickly identify materials with good potential in the field and the components of said material that make it promising. This figure allows for a quick and universally understood classification of materials' thermoelectric potential based on a few key properties displayed below (Equation 1.1): S is the Seebeck coefficient, σ is the electrical conductivity and κ is the thermal conductivity from both electronic and lattice (or phonon) contributions. T represents the average system temperature based on the hot (T_H) and cold (T_C) gradient temperatures: $T = \frac{T_H + T_C}{2}$.

$$ZT = T\frac{S^2\sigma}{\kappa_{el} + \kappa_{ph}}$$

Equation 1.1 Dimensionless figure of merit

Hence it follows that a good thermoelectric material must have a high Seebeck coefficient, high electrical conductivity and low thermal conductivity. Designers of materials consequently attempt to decouple S and σ, or σ and κ – a daunting task, but nevertheless necessary to achieve a functionally high ZT factor. Expressed below, in Table 1.1, are ZT values of well-known compounds in the field:

Table 1.1 ZT values for selected thermoelectric compounds.

Compound Name	Chemical Formula	Max ZT @ Temperature (K)	Reference
Bismuth Telluride	Bi_2Te_3	0.6 @ 400	[13]
Lead Telluride	PbTe	0.8 @ 773	[14]
TAGS-85	$(AgSbTe_2)_{0.15}(GeTe)_{0.85}$	1.4 @ 750	[15]
Cs-Bismuth Telluride	$CsBi_4Te_6$	0.85 @255	[16]
Clathrate-1	$Ba_8Ga_{16}Ge_{30}$	1.35 @ 900	[17]
La-Skutterudite	$LaFe_3CoSb_{12}$	1.40[i] @ 1000	[18]
LAST	$AgPb_mSbTe_{2+m}$	1.7 @ 700	[19]
SALT	$NaPb_mSbTe_{2+m}$	1.6 @ 675	[20]
LASTT	$Ag(Sn,Pb)_mSbTe_{2+m}$	1.4 @ 700	[21]
Zinc Antimonide	β-Zn_4Sb_3	1.3 @ 660	[22]
Silicon Germanium	$Si_{1-x}Ge_x$	0.9 @ 900	[23]
Mo-Antimonide	$Ni_{0.06}Mo_3Sb_{5.4}Te_{1.6}$	0.93 @ 1023	[24]

Since the figure of merit is used only locally (in this particular field), it is often useful to speak of thermoelectric efficiency in alternate, or more global terms – namely efficiency (η). Carnot Efficiency, universally understood as a measure of thermal energy being converted into work energy, is the first part of Equation 1.2, with the TE-loss term on the right-hand side. The representation (Equation 1.2) for η in terms of ZT is displayed below:

$$\eta = \frac{T_H - T_C}{T_H} \cdot \frac{\sqrt{1+ZT}-1}{\sqrt{1+ZT}+{}^{T_C}/_{T_H}}$$

Equation 1.2 Efficiency relationship (Carnot·TE).

Utilizing this equation enables one to speak of how much energy thermoelectric materials output based on how much energy is input via heat. Since no system anywhere is perfect, this percentage makes for a quick comparison of systems and their efficiency. For example, a standard combustion engine has $\eta \approx 33\,\%$, a full-sized refrigerator or cooling system has $\eta \approx 60\,\%$ and, to sample current thermoelectric materials, bulk *n*-type PbTe has $\eta = 9.87\,\%$ with a temperature gradient between 373

[i] Postulated

and 873 K.[25] Likewise, *p*-type TAGS can achieve $\eta = 10.45\ \%$ with a temperature gradient between 373 and 798 K.[15]

The TE figure of merit can be looked at as one single term similar to the examples above, but this is generally found only in experimental conclusions. For the purpose of research, each *term* in the ZT equation is looked at individually to ascertain comparisons between different samples and variations in terms therein. It is therefore an important facet to discuss what physical factors affect each term in the figure of merit equation.

1.2.1. The Seebeck Coefficient

The Seebeck coefficient (S), also referred to as the "thermopower", represents the material's ability to migrate charge carriers[ii] away from regions of high concentration. Thermopower was described in **1.1** as $S = \frac{\Delta V}{\Delta T}$, which is its most basic form. Breaking S into its components yields **Equation 1.3** shown here:

$$S = T\frac{8\pi^2 k_B^2 m^*}{3eh^2}\left(\frac{\pi}{3n}\right)^{2/3}$$

Equation 1.3 Seebeck coefficient for metals and degenerate semiconductors

Temperature aside, there are two key variables in this equation: the effective mass for the material (m^*) is directly proportional to S, while a small number of charge carriers, n, leads to a large S. Therefore one can think of variations in the Seebeck coefficient due to changes in either, or both, of these variables. The other terms of the equation are constants k_B, e, h: the Boltzmann number, the electron's charge, and Planck's constant respectively.

1.2.2. Electrical Conductivity

The electrical conductivity (σ) is quite simply a material's ability to move charge carriers (electrons or the lack thereof – holes) through its crystal lattice. Applying this idea, σ can be calculated with **Equation 1.4 (a)** shown below encompassing the number of charge carriers (n), the mobility of the carrier (μ), and the charge of an electron (e). Together, these convey important information regarding different materials' behaviour with current flow and their electrons traversing energy gaps.

[ii] Charge carriers are further explained in **2.3** on p20.

$$\text{(a) } \sigma = n\mu e \qquad \text{(b) } \mu = \frac{e\tau}{m^*}$$

Equation 1.4 (a) Electrical conductivity (b) Carrier mobility

The charge of an electron is constant, which leaves two variables in this equation: n and μ. While n is simply a concentration – albeit one with numerous classifications and applications – μ relies on the additional conditions shown in Equation 1.4 (b): τ – the relaxation time or time between carrier-carrier collisions, and m^* – the carrier's effective mass.[26]

1.2.3. Thermal Conductivity

Thermal conductivity (κ) is also rather self-explanatory; it is a measure of how much heat (i.e. *phonons*) travels through a material. Of the three factors featured from Equation 1.1, κ is the only one that is typically divided into two (or more) sub-variables as demonstrated by Equation 1.5 (a):

$$\text{(a) } \kappa = \kappa_{\text{el}} + \kappa_{\text{ph}} \qquad \text{(b) } \kappa_{\text{el}} = L\sigma T \qquad \text{(c) } \kappa_{\text{ph}} = \tfrac{1}{3} C_{\text{v}} l_{\text{ph}} v_{\text{ph}}$$

Equation 1.5 (a) Thermal conductivity (b) Electronic contribution (c) Lattice contribution

The process of thermal conductivity can further be divided into κ_{el}: the heat contributed from the charge carriers (electrons and holes) in the structure, and κ_{ph}: the heat contributed from vibrations in the crystal lattice as a result of heat waves (phonons). The first of the terms, κ_{el}, can be approximated by the *Wiedemann-Franz law*[27] (Equation 1.5 (b)) for metals and narrow band gap semiconductors.[28] L is known as the *Lorenz number*, theoretically calculated by Sommerfeld in 1927[29] for metals and heavily-doped semiconductors as $2.45 \cdot 10^{-8}$ $\text{W}\Omega\text{K}^{-2}$. Empirically, it has also been measured realising slightly different values for specific elements and compounds; PbTe ($1.70 \cdot 10^{-8}$ $\text{W}\Omega\text{K}^{-2}$)[30] for example. The Wiedemann-Franz law affords a convenient approximation of the electronic contribution, κ_{el}, via examination of σ's behaviour. κ_{ph} (Equation 1.5 (c)), based on the *kinetic theory of gases*, is dependent on the specific heat per volume (C_{v}) of the material, the phonon mean free path (l_{ph}), and the speed of sound (v_{ph}) due to the acoustic nature of lattice phonons. Though heavily doped semiconducting materials are often dominated by the latter term, κ_{ph} is a crucial component to the behaviour and subsequent optimization of thermoelectric materials.[28] While the overall thermal conductivity is useful, advances towards nanostructured materials direct more and more interest towards the individual components including possible κ_{ph} reductions with nano-boundaries, impurity scattering, and other routes further discussed in 2.5.

1.3. Modern Thermoelectric Materials and Their Applications

Researchers in the field of thermoelectrics have since investigated much of the periodic table, discovering semiconductors and variations thereof that can produce new and efficient materials for further practical uses. Historically, mixed semiconductors and solid solutions have been investigated for their key charge carrier concentrations (2.3), while researchers routinely upgraded and increased the number of tools and theories at their disposal for improvement and optimization of said materials. The selection (Table 1.1, p5) of better-known popular compounds conveyed above highlights those materials possessing a unique physical advantage that enables respectable thermoelectric performance, making them quite useful on the current market.

1.3.1. Applications

The niche market for thermoelectric materials has started to expand in the past few decades moving from specific military and space applications to day-to-day production and use. As more demand for high-efficiency and easy-to-implement thermoelectric materials is recognized, further study and optimization of the above-mentioned materials will become a critical task for chemists, materials scientists and of course, engineers. Those tasked with the construction of TE materials will use dozens of the thermoelectric generators displayed in Figure 1.1 (b) previously. All are connected by a series of metallic shunts, which are often Cu-based due to the excellent conductivity and relative inexpensiveness, that when attached to a substrate of the designers' choice, produces a typical TE module as displayed below:

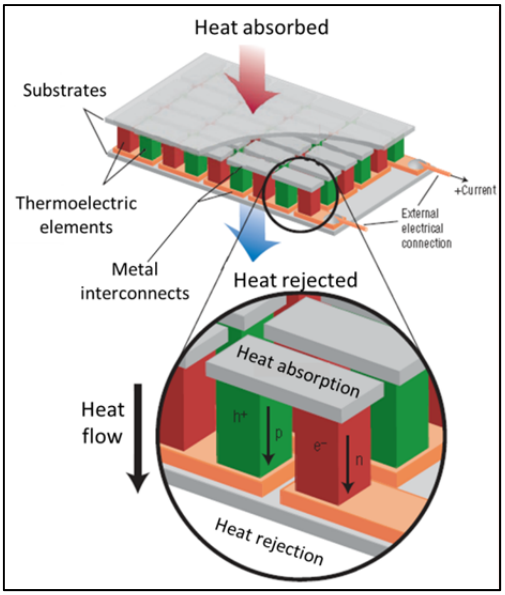

Figure 1.3 Thermoelectric module.[31]

Historically, thermoelectric materials have been most naturally paired with spacecrafts such as Voyager I and II, which were launched in 1977 and are still functional to-date with an average efficiency (Equation 1.2) of ~8 %. These materials work so well, they have been included in Mars Landers, Ulysses, Galileo, Cassini, and Apollo missions. TE materials are ideal in these deep-space applications; the barren cold of outer space combined with the constant radioactive decay of the PuO_2 fuel, creates an ideal temperature gradient for thermopower.[32] Of the aforementioned materials, Bi_2Te_3, PbTe, SiGe, and TAGS have all been implemented in space travel missions.[14, 23, 33] Materials are installed in a radioisotope thermoelectric generator (RTG) which uses high-energy radioactive fuel to generate heat such as ^{238}Pu in the form of PuO_2. As the fuel creates heat, it is transferred to thermocouples, moving into the TE modules which are also connected to a heat sink. The electricity is collected and then used by the craft similar to a typical battery's use. This generator is shown conceptually in Figure 1.4 (a):

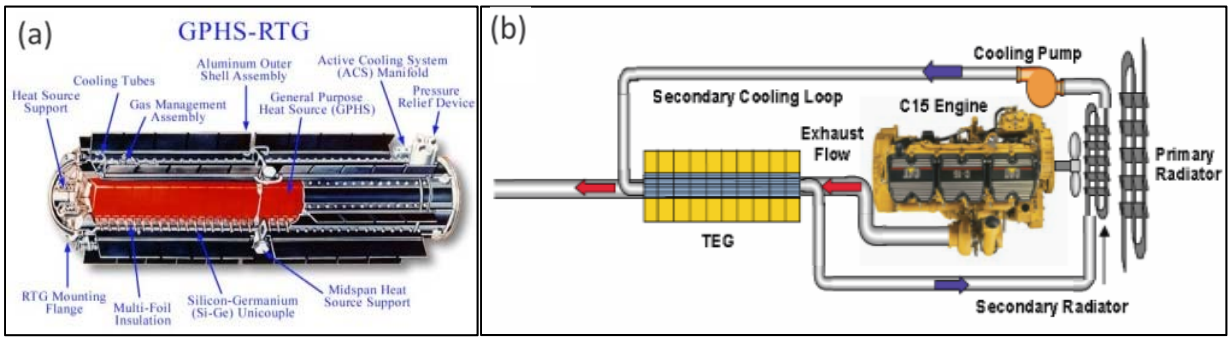

Figure 1.4 (a) RTG[32] (b) Automotive generator[34]

Cooling devices use an array of Peltier couples similar to Figure 1.3, all connected in series. As batteries or other current sources can be utilized to drive high-temperature electrons (or holes) away from the cold end of the couples, heat is transported towards the opposite side of the device.[35] If this particular side of the device is outside of a closed system, such as an insulated vessel, then the heat is drawn out into the surroundings. Thus an electric refrigerator is created where electrons serve as coolants! Thanks to the Peltier Effect, manufacturers have produced thermoelectric refrigerators for the inside of cars[36] to run on a 12V DC automotive adapter or those of similar size and functionality to that of bar fridges (38 L). These types of refrigerators are capable of cooling to about 288 K with almost no noise or vibration (excluding of course, the in-car cooler) and carry only the weight of the device casing.[37] Unfortunately, for a thermoelectric refrigerator to rival that of a typical compressor-based home refrigerator, one would need a $ZT \approx 9.2$; the current market thermoelectrics have only recently broken $ZT > 1.0$.[38] That being said, a $ZT > 2$ would yield practical applications for home and commercial heating/cooling. Other potential applications for these types of devices are in-car climate-

control seats[38] – now distributed by Amerigon Technology,[iii] infrared detector cooling systems,[13] or chip/computer cooling devices.[39]

The major application intended for the presented research will be the automotive industry. Since the combustion engine generates almost 60 or 70 % waste heat from the incomplete combustion process, it is profitable and desirable to regain any of that lost energy as something useful. By attaching thermoelectric modules (Figure 1.3) to either the exhaust system, brake pads, or engine, one can yield a temperature gradient comprised of ambient temperature (~298 K) and the temperature of the automotive systems (~673 – 873 K).[25, 32] For example, between 2010 and 2014, BMW expects to have their 5 and 7 series vehicles equipped with thermoelectric generators, creating 750 W of power during highway driving – a 5 % improvement to the vehicle's fuel economy.[40] Likewise, General Motors is exploring similar venue through the creation of a waste heat recovery device (Figure 1.5) through the use of type-I clathrates (*1.3.3.3*) doped with transition metal ions on the Ga site.[41] A recent test of a Chevy Suburban utilizing Bi_2Te_3 modules may eventually make use of skutterudites to fulfill the waste heat recovery goal. Similar success was had with a Toyota Starlet yielding improved highway efficiencies between +2.5 % and +3.2 %.[36] The device on the test vehicle is fastened to the base of the automobile's underside beneath the back passenger seat adding to the exhaust pipe setup with a water-cooling system (depicted as a blue pipe). Of the research completed in this document, **Chapters 7** through **Chapter 12** represent collaboration with General Motors R&D.

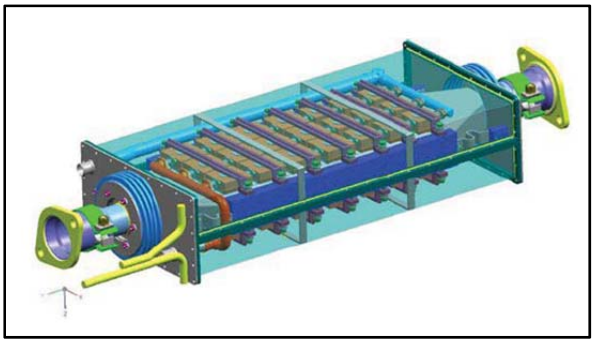

Figure 1.5 GM's TEG diagram with modules displayed in brown.[41]

[iii] http://www.amerigon.com/thermoelectrics.php

1.3.2. Advantages and Disadvantages

Like any device or material on the market, the good must be weighed against the bad. In the case of TE materials, there are many wonderful advantages – many of which can be postulated from the applications recently discussed. Possessing no moving or mechanical parts allows these materials to function for a substantially long time without need for repair. Additionally, the lack of moving parts can allow one to conclude that these devices are extremely quiet; compare a TE refrigerator to a standard refrigerator, and the lack of a compressor leaves the TE device both quiet and light-weight. Another advantage that can be related to the applications is there are no bi-products with TE devices such as CFCs inside old refrigerators, or greenhouse gasses from combustion engines.

The major disadvantage of using TE materials is their low efficiency. A typical efficiency for a combustion engine is between 30 and 45 % while thermoelectrics have been found to achieve between 2 and 12 % currently. The idea of efficiency will be further evolved in the following section in terms of ZT information. Another consideration with respect to disadvantages of TE materials is the cost involved. At this point the TEG alone is approximately $1200 USD, as is the module's assembly; the total cost is projected at $4800 USD (1 kW) or nearly $20,000 for a 5 kW system in the preliminary stages.[42] It should also be noted that a TEG requires two TE semiconductor (*p*- and *n*-) types, and the system is only as efficient as its weakest material. Thus, one must assemble a device from the best *p*- and *n*- types known.

1.3.3. State-of-the-Art Materials

1.3.3.1. Chalcogenide Materials

The chalcogenides were the first TE materials to be studied with the intense thermoelectric push of the late 1950s, where a significant topic of interest was the Bi_2Te_3 compound – a semiconductor that could serve as both a *p*- and *n*- type material depending on whether the deficiencies were placed on the Bi sites or on the Te sites.[4] With a layered structure (discussions within Section III), a high ZT value near room temperature, and rampant opportunities for doping, this material is an understandable topic of interest. From the mid-1900s work commenced – much by Caillat *et al.* – on improving Bi_2Te_3's thermoelectric properties. From mixing it with Bi_2Se_3 or Sb_2Te_3 starting in the early '80s,[13] on to using nanostructuring techniques around the late '90s, such as nanotube creation by Zhao *et al.*[43] Closely following the work on Bi_2Te_3, were studies on other tellurides including PbTe – also having an extensive array of studies such as doping, deficiencies, alloying, etc. Like PbTe, the closely related Te-Sb-Ge-Ag (TAGS),[44] which is a compound comprised of the four elements based on the solid solution

$(AgSbTe_2)_{1-x}(GeTe)_x$ that has the same rock salt structure as PbTe for $x > 0.8$. With $x < 0.8$, the TAGS structure transforms into rhombohedral-type where $x = 0.7$ is preferential for structure-formation.[45] TAGS performs optimally between $0.8 < x < 0.85$[44, 46] and is a popular thermoelectric chalcogenide that has been used in several of the applications mentioned in 1.3.1.

1.3.3.2. The Low-Temperature Thermoelectric, $CsBi_4Te_6$

In particular, $CsBi_4Te_6$ is a well-known chalcogenide for low-temperature thermoelectric applications, as its best performance is at temperatures below 298 K. $CsBi_4Te_6$ can be considered a variant of Bi_2Te_3 with $[Bi_4Te_6]^-$ anion layers in the structure. It is analogous to localizing one extra electron around the Bi atoms which in turn will form Bi–Bi bonds (3.24 Å). Alternating between these slabs are layers of Cs^+ cations which have atomic displacement parameters[iv] 1.6 times larger than that of Bi or Te; evidence for a rattling effect likely further reducing heat transport through the material. Likewise, the structure – namely the $[Bi_4Te_6]^-$ sheets – is quite anisotropic, having the majority of its bonds along the *b* axis and likely functioning with reduced dimensionality for electron flow.[16, 47, 48] The unit cell of $CsBi_4Te_6$ is illustrated in Figure 1.6.

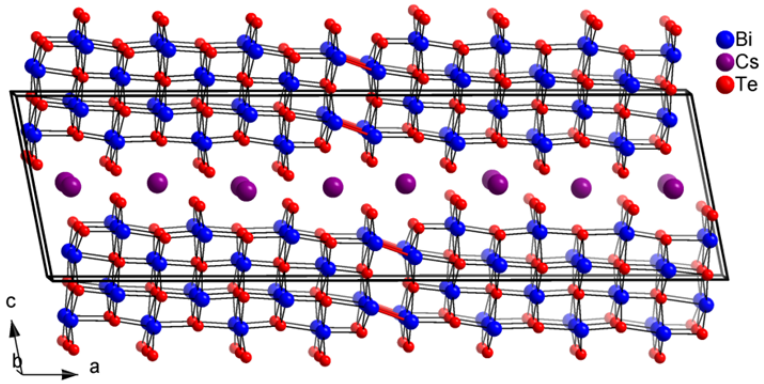

Figure 1.6 Unit cell of $CsBi_4Te_6$ (Bi–Te bonds – black, Bi–Bi bonds – red).

1.3.3.3. Cage Structures – Clathrates and Skutterudites

Clathrates are well-known materials that can accept and trap foreign atoms within their large cage-like structures. Clathrates, or *cage-structures*, comprise a series of 20-atom dodecahedra and 24-atom tetrakaidecahedra, which form around large "rattling" (loosely bound in an oversized crystallographic site) guest atoms, typically with a cubic space group[v] $Pm\bar{3}n$ for inorganic type I.[51] A

[iv] That is, the extent and uniformity of atoms' vibrations in a crystal structure.
[v] Further explained in 2.1 of this thesis, with details included in most crystallographic textbooks.[49, 50]

common stoichiometry studied with clathrates is $A_8Tr_{16}Tt_{30}$ (*A* = Sr, Ba; *Tr* = Al, Ga; *Tt* = Si, Ge). These compounds are usually narrow band-gap semiconductors, which can generally be improved by optimizing the electrons near the Fermi level: minor variations in the valence electrons associated with different guest atoms and cage-vacancies therein. Clathrate uniqueness arises from a thermal conductivity (1.2.3) < 1 $W \cdot m^{-1}K^{-1}$, known to be diminished by the rattling of guest atoms in the oversized cage.[52] This is an excellent example of a phonon glass, or a material that relentlessly scatters phonons. The crystal structure of $Ba_8Ga_{16}Si_{30}$ is shown in Figure 1.7 (a).

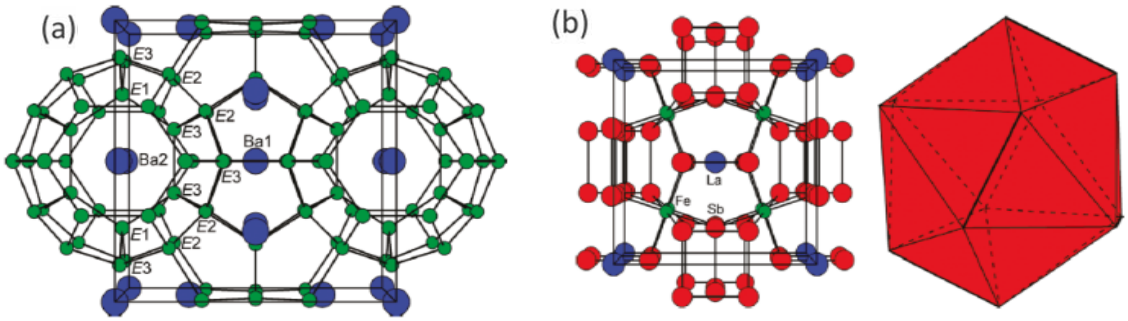

Figure 1.7 Unit cells for (a) Clathrate $Ba_8Ga_{16}Si_{30}$ (*E* = Ga, Si) (b) Skutterudite $LaFe_4Sb_{12}$ & $LaSb_{12}$ icosahedron[52]

Mo_3Sb_7,[53] a Zintl compound[vi,50] (i.e. the $ZT > 1$ compound $Yb_{14}MnSb_{11}$[54]) was discovered as a promising thermoelectric by the Kleinke group.[55] A related large family of compounds is termed *skutterudites* (Figure 1.7 (b)) – named after Skutterud, Norway where the aristotype $CoAs_3$ was discovered. The aristotype crystallized in cubic symmetry as $Im\bar{3}$ and similar to the clathrates, skutterudites are known for forming complex cage structures with numerous Sb–Sb interactions including structures $LaFe_4Sb_{12}$[56] and β-Zn_4Sb_3.[57] Unlike clathrates however, strong guest-host coupling in skutterudites likely rules out any rattling effects, better demonstrating electron crystal – phonon *crystal* characteristics instead of PGEC concepts (1.1).[52, 58] Skutterudites are promising enough to be engineered into TEGs between 5 and 100 kW power generation in automobile tests.[42] While quite similar to the skutterudite family, Mo_3Sb_7 does not have the filled $CoAs_3$ structure necessary for classification under the same name. The Mo_3Sb_7 structure comprises $MoSb_8$ square antiprisms which include Mo–Mo interactions and empty Sb_8 cubes that are connected via Sb–Sb bonds to the next square antiprisms – a representative of the Ir_3Ge_7 ($Im\bar{3}m$) structure-type.[53] The tuning of this Ir_3Ge_7 compound, with respect to its thermoelectric properties, commenced in 1997 with experiments involving substitution of Te for Sb in the structure.[55] For further attempted improvement of the

[vi] Compounds with polyanionic or polycationic bonds formed to complete the octet rule with counter ions.

material, one can consider $M_yMo_3Sb_{7-x}Te_x$: *M* partly fills the Sb_8 cubes while Te can substitute for some of the Sb sites. *M* can be set to transition metals Mn, Fe, Co, Ni, Cu and makes further alterations to the material's electron count.[59-61]

1.3.3.4. Nanostructured Materials

Following the push in the 1980s that inspired researchers to investigate thin-film AlAs/GaAs superlattices,[62] were attempts to lower the dimensionality of thermoelectric materials. A 0-D type material has completely isolated particles such as PbSeTe/PbTe quantum dot superlattices (QDSLs), found to have a ZT increase of approximately 55 % from 0.9 in the bulk phase (300 K) to 1.6 as QDSLs.[63] Most studies currently suggest that this is driven by drastic reductions in lattice thermal conductivity from the discontinuity of the nanodots.[64] See **Figure 1.8 (a)**. A 1-D system would be a nanowire – hence the material's electrons are confined to movement in one direction. Likewise studies from Boukai *et al.*[65] and Hochbaum *et al.*[66] demonstrate that bulk silicon with a room temperature $ZT \approx 0.01$ can be improved to a whopping 0.6 by growing Si as nanowires. There have yet to be sufficient studies on the effects of nanowires towards effective thermoelectrics,[64] but interest in Bi and Bi_2Te_3 nanowires due to their metal-semiconductor state is growing.[43, 67, 68] An example of nanowires of Bi_2Te_3 is shown in **Figure 1.8 (b)**. Lastly, carriers confined to movement in two directions – quantum wells are depicted in **Figure 1.8 (c)**. A Nature article in 2001[69] wrote about this for Bi_2Te_3/Sb_2Te_3 predicting a room temperature $ZT \approx 2.4$ – practically double that of "standard" materials! Superlattices of Bi_2Te_3 intermixed with Sb_2Te_3 were grown with periods between 10 and 60 Å leading to reduction of the phonon mean-free-path discussed in **Equation 1.5 (c)** on page 7; long-range phonons are reflected at the lattice boundaries producing an abnormally low lattice thermal conductivity.[70] Similar studies have been conducted on several compounds including $In_xGa_{1-x}As/Al_yIn_zGa_{1-y-z}As$, where the authors[71] attempted to show decoupling of the Seebeck and electrical conductivity terms, as predicted possible via modification of the DOS at the Fermi level (**2.4.1**). Electron filtering allows only high-speed electrons to cross superlattice barriers, thusly causing a minor drop in the electrical conductivity with a large increase in Seebeck coefficient (**1.2.1**). That being said, quantum wells simultaneously affect lattice thermal conductivity.[69, 72, 73]

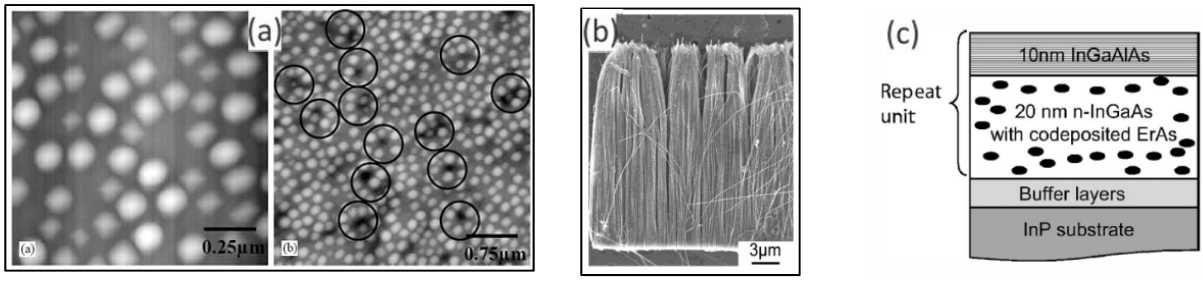

Figure 1.8 (a) Ge Quantum Dots[74] (b) Bi_2Te_3 Nanowires[75] (c) $In_xGa_{1-x}As/Al_yIn_zGa_{1-y-z}As$ Thin Films[71]

1.3.3.5. LAST Materials

Since evolution of the phonon-glass electron-crystal (PGEC) concept – that is to significantly lower thermal conductivity without affecting electrical conductivity,[76] research groups have used the model to design many new compounds. From such materials as clathrates and Zn_4Sb_3,[77] to complex chalcogenides, groups have applied the idea towards construction of nano-impurities in bulk materials. LAST (lead-antimony-silver-tellurium) materials were popularized by the Kanatzidis group by 2004.[78] LAST has a chemical formula of $AgPb_mSbTe_{2+m}$ and a NaCl-type crystal structure forming a solid solution between $AgSbTe_2$ and PbTe, though this particular compound is the forerunner for a family of compounds having similar behaviours for other elements following for example SALT ($Na_{1-x}Pb_mSbTe_{2+m}$),[20] PLAT ($K_{1-x}Pb_mSbTe_{2+m}$),[79] and LASTT ($Ag(Sn_yPb_{1-y})_mSbTe_{2+m}$).[21] Its average unit cell is displayed in Figure 1.9 (a). LAST is a prime example of matrix-encapsulation, possessing regions of (Ag,Sb)-rich nanoinclusions within the PbTe (rock salt) matrix creating a greater breadth of phonon scattering (2.5.3). While on its own this phenomenon is quite remarkable, what further improves it is the fact that the (Ag,Sb)-rich nanoclusters are thermally stable. This allows for temperatures of at least 800 K[80] therefore giving the LAST family a significant advantage over the low-dimensional materials discussed above. Lattice thermal conductivity has been found in LAST materials to possess between 0.5 – 0.8 $W \cdot m^{-1}K^{-1}$ [78] as opposed to 2.2 $W \cdot m^{-1}K^{-1}$ for bulk PbTe[81] at room temperature; the power factor is largely unaffected by the presence of nanoinclusions. Proof of not only nanostructuring, but multiple nanodomains can be seen in Figure 1.9 (b) through TEM imaging where section "b" shows one domain and "c" shows another, twice as big.[19] The parent LAST material has been classified as an excellent *n*-type thermoelectric material and numerous groups have continued investigations of the family (and the PbTe matrix), searching for further improvements and a complimentary *p*-type material – including potentially SALT and LASTT – that shows an equal or greater ZT value. To present an example of these investigations, one may consider $Tl_{1-x}Pb_mATe_{m+2}$ (A = Sb, Bi).[82]

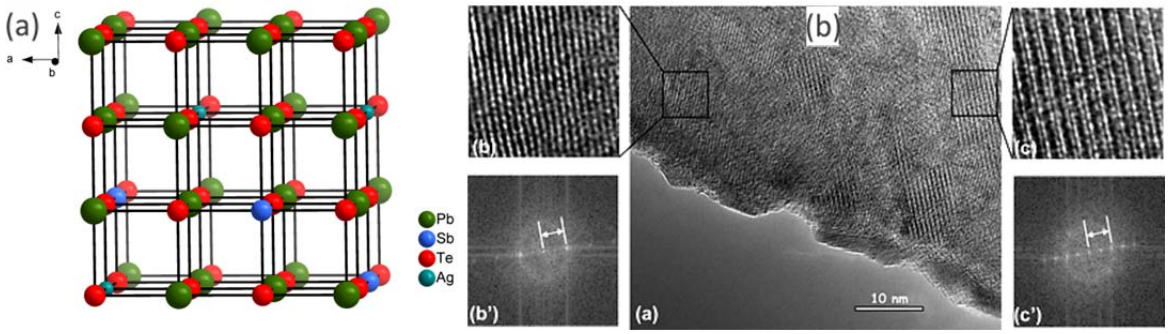

Figure 1.9 (a) average LAST structure (b) LAST TEM[19]

The compounds mentioned in this section are the results of not only decades of research, but several of the theories mentioned previously in this thesis. Unique crystal structures are typically found though exploratory synthesis when chemists discover the phase ranges between two or more elements to create a *phase diagram* – that is, the compound(s) formed at varying mol % with varying temperature. Such compounds as $CsBi_4Te_6$ (above) as well as those in the Ag-Tl-Te system (**Chapter 14**) for example were discovered in this fashion. Addition of extra elements such as in the aforementioned LAST system is a popular strategy for ZT improvement as is the more recent strategy of reduced dimensionality. These improvement strategies and expanded theories involving ZT will be explained through other standard solid state principles.

Chapter 2. Background of the Solid State Sciences

While there are many fundamental theories unique to thermoelectric materials and their applications as discussed before, much of the supporting theory can be applied to broader fields of solid state chemistry and physics, crystallography, and theories of semiconductors, semimetals, and metals. Though the very general ideas summarized herein comprise fundamental ideals in *thermoelectrics*, their application is of a much broader nature and serves as basic theories behind most known ordered-solid materials. A concrete foundation in solid state and the associated sciences will generate a deep understanding of thermoelectric materials and how they function.

2.1. Symmetry and Crystallography

As the materials in this thesis are all crystalline, it is necessary to briefly discuss crystals and how they are classified based on mathematical symmetry operations. A crystal is defined as a solid material comprised of atoms, molecules, or ions that are arranged in an ordered repeating fashion in three dimensions[49] and can range from nanometers to meters in size depending on growth techniques and time. The *unit cell* represents the smallest 3-D unit of periodicity in the crystal. Atoms can pack in a nearly infinite combination of patterns and orders, but there are only seven different crystal systems, in which each unit cell can be classified (Table 2.1). Each system then has one or more Bravais lattices (*P, F, C, I*) depending on atomic centering within the crystal. If there is no unit cell centering, the crystal is primitive (*P*); if atoms are centered on every *face* such as (*x y z*); (*x*+½ *y*+½ *z*); (*x y*+½ *z*+½); (*x*+½ *y z*+½), it is denoted *F*; if only one unit cell face has centering, it is *side-centered*, *C*; lastly, crystals with atoms (*x y z*) having equivalent atoms located at (*x*+½ *y*+½ *z*+½) are called *I* or *body-centered*. These make up 14 Bravais lattices in nature when combined with the 7 crystal systems (Table 2.1).

Table 2.1 Crystal systems and shapes.[83]

Crystal System & Bravais Lattice	Dimensions	Angles	Defining Directions
Cubic *P, I, F*	$a=b=c$	$\alpha=\beta=\gamma=90°$	[100][111][110]
Hexagonal *P*	$a=b\neq c$	$\alpha=\beta=90°$; $\gamma=120°$	[001][100][210]
Monoclinic *P, C*	$a\neq b\neq c$	$\alpha=\gamma=90°$; $\beta>90°$	[010]
Orthorhombic *P, I, F, C*	$a\neq b\neq c$	$\alpha=\beta=\gamma=90°$	[100][010][001]
Tetragonal *P, I*	$a=b\neq c$	$\alpha=\beta=\gamma=90°$	[001][100][110]
Triclinic *P*	$a\neq b\neq c$	$\alpha\neq\beta\neq\gamma$	–
Trigonal *P*, (*R*)	$a=b\neq c$	$\alpha=\beta=90°$; $\gamma=120°$	[001][100][210]

Crystals are generally understood by the symmetry operations that occur within the unit cell (point symmetry: rotations, mirror planes, inversion centres) and the symmetry operations that repeat through infinity (space symmetry: glide planes, translations, screw axes). Based on the unit cell, these symmetry operations generate a repeating pattern of closely-packed atoms that form a series of planes – some of which help define crystal systems. Miller indices define parallel crystallographic planes in reciprocal space. When a plane intersects a unit cell, said direction ($\vec{x}$, $\vec{y}$ or $\vec{z}$) is divided into an integral number of parts thus, Figure 2.1 (a) shows a plane intersecting $\vec{x}$ every one full unit cell (say, of dimensions a, b, c), but carries on infinitely in the $\vec{y}$ and $\vec{z}$ directions. Reciprocally, this would represent $(\frac{1}{1}\frac{1}{\infty}\frac{1}{\infty})$ leading to the plane (100) – should one speak of the middle (1) plane in the diagram – or [100] as the generic direction in the crystal lattice. Likewise, (110) would be a diagonal plane in Figure 2.1 (b), intersecting the unit cell once in the $\vec{x}$ and once in the $\vec{y}$ directions. Likewise, (021) never intersects $\vec{x}$ $(\frac{1}{\infty})$, intersects $\vec{y}$ twice, as in the half-cell and the full-cell (i.e. $b/2$ and b yielding $\frac{1}{2}$), and intersects $\vec{z}$ once $(\frac{1}{1})$.

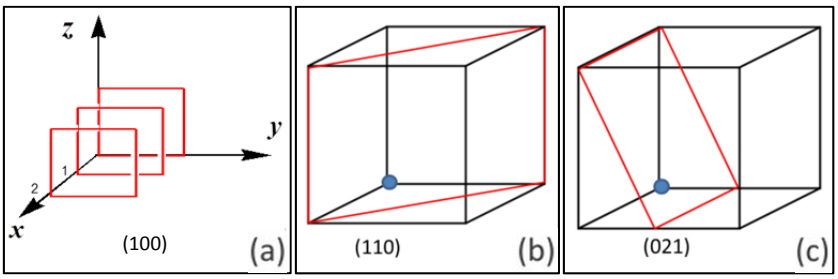

Figure 2.1 Miller Indices (a) (100) (b) (110) (c) (021)

As displayed in Table 2.1, up to three directions can define a space group, and when combined with the 14 Bravais lattices, make up 230 possible space groups for all crystal structures occurring in nature. Thus, proper space group notation incorporates the crystal's cell setting $(P/F/I/C)$ with a symmetry operation symbol (i.e. *m*, *c*, 2_1, 4, etc.) existing on each system's defining directions shown in the final column of Table 2.1. For example, monoclinic $C2/m$ describes a side-centered monoclinic system with a 2-fold axis parallel to, and a mirror plane perpendicular to, the [010] direction; orthorhombic $Pmm2$ therefore describes a primitive unit cell having mirror planes (*m*) in [100] and [010] directions with a 2-fold rotation around [001]. Thus space group notations provide a quick snapshot of the inherent crystal unit cell shapes.

2.2. Defects, Non-Stoichiometry and Solid Solutions

Perfection is boring. Such is true with most crystals and materials: *"Certain flaws are necessary for the whole" ~Goethe~*. When it comes to defects and non-stoichiometry, the simplest of the classifications are *point defects* such as Schöttky and Frenkel, both *intrinsic*, primarily dealing with ionic compounds in which an cation-anion pair is vacant from the lattice or displaced to an unusual interstitial site, respectively.[84] The *extrinsic* point defects are then called *dopants* or *substituents* depending on their valence electron count. A dopant typically has a different valence electron concentration such as an Al/P atom sitting on a Si site, while a substituent would have the same number of valence electrons, such as Ge on a Si site. These two critical types of defects have a strong impact on most bulk materials' properties.[85] Consider as a more concrete example (Figure 2.2), the intercalation compound Li_xCoO_2: being analogous with the $CdCl_2$ structure-type, this compound ($R\bar{3}m$) has alternating layers of oxygen "A" and "B" octahedral (Co-centered) orientated in [111]; by adding a Li non-stoichiometry ($0 < x < 1$), the tiny atoms are able to fit in between the oxygen AB layers creating an ABC repetition and a very effective battery cathode through mobile Li^+ ions.[86, 87] Since the quantity of Li atoms cannot be predicted as an exact ratio with respect to Co or O, it is considered *non-stoichiometric*.

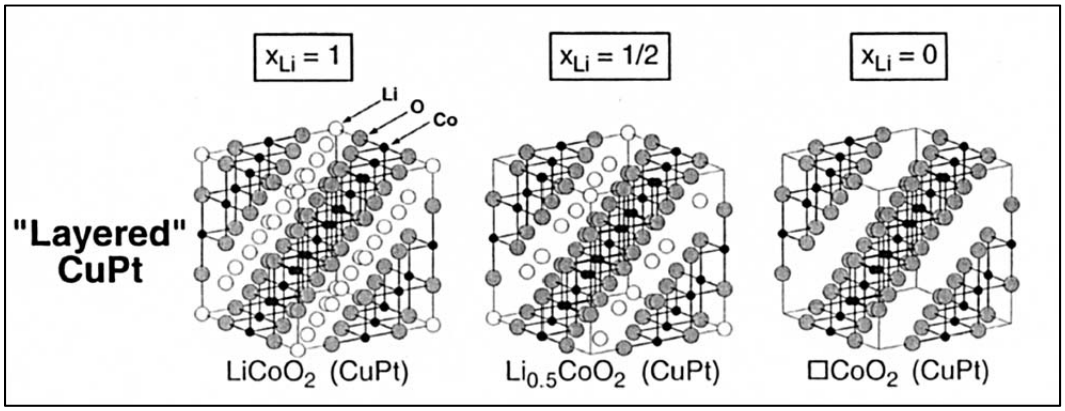

Figure 2.2 Li mobility and crystal structure of $LiCoO_2$.[87]

Unlike dopants, substituents do not increase charge carrier concentration (since they have the same valence electron count). Consider for example rock salt with added potassium impurities $Na_{1-x}K_xCl$, Na/K sit on the same crystallographic sites and have the same one valence electron, but their ionic radii are 2.27 and 2.75 Å, respectively. One advantage for substituents is increasing the complexity of the unit cell which, as mentioned in 1.2.3, generally decreases the lattice thermal conductivity (κ_{ph}) through increased phonon scattering. Recall the Sb_2Te_3-Bi_2Te_3 mentioned in 1.3.

The logical rise in dimensionality that follows increasing a 0-dimensional point defect into a 1-D line (i.e. edge dislocation), 2-D plane (i.e. grain boundary), or 3-D volume (i.e. nanoregions) leads the idea of imperfections at the macro- and microscopic or even nanoscopic levels, driving properties such as mechanical strain or even colour. Consider for example diamonds (band gap ~5 eV) with boron or nitrogen impurities causing blue or yellow tints from acceptor (0.4 eV) and donor (4 eV) states respectively, via energy transitions in the band gap.[85] Examining now a 2-dimensional defect, grain boundaries are frequently encountered in crystalline materials due to manufacturing inconsistencies, inhomogeneity in powder size, and growth in multiple directions, yielding some or all of the boundary types illustrated in Figure 2.3 (a). Grain boundaries play a large role in thermoelectrics due to their effect on carrier mobility throughout the crystal structure, which is demonstrated in studies on PbTe; several types of boundaries are examined (coherent, incoherent and semi-coherent) on various off-stoichiometry defect interfaces and their effective reduction of the lattice thermal conductivity, κ_{ph}.[88] TEM at the atomic scale (~1 nm) reveals one such boundary in the following image:

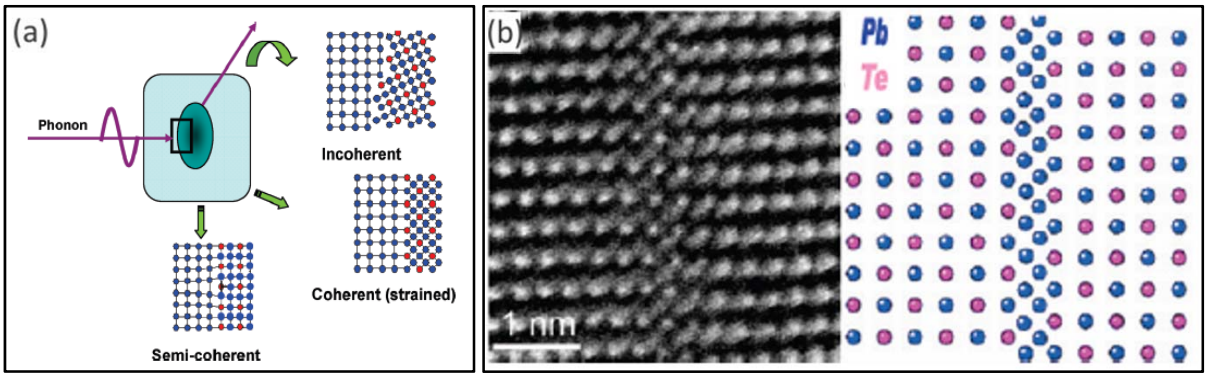

Figure 2.3 (a) Different grain boundary types (b) Grain boundary in PbTe–2%Pb via TEM[88]

2.3. Charge Carriers and their Effects

Charge carriers are any free-moving particles that carry an electric charge. When it comes to metals – and every solid to an extent – charge carriers are electrons (i.e. recall Equation 1.4 (a)). With extrinsic semiconductors, charge carriers are considered in two categories: free electrons (*n*-type) in the crystal lattice and a deficiency of electrons (*p*-type), or a positive charge moving in a direction opposite of electron-flow. Free electrons produce additional "donor states" close to the conduction band, to be released with very little energy (i.e. $P_{0.01}Si_{0.99}$); *p*-type semiconductors however, can only achieve a full octet by breaking a neighbouring bond in the lattice. Additional "acceptor states" are therefore created close above the valence band for energetically inexpensive conduction (i.e. $Al_{0.01}Si_{0.99}$). *P*-type conduction is referred to as "holes" due to the *appearance* of vacancies being promoted, since an

electric field draws electrons towards it, filling in the deficiency as they move, the hole drifts away from the field just like a positron.[89] This concept will again be discussed in 2.5.1 and Figure 2.9 (a).

In the process of tuning the thermoelectric figure of merit, one must consider the charge carrier concentration and how it varies, in order to see improvements in the ZT factor. Charge carriers govern most of the physical properties and must be understood to properly design materials. Typically, insulators are considered to have a charge carrier concentration (n) less than 10^{18} (per cm^3), while metals should have $n > 10^{20}$. As depicted in Figure 2.4, the tuning of ZT becomes a difficult task as insulators boast a high Seebeck coefficient whilst metals have extremely high electrical and thermal conductivity. Researchers therefore look to semiconductors with $\sim 10^{19} < n < \sim 10^{20}$ for a reasonable compromise between the three primary components of ZT.

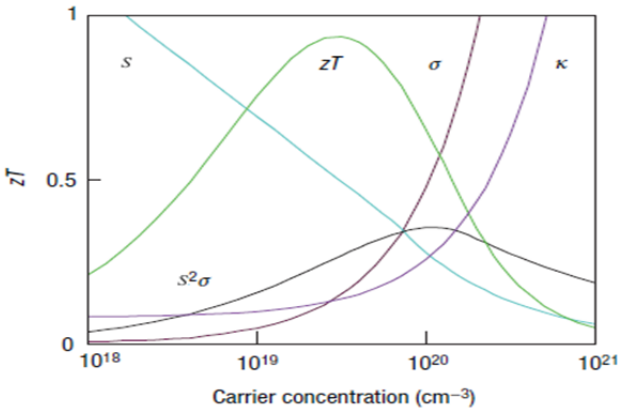

Figure 2.4 ZT as a function of carrier concentration (n)[31]

2.3.1. Electrical Conductivity (σ) as a function of charge carriers (n)

A brief summary of different materials' behaviours according to Equation 1.4 (a): A metal has the highest concentration of charge carriers of all known materials; copper, for example, having $8.42 \cdot 10^{22}$ cm^{-3} electrons,[26] means n can be considered constant (or at least negligibly variant) and as temperature increases, mobility (μ) is obstructed by increased atom vibrations, and thus σ decreases slightly with increasing temperature. This is observed with σ vs. T as a linear decrease. An intrinsic semiconductor can be understood to have no mobile carriers $(n = 0)$ at absolute zero, but as the temperature increases, carriers are increasingly able to cross the energy gap between valence and conduction bands, thus leading to a dominant (n) term with increasing temperatures. An extrinsic semiconductor can now be considered as a material with a limited number of additional charge carriers to donate to the conduction band. As these extrinsic carriers begin crossing the energy band gap with a rising temperature, the material is behaving as a typical semiconductor (albeit higher σ) by exponentially

increasing n. However upon their exhaustion, the dominant term is again μ causing the material to behave as a metal until the intrinsic carriers are activated and the material returns to semiconducting behaviour with another sharp increase in conductivity.[84] Traditional semiconductors display an exponentially increasing σ vs. T plot.

2.4. Electronic Structure and Band Theory

Modern chemistry was revolutionized around the early 1900s by the discovery and subsequent evolutions of quantum mechanics which led to a refined understanding of atoms, electrons, and their energies or shapes. The theories evolved into valence bond theory and molecular orbital theory[90, 91] – two key ideas towards understanding (and predicting) the behaviour of molecules. Crystalline solids however, are different than discrete molecules in the sense that they extend into the infinite, repeating a pattern of individual atoms, whereas molecules have a finite structure and defined shape. Consider then, a series of increasingly large molecular orbital Hückel diagrams as displayed below in Figure 2.5. As the rings of atoms expand towards an infinite (or crystalline, N_A) quantity of atoms, the corresponding energy gaps between the levels become increasingly smaller until they amalgamate into the bulk form. The creation of one such energy band in a crystalline solid occurs when the levels shown on the right side become so numerous there are no longer gaps between them:

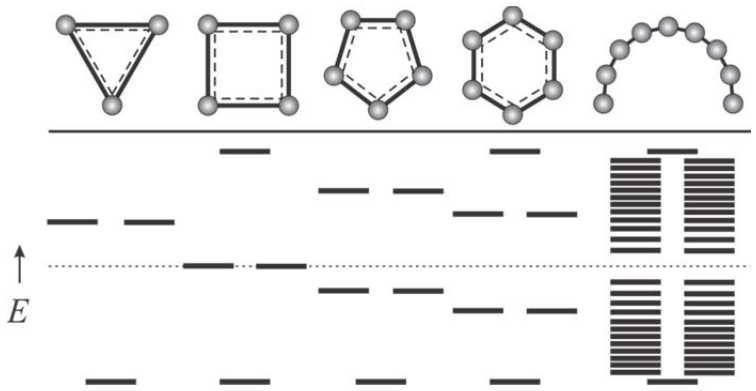

Figure 2.5 Orbital diagrams for increasingly large atomic rings.

The idea behind band theory is to observe how orbital energies change as one "walks around" the crystal's unit cell – different locations in reciprocal space (k points) which simultaneously symbolize irreproducible representations of the wavefunction ψ. The simplest way to conceptually evolve band theory is to examine infinite chains of simple *s* or *p* orbitals – in this case, a linear chain of hydrogen atoms will suffice (Figure 2.6). To describe the behaviour of each H(1*s*) orbital, a basis function is used (φ_n) such that the behaviour of all the basis functions produces a solution to Schrödinger's equation:

$\psi_k = \sum_n e^{ikna}\,\varphi_n$ known as a *Bloch function*, where n is an integer between 0 and ∞ representing the individual atomic orbitals, and a represents the spacing between atoms i.e. the lattice parameter.[92] The index of the irreproducible representation called k is in reciprocal or momentum space according to $k = \frac{2\pi}{\lambda} = \frac{2\pi p}{h}$.[93] When the atoms are all in phase with respect to their wavefunctions, all orbitals will be bonding and one obtains the lowest energy state ($E(0)$). If the wavefunctions shift out of phase ($E(\pi/a)$), the outcome is synonymous with antibonding orbitals in this case, which yields the chain's highest energy state. Connecting the two extreme states from $0 \leq k \leq \pi/a$ (known as the first Brillouion zone) with intermediate energies, constructs the simplest band diagram displayed on the left of Figure 2.6.

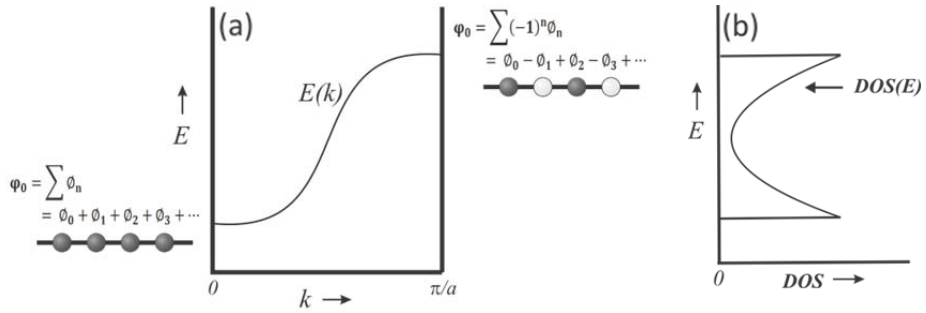

Figure 2.6 Theoretical hydrogen chain. (a) Band structure (b) *DOS*

Looking at the band structure for a hypothetical infinite chain of hydrogen atoms, one can begin to understand how these often very complex diagrams begin to evolve, and learn which orbital contributions are stable in what lattice direction. Such bands also provide an efficient guide to energy differences via the *band width*, or dispersion. For example a perfectly flat band would indicate an energy difference of zero from one k point to another, while a very steep band implies a significant energy difference such as a change in σ bonding character.

The density of states (Figure 2.6 (b)) is an alternate way of conveying the information found in band structures, in what many would consider a more useful and compact manner. Since bands represent nearly an infinite number of orbitals, it is often useful to group said orbitals into energy increments such that more levels would result in a greater density. This can be observed using the first derivate of the bands, or $DOS(E)\,dE = \text{number of levels between } E \text{ and } (E + dE)$, which states that the steepest bands contain the fewest quantity of orbitals, and the flattest bands possess the greatest quantity of contributions;[94] visually this depicts broad and sharp densities respectively such that the inverse of the band slope is then directly proportional to the DOS magnitude. DOS plots are created

(in chemistry fields) with the number of orbitals on the x-axis and increments of E on the y-axis. As can then be seen from the diagram, the flatter the band to a given energy, the larger the DOS at the same energy.

This simple hydrogen band diagram can then be extended to an infinite chain of eclipsed square planar $Pt(CN)_4$ groups found in $K_2[Pt(CN)_4]$[95] with the same k bounds as the H chain above, exhibiting Pt—Pt contacts (a-direction) of 3.3 Å. By looking at the different orbitals for …Pt—Pt—Pt… it can be seen that some are bonding or antibonding at $k = 0$ or π/a depending on their in-phase orientations.

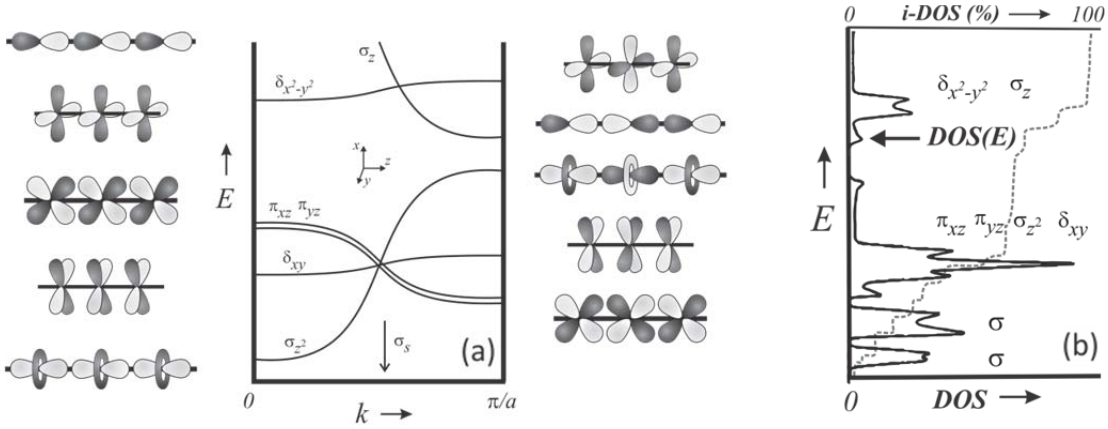

Figure 2.7 Eclipsed PtH_4 chain. (a) Band structure (b) DOS

Similar to the molecular orbital diagram, there are energy gaps – the gap of interest for semiconducting materials is that between the filled *valence band* and empty *conduction band*, where it is assumed that semiconductors have an energy gap no larger than 3 eV. Note the variations in bands' widths based on the strength of the bonding (σ vs. π vs. δ) in this example. In band structures, all of these features close to the Fermi level – that is, the highest energy band containing electrons – describe the nature, properties and characteristics of the material: a map of its potential applications. This information can be viewed in a simple manner with the DOS presented in Figure 2.7 (b): the contributing orbitals, once labeled, can be quickly seen; one can estimate the material's properties based on band gap size; whether the Fermi level falls in a gap, a steep DOS or a thin DOS; and what elements or dopants are contributing to the DOS at a given energy level (i.e. can changing one element concentration greatly affect the material's performance?).

It is worthwhile to mention that it can be useful to plot an integrated density of states, or i-DOS, on the original plot. This simple dashed line tallies all the orbitals in the calculation and if the i-DOS reaches 100 % (or close to it, say, >95 %) then all of the significant energies are accounted for. A crystal

orbital Hamilton population ($COHP$)[96] is another useful variation on the DOS (Figure 2.8). Since the DOS is only a representation of the inverse band-slope, there is no depiction of bonding or anti-bonding (or non-bonding) states. Thusly, the energy of the bands is separated into positive overlap, negative overlap or zero-overlap by multiplying the DOS term by the Hamiltonian term representing overlap population. The resulting plots depict the DOS only of the selected bond(s) (i.e. Atom1—Atom2) which would appear on the right-hand side for bonding character or the left-hand side for anti-bonding character, with more intense lines representing stronger character.[97] The x-axis is plotted with "$-COHP$", as the Hamiltonian term has a negative value in the bonding state and vice-versa.

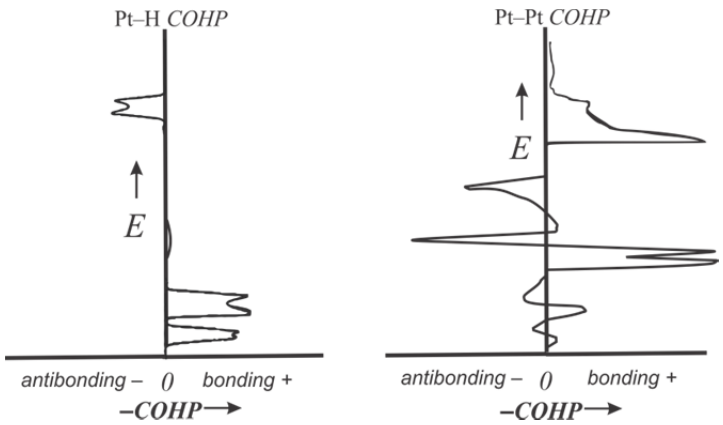

Figure 2.8 *COHP* curves for PtH_4 chains (eclipsed)

2.4.1. Relationship to Materials' Physical Properties

Physicists have been using band theory as their primary tool for the prediction of materials' physical properties. Since the electronic structure reveals many useful pieces of information such as bonding/antibonding regions, energy gaps, electron concentrations at a given energy, etc., one can derive with such theories as perturbation theory, relationships between the electronic structure and the material's behaviour via physical properties. Band theory is thusly an essential component in the understanding and prediction of the behaviour of thermoelectric materials and their subsequent improvement. Take for example the energy (E) of the bands which is proportional to the square root of the wavevector (k) and inversely proportional to the effective mass (m^*) of the charge carriers (Equation 2.1).[93] As indicated below, the second derivative ($\frac{d^2E}{dk^2}$) of E, or the bands' concavity, is then inversely proportional to only m^*, which as demonstrated in 1.2, has significant impact on S and σ.

$$E = \frac{h^2k^2}{8\pi^2m^*} \qquad \frac{dE}{dk} = \frac{h^2k}{4\pi^2m^*} \qquad \frac{d^2E}{dk^2} = \frac{h^2}{4\pi^2m^*}$$

Equation 2.1 Relationship between energy (E) and wave vector (k)

By using equations derived by Nevill F. Mott in the 1950s, relationships between densities of states at the Fermi level can be related to physical properties such as Seebeck and electrical conductivity. Tuning the DOS as a strategy for improving the properties and as an inquiry towards why certain doping techniques cause property improvements can be found in the Mott relation:[98]

$$S = \frac{\pi^2}{3} \cdot \frac{k^2 T}{e} \cdot \frac{d \ln \sigma(E)}{dE}\Big|_{E=E_F} \qquad S \propto \frac{1}{\mathrm{DOS}(E)} \cdot \frac{d\mathrm{DOS}(E)}{dE}\Big|_{E=E_F} \qquad \sigma \propto \mathrm{DOS}(E)|_{E=E_F}$$

Equation 2.2 (a) Mott relationship (b) S vs. DOS (c) σ vs. DOS

where k is the Boltzmann constant, T is the temperature, e is the electron's charge, and $\frac{d \ln \sigma(E)}{dE}$ is the first derivative of the natural logarithm of the electrical conductivity; E_F is the energy of the Fermi level, or the highest state(s) filled with electrons. Derivations based on this Mott relationship[99, 100] allow one to connect both S and σ individually to the densities of states. This is highlighted above in **Equation 2.2 (b)** and **Equation 2.2 (c)** respectively: the Seebeck coefficient is proportional to the first derivative of the DOS, implying flat bands produce a large S;[13] it can also be seen $DOS(E)$ is directly proportional to electrical conductivity, which is also a term present in **Equation 2.2 (b)** – another reason why researchers are interested in decoupling S and σ (**1.2**). Utilizing these relationships, one can make predictions of the physical properties by looking at the band structure and densities of states close to the Fermi level. Consider then the Seebeck coefficient. When proportional to the first derivative, it can be expected to be largest on observation of a "sharp" density of states. Similarly, a high density of states at the Fermi level can be presumed to generate a large electrical conductivity.

2.5. Solid State Theory for Strategic Improvement of ZT

Many of the basic solid state ideas discussed in this chapter can be directly applied towards thermoelectric improvements. Since Ioffe's initial estimate of materials' ZT values, investigators have considered numerous strategies for improvement as most (or any) materials in their standard forms are not strong enough to succeed on the market. Based on the different investigator backgrounds, people were able to suggest many approaches towards improvements which have to some extent, been discussed previously. Consideration of such properties as the band structure of materials (especially near the Fermi level), charge carrier concentrations, decoupling thermal and electrical conductivity, altering size and dimensionality of materials and introducing chemical (i.e. different atoms) or physical (i.e. grain boundaries) impurities into a material are all examples of strategies employed to change an acceptable ZT into a great ZT. Discussed henceforth are three major strategies of interest.

2.5.1. Doping and Substitution: Tuning the Band Structure

A semiconductor's band gap drives its properties – and by making minor changes to this, one is able to realize improvements to ZT's components. One of the oldest and best-studied of these strategies involves *doping* – that is, replacing a small percent of atoms in a crystal structure (e.g. 1 – 10 %) with an element of similar size and electronegativity, but with a different electron-count; this will most often affect the power factor, $S^2\sigma$ via a change in n. For example Sn and Sb have about the same size and electronegativity based on their location on the periodic table, but their ionizations yield a different electron count (i.e. Sn^{2+} vs. Sb^{3+}). Doping is able to change an intrinsic semiconductor into an extrinsic semiconductor meaning within the band gap, extra levels are created either directly above the valence band (acceptor state) or directly below the conduction band (donor states).[93] If the dopant has fewer electrons than the original element, acceptor states are created above the valence band for electrons to fill; if the dopant has more electrons than the original element, donor states are created below the conduction band, which are easily promoted to conduction before the intrinsic electrons are activated; see Figure 2.9 (a). This offers a method for fine-tuning the Fermi level of a material.

A study on doping PbTe with group 13 elements involves DOS calculations of In-doping that showed *deep defect states* (DDS)[101, 102] in this narrow band-gap PbTe semiconductor – additional sharp impurity states in the band gap of the host compound. Studies on $InPb_{31}Te_{32}$ highlighted the appearance of two additional energy states in the compound's DOS as a result of In: one from the strongly-bound In-*s* state interacting with the Te orbitals and one from the In-*p* state. Because of the heavy group 13's ability to form either a +1 or a +3 valence, two In^{2+} atoms after donating their electrons to the Te-*p* valence bands dissociate into localized In^{1+}, In^{3+} pairs giving the deep In-*s* state below the valence band and a new DDS state pinned in the centre of the Fermi level.[103] Experimentally, Tl-PbTe shows a similar concept in Figure 2.9 (b) "A" with regular PbTe DOS as dashed lines and the DDS Tl-PbTe as a solid line in the compound's valence band. The evidence can be seen via a ZT increase, "B", of almost threefold:

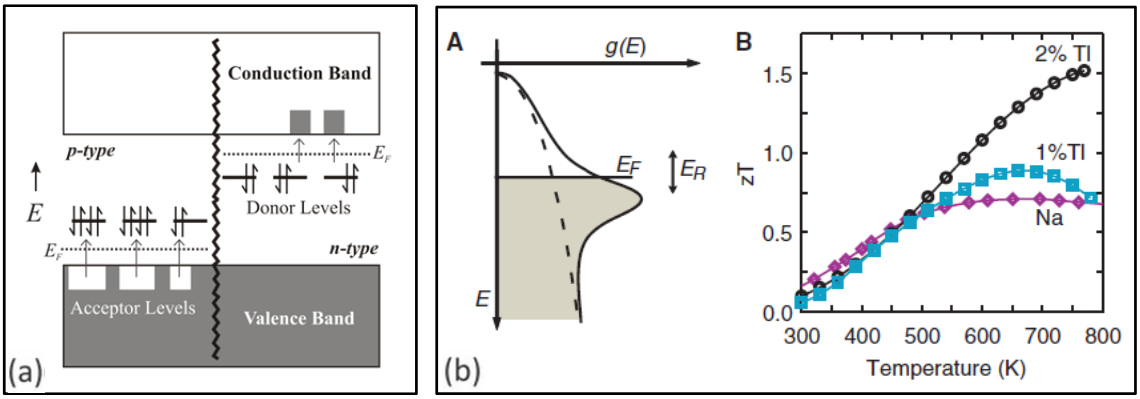

Figure 2.9 (a) Donor and acceptor states (b) Tl-PbTe DOS and resulting ZT[104]

2.5.2. Nanostructuring: Materials with Reduced Dimensionality

Mentioned in terms of ground-breaking compounds in 1.3, nanoscopic materials such as Bi_2Te_3/Sb_2Te_3 quantum wells,[69] created a surge of new excitement in the thermoelectrics field with evidence of ZT values such as 1.6,[63] 2.2,[78] and 2.4[69] – sometimes 2 or 3 times higher than the current state-of-the-art devices. Reducing dimensionality via nano-sized components, or *quantum confinement*, was a theory put forth by Hicks & Dresselhaus[105] whereas ZT (Bi_2Te_3) was calculated at 0.52 and projected to increase to ~1.5 with the transition from 3-D to 2-D materials. This affects the DOS of thermoelectric materials near the Fermi level as follows:

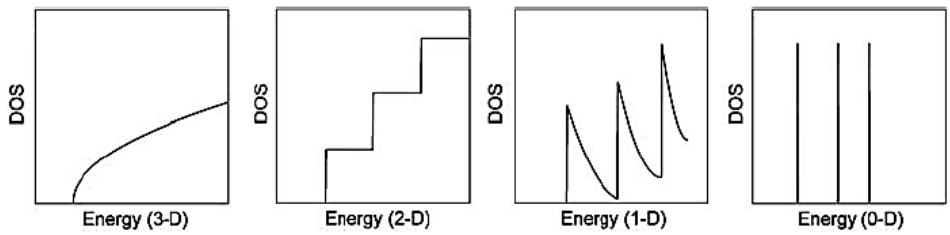

Figure 2.10 Effects of reduced dimensionality on the DOS[106]

This increasing sharpness of the states near the Fermi level separates charge carrier mobility (μ) from energy (along the nano-sized direction) such that $E(\mu) = \mu$,[106] or an energy-independent σ, which is directly proportional to the DOS (as in Equation 2.2 (a) & (c)) via charge carrier confinement in one or more directions. This can be alternately understood by re-examining Equation 1.3 which explains that the effective mass (m^*) is increasing from a lack of carrier dispersion caused by the sharp increase in the DOS at the Fermi level. The resultant confinement causes a decoupling of the inter-reliant parameters S and σ – therefore offering significant gains in the power factor, $S^2\sigma$. Quantum confinement has yet to gain experimental momentum, but progress such as Harman[63] and Venkatasubramanian[69] continue to capture the attention and imagination of researchers.

The major problem with exclusively nano-sized materials is their instability at high temperatures; a high surface free energy (disruption of bonds from the creation of a surface) yields them thermodynamically unstable and if provided the proper mechanism, would return to a more stable bulk state.[107] It therefore becomes necessary to disperse nanostructures within a bulk matrix to give the compounds added stability. This is the case with the LAST family of materials mentioned in the applications subsection (**1.3**) of this document. Fabrication of pure-nanomaterials is also a costly and time-consuming venue, which sends a strong signal to experimentalists to begin exploring supplementary approaches such as bulk nanostructuring.

2.5.3. Breaking the Alloy Limit: Bulk Nanostructuring

Though bulk materials can easily be doped and the power factor tuned, efforts are now turning towards the other component of ZT: κ – more specifically, κ_{ph}. The one parameter in the ZT equation thought to be inherent to the material and unwavering. Alloying the material was the technique required to achieve the lowest thermal conductivity – the additional atoms and bond strengths in the alloy create scattering points for short wavelength phonons, effectively preventing them from passing through the lattice.[12] $Si_{1-x}Ge_x$ for example has numerous point defects generated alongside an electronegativity difference effectively reducing charge carrier mobility with increasing [x].[108] In bulk crystalline materials, this "alloy limit" is as low κ can go without creating voids, displacements or defects. More often than not, this worsens the properties and structural integrity.[12, 85] Until the implication of nanostructuring, the wavelength of these mid and long range phonons could not be blocked but they happen to be similar in size to the nanoinclusions, providing the necessary mechanisms to surpass the alloy limit. Take for example ErAs:InGaAlAs[109, 110] which has randomly distributed ErAs particles similar to the depiction in **Figure 2.11**, in a matrix of $In_{0.53}Ga_{0.28}Al_{0.19}As$. The spherical particles range in concentration between ~0.3 – 6 % and are less than 5 nm in diameter, therefore providing an extra scattering mechanism not seen in the aforementioned bulk structure, $Si_{1-x}Ge_x$. The resultant decrease in κ from ErAs:InGaAlAs displays approximately 3x less conductivity than the original alloy.[111]

Bulk nanostructuring can be quickly and inexpensively made in large quantities with relatively simple techniques such as ball-milling (or other grinding methods) as demonstrated with Bi_2Te_3,[111] Si,[112] or $CoSb_3$[113] followed by incorporation with the bulk phase or, particularly in certain systems (i.e. $AgSbTe_2$-[Tt]Te[78] or LAST[19]), self-precipitation within a matrix. Similarly, investigations into the incorporation of carbon nanotubes in and around thermoelectric materials are underway.[68, 114, 115] The advantages of bulk nanostructuring have already been mentioned with the LAST-family of materials in

1.3.3.5. The simplicity of placing the powder in a ball-milling instrument followed by sample hot pressing is an appealing idea for those in the industry, as reported by Yan *et al.*[116] in a recent publication which highlighted the effects of ball-milling on $Zr_{0.5}Hf_{0.5}CoSb_{0.8}Sn_{0.2}$ (Half Heusler). This caused a minor decrease in σ, a minor increase in S, and a major (~30 %) decrease in κ, leading to an overall increase in ZT of 60 % of that with the ingot. The appeal of this attempt is clear: efficient, inexpensive, and relatively simplistic.

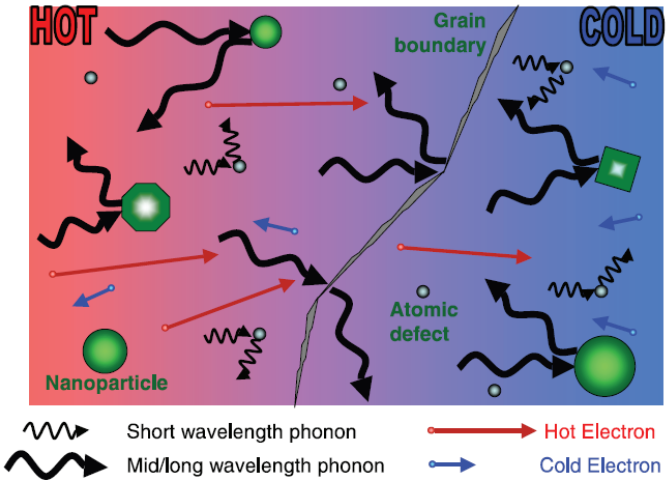

Figure 2.11 Electron and phonon scattering points in a crystal structure.[64]

Bulk nanostructuring theories are functionally more promising than pure nano-materials, as the bulk matrix is able to maintain the stability upon increase of the temperature; empirically, this seems to sustain the features to often ~100 degrees below the compound's melting point before one begins to observe degradation in the material's properties.[80] To revisit an old standard, $(Bi,Sb)_2Te_3$ once hot pressed and ball-milled, boasts a ZT = 1.4 instead of 0.9 as studied by Poudel *et al.*[111] The current favourite options with this strategy are a small quantity of nanoscopic material in a matrix – good for lower temperature melting points – and for those stable at high enough temperatures, complete reduction in size followed by hot pressing.

Chapter 3. Synthesis Techniques

All materials utilized and studied in this work were in a solid state of matter, and techniques included classical and improved solid-state reactions. Samples were therefore prepared or weighed under an inert atmosphere to prevent unwanted oxidation or moisture-reactivity on the idle solids; an argon-filled glove box was of course an ideal choice for preparation. The glove box (Figure 3.1 (a)) is capable of maintaining concentrations of O_2 and H_2O less than 2 ppm whilst maintaining ambient temperature and a variable argon pressure controlled by pedals below the box. A plethora of elements, binary compounds, and salts (and completed reaction ingots) are stored in the glove box generally as fine powder, on the order of 50 – 200 mesh[vii], or crushed into powder with a mortar and pestle, or for soft solids, cut into millimetre-sized pieces. Chemical reactions were afterwards purged of the argon atmosphere utilizing a Schlenk line under vacuum with pressure on the order of 10^{-3} mbar (Figure 3.1 (b)), achieved via an Edwards rotary oil pump (RV5 model) and monitored by an Edwards manometer. The vast majority of samples were placed directly in silica tubes enabling them to be sealed with an oxyhydrogen torch, generating a flame hot enough to soften silica (>1923 K). This allows synthesis to occur under a static vacuum environment with minimal external contamination. Those samples that were at risk of reacting *with* the SiO_2 tubes were instead weighed in glassy carbon crucibles before placement inside the tubes to avoid the formation of silicides, or oxides – especially if the reaction is exothermic enough to crack the silica glass, the added sturdiness (alongside a reasonable reaction rate) helps alleviate this.

Figure 3.1 (a) Argon-filled glove box (b) Vacuum line and quartz sample tube (c) Manual (top), tube (middle), and programmable furnace (bottom).

[vii] Mesh is the size of the sieve powder can fall through. Larger mesh numbers mean finer powders.

Reactions are placed in furnaces (Figure 3.1 (c)) with up to six samples per furnace. Depending on the heating profile, different furnaces can be used: for constant temperature reactions, manual furnaces are typically used (Barnstead International, 1373 K FB1300 & FB1400 models); for controlled heating rates programmable furnaces are used (Lindberg/Blue, 1373 K Box Furnace, BF51800 series); controlled growth and chemical vapour transport, or CVT (3.3), can be performed with a two-zone furnace (1473 K, MTI Co. OTF-1200-2 Dual Zones Tube Furnace). Reactions typically take between 5 and 14 days to complete initially. Simple element information regarding this work can be found in Table C.1 and in general, from such tables as those found under Webelements.[117]

3.1. Traditional Solid State Synthesis

Solids generally do not have the ability to react quickly, if at all, at room temperature. In fact, to have a proper solid state reaction, it is generally assumed one must first have two key solid state components: adequate surface-surface contact, and the subsequent diffusion/counter-diffusion between reagents. The easiest way to cross the necessary energy barriers for these reactions to occur, involves mixing stoichiometric quantities of solids and heating them to hundreds or even thousands of degrees. In this case, powdered solids are ideal as surface area is maximized allowing for an efficient and complete reaction. To contrast, large single crystals or ingots have surface area with orders of magnitude fewer contacts, significantly reducing diffusion. A simple example of diffusion can be seen in Figure 3.2 (a). There are two key processes in solid state synthesis: the first of which is called *nucleation* or the solid-solid interface beginning the reaction; the second is the subsequent *growth* of the product or diffusion of the ions from the reactant surfaces to the product surface.[84] The traditional diffusion process depicted below is analogous to a semiconducting *p-n* junction, but similarly interstitial diffusion such as Li_xCoO_2 mentioned in 2.2 may occur when smaller atoms have enough energy to move throughout the crystal lattice (Figure 3.2 (b)); the aforementioned Schottky and Frenkel defects are crucial to diffusion processes.

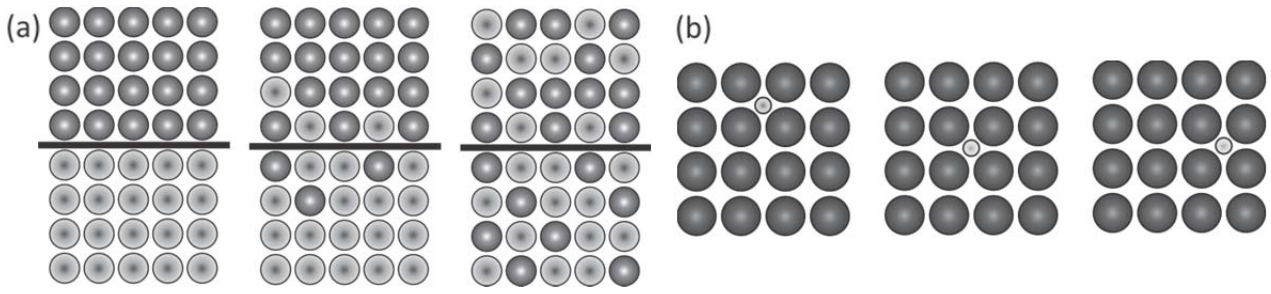

Figure 3.2 (a) Solid state diffusion process (b) Interstitial diffusion

Since reactions are driven by both time and energy, two different factors will aid in the success, purity, and rate of solid state reactions. These are the thermodynamic and kinetic factors. Thermodynamic factors determine whether the reaction can occur and whether its formation is favourable with respect to energies – or in other words, has the system reached a lower internal energy by formation of this new compound? Kinetic factors determine the time required for the formation or decomposition of a material and is usually driven by a limiting step in the reaction. For example, of the three diffusion processes: transport to the interface, reaction at the interface, and diffusion away from the interface – one must be the limiting factor. Other rate-affecting kinetic factors will be further discussed below such as temperature variation or different transport media for products. Empirical syntheses regarding the major reactions discussed in this work can be found in Table C.2 as well as descriptions found in corresponding chapters.

3.2. Flux Method

Even at high temperatures, diffusion can be a slow and cumbersome process. Not only do high temperatures use a lot of electricity, but may lead to inhomogeneity in the sample due to incomplete or sterically hindered diffusion processes. The flux method is a time-tested solid state technique that utilizes molten solids as a type of solvent in the reaction, which is usually added to the vessel in excess (say, >5x the moles) of the target compound. Often high temperatures can lead to (unwanted) binary and ternary compounds which are inherently thermodynamically stable, possessing high activation energies (E_a) and an inability to further react. To use a flux is to lower the E_a of a solid by greatly increasing the diffusion whilst maintaining a reasonably low temperature. Due to this decrease in temperature and in E_a, new compounds can be synthesized and large single crystals are able to grow at attainable temperatures. By having a solid-liquid mixture solids are drawn into solution therein lowering their melting points, and likewise this drops compound activation energy and allows diffusivity – and therefore homogeneity/crystal growth – to dramatically improve.

A *reactive flux* is defined as a chemical that simultaneously acts as a reactant and solvent. If an element chosen as a flux is also a component of the desired stoichiometry, it is an ideal scenario significantly reducing the risk of fluxes forming additional unwanted stable phases – especially binaries. For example, when In (melting at ~430 K) and Te (melting at ~723 K) are combined and heated to ~473 K, molten In is able to draw Te into solution and quickly form InTe. Since both reactants are now in a melt (liquid), diffusion rates are increased by orders of magnitude. Upon subsequent cooling of the compound, the flux matrix can be dissolved through various chemical (or mechanical) techniques to

obtain good quality crystals. Take for example the Zintl phases $Ba_2Sn_3Sb_6$[118] and $Ba_3Sn_4As_6$,[119] which were reported as not accessible from simple stoichiometric powders, however with excess Sn, typically on the order of equal atomic parts Sn versus the compound,[120] excellent crystals of both were obtained following dissolution of the tin matrix in dilute HCl. Homogeneity is greatly improved due to the presence of a high-temperature liquid during the reaction process; solid state reactions on the contrary, require direct face-on-face contact for a reaction to occur, increasing reaction time and making uniformity difficult – sometimes impossible – to obtain.

It should be noted that metals possessing low melting points such as Sn, Pb, Ga, In, etc. can be very effective flux materials as described above in the 2005 review by Kanatzidis *et al.*[120] Somewhat more care is often necessary with non-reactive metal fluxes as the common practice of washing away with dilute acid can also affect the target compound assuming it has similar stabilities. Due to the nature of the major compounds studied, these fluxes were generally avoided for a number of reasons: The structures are already doped with similar elements, precise stoichiometries are much more difficult to achieve/prove when containing unknown metal concentrations and there is a wide selection of stable binary tellurides formed by means of metal-flux reactions (i.e. PbTe when using a Pb flux).

Alternatively, binary salts can be used as a flux in a reaction. Though individual binary salts such as KCl have relatively high melting points, eutectic[viii] combinations of two salts allow chemists to precisely choose a melting point that best suits the reaction. Tables such as **Table 3.1** are therefore routinely used in a solid state chemistry laboratory to optimize crystal growth. Advantageously, most binary salt matrices can be easily dissolved in water to obtain the reaction crystals and with most materials herein, these are inert fluxes or non-reactive. There are a few disadvantages regarding the use of salt fluxes that include efforts afterwards to remove the salt matrix such as washing the ingots with water or applicable solvents; this of course adds the potential risk of the sample reacting with the solvent in the process. If crystal growth is the only intention, it is optional to remove the salt, but one must always be aware of potential alkali-doping within the target crystals and would need EDX (**6.2**) or another analysis technique to prove the flux was truly inert in each case. The salt's elements should always be considered when attempting to solve the forthcoming crystal structure should they react – special care with Li-based salts is advisable since Li is nearly if not impossible to see via standard EDX or XRD techniques.

[viii] A mixture of elements or compounds that possess a lower melting point than the individual components.

Table 3.1 Commonly used fluxes.[121]

Flux	Melting Point (K)	Stoichiometric Ratio (mol %)
LiI-RbI	525	38 : 72
KCl-LiCl	626	60 : 40
LiI-KI	659	36 : 64
KCl-$MgCl_2$	696	70 : 30
RbCl-$MgCl_2$	720	26 : 74
NaCl-RbCl	823	56 : 44
KCl-KI	872	60 : 40
KCl-KBr	990	65 : 35

3.3. Chemical Vapour Transport

Known for its ability to generate large crystals from small sample quantities, chemical vapour transport (CVT) is an excellent method for growing reacted, annealed powders into measureable single crystals. These types of reactions are generally performed over a small temperature gradient just below the melting point of the compound; it therefore must be reserved for pure samples with a known (or estimated) melting point to succeed. The horizontally-set reaction tube can be conducted with a standard tube furnace or a gradient zone furnace. The 2-zone furnace is typically used. CVT is a chemical reaction where a solid phase, A, and a gaseous transport agent, X, form a gaseous intermediate which is able to diffuse from a hot temperature, T_H, to a cold temperature, T_C, or vice-versa depending on the ΔH° of the reaction. At equilibrium in the simplest case:

$$A_{(s)} + n{\cdot}X_{(g)} \rightleftharpoons AX_{n\,(g)}$$

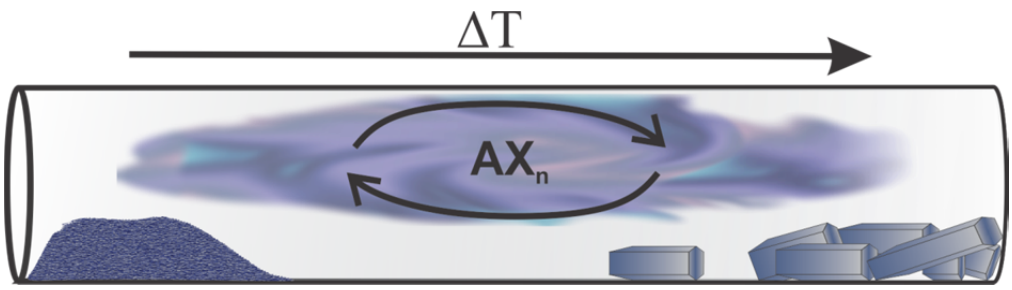

Figure 3.3 Chemical vapour transport reaction.

The direction of diffusion is dependent on the E_a of the unstable intermediate. If its formation is exhothermic, the compound will diffuse towards T_H, but if it is endothermic, it will diffuse towards T_C. A good transport agent must form semi-stable (typically binary) compounds with each chemical element in the reaction, each having boiling points (ideally) significantly below the temperature selected for CVT.

For example, if Bi_2Te_3 is the powder, X must form intermediates with both Bi and Te for the reaction to work. Typically halogens can achieve this; the solid halogen I_2 as well as Cl_2 gas – generated, in this case from powdered $TeCl_4$ – were both utilized in this work to achieve crystal growth from powders; to avoid Te contamination, $TeCl_4$ (thus Cl_2 CVD) was saved only for reactions designed to contain Te. Typically a small quantity of $X_{(g)}$, on the order of 5 – 10 mole percent, is utilized in the reaction to avoid the formation of undesirable iodides or chlorides or cracking of reaction tubes from thermal expansion.

3.4. Arc Melting Reactions

Because many transition metals – in the case of this work, namely exploratory syntheses – have melting points on the order of thousands of degrees Kelvin, a typical solid state reaction on the order of 923 or 1073 K may be insufficient to react the elements, depending on their melting point – even if some ingredients are in a molten state. Producing a massive amount of current from a generator, an arc of argon plasma is created in a chamber filled with the solids to be melted. The resultant electric arc is capable of producing temperatures around 2773 K in seconds. Due to the volatility of many of the studied elements such as Sb or Te, this procedure is not recommended when said powders are in their elemental forms; in this case, excess powder should be used to offset the loss. Generally, a sample that is to be arc-melted is first placed in a resistance furnace between 773 – 1073 K to form a series of binary compounds. After pressing the sample into a cylindrical (8mm diameter) pellet, it is arc melted for seconds; enough to minimize any stoichiometry losses whilst still initializing the high-temperature reaction. This homemade setup is displayed in Figure 3.4.

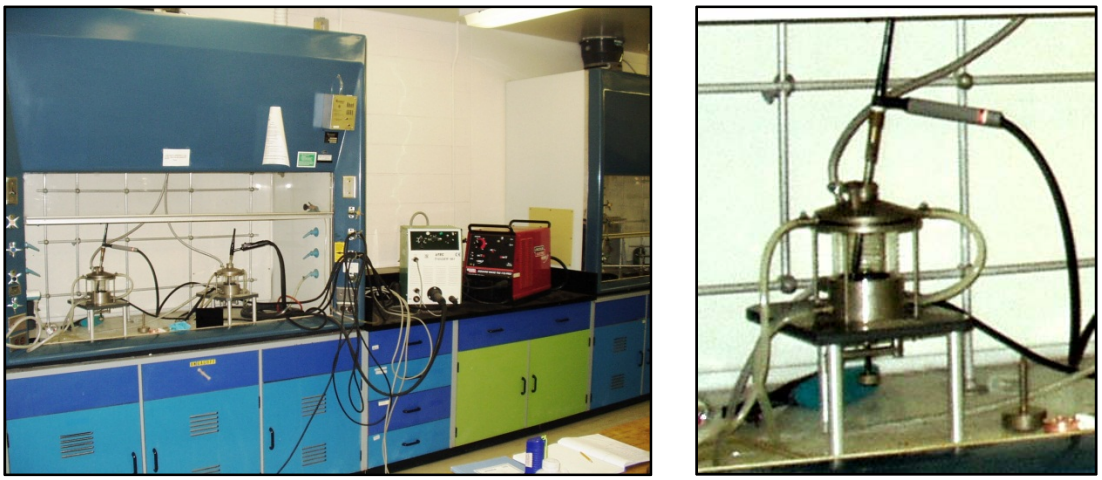

Figure 3.4 Arc-melting setup.

The procedure is carried-out on a cylindrical copper block under dynamic argon flow with cooling water travelling throughout the setup. The copper block is surrounded by steel and encapsulated in quartz glass and the arc is created by a tungsten filament and a current source running at 20 A (Lincoln Electric Square Wave TIG 175 Pro). An ingot of Zr metal is first arc-melted such that any remaining oxygen in the system is neutralized before it potentially reacts with the sample. Following the Zr ingot, the sample pellet (or pellets) is arc-melted for approximately 30 seconds per side. Samples are then re-crushed, X-rayed and typically returned to a tube furnace for annealing or the aforementioned transport reactions for single crystal growth.

3.5. Ball-Milling Technique

Though typically utilized to reduce the grain size of previously synthesized materials (i.e. top-down synthesis), this is still considered a preparatory step for obtaining the desired materials. The technique can however, suffice for compound synthesis as executed by Yu *et al.*[122] as the primary synthesis technique for Bi_2Te_3 from the elements. Powders are placed in balanced stainless steel grinding bowls with ZrO_2 marbles of 2 mm diameter. The material is typically mixed with a neutral solvent for heat-absorption which in this case is 2-isopropyl ethanol of at least 99.8 % purity. Following sealing of the bowls, the apparatus is centrifuged at 1000 rpm for 5 to 10 minute intervals, ensuring the heat generated does not melt the material or destroy the instrument and allowing one to release the excess pressure from the bowls. The setup used in the Kleinke lab is a Fritsch Pulverisette 7 Premium Line ball-miller. Materials can be ground on several settings depending on what is programmed into the instrument, but the choice for experiments in this work was 15 – 20 minutes of ball-milling in intervals of 5 minutes on, with 10 minutes rest. Materials are extracted via syringe and allowed to dry on evaporating dishes, typically yielding 50 to 70 % of the original powder, which is balanced to ~1 g per bowl.

Section II: Analysis Tools and Techniques

Instruments and theories utilized in the field for understanding samples

Chapter 4. X-Ray Diffraction Analysis

As all of the structures mentioned in this document are inorganic crystalline solids, the primary form of sample analysis are techniques utilizing X-rays and the theory of diffraction. The X-ray radiation itself was discovered between 1875 and 1895 by the German physicist Wilhelm Röentgen (1845 – 1923), effectively proving the existence of X-rays via their emission by means of experimental discharge tubes. X-rays, being electromagnetic radiation, are defined by their wavelengths, which lie between 0.1 and 100 Å – between gamma-rays and ultraviolet radiation. Since X-ray waves should commensurate between atom size and atomic bond distances in order to interact with crystalline materials, the X-rays used here are between 0.7 – 1.5 Å: the same order of magnitude as crystal lattice spacing.[83] X-rays' use in the field of crystallography was not known until 1912 when Max von Laue discovered the capability of crystals to diffract the beam, similar to a 3-dimensional grating, during studies on the radiation's wave versus particulate nature. The outcome of this Nobel prize-winning discovery was a series of equations relating the incident and diffracted X-ray beams, defined by Laue as follows:[123]

$$\text{(a) } a(\cos\alpha - \cos\alpha_0) = h\lambda \qquad \text{(b) } b(\cos\beta - \cos\beta_0) = k\lambda \qquad \text{(c) } c(\cos\gamma - \cos\gamma_0) = l\lambda$$

Equation 4.1 Laue relationships.

where $a/b/c$ are the crystal unit cell dimensions, $\alpha/\beta/\gamma$ are the angles created by the diffracted beam and the affected crystallographic plane, $\alpha_0/\beta_0/\gamma_0$ are the angles created by the incident beam with the affected crystallographic plane, $h/k/l$ are the corresponding Miller indices – integers corresponding to scattering planes, and λ is the wavelength of the X-rays. This yields three crystallographic conditions for crystal scattering in each of the directions in the crystal lattice – but if combined and related to simple reflection phenomena, can these broad relationships be simplified? Soon thereafter, the father-son duo Sirs William Henry and William Lawrence Bragg discovered that in order for the aforementioned parallel relationships to interfere constructively in ordered solids, they can be reduced to a simple relationship known as Bragg's law:[124]

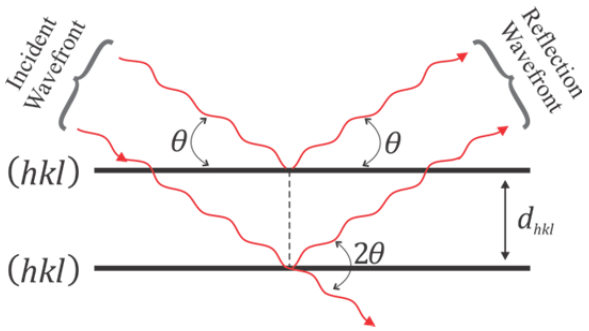

Equation 4.2 Bragg's law: $n\lambda = 2d_{hkl}\sin\theta$

Having d_{hkl} represent the distance between crystallographic planes (hkl), θ the angle between the plane and the X-ray beam, n an integer value and λ, again, the wavelength of the X-ray beam. Therefore two X-ray beams diffracting off the sample at the same times must travel a distance of $n\lambda$ if they are to be observed during experimental data acquisition. Since all diffraction experiments used take advantage of a monochromatic wavelength, λ is precisely known allowing one to observe different combinations of d and θ. As values of d versus θ progress, differentiations can be made between possible space symmetries (i.e. tetragonal, cubic, etc.) based on the reflections that are present in the X-ray patterns. Higher symmetry patterns consist of reflections having fewer unique (hkl) values than their respective lower symmetry equivalents because many reflections will be related to each other through symmetry operations. Consider both a cubic and orthorhombic system. In the cubic system, all dimensions are equivalent, leading to the same observed reflection for (100), (010), (001) planes whilst the orthorhombic system, containing three different directions, has separate reflections for each. This phenomenon can be used to follow the distortions along *a*, *b*, *c* of structures as a function of chemical substitution or temperature, etc.

The observed reflections in reciprocal space and their corresponding position and intensity comprise the raw experimental information. The complete description of scattering within the crystal is described by the equation for the scattering factor F_{hkl}, which is the sum of the atomic scattering, f, of each unique atom, j, in the crystal and its relation to Miller Indices and atomic position (xyz). This relationship is depicted below in Equation 4.3 (a). All information about the crystal structure and its atoms is contained within F_{hkl}, whose square is proportional to the intensity, I_{hkl}, as follows: $I_{hkl} \propto |F_{hkl}|^2$.

$$\text{(a) } F_{hkl} = \sum f_j e^{2\pi i(hx_j+ky_j+lz_j)} \qquad \text{(b) } \rho_{xyz} = \frac{1}{V}\sum_h \sum_k \sum_l F_{hkl} e^{-2\pi i(hx+ky+lz)}$$

Equation 4.3 (a) Structure factor - exponential form. (b) Electron density within crystal.

The closely related electron density (Equation 4.3 (b)) is associated with the structure factor via the Fourier transform function, which allows for a convenient scientific relationship: If a crystal's structure factors are known, one can calculate the precise locations of electron density in the crystal and therefore, know the precise location of the atoms and their sizes within. Diffraction is the affected X-rays, in this case, bending or modulating due to the presence of electrons. Electron density not only controls diffraction, but provides information on the size of the atoms involved due to each element's unique electron density. Because the scattered X-ray beam is reduced during diffraction as with the amplitude, a scaling factor, s, and two corrections – Lorentz, L, (geometrical) and p (polarization) – are added to Equation 4.4 displayed below, the experimental intensity (I_{hkl}) is equivalent to the square of the wave's amplitude or structure factor (F_{hkl}).

$$I_{hkl} = sLp \cdot F_{hkl}^2$$

Equation 4.4 Diffracted intensity.

This provides a comparison between the observed reflections in reciprocal space and their corresponding calculations determined from a structural model.

4.1. Powder X-Ray Diffraction (p-XRD)

Experimentally, a polycrystalline solid-state sample is undoubtedly easier to obtain than a single crystal of the same sample. That is, a sample that is comprised of small crystallites typically on the order of 0.1 – 100 µm and randomly oriented, or stacked along specific orientations. When a monochromatic beam of X-rays hits a powdered sample, the diffraction no longer occurs in a set direction as discussed above, but continues in all directions (that obey Bragg's Law) as a *Debye-Sherrer diffraction cone* (Figure 4.1) – named for the Dutch and Swiss physicists who, in 1915, first attempted the technique with a strip of photographic film surrounding their sample as a collection method for the diffracted marks.

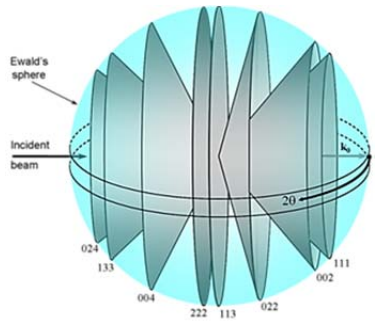

Figure 4.1 Debye-Scherrer powder diffraction cone.[125]

Upon completion of the experiment, when the photographic film is unrolled, there is a series of lines each with their own unique 2θ angle and intensity (I), or thickness, when read off the film. In modern times however, films are infrequently used since the invention of detectors such as charge-coupled devices (CCDs), scintillation-style and others which can achieve more convenient diffraction detections. Since diffraction and crystal spacing are generally understood in the reciprocal space frame of reference, it is beneficial to explain the phenomenon from the same perspective. Thusly, one is able to discuss an Ewald sphere (Figure 4.2). Diffracted planes from crystallites in real space can be depicted pictorially as nodes (or points) in reciprocal space via a Fourier transform. In order to graphically display this, the Ewald sphere is constructed with the sphere's centre being the selected origin in reciprocal space and the sphere's radius being defined as $1/\lambda$, where k_o is the incident radiation, k_1 is the diffracted radiation that has moved by angle 2θ. The diffracting crystallographic plane (hkl) is then located at angle θ. The construction of this sphere is depicted below on the left of Figure 4.2.

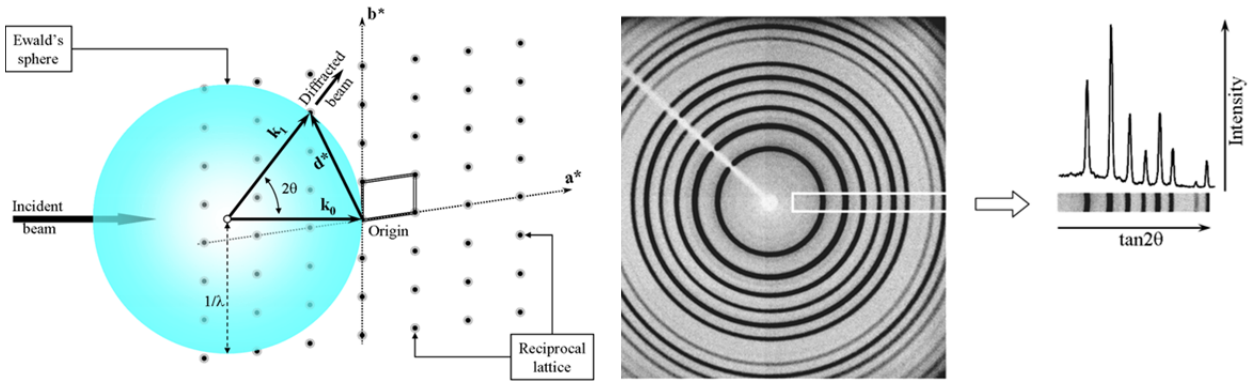

Figure 4.2 Ewald sphere: Origin of a powder diffractogram.[125]

The Ewald sphere depicts diffracted rings of X-rays with varying angles and intensities. When projected into a linear plot, as in the right half of Figure 4.2, it becomes a typical powder diffractogram, which is observed during PXRD experiments and comprises the basis of the X-ray fingerprint for crystalline solids. Outcome is therefore a histogram of 2θ ranges with varying intensity, each peak of which can be assigned a unique (hkl) value that can later be indexed once the cell was determined. Consequently, this loss of dimensionality in reciprocal space also leads to some of powder diffraction's disadvantages such as overlap of peaks, difficulty with accurately subtracting pattern backgrounds, and preferential orientations – systematic intensity gains due to crystallites stacking in a non-randomized format. [126]

The majority of samples emerge from the furnaces as ingots which are subsequently crushed into a fine powder via a mortar and pestle. Samples can then be placed on an Al-sample holder, flattened and examined by an INEL powder diffractometer (Figure 4.3 (a)) with a curved position-sensitive detector (PSD) utilizing Cu-$K_{\alpha 1}$ radiation produced by an X-ray tube. The PSD uses the sample's X-ray photons to release electrons on a positive electrode whose travel time is subsequently measured as it reaches the end of the detector which corresponds to the photon`s original position; it is an efficient detector that measures with good resolution. As displayed by Figure 4.3 (b), the sample is mounted in the center on an adjustable rotating aluminium sample holder with the Cu-K_{α} beam discharging on the right-hand side with the curved black PSD capturing the diffracted radiation between >0° (horizontal) and 120° 2θ angles.

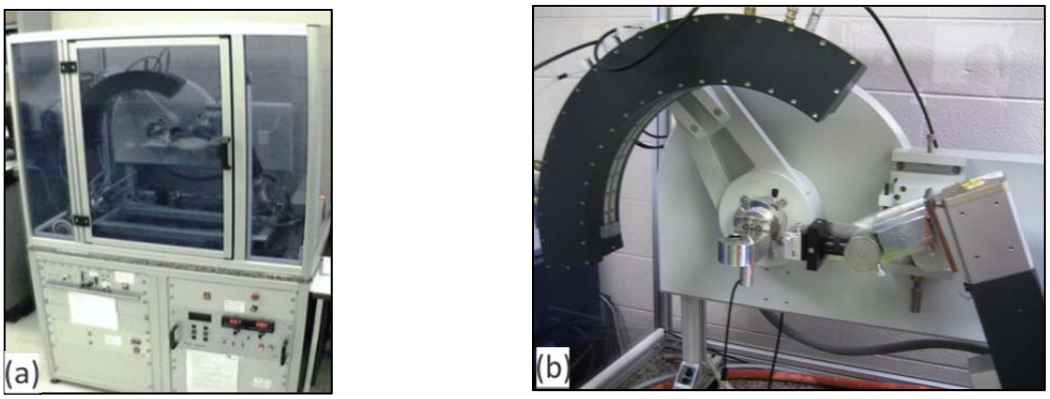

Figure 4.3 (a) INEL powder diffractometer. (b) Position sensitive detector (PSD).

The supporting computer will then read and plot the angle of diffraction (2θ) on the x-axis and the intensity of the peaks (I) on the y-axis. Conventionally, samples are measured using a PSD between 10 and 20 minutes each for a reliable distinction between low-intensity peaks and background radiation.

4.2. Single Crystal Diffraction

Specific growth techniques mentioned in **Chapter 3** will yield large single crystals (generally 20 – 400 μm depending on the elements present in the sample) that can be analyzed via a different diffraction technique: Single crystal diffraction. Due to the loss of dimensionality with the p-XRD method from production of cone signals (2-D) and further reduction to a histogram (1-D), one requires a reference diffractogram before the data can be analyzed and understood, which is quite obviously difficult for samples containing yet-to-be catalogued materials, neither studied nor even known. In order to understand the atomic ordering and space symmetry, a single crystal diffractometer with an area detector such as CCD can be utilized for a more complete analysis.

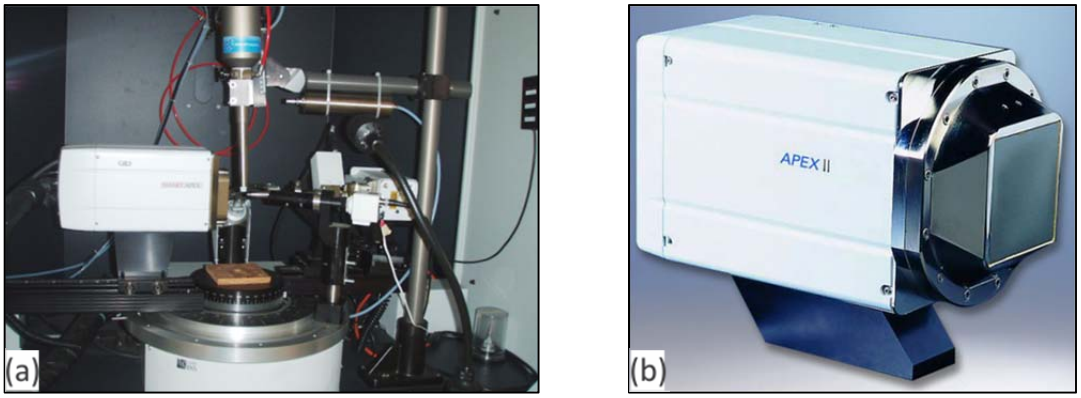

Figure 4.4 (a) Bruker instrument. (b) Bruker APEX II CCD detector.

The Department of Chemistry at the University of Waterloo utilizes a Bruker single crystal instrument (displayed above) including an X-ray tube emitting graphite-monochromatized Mo-K_α radiation ($\lambda = 0.71073$ Å), whilst the instrument contains a Bruker Smart APEX CCD detector (Figure 4.4 (b)), possessing the APEX SMART[127] software to collect diffraction frames. This is a *charge coupled device* detector which utilized pixels that detect locations of diffracted waves once converted into visible light. The instrument uses an ω-scan to collect its blocks of data. This data undergoes a series of corrections known as *data reduction*. As briefly mentioned before, the Lorentz (geometric) correction (L) corresponds to the variant path length of travelling waves in reciprocal space before passing though the aforementioned Ewald sphere, whilst the polarization correction (p) readjusts the partial polarization of the monochromated X-ray beam in the direction perpendicular to the plane. While the Lorentz correction varies from instrument-to-instrument, the polarization is only slightly affected by the nature of the instrument; combining them yields the parameter L_p shown in Equation 4.5 (a). The magnitude for the scattering factor, with corrections, is thusly calculated as below (Equation 4.5 (b)) via a rearrangement of Equation 4.4,

$$L_p = \frac{1+\cos^2\theta}{2\sin^2\theta} \qquad |F_{hkl}| = \sqrt{\frac{sI_{hkl}}{Lp}}$$

Equation 4.5 (a) Lorentz-polarization correction (b) Data reduction factors.

where s is the scaling factor. The SAINT[128] software is used to apply these corrections to the data and then following, it performs a unit cell refinement, while SADABS[127] software applies an absorption correction to the data, because the heavy atoms (many of which are used in this document) absorb a disproportionately large quantity of radiation as opposed to their lighter counterparts. By making a comparison between the observed structure factors, F_o, one is able to determine the quality of collected data. This is calculated using Equation 4.6 (a), R_{int}.

$$R_{\text{int}} = \frac{\sum\left|F_o^2 - F_{o\,(\text{mean})}^2\right|}{\sum F_o^2} \qquad\qquad F_{hkl} = |F_{hkl}|e^{i\phi}$$

Equation 4.6 (a) Internal residual value. (b) Phase factor.

Following the raw data processing, it is necessary to solve the crystal structure and therefore identifying the internal atomic positions (Wyckoff sites). This must be done via a structural solution to solve the phase followed by a refinement process, as only the magnitude of the scattering factor is known from the experiment ($|F_{hkl}|$), shown in **Equation 4.6 (b)**. The phase (ϕ) of the structure factor must be determined since the experiment cannot give this piece. There are two classical ways of finding the phase. The first method is known as the *Patterson method*, a strategy that is utilized in the presence of one particularly heavy atom; the coordinates are then extracted from the bond distances between the peaks.[83, 129] Since this research is generally concerned with compounds that contain numerous comparably heavy elements such as $TlBiTe_2$ or $Ba_3Cu_{17-x}(Se,Te)_{11}$, etc., the *direct method* is almost exclusively used here. The direct method is the most used crystal solution technique for small molecules and is applied to systems containing many heavy – or light – scattering powers. This strategy involves inequalities, probabilities, and separate solutions for centro- and non-centro- symmetric crystals.

The SHELXTL[130, 131] solution software is employed to systematically refine atomic positions, split sites, occupancy, thermal motion, etc. by a series of least-square iterations performed by the user until a satisfactorily small difference between observed and calculated structure factors, F_o and F_c respectively, is found. This is verified by looking at statistical factors found below in **Equation 4.7 (a) & (b)** which are two ways of observing the difference between observed and calculated values; acceptable R values are conventionally less than 5 and 10 % respectively, but vary from refinement to refinement.

$$\text{(a)}R_1 = \frac{\sum||F_o|-|F_c||}{\sum|F_o|} \qquad \text{(b)}wR_2 = \sqrt{\frac{\sum w\left(F_o^2 - F_c^2\right)^2}{\sum wF_o^2}} \qquad \text{(c)}GOOF = \sqrt{\frac{\sum w\left(F_o^2 - F_c^2\right)^2}{n-p}}$$

Equation 4.7 (a) Residual factor. (b) Weighted residual factor. (c) Goodness of fit.

The goodness of fit ($GOOF$) is also displayed above, as it compares observed versus calculated structure factors with the number of reflections used (n) and the number of parameters refined (p). An acceptable $GOOF$ implies data has been obtained with a significant number of useable reflections and a logical refinement or in other words, a reasonable quantity of refined parameters such that $GOOF \approx 1$ denoting a sufficient similarity between observed and calculated factors.

4.3. Powder Diffraction Refinements

When it becomes difficult to produce a single crystal for structure determination, there are alternative methods that can be utilized on powdered samples of high purity to ascertain the unit cell and crystallographic information for a sample. All of the information obtained in a single crystal X-ray measurement is still contained in a powder diffractogram, but the dimensionality of the data is lost as the 3-dimensional reciprocal reflections are depicted in a 1-dimensional histogram. A known and well-analyzed sample functioning as a model however, can be used as a method of comparison with a high-quality experimental powder diffractogram. The subsequent changes of unit cell dimensions, angles, etc. can reveal how an experimental X-ray pattern has changed from the model pattern.

The aforementioned powder X-ray equipment can still be utilized to obtain high-accuracy patterns. Differences arise in the execution of the experiment: the instrument should be aligned with a proper calibration; samples are left overnight (typically 12 hours), as opposed to 15 minutes, to reduce the background signal to a minimal state and to minimize peak overlap by reducing peak width; all refinement samples are placed on the same aluminium sample holder, namely the holder containing silicon powder measured daily to monitor any 2θ shifts; samples are sometimes mixed with a reference In_2O_3 powder or other very well-known patterns to accurately track any instrumental zero-point shifts the machine may encounter from a run-to-run basis. The corresponding data is fed into the General Structure Analysis System (GSAS) software[132, 133] run under the EXPGUI[134] (graphical user interface) downloaded for free from the CCP14 website.[135] This software package allows the user to process and analyze the data with the input of 3 additional files: The experimental X-ray pattern, the model of interest as a cif (ideally sharing the same space group and similar atomic positions), and the parameter file (.prm) corresponding to specific instrumental characteristics, such as the wavelength used. A completed refinement is observed graphically when the model and experimental diffractograms overlap (almost) exactly. Mathematically, this can be observed utilizing the same R-values presented in **Equation 4.7**. It is prudent to note that following the pattern collection, additional programs such as Crysfire,[136] Dash,[137] or Fox[138] can be used to index the powder pattern and therefore obtain unit cell parameters. This intermediate step preceding refinement is sometimes necessary when the model being input into GSAS software is either poor or non-existent.

4.3.1. Rietveld Method

In 1967, Hugo Rietveld published his first study of a structural refinement involving a neutron diffraction pattern.[139] By 1969 a full refinement of the $CaUO_4$ crystal structure was performed from a neutron diffractogram via Rietveld's strategy.[140] Dr. Rietveld was more partial towards neutron diffraction at the time due to the simple Gaussian shape of the peaks, a problem that was not resolved for X-ray diffraction until Malmros and Thomas' peak-shape functions, such as pseudo-Voigt and Lorentzian functions in 1977[141] allowed researchers to simulate peaks beyond the simple Gaussian type; those that make neutron patterns so simplistically appealing in this case. A Rietveld refinement, or *full pattern refinement*, uses the *method of least squares* to minimize the differences in the pattern's experimental and modeled parameters. This function depicted below (Equation 4.8) sums the weighting factors ($w_i = 1/y_{i(\text{obs})}$) with the observed ($y_{i(\text{obs})}$) and calculated ($y_{i(\text{calc})}$) pattern intensities for i data points.

$$S = \sum_i w_i (y_{i(\text{obs})} - y_{i(\text{calc})})^2 \ (= \text{minimum})$$

Equation 4.8 Method of Least Squares.

The entire diffractogram is converted into a series of thousands of points with varying $y_{i(\text{obs})}$ shown in Equation 4.8 versus 2θ, other angles or energy-based factors such as neutron time-of-flight or X-ray wavelength on the x-axis.[142] Rather than treating the diffraction pattern as a series of intrinsic overlapping peaks, the entire image is thusly treated as an experimental observation where peak shape (i.e. Gaussian, Lorentzian, etc.), peak width (i.e. full width at half maximum), preferred orientation, and strategies behind calculation (i.e. order and quantity of parameter-refinement, least square steps, etc.) can be adjusted such that a calculated pattern (input as a model) matches the one observed in the experiment. Shown below (Equation 4.9 (a)) is the Pseudo-Voigt function for peak shape which combines both Gaussian (C_G) and Lorentzian (C_L) functions to generate a better fit than either alone. The variable η determines the proportion of Gaussian:Lorentzian character.

$$y(x) = PV\ (x) = \eta \frac{C_L^{1/2}}{\sqrt{\pi H}} e^{-C_G x^2} + (1-\eta)\frac{C_L^{1/2}}{\pi H}(1 + C_G x^2)^{-1} \qquad H = (U\tan^2\theta + V\tan\theta + W)^{1/2}$$

Equation 4.9 (a) Pseudo-Voigt function.[126] (b) Cagliotti formula.[143]

The full width at half maximum ($FWHM$) is also used in Equation 4.9 (b) as a key component in the pseudo-Voigt fitting function; U, V, and W comprise variables that are refined during the Rietveld process.[126] In order to construct a viable crystal structure refinement, almost all parameters one can

imagine are simultaneously modeled including representations of the proposed crystal structure, effects caused by diffraction on the powder, inherent characteristics of the sample such as lattice parameters, and effects unique to instruments such as zero-point correction.[142] The true strength in this method is the exceptionally large quantity of parameters that can be simultaneously refined. For example, in 1984 Baerlocher managed to refine 181 parameters with X-ray data corresponding to ZSM-5 zeolite minerals.[144] By observing the shifting of 2θ peak positions, the unit cell parameters can be determined and with the insertion of a similar structural model (typically in the form of a cif), refinement of atomic positions, thermal displacement parameters, and mixed atomic sites can further correlate the experimental peaks with the calculated peaks. The outcome is a new cif with accurate experimental unit cell dimensions, bond angles/distances, space group, atomic positions and mixed occupancies – in other words, a refined crystal structure.

4.3.2. Le Bail Method

Quite similar in practice to the Rietveld method, Le Bail refinements are often performed when little information can be gained from the refinement regarding Wyckoff sites or adjustment of most parameters corresponding to F_{hkl}. This typically suggests a sole interest in the change in unit cell size. In 1988, Armel LeBail studied the Rietveld method[145] and asked the question: "Can this same approach be used if there is no structural model present?" The outcome of his pursuit was known as *whole-powder pattern decomposition* and no longer required the atomic coordinates to calculate peak-intensities before undergoing the least squares refinement. Instead, the integrated peak intensities were treated as arbitrary values and refined to their correct stature as independent parameters. This means the pattern is decomposed into its Bragg components piece-by-piece instead of utilizing a structural model as with Rietveld to govern the intensities.[126] The technique can be used to fully analyze an unknown powder pattern,[145, 146] but can also be used as a preliminary step in solution of a Rietveld problem by first obtaining a reasonable model via decomposition, then switching to Rietveld afterwards for a full refinement. The Le Bail method is primarily used here as a quick solution method for unit cell parameters as opposed to a fully executed refinement on atomic positions and thermal parameters.

Chapter 5. Physical Property Measurements

Physical property measurements are a critical component to understanding and analyzing thermoelectric materials. Since thermoelectric materials are governed by the dimensionless figure of merit (ZT) discussed in Section I, the instruments in this chapter generally measure one or more of those pertaining variables. Physical property measurements not only determine whether a material will make a good potential application-grade thermoelectric, but how a material's behaviour changes with experimental variations. These property trends are quite valuable as they give an idea of how the charge carriers within are behaving – something that is typically not directly measured through instruments. For example, an increase in the electrical conductivity (σ) magnitude can suggest that there are more charge carriers available to travel through the crystal lattice whilst the shape of the electrical conductivity curve can imply changing behaviours such as intrinsic semiconductor, extrinsic semiconductor, semimetal, etc. These concepts (with some examples) were discussed in the previous Section I.

The vast majority of samples were measured on-site with instruments belonging to the Kleinke group utilizing cold-pressed pellets annealed at temperatures ~100 – 150 K below the material's melting point. As a result, pellet densities (ρ) were between 80 and 90 % of $\rho_{\text{theoretical}}$; this was determined by weighing the pellet on an analytical balance and measuring the dimensions with a Vernier calliper, accurate to a 100$^{\text{th}}$ of a millimetre. In order to make proper pellets, powder on the order of 200 – 400 mg was typically used. Selected samples were sent to Professor Donald Morelli of Michigan State University for hot-pressing, which entails simultaneously heating the sample and pressing it into pellet form with an 11.7 mm diameter. This technique generally yields ρ's between 95 and 98 % of $\rho_{\text{theoretical}}$, further improving the outcome of physical property results. Due to the presence of air pockets, grain boundaries, or potential internal cracks, it is inaccurate to perform property measurements on purely cold-pressed samples, as the aforementioned deformities can lower σ by almost three orders of magnitude and κ sometimes to ½ of its realistic value; while the S magnitude is generally unaffected, strange curve shapes, or behaviours, and even bogus *p*-*n* transitions have empirically been observed on cold-pressed samples.

5.1. Power Factor Measurements: ZEM-3 Instrument

The numerator of Z, $S^2\sigma$, is known as the Power Factor (PF) and is the product of the Seebeck coefficient squared and the electrical conductivity. The ULVAC-RIKO ZEM-3 setup is the most frequently used instrument in the Kleinke group at this time, due to simultaneous measurement of S and σ over a wide temperature range – generally between ambient temperature and 673 K in this work because conventionally, materials are examined 100 K below their melting point to ensure the machine is not affected by melting compounds or vaporizing elements.

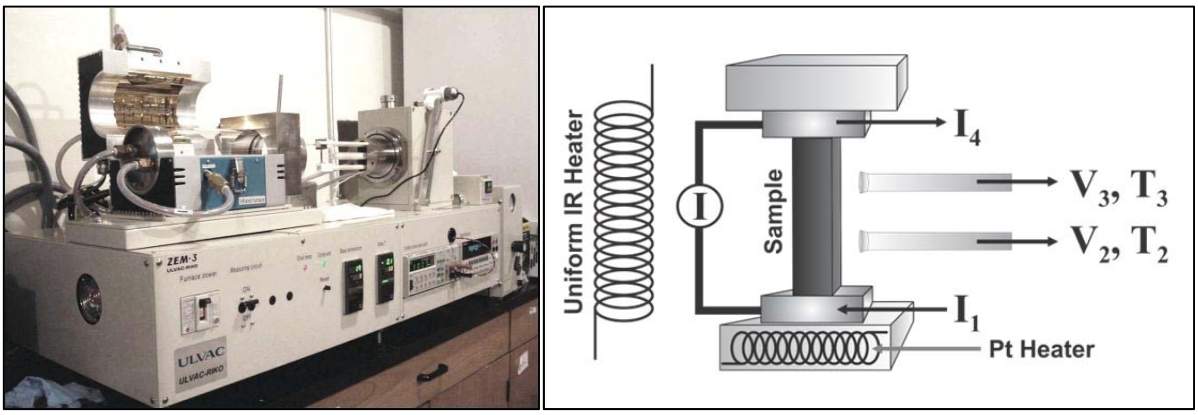

Figure 5.1 (a) ULVAC ZEM-3 (left) ZEM schematic (right)

Pellets for the ZEM must have a minimum of 6 mm length in order to be properly measured by the horizontal probes displayed in Figure 5.1 (b), which are capable of 3, 5 or 8 mm separations. The four visible points of contact in the ZEM pellet mount are displayed in Figure 5.1 (b) along with conceptual representation of the instrument's functionality. A digital microscopic camera (Dino-lite plus, AnMo Electronics Co.) and analysis software is used to obtain accurate measurements of pellet dimensions and probe separations along with the Vernier calliper initially used to measure pellets.

The Seebeck coefficient, S, is simply defined in **Chapter 1** as $\frac{\Delta V}{\Delta T}$. This is achieved by the instrument creating a temperature difference between the platinum-iridium thermocouples, then measuring the voltage difference (ΔV) utilizing the same probes. ΔT is created by taking the average of three manually input temperature targets for the internal platinum heater (Figure 5.1 (b)) which in this case are set to '10', '15' and '20' K, leading to ~2-3, ~3-4 and ~4-5 degree differences above the target ambient temperature (T) respectively. This leaves enough space between measured values for the system to create a reasonable line-of-best-fit such that this slope becomes the measured ΔT taken to achieve the experimental S values at each T.

The electrical conductivity, σ, is measured via the four-point probe method (Figure 5.2). Current (I) is passed through the vertical electrodes (in alternating directions to average $\pm V$ – further discussed in 5.5) while V is measured between the horizontal probes, as with S. With the maintenance of a constant, uniform current flow over the area (A) through the length of the pellet, the physical length (L) between V_1 and V_2 allows one to observe the electrical potential difference and ascertain the material's resistance (R). With the following three relationships in Equation 5.1, σ can then be calculated utilizing Ohm's law and accurate pellet dimensions:

$$\text{(a) } R = \frac{V}{I} \qquad \text{(b) } \sigma = R^{-1} \cdot \frac{L}{A}$$

Equation 5.1 (a) Ohm's Law (b) Specific resistivity

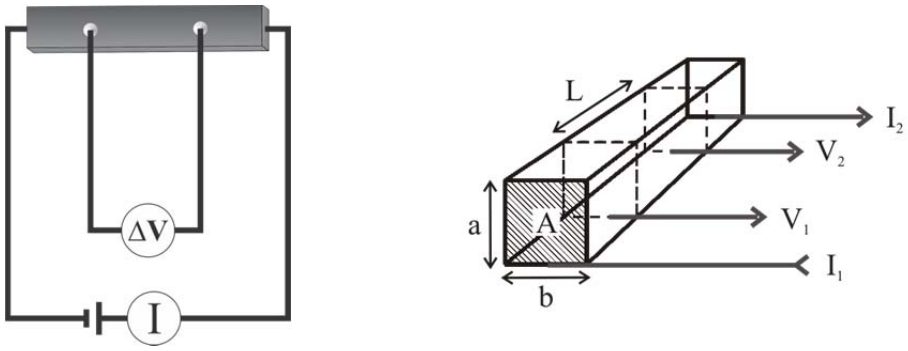

Figure 5.2 Four-point probe method.

It should however be noted that practically, the measured voltage (V_{meas}) possesses several contributions to Ohm's law (Equation 5.1 (a)): $V_{\text{meas}} = Ir_{\text{wire}} + Ir_{\text{contact}} + IR$. Instrumentation within the ZEM ensures that $Ir_{\text{wire}} + Ir_{\text{contact}}$ are minimized to ensure an accurate voltage measurement; this is compensated for by utilizing an input impedance ≥1 GΩ such that $IR \gg Ir_{\text{wire}} + Ir_{\text{contact}}$. The aforementioned camera gives the values necessary for the dimensions included in the conductivity units. This allows for accurate calculation of σ via Equation 5.1 (b).

In a recent two-step international round-robin study on *n*- and *p*-type Bi_2Te_3, machines from seven labs including the Kleinke lab revealed that measurements were not only reproducible on a measurement-to-measurement basis, but also from a lab-to-lab basis. Seebeck measurement is the most precise with a spread of approximately ±4 % across the temperature range of 298 K to 573 K. Measurement of σ was between ±10 % and ±12.5 % not only because of the measurement itself, but the added error of measuring pellet dimensions and probe separation.[147] The error bars for the ZEM plots featured in this work are therefore approximately as large as the displayed points.

5.2. Thermal Conductivity Measurements: Flash Line 3000

The denominator of Z, κ, is a combination of both components explained in **1.2.3** – the lattice and electronic contributions towards total thermal conductivity, κ. Thermal conductivity measured in the Kleinke group is done so via a Flash Line 3000 thermal diffusivity setup (ANTER Corp.) run under argon gas flow utilizing the flash method. The laser flash method is known for its quick and reproducible measurements that function at low temperatures, room temperature and reasonably high (at least 1073 K) measurement range[13] (**Figure 5.3**).

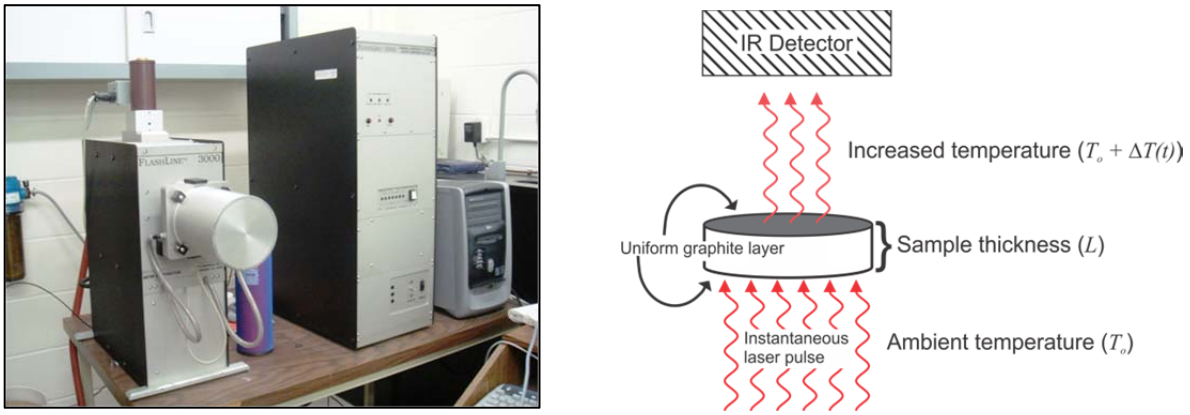

Figure 5.3 Flash Line 3000 (left) Flash method (right)

Thermal conductivity is determined from the **Equation 5.2 (a)** displayed on p53, where α represents the thermal diffusivity, ρ represents the pellet density and C_p, the specific heat capacity of the material. To digress slightly, all of these parameters are best determined experimentally, there are however some limitations to this idea. First of all, the density (ρ): Since there is no hot press on-site in the Kleinke group pellets are annealed, typically leaving materials 15 % short of their ideal density. Secondly, the heat capacity (C_p) is ideally measured via DSC and a standard reference material. The DSC setup discussed in the following subheading is insufficient to accurately measure the specific heat of samples. Resuming discussion of the thermal conductivity, α is represented by **Equation 5.2 (b)** with sample thickness L, and halftime ($t_{1/2}$) for the underside to reach half of its maximum temperature rise. The density, ρ, is calculated simply by weighing the pellet and dividing it by the volume of its cylindrical shape ($V_{\text{cylinder}} = \pi r^2 h$). Lastly, the heat capacity is estimated following **Equation 5.2 (c)**, the Dulong-Petit law, where R is the gas constant $(\text{J}\cdot\text{K}^{-1}\text{mol}^{-1})$ and M_{avg} is the average molar mass $(\text{kg}\cdot\text{mol}^{-1})$ of the material. The Dulong-Petit law uses classical physics to empirically state the heat capacity of a crystal. The law is valid for heavy elements at room temperature (and up) or lighter, strongly bound elements (i.e. metallic beryllium) only at high temperatures and is therefore valid in these experiments.

$$\text{(a) } \kappa = \alpha \rho C_{\mathrm{p}} \qquad \text{(b) } \alpha = 0.1388 \frac{L^2}{t_{1/2}} \qquad \text{(c) } C_p = \frac{3R}{M_{\mathrm{avg}}}$$

Equation 5.2 (a) Thermal conductivity (b) Thermal diffusivity (c) Specific heat capacity

Samples are coated in graphite on both sides to ensure an even heating of the entire surface and then placed in an 8 mm sample mount with capacity for up to five samples. After vacuuming, proper argon flow and subsequent cooling of the indium detector with liquid nitrogen, the instrument executes the flash method thrice per sample at each desired temperature. The three measurements are averaged and κ is calculated with **Equation 5.2 (a)**. Round-robin measurements estimate a spread of ± 5 – 10 % for this technique.[147] To briefly reiterate the theory, κ_{el} can be separately estimated by combining the Wiedemann-Franz law (**Equation 1.5 (b)**) and any available measurement of σ.

5.3. Differential Scanning Calorimetry and Thermogravimetry

It is often necessary to understand how a compound is changing during a chemical reaction, or heating procedure. DSC is defined by the International Confederation for Thermal Analysis and Calorimetry as: *A technique in which the heat-flow rate (power) to the sample is monitored against time or temperature while the temperature of the sample, in a specified atmosphere, is programmed.* This type of technique can be traced as far back as 1827 with Ritchie's first description of a differential air thermometer, or even back to 1821 with the development of thermocouples and Seebeck's observation of the thermoelectric effect. DSC specifically was developed in 1960 by Watson and O'Neil.[148] It is a technique that requires a reference with a well-known heat capacity in order to compare it with that of the sample in question.[149]

A computer-controlled NETZSCH STA 409 PC Luxx instrument (**Figure 5.4 (a)**) is used under argon flow (40 mL/min) with a heating rate of 5 – 20 K/min (though 10 is typically used) in order to observe different phase changes (DSC) – i.e. enthalpy changes and sample heat capacity – and gains or losses in mass (ThermoGravimetry). The argon flow used is 80 and 50 mL/min for sample and balance chamber respectively. Following the measurement, samples are X-rayed to determine their change – if any.

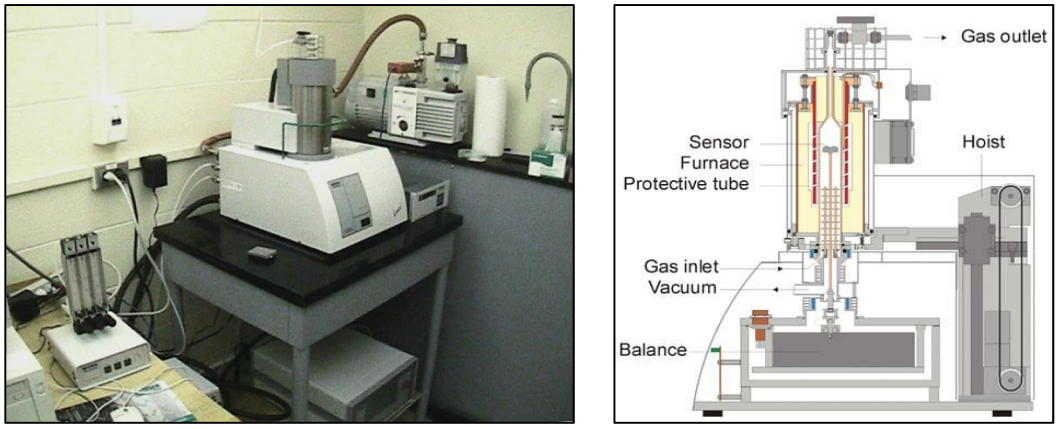

Figure 5.4 NETZSCH STA (left) STA Schematic (right)[150]

The NETZSCH setup is capable of simultaneous DSC and TG measurements. As displayed in Figure 5.4 (b) on the sensor, approximately 40 mg of lightly-pressed powder is placed in an alumina crucible and placed on this silver sample holder to ensure uniform heat distribution. A sapphire reference disk is placed in another alumina crucible on the opposite side of the silver holder and both are sealed in the upper chamber which is purged followed by regulated Argon flow; the setup is also capable of atmospheric measurements. The temperature difference (ΔT) between both holders is measured via chromel thermocouples as electrical voltage, and converted into heat flow rate (Φ, usually µW or mW) by an internal calibration file produced by NETZSCH such that $\Phi = -k \cdot \Delta T$, where k is a constant. This type of setup – sample and reference in one furnace chamber – is known as Heat Flux DSC, a heat exchange calorimeter utilizing thermal resistance along a known heating path.[151] With both reference and sample in the same chamber, one can then use a set of thermocouples to monitor the difference between sample and reference crucibles whilst a second thermocouple set measures the temperature of the furnace versus the sensor plate. The sample mount is also balanced on a highly sensitive scale that can track the weight throughout the measurement in order to follow gains (i.e. a compound oxidizing during heating) and losses (i.e. Te vapourizing out of chalcogenides) in mass to produce a thermogravimetry line as well. These are sensitive on the µg order.

Both the reference and sample are in a steady-state equilibrium with Φ and remain this way until the sample undergoes a change in enthalpy at which point the steady-state is disturbed and a differential peak is created.[152] An exothermic differential (i.e. crystallization) will result in an increase in heat flow rate whist an endothermic differential (i.e. melting) creates a minimum; a change in heat capacity can also be detected as a sudden drop (or rise) in the baseline such as a glass transition. TG is quite simply a recording of the scale's mass at every point; a straight line through the entire TG

measurement implies that there was no noticeable mass change. Since Φ is directly proportional to time (t), which is linearly proportional to the temperature (T) the x-axis can be both time and temperature.[152]

5.4. Seebeck Measurements: MMR technologies

For those samples produced before July 2009 or for samples having fewer than 200 mg worth of powder, the SB-100 Seebeck controller, manufactured by MMR Technologies Inc., was used. This instrumental setup requires the use of 5×1×1 or 6×1×1 mm pellets and is capable of measuring S over a similar temperature range as the ZEM. While the overall principles of S-measurements are the same, the experimental setup differs slightly from the other instrument. The MMR setup utilizes a constantan thermocouple (Cu:Ni = 55:45 wt-%) reference bar with a known Seebeck coefficient and silver (Leitsilber 200 paint, Ted Pella Inc.) leads.

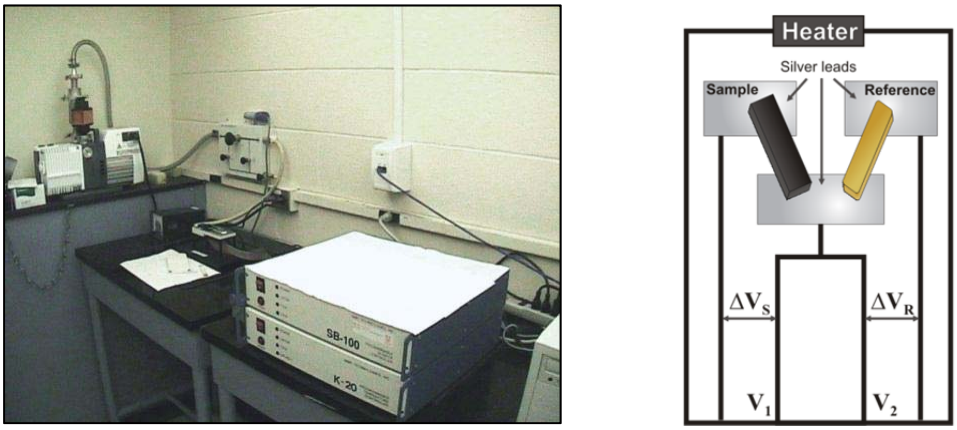

Figure 5.5 MMR Seebeck system (left) MMR Schematic (right)

The second thermocouple is a block of the sample material with silver leads. A heater on the stage creates a temperature difference (ΔT) between the tops and bottoms of the samples, while a computer-controlled power function (P) generates a voltage difference (ΔV), thusly calculating S for the sample.

$$(a)\Delta V_{\text{sample}} = S_{\text{sample}}\Delta T(P) \;\&\; \Delta V_{\text{ref}} = S_{\text{ref}}\Delta T(P) \qquad (b)S_{\text{sample}} = S_{\text{ref}}\frac{\Delta V_{\text{sample}}}{\Delta V_{\text{ref}}}$$

Equation 5.3 (a) Voltage relationships (b) Absolute Seebeck coefficient

The resultant voltages created from the power function are quite small. Combine this with the fact that substantial experimental error can be encountered from calculation of a single point or from thermo-voltage contributions (ΔV_{therm}) by the wires/contacts, the measurement is necessarily taken at two different power settings with two different ΔT values (Equation 5.3) which eliminates ΔV_{therm} via subtraction of both powers ($P1/P2$) yielding a more complex Equation 5.3 (b):

$$S_{\text{sample}} = S_{\text{ref}} \frac{\Delta V_{\text{sample}}(P_1) - \Delta V_{\text{sample}}(P_2)}{\Delta V_{\text{ref}}(P_1) - \Delta V_{\text{ref}}(P_2)}$$

Equation 5.4 MMR Seebeck coefficient.

With the thermal contributions effectively eliminated and the S measured with respect to a known constantan reference, one achieves an accurate measurement at regular temperature intervals. This is conditional on the pellet density and proper $P1/P2$ inputs of course, but produces reproducible values comparable to that of the ZEM instrument.

5.5. Electrical Conductivity Measurements (low-temperature)

Those samples (again) measured before July 2009 or requiring data below ambient temperature or with less than 200 mg of powder can also be measured for σ utilizing a homemade measurement system displayed in Figure 5.6 (a) from ambient temperature to approximately 10 K. Pellets required for this setup are the same as those used in 5.4 and are similarly connected via silver paint to the voltage and current leads which can be seen in Figure 5.6 (b). Like the ZEM, this instrument uses the four-point method for measurement via Ohm's law: Equation 5.1 (a). The pellet is placed under vacuum (~10^{-3} mbar) and slowly cooled via a closed-cycle helium refrigerator using the Joule-Thomson effect in the possible temperature range of 320 – 5 K. Any and all necessary readings, power/temperature changes and voltage adjustments are made through manual controllers attached to the instrument. The experimental setup is as follows:

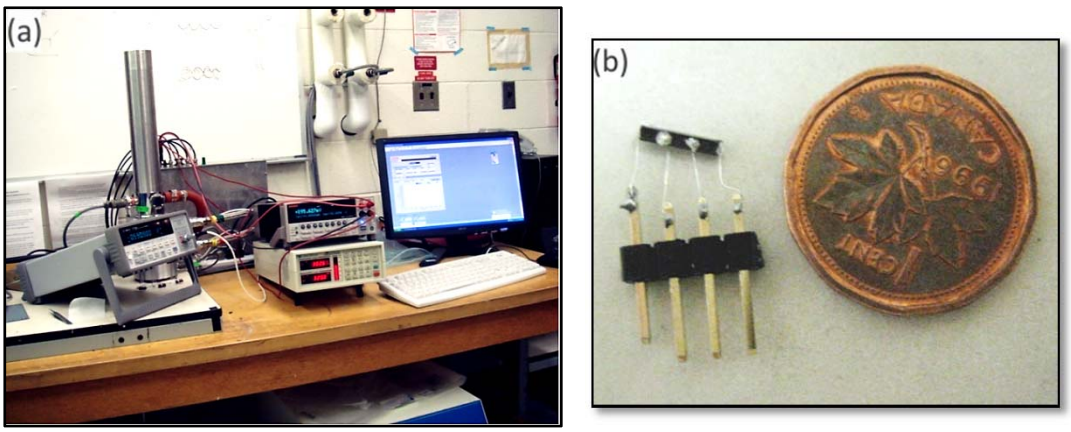

Figure 5.6 Home-made electrical conductivity: (a) σ experimental setup (b) σ pellet mount

The power source used on the instrument is a Keithly 2400 with an input impedance of 1 GΩ to eliminate the $Ir_{\text{wire}} + Ir_{\text{contact}}$ terms mentioned in 5.1, which ensures the proper measuring of semiconducting materials which rarely reach even 1 kΩ. A Lakeshore 330 temperature controller is used for assessing the temperature throughout the measurement. During the measurements, samples are measured with both negative and positive voltage to ensure the instrument is accurately measuring correct values; another undesirable voltage is the thermal voltage, V_{therm}, (or additionally a thermoelectric effect) caused by dissimilar circuit junctions such as copper wires on silver paint, which can be written as $V_{\text{meas}} = IR + V_{\text{therm}}$. By reversing the current flow however, we can obtain $V_{\text{meas2}} = -IR + V_{\text{therm}}$ such that subtraction of the two equations yields $R = \frac{V_{\text{meas1}} - V_{\text{meas2}}}{2I}$ which eliminates the thermal effects that lead to measurement error. Likewise to avoid Joule heating (I^2R), one must choose as low a current as possible to still observe four significant voltage figures – in this work, around 10 mA; activation and deactivation of the measurement instrument must also be quick (say, ≤ 1 second) or heating effects on voltage will lead to an erroneous measurement. Lastly measurements are typically executed in both heating directions, that is, cycling cooling and successive warming to ensure experimental consistency through averaging both cycles. Following measurement of the pellet with a Vernier calliper, the electrical conductivity σ can be calculated. This strategy (Equation 5.1) is the same as that of the ZEM setup.

Chapter 6. Structural Analysis Methods

Structural analysis is a very broad term encompassing techniques and predictions regarding a compound's composition: Its defects, orbitals, topology, symmetry, and ordering can all be better understood with the proper structural analysis techniques. XRD is the principal structural analysis tool in (crystalline) solid state chemistry, which is why it was discussed in greater detail in an independent chapter. Since X-ray diffraction reveals a structure's atomic ordering, it is often useful to have a plethora of additional techniques to gain a more complete understanding of the material. This would include supporting measurements such as determination of the ratio of elements within a sample or a visual representation of the macroscopic grain boundaries governing some of the materials' behaviours. Some of the other (non-X-ray diffraction) structural analysis methods of interest are discussed henceforth.

6.1. Scanning Electron Microscopy

When a beam of electrons is focused to a small point via a series of condenser lenses and deflection coils, it can be raster scanned across an area of sample producing a detailed 3-D–like image. This follows those principles used in the design and construction of a cathode ray tube. The major difference being the wavelength utilized in the instrument – in an optical microscope, the wavelength is in the optical region, on the order of hundreds of nm; in a scanning electron microscope, the wavelength is between 1 and 20 nm allowing for a much higher resolution (~300,000x). This gives a simple and relatively fast method for observing sample size, shape and supporting evidence of homogeneity based on the images produced. There are two detectors for the SEM, the first being the *secondary electron* detector. It takes advantage of low energy electrons nearer to the surface that are inelastically scattered, producing an image with excellent depth of focus and dimensionality – a good choice for verifying the size of crystallites including proof of nanoscopic inclusions within samples. The second detector is the *backscatter* detector and it reads the (often) higher energy electrons that are elastically scattered from the sample. Since the larger nuclei have stronger backscattering capability, heavy atoms will appear significantly brighter here, contrasting them from their lighter counterparts. Due to the higher-penetrating backscattered electrons, dimensionality is lesser. Thus, the image contrast is excellent and it can be used to quickly look for inhomogeneities or impurities such as glass by brightness, but due to the lack of surface effects the image is significantly more 2-dimensional than the latter.

The SEM is constructed from an electron source and a series of focussing electromagnets. The beam is produced by a tungsten filament (anode) and travels through a series of condenser lenses to focus the beam before traveling through scanning coils and objective lenses in order to further focus and narrow the beam before it reaches the sample (cathode). The signals are then picked up by a series of detectors and sent to the computer screen. SEM in this case, is performed under a vacuum of approximately 10^{-6} mbar. The SEM used in this work is located in Watlabs at the University of Waterloo, which is a LEO 1530 field emission microscope (Figure 6.1 (a)) with a rotating 8-sample mount.

6.2. Energy Dispersive X-Ray (EDX) Spectroscopy

As X-ray diffraction techniques alone cannot uncover the exact ratio of elements in the final product, some form of supporting elemental analysis is advisable to supplement and enhance these diffraction findings. Energy dispersive X-ray spectroscopy or EDX is therefore a valuable technique for solid state materials and is accessible via scanning electron microscopy. Generally speaking, elemental analysis is any technique that can elaborate on a sample's composition by giving an accurate, often quantitative, ratio or percentage of the elements within.

When a high-energy (in this case) beam of electrons impacts the surface of the sample, the innermost energy shells of the atoms are affected which leads to different phenomena as the aforementioned backscattering or below-mentioned transmitted radiation. The energy is great enough to dislodge a core electron from the atom, leaving an unstable gap in the 1*s* shell. The atom adjusts to this destabilization by migration of an outer electron into the lower energy state, followed by release of X-ray photons (i.e. ΔE). The wavelengths of the emitted photons are correlated with Z, giving a unique spectrum for every element in the periodic table – additionally, since photons can be recognized by the particular outer shell released, there are numerous emissions from each element (Figure 6.1 (b)). Photons released from 1*s* shell are designated 'K', from the second shell are designated 'L', the third shell is designated 'M' and so-on and so-forth. Additionally, electrons that migrate by one energy level are designated 'α', migrating two energy levels designated 'β', etc. Thus the energy associated with an electron travelling from the M shell into the K shell would be designated K_β; this is traditionally understood with the Bohr-Rutherford model of the atom. These photons are then captured by the EDX detector to be collected as a spectrum.

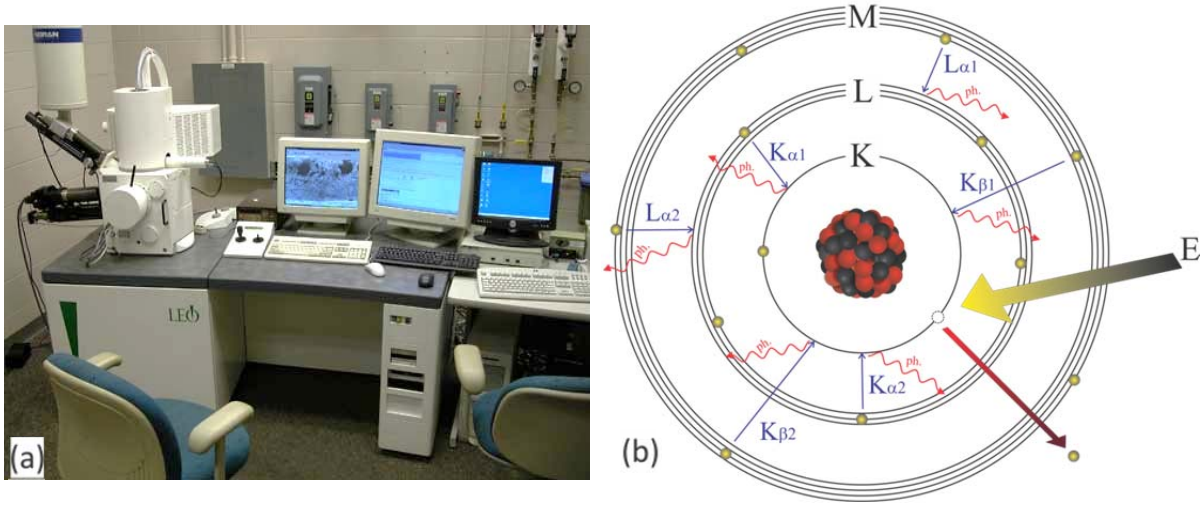

Figure 6.1 (a) LEO 1530 SEM (b) EDX Process

Samples are attached to conductive carbon tape in < 10 mg powders or single crystals and attached to an aluminium sample holder. The data is collected as relative intensity on the y-axis and energy (in eV) on the x-axis as displayed in Figure 6.2 (a). Spectra are collected for each sample in full area scans, partial area scans or point scans, each having its own advantage. For example, a full area scan (overall) will give the user an understanding of the spectra for hundreds of crystals at once whilst a point scan will read a token pixel or two from the screen. While the area scans capture other elements such as pieces of glass or carbon tape in the sample, the point scans may not represent the majority, should the crystallite belong to an obscure phase or be resting on another crystal; the energy is high enough to penetrate thin materials. Several scans are therefore collected for a more comprehensive data set. Results are collected as weight or atomic percent (Figure 6.2 (b)) and can be assumed to be ± 1 %, while the technique can detect any elements having nuclei around the size of carbon or larger.

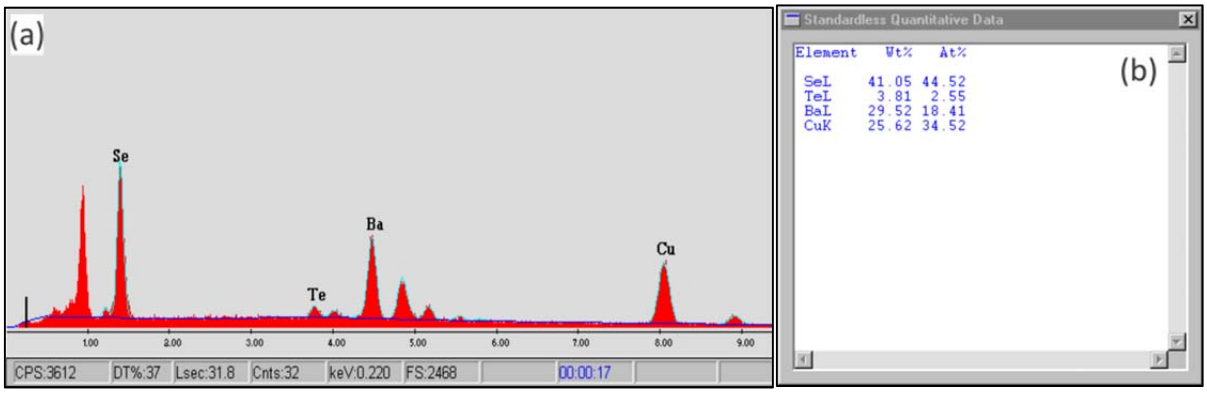

Figure 6.2 Sample EDX (a) Spectrum (b) Results

The EDX measurement system utilized by the University of Waterloo is an EDAX Pegasus 1200 detector under high dynamic vacuum with an ultrathin polymer window to ensure detection up to and including carbon. Computer software EDAX Genesis was used to analyze the spectrum with a standard less ZAF fit function for peak-fitting. The electron beam used in the process ranges between 20 and 25 eV and data is collected on average for 30 second intervals, having at least 1 full area scan and approximately 6 partial area or point scans per sample.

6.3. Transmission Electron Microscopy

When one is required to examine a sample at an atomic level, the SEM resolution does not achieve the means (nm – μm range). First constructed in 1931 by Max Knoll, the transmission electron microscope (TEM) also utilizes the small wavelength of electrons to achieve a high resolution, albeit via a different phenomenon. In order for electrons to pass unobstructed, the microscope requires the use of an ultra-high vacuum chamber. The TEM requires use of ultra-thin samples as the beam of electrons travels through condenser lenses, straight through the sample – to avoid absorption, samples must be thin – through objective lenses, to projector lenses where the image is finally obtainable on a screen or film.[84] Since most electrons are penetrating through the sample, depth-perception or dimensionality is lost – all samples appear 2-dimensional however, the resolution is good enough to view materials on an Å – nm scale. As the beam travels through the sample, the direct beam and diffracted beam can be utilized, for example the interference patterns from differences in electron density or crystal lattice. Therefore crystallographic planes and unit cell sizes can be recognized via TEM (direct lattice imaging). The technique is also useful for examining defects such as dislocations, and grain boundaries or inhomogeneities such as nanodots, nanodomains, etc.

In this work, TEM imaging was carried out at McMaster University, Hamilton, Ontario, in collaboration with Prof. Gianluigi Botton. High resolution transmission electron microscope (HRTEM) analysis was performed on a Cs corrected FEI Titan TEM operated at 300 keV. TEM samples were prepared by crushing small sections of bulk samples between glass plates. The crushed crystals were deposited onto a 3mm lacey carbon TEM grid before insertion into the chamber. Thin, electron transparent crystals, whose thin edges extended into vacuum on the lacey carbon support, were selected for high resolution imaging. Prior to imaging, the TEM stage was tilted such that the electron beam was parallel to a major crystal zone axis orientation.

6.4. Electronic Structures Calculations

One of the most valuable tools in the arsenal of a solid state research group is its ability to predict materials' physical properties (2.4.1) and the effects doping may have on their electronic structure. Thanks to the advancement of modern computers, scientists can easily and accurately predict complicated structures with little time consumption. Through the use of the Linux operating system and a software package called LMTO47c[153, 154] (Linear Muffin Tin Orbital), one can make predictions on energies by knowing a compound's crystal structure and the atomic positions within. The WIEN2k software is also employed in parts of this work.[155] One requires a qualitative understanding of band theory (2.4) and a computer/software package to execute calculations, based on Density Functional Theory (DFT). To solve the many-body Hamiltonian in quantum mechanics, i.e. Equation 6.1 originating from the Schrödinger equation, $\hat{H}\psi = E\psi$; when considering a wave function for every electron in the system in three dimensions with spin coordinates, etc. the equation is far too complex to directly solve.

$$\hat{H} = -\frac{\hbar^2}{2}\sum_i \left[\frac{\nabla^2_{\vec{R}_i}}{M_i} - \frac{\nabla^2_{\vec{r}_i}}{m_e}\right] - \frac{1}{4\pi\epsilon_0}\sum_{i,j}\frac{e^2 Z_i}{\left|\vec{R}_i - \vec{r}_j\right|} + \frac{1}{8\pi\epsilon_0}\sum_{i\neq j}\left[\frac{e^2}{\left|\vec{r}_i - \vec{r}_j\right|} + \frac{e^2 Z_i Z_j}{\left|\vec{R}_i - \vec{R}_j\right|}\right]$$

Equation 6.1 Many-bodied Hamiltonian (full version)

By making the assumption that the nuclei are so large with respect the electrons that they do not move, the first term $\frac{\nabla^2_{\vec{R}_i}}{M_i} = 0$ as the nuclei no longer have kinetic energy; likewise the final term (nucleus-nucleus interactions, $\frac{e^2 Z_i Z_j}{\left|\vec{R}_i - \vec{R}_j\right|}$) becomes constant.[156] This is the Born-Oppenheimer approximation and leaves the user with an electron gas having $\hat{H} = \hat{T} + \hat{V} + \hat{V}_{\text{ext}}$ or kinetic energy, potential energy and external potential energy. In 1964, Hohenberg and Kohn[157] postulated that systems' ground-state energies can be calculated via the electron density (ρ) such that $\psi_{\text{GS}} = \psi[\rho]$ – the electron density is an exact functional of the ground state wave function and therefore, the energy. Thus the calculation process begins by the user inputting the compound's space group, atom-types and Wyckoff positions. This value for $E_{V_{\text{ext}}}[\rho]$ and following, in 1965, the Kohn-Sham equations[158] provided a practical use for DFT by proposing a solution for $\hat{T} + \hat{V}$ as well. The resulting Hamiltonian is only left with kinetic energy, Coulomb, exchange-correlation and external potential terms respectively:

$$\hat{H} = -\frac{\hbar^2}{2m_e}\nabla^2_{\vec{r}_i} - \frac{e^2}{4\pi\epsilon_0}\int \frac{\rho(\vec{r}_i)}{|\vec{r}_i - \vec{r}_j|}d\vec{r}_i + \hat{V}_{xc} + \hat{V}_{\text{ext}}$$

Equation 6.2 Many-bodied Hamiltonian (Kohn-Sham) for one particle

By treating this system as a series of separate non-interacting particles with the same density and energy such that $\psi = |\phi_1, \phi_2, \dots, \phi_N|$, every term in the Hamiltonian can be accounted for except $\hat{V}_{xc}$, the exchange-correlation term. This term, defined as $V_{xc}(\vec{r}) = \frac{\delta E_{xc}[\rho]}{\delta\rho(\vec{r})}$ for every point $\vec{r}$ in space, then needs to be fit with an approximation such as simply assuming a homogenous electron gas, or for a real system a local (spin-)density approximation (LDA) where $\delta E_{xc}[\rho]$ can be fit as an electron gas whilst $\delta\rho(\vec{r})$ can be solved at every $\vec{r}$.[159-161]

The calculations in this research are carried out on a LINUX system under the Tight-Binding Linear Muffin-Tin Orbital (TB LMTO) algorithms[154] based on theories created by Andersen in the mid-70s[153] using the Atomic Spheres Approximation (ASA).[159] ASA further simplifies this *muffin tin* approximation such that the system is comprised of barely overlapping spheres – including dummy spheres in empty space. The volume of the sphere-sphere overlaps can then be neglected as interstitial space, making for a very efficient calculation. Density functional theory is then applied with a local density approximation (LDA).[161] LDA assumes spherical (uniform) densities localized on the reference electrons – as opposed to the "real life" angular hole – throughout a homogeneous hypothetical electron gas.[162] WIEN2k on the other hand, solves the Kohn-Sham equations utilizing the basis full potential linearized augmented plane wave method (LAPW), allowing for a precise estimation of atomic (spherical) potentials but fitting spatial regions with (non-spherical) plane waves.[163] This software also uses a generalized gradient approximation (GGA),[164] which allows for improved energies, softened bonds, and density inhomogeneities through a gradually changing density term in the $E_{xc}[\rho]$ functional.

Within LMTO, a calculation is preceded by the user-input crystallographic parameters producing the "INIT" and "CTRL" files ("lminit"), containing rudimentary crystallographic information for the DFT calculation. The Hartree potentials are calculated ("lmhart"), approximating the atomic radii in the modelled structure, and empty spheres ("lmes") are added to the unit cell to fill the vacant space; in this approach, tight-binding spheres are required to completely occupy the unit cell. Once set up, the density functional theory iterations commence ("lm"), an energy minimum (ground state) is calculated, followed by the density of states ("lmdos"), band structure calculations ("lmbnd") and optionally, bond interactions via $COHP$ ("lmcohp").[96] The above concepts have been discussed in **2.4.** Following standard calculation, one is able to plot the predicted band structure of the compound, its density of

states, *COHP* interactions, or “fatbands”, which depict the additional information regarding the electron quantities contributed by those orbitals comprising the valence bands (i.e. ~2 eV below the Fermi level). These plots are incredibly useful with respect to the prediction of solids’ behaviours towards the explanation of physical property trends measured in **Chapter 5**. In fact, utilizing the calculations obtained from WIEN2k allows one to predict the shape and intensity of the Seebeck coefficient and other band structure dependant parameters through the use of BoltzTraP software.[165]

Section III – Layered Bi_2Te_3 Compounds

Effects of doping and substitution on the SnTe–Bi_2Te_3 system.

Chapter 7. Layered Ternary Structures in $(SnTe)_x(Bi_2Te_3)_y$

7.1. Introduction to Layered Bismuth Tellurides

Since the discovery in the 1950s of bismuth telluride's thermoelectric potential, researchers have been attempting to understand why Bi_2Te_3 is such an effective TE material and expanding on ways to further improve it. With all of the studies performed, Bi_2Te_3 and its composites warrant a book of their own. Now with respect to thermoelectrics, one can consider such contributions as solid solution work like $(Sb,Bi)_2Te_3$ or $Bi_2(Se,Te)_3$,[13] extensive studies on doping,[166-168] crystal structures,[169] calculations,[170, 171] phase diagrams and of course, physical properties such as Seebeck coefficient and charge carrier concentration (Hall measurements).[81, 166, 167] Recent efforts towards nanoscopic studies have produced thin films, nanowires, nanocrystals and numerous other property-related studies.[172-175] In this chapter, new compounds with similar features are formed based on the parent Bi_2Te_3 structure by combining it with other (in this case) binaries expecting the child compounds to show similar characteristics and therefore similar, possibly enhanced physical properties.

Bi_2Te_3 is a layered compound of the rhombohedral space group $R\bar{3}m$. Forming perpendicular to the *c*-axis, are alternating layers of covalently bonded Bi and Te atoms in five segments (a *block*) starting and ending with Te: Te–Bi–Te–Bi–Te. The Bi–Te bond lengths in this layer are 3.07 and 3.26 Å.[169, 176] The interactions between blocks are predominantly van der Waals forces. A Te–Te van der Waals interaction of 3.65 Å connects the blocks in a stacked structure. This can be seen on the left side of Figure 7.1 displayed below.

The search for related layered compounds led to investigations into the $(TtQ)_x(Pn_2Q_3)_y$ (*Tt* = Ge, Sn, Pb; *Pn* = Sb, Bi; *Q* = Se,[177] Te) materials, where *x* and *y* are integers. The resulting studies uncover a series of increasingly longer unit cells with similar layering to that of bismuth telluride. Further discussion regarding layering in the crystal structures is discussed below. It has since been postulated that the lead-based system's phase diagram[178, 179] includes (PbTe)-(Bi_2Te_3), (PbTe)-$(Bi_2Te_3)_2$, (PbTe)-$(Bi_2Te_3)_3$, $(PbTe)_2$-(Bi_2Te_3) and arguably (PbTe)-$(Bi_2Te_3)_4$ which can be written as proper ternary compounds: $PbBi_2Te_4$, $PbBi_4Te_7$, $PbBi_6Te_{10}$, $Pb_2Bi_2Te_5$, and $PbBi_8Te_{13}$ respectively. Due to the extensive layering along the *c*-axis and the widespread occurrence of heavy *p*-block elements, said structures may have potential for thermoelectric applications.[16] Though crystal structures have been predicted for this system, ordering beyond $PbBi_2Te_4$ cannot be verified due to the indistinguishable nature of Pb versus Bi in XRD studies – a feature that could be more apparent in the Sn-Bi-Te system. Though many of the

aforementioned studies address the Pb-Bi-Te system, its structure, and its properties, little is known on the behaviour and thermoelectric properties of the Sn-Bi-Te system. The suggested layering of the three best-known ternaries in that system (versus Bi_2Te_3) is displayed below:

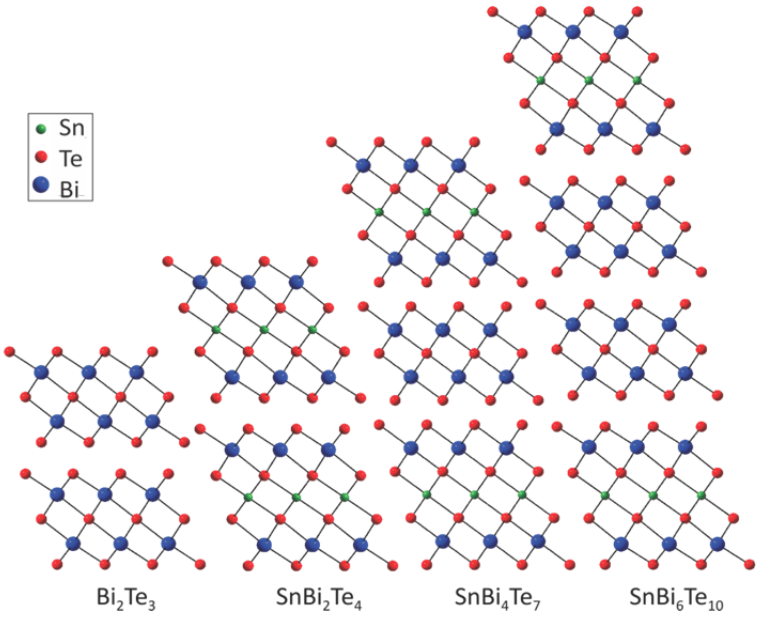

Figure 7.1 Layering motifs of Bi_2Te_3 and compounds in $(SnTe)_1(Bi_2Te_3)_y$; y = 1, 2, 3.

It can be seen from the diagram that all compounds in this family are composed of repeating patterns of covalently bonded blocks connected by Te–Te van der Waals interactions. Bi_2Te_3 and $SnBi_2Te_4$ are the simplest of the family, being made up of 5-member Bi-Te blocks for Bi_2Te_3 (5-5), and 7-member Sn-Bi-Te blocks for $SnBi_2Te_4$ (7-7). The larger compounds are then created by mixing blocks: The $SnBi_4Te_7$ motif is comprised of a 5-member block sandwiched between two 7-member blocks (7-5-7), whilst the $SnBi_6Te_{10}$ motif comprises two 5-member blocks flanked by two 7-member blocks (7-5-5-7). It can therefore be seen that as x and y are altered throughout the system, one simply takes different combinations of the Bi_2Te_3 and $SnBi_2Te_4$ motifs to build a plethora of plate-like ternary compounds – each with very similar a/b dimensions, differentiated by the c length which varies from structure to structure. As mentioned above, in lieu of many studies revolving around Pb-Bi-Te, there is still uncertainty about the 7-member blocks and whether there is mixing between Bi and *Tt* or if it is fully ordered as shown in Figure 7.1. It is also worth mentioning that when $x > 1$, the layering motifs are not as above. With the majority of studies focusing on this group of materials, studies included this work were performed on each of $SnBi_2Te_4$, $SnBi_4Te_7$, and $SnBi_6Te_{10}$. Chapters 8 and 9 detail much of the work featuring individual ternary compounds and the resulting findings.

The identification and subsequent purification attempts in this Sn-Bi-Te system have proven a great challenge to those who study it. As a result, many of the past publications on $SnBi_2Te_4$ and the like, were primarily studies on the phase diagram SnTe versus Bi_2Te_3; attempts by researchers not only to discover the phases within, but to determine whether they melt congruently, at what temperature, their alleged stability and whether representatives with smaller Sn:Bi ratio (i.e. $SnBi_6Te_{10}$ or $SnBi_8Te_{13}$) truly exist. With slow equilibration of the compounds[180] and several of them incongruently melting, there is much conflicting information on the subject. The most to-date, detailed phase diagram published is displayed below:

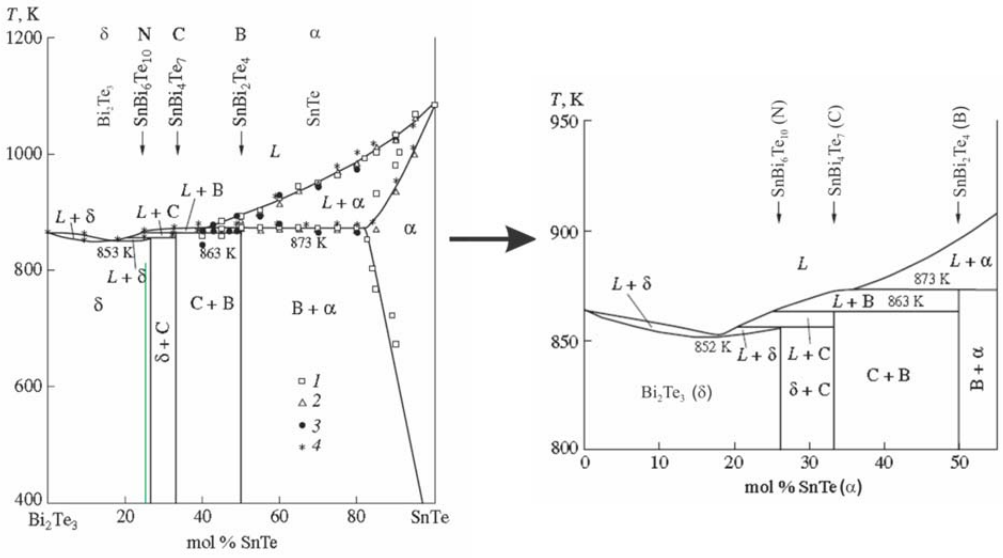

Figure 7.2 Phase diagram of SnTe-Bi_2Te_3 system.[180]

It is predicted that $SnBi_2Te_4$ melts congruently between 843 K and 873 K,[181] which is reasonably consistent with empirical data contained herein. On the contrary $SnBi_4Te_7$ as shown above melts incongruently around 863 K, where it reacts into $SnBi_2Te_4$ and liquid – an occurrence consistent with experiments in this thesis. At the time of the study, $SnBi_6Te_{10}$ could not be accurately placed on the phase diagram, but past publications[179, 180] and empirical data from this thesis suggest that it forms at temperatures near to that of $SnBi_4Te_7$ and may decompose at higher temperatures – though no current studies are thorough enough to prove this. An extra vertical (green) line has been added at 25 % SnTe to visualize the position of $SnBi_6Te_{10}$ on the current phase diagram.

With respect to literature-based thermoelectric properties, Seebeck measurements were used to compare $GeBi_4Te_7$, $SnBi_4Te_7$, and $PbBi_4Te_7$: The Ge compound was found to be an *n*-type semiconductor with a maximum Seebeck coefficient value around -125 $\mu V \cdot K^{-1}$ at 400 K,[182, 183] as was the

Pb-based compound (~-60 μV·K^{-1} at 325 K).[179, 182, 184] The Sn-based compound however, was found to be *p*-type in one case (~105 μV·K^{-1} at 325 K)[184] but *n*-type in other cases (~-105 μV·K^{-1} at 325 K).[183, 185] From the few studies on *Tt*Bi_4Te_7 that contain all of $\mathcal{S}$, σ, and κ, thermoelectric figures of merit were as follows: $\mathcal{ZT}$ = 0.5 (600 K) Pb; $\mathcal{ZT}$ = 0.5 (470 K) Sn;[186] $\mathcal{ZT}$ = 0.26 (300 K) Ge.[187] Most of the remaining studies are focused around $PbBi_4Te_7$, its nonstoichiometry, and less-so, $PbBi_2Te_4$;[184, 188, 189] the publicity of PbTe[104, 190] and its related successes – LAST,[78, 81] for example – make $(PbTe)_x(Bi_2Te_3)_y$ an appealing subject. Additional studies have been published on the $GeBi_4Te_7$ system such as the effects of nonstoichiometry on transport properties[191] and the effects of Cu-doping.[187] Similar studies on phase range and thermoelectric properties of the Pb-Bi-Te system (namely $PbBi_2Te_4$ and $PbBi_4Te_7$) have been performed in the Kleinke group in parallel with the Sn-Bi-Te work contained herein.[189] Present research on $(TtQ)_x(Pn_2Q_3)_y$ notwithstanding, few studies have specifically targeted the use of Sn-Bi-Te compounds, for example early studies into Bi_2Te_3, $SnBi_2Te_4$, and $SnBi_4Te_7$[192, 193] with the initial property data.[194] The Sn-Bi-Te system, like the Pb-Bi-Te system, is rich with potential for thermoelectric improvement through traditional doping or substitution experiments; hence phase range studies, crystallographic studies, and investigations towards potential nanostructuring are of interest.

Showing literature predictions of congruent melting in this system for most of the investigated ternary compounds speaks well for the synthesis experiments that would attempt to optimize heating schemes and phase-purity for these compounds. Though current experiments in the literature imply fast-cooling for the purposes of completing the known ternary phase diagrams, single phase samples of each ternary compound should feasible following similar techniques. With the complex layering schemes predicted by crystallographic studies on this series as well as the mass differences between these layers, the structures show excellent potential with respect to thermoelectric performance – likely this includes lower κ, as κ_{ph} appears in the range of (5.5 – 10)·10^{-3} W·cm^{-1}K^{-1}.[194] Should additional elements be incorporated into this structure, additional size-variance may further improve this performance. The Seebeck coefficient values measured that yield maximum values above room temperature on the order of 100 μV·K^{-1}, imply that this system is in an ideal range for improvement as does the preliminary $\mathcal{ZT}$ = 0.5 for the $SnBi_4Te_{6.93}$ compound.[186]

7.2. Experimental Synthesis and Structural Analysis

Like most compounds herein, these compounds can be synthesised from the elements (Sn: 99.999 %, powder -100 mesh, ALFA AESAR; Bi: 99.5 %, powder -100 mesh, ALFA AESAR; Te: 99.999 %, ingot, ALDRICH) combined in stoichiometric ratios in the argon-filled glove box (**Chapter 3**) mentioned

previously. Compounds in this section (Section III) were mostly synthesized between 1 g and 1.5 g to ensure accurate weighing for all samples including those with small quantities of dopants. Elements were weighed and placed directly in quartz tubes for vacuuming and sealing and were then ramped in manual and programmable furnaces to 923 K where samples were left to homogenize in the melt for up to 24 hours before respective cooling schemes were attempted. In attempt to further improve homogeneity, some samples were shaken in the melt for approximately two days on rocking platforms. Upon cooling to room temperature, the samples emerged as lustrous silver-coloured ingots that when broken, split into plates or slabs. Though quite resistant to crushing, ingots were eventually ground into a fine powder and examined by XRD (**4.1**). The differences between diffractograms of Bi_2Te_3, $SnBi_2Te_4$, $SnBi_4Te_7$, $Sn_2Bi_2Te_5$, $SnBi_6Te_{10}$, and even $SnBi_8Te_{13}$ are subtle, but are most easily recognized (in the red box) between 17 and 20° in 2θ (Cu-$K_{\alpha 1}$) as displayed in **Figure 7.3**:

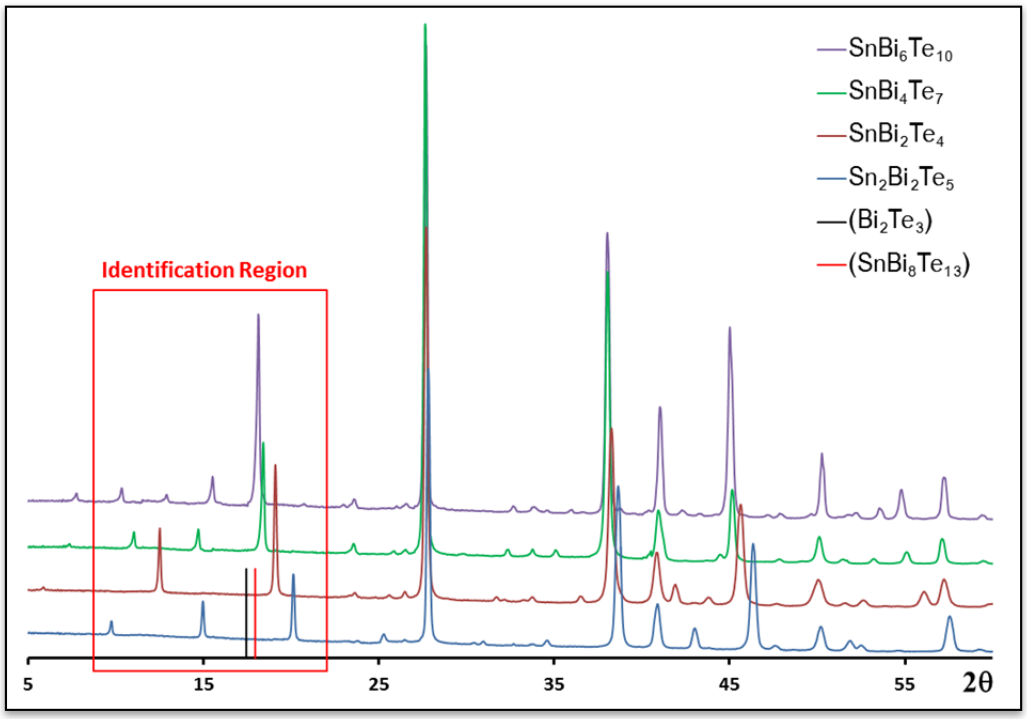

Figure 7.3 Experimental powder X-Ray patterns (Cu-$K_{\alpha 1}$) radiation for layered Bi_2Te_3-like compounds.

As highlighted on the above diagram, the patterns are best distinguished by their varying [0 0 *z*] reflections that are unique in 2θ for each member of this system including an intense peak to the left of the major peak: $Sn_2Bi_2Te_5$ – (0 0 4), 20.1°; $SnBi_2Te_4$ – (0 0 9), 19.1°; $SnBi_4Te_7$ – (0 0 5), 18.4°; $SnBi_6Te_{10}$ – (0 0 21), 18.1°; in red, $SnBi_8Te_{13}$ – (0 0 27), 18.0°; in black, Bi_2Te_3 – (0 0 6), 17.4°. This fourth-most intense peak is also illustrated for $SnBi_8Te_{13}$ and Bi_2Te_3 on the diagram above to indicate those structures

also differ in 2θ there, while the rest of their patterns are virtually identical to the others. This peak appears to shift leftwards as the ratio of x:y in $(SnTe)_x(Bi_2Te_3)_y$ decreases. The rest of the pattern is difficult to distinguish, albeit all peaks to the left of the major ($I = 100$ %) peak do shift slightly according to the differing-layer motifs, most intensities are near-zero; similar circumstances arise for a small, wide peak near 53 – 57 2θ. Though no impurities (i.e. oxides, etc.) were found on production of these samples, additional reheats were routinely necessary as most ingots would emerge as mixtures of two to four of the $(SnTe)_x(Bi_2Te_3)_y$ compounds (Table 7.1). All reflections were indexed through previous crystal data of *Tt* = Ge or Pb, and experimental lattice parameters for each were adjusted through powder X-ray refinements. Experimental peak positions were initially matched through software replacements of Ge/Pb with Sn, followed by calculation of the modified pattern.

Table 7.1 XRD result summary for binary compounds and the Sn-Bi-Te system.

Target	$(SnTe)_x(Bi_2Te_3)_y$	Layers	Optimized T (K)[a]	Best XRD Results	Typical XRD Results (843 K)
Bi_2Te_3	$x = 0$; $y = 1$	15		**Bi_2Te_3**	**Bi_2Te_3**
SnTe	$x = 1$; $y = 0$			**SnTe**	**SnTe**
$SnBi_2Te_4$	$x = 1$; $y = 1$	21	843	**$SnBi_2Te_4$**	**$SnBi_2Te_4$**
$SnBi_4Te_7$	$x = 1$; $y = 2$	12	823	**$SnBi_4Te_7$**	**$SnBi_4Te_7$** + $SnBi_2Te_4$
$SnBi_6Te_{10}$	$x = 1$; $y = 3$	52	803	**$SnBi_6Te_{10}$** + 2 % $SnBi_4Te_7$	**$SnBi_6Te_{10}$** + $SnBi_4Te_7$ + $SnBi_2Te_4$
$SnBi_8Te_{13}$	$x = 1$; $y = 4$	*22*[b]	N/A	**$SnBi_8Te_{13}$** + 40 % $SnBi_6Te_{10}$ + 10 % $SnBi_4Te_7$	N/A
$Sn_2Bi_2Te_5$	$x = 2$; $y = 1$	9	798	**$Sn_2Bi_2Te_5$**	**$Sn_2Bi_2Te_5$** + $SnBi_2Te_4$
$Sn_3Bi_2Te_6$	$x = 3$; $y = 1$	33[c]	N/A	$Sn_2Bi_2Te_5$ + 30 % Sn_3BiTe_4 + 20 % $SnBi_2Te_4$	N/A

[a] Maximum reaction temperature that the yielded the best results.
[b] Predicted from feasible motif
[c] Taken from $Ge_3Bi_2Te_6$[195]

Samples found to be pure phase were routinely examined via EDX spectroscopy (6.2) to validate their composition, and several ternaries were examined via DSC (5.3) for information regarding melting and/or stability. The experiments were run up to 923 K as inside the furnaces, at a heating/cooling rate of 10 °/min, with no significant change in the thermogravimetric components. $SnBi_2Te_4$ had an average melting/crystallizing peak of 868 K, $SnBi_4Te_7$ showed an (expected) lower peak of 845 K, whist $SnBi_6Te_{10}$ showed a melting peak at 852 K, but two smaller crystallization peaks were found upon cooling: A wide one at 829 K and a narrow one at 665 K. Though p-XRD data following $SnBi_6Te_{10}$ DSC/TG measurements

were inconclusive, this implies the sample may have decomposed into $SnBi_6Te_{10}$/$SnBi_4Te_7$ and Bi_2Te_3 – hence the much lower 665 K peak – after melting. EDX data was also collected, verifying the stoichiometric ratios for samples within an acceptable ±5 % of predicted elemental ratios. Each compound studied in the $(SnTe)_x(Bi_2Te_3)_y$ ternary system can be found recorded in Table 7.1 along with XRD data after reheating samples and results following initial cooling schemes. As shown in the table above, the compounds in this system were expanded to encompass $(SnTe)_1(Bi_2Te_3)_4$ and $(SnTe)_3(Bi_2Te_3)_1$. The number of phases encountered experimentally increased with the layering complexity of the target compound, so for example $SnBi_2Te_4$ could be obtained with relative ease while $SnBi_6Te_{10}$ would rarely be encountered without two or more additional phases.

It has been hypothesized that $x > y$ would not yield ternary compounds unless *Tt* = Ge;[179] GeTe undergoes a phase transition at 700 K[196, 197] between the high temperature β-phase ($Fm\bar{3}m$) and the low temperature α-phase ($P\bar{3}m1$), while the other *Tt*Te phases remain cubic above room temperature. Studies in this work however have produced single-phase p-XRD patterns for $Sn_2Bi_2Te_5$, fit with a $Ge_2Bi_2Te_5$ ($P\bar{3}m1$) pattern[198] during phase studies. $Sn_2Bi_2Te_5$ was produced stoichiometrically, but can also be produced with slight Bi-deficiencies as shown in Table 8.2 during a phase range study on $Sn_xBi_{3-x}Te_4$ where, for example, $Sn_2Bi_{1.75}Te_5$ (aka. $Sn_{1.6}Bi_{1.4}Te_4$) was found pure phase as well. Differential scanning calorimetry on the same sample displays a sharp single peak for melting at 863 K with no gains or losses in sample mass. LeBail refinements on a pure phase sample produced lattice parameters of a = 4.42 Å, c = 17.6 Å, V = 298 Å^3, based on data published by Matsunaga *et al.* on $Ge_2Bi_2Te_5$;[198] attempts at a following Rietveld refinement were largely unsuccessful as nearly all atoms' temperature factors (U_{iso}) converged negatively despite attempts involving fully ordered metal atoms and mixing metal sites separately. Better results are still gained with mixing Sn/Bi as was suggested with the authors of the Ge model, having ~60 % Ge on one site and ~40 % Ge on the alternate. This, along with LeBail refinements for other pure phase compounds in this series, is summarized in Table 7.2. In most cases, attempts at a full Rietveld refinement were problematic. Though successful, $SnBi_2Te_4$ and $SnBi_4Te_7$ will be discussed in the following chapters respectively. $SnBi_6Te_{10}$, showed distinct software problems due to its most accurate model having c ≈ 120 Å, – the LeBail refinement was eventually successful with high damping and fewer profile parameters freed in GSAS. Likewise, this model is only hypothetical and detailed crystallographic data is currently unavailable.

Table 7.2 LeBail data for phase-pure layered compounds and binary tellurides.

Target Compound	M (g·mol^{-1})	Space Group	a (Å) = b	c (Å)	V (Å^3)	Z	R_P[a] \ R_B[b]
Bi_2Te_3[169]	2402.28	$R\bar{3}m$	4.395(1)	30.44(1)	509.21	3	–
SnTe[199]	985.24	$Fm\bar{3}m$	6.317(1)	6.317(1)	252.08	4	–
$SnBi_2Te_4$	1047.16	$R\bar{3}m$	4.423(2)	41.82(2)	708.5(9)	3	5.55 \ 9.64
$SnBi_4Te_7$	1854.86	$P\bar{3}m1$	4.4037(1)	24.0671(4)	404.19(2)	1	3.57 \ 4.16
$SnBi_6Te_{10}$	2737.08	$R\bar{3}m$	4.3835(9)	102.42(2)	1704.3(9)	3	5.13 \ 7.85
$Sn_2Bi_2Te_5$	1293.34	$P\bar{3}m1$	4.415(1)	17.635(5)	297.7(2)	1	4.41 \ 6.45

[a] $R_P = \Sigma|y_o - y_c| / \Sigma|y_o|$ [b] $R_B = \Sigma|I_o - I_c| / \Sigma|I_o|$

All refinements show excellent to very good fits based on their R values which suggests the general motifs mentioned above and more so, the suggested models and space groups from *Tt* = Ge, Pb appear to work in the less-known *Tt* = Sn system. While the space groups are in agreement and proposed *c*-axes layering generate a good experimental fit, Sn-Bi ordering within the cells still cannot be confirmed utilizing LeBail refinements.

7.3. Electronic Structure and Physical Properties of $(SnTe)_x(Bi_2Te_3)_y$

Though studies have been released on physical properties and the proposed phase diagrams for $(SnTe)_x(Bi_2Te_3)_y$, few documents regarding the electronic structure accompany these. One exception however, compared two different models of $PbBi_4Te_7$, and $GeBi_4Te_7$ to a generic band structure of Bi_2Te_3, which describes $PbBi_4Te_7$[200] as having identical band structure characteristics with a wider gap and an additional Pb *6s* contribution in the valence band. The results yield a weaker Bi–Te bonding interaction, but also additional phonon scattering abilities because of the presence of Pb.[201] Calculations of the electronic structures of $SnBi_2Te_4$, $SnBi_4Te_7$, $SnBi_6Te_{10}$ and $Sn_2Bi_2Te_5$ executed via LMTO software (6.4) show that these compounds should be narrow-band gap semiconductors. The following wavefunctions were used: For Bi *6s*, *6p*, and *6d* and *5f* (the latter two downfolded[202]), and for Sn and Te *5s*, *5p*, and *5d* and *4f* (the latter two downfolded). The eigenvalue problems were solved on the basis of 1728 to 4096 irreproducible k points depending on the compound and its reciprocal unit cell size. Points were chosen with an improved tetrahedron method.[203] The aforementioned Table 7.2 provided the necessary space groups, Wyckoff sites, and unit cell dimensions.

The calculations on the ternary tellurides were first performed assuming no Sn-Bi mixing. This produces a similar model to the structure motifs given in the introduction section and is consistent for all four calculated structures. Likewise, the calculated band gaps are comparable, with $SnBi_2Te_4$ showing a gap of 0.48 eV, $SnBi_4Te_7$ showing a gap of 0.35 eV, $SnBi_6Te_{10}$ showing a gap of 0.61 eV, and $Sn_2Bi_2Te_5$ having the largest calculated gap with 0.64 eV. The Te-*p* orbitals in each case make up the majority of the contributions below the Fermi level followed by Bi-*s* and Sn-*s* respectively – as above, the extra contribution discussed by Imai and Watanabe[201] in $PbBi_4Te_7$. The conduction band is a broad mixture of Sn-*p*, Bi-*p*, and Te-*p* orbitals which due to covalent interactions, are also strongly present in the valence band. As previously mentioned, sharp increases in the DOS at the Fermi level can be beneficial for thermoelectricity which would suggest from these initial calculations that $SnBi_4Te_7$ is a very good choice with its 0.35 eV band gap and very steep valence bands at the Fermi level. The ternaries themselves do not appear to have any unique vacant states in or near the band gap such as orbitals pinned at the Fermi level,[204] which may have led to further property improvements and/or interesting behaviours. As can be seen from the DOS calculations performed (Figure 7.4), removal of a small quantity of electrons from the stoichiometric ternaries should lead to the Fermi level being placed on a desirably sharp DOS region:

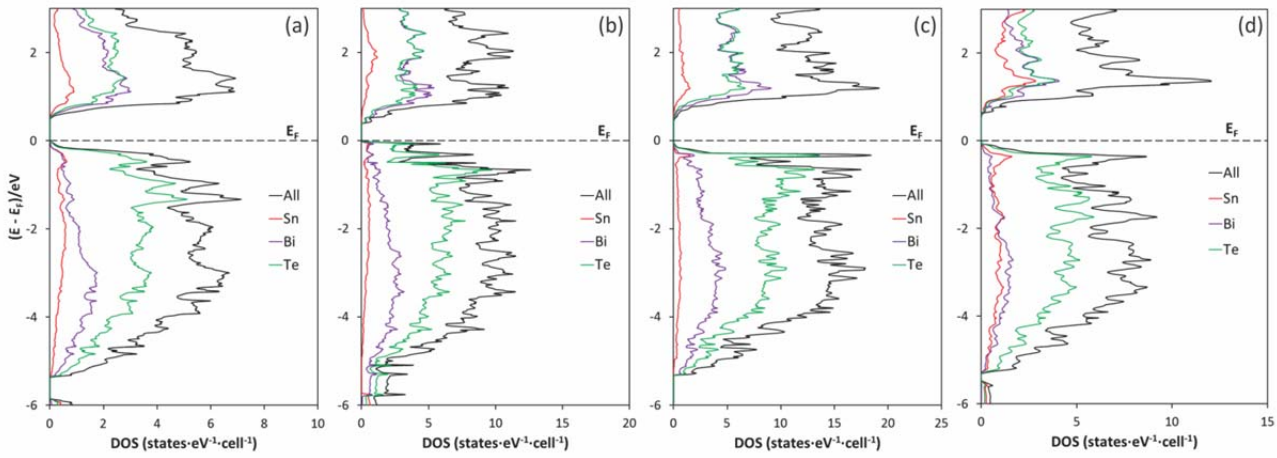

Figure 7.4 DOS calculations for (a) $SnBi_2Te_4$, (b) $SnBi_4Te_7$, (c) $SnBi_6Te_{10}$, and (d) $Sn_2Bi_2Te_5$.

The physical properties, as mentioned in this chapter's introduction, are scarce for Sn-based ternaries and were primarily in the form of Seebeck coefficients. Of the known literature, the $SnBi_2Te_4$ and $SnBi_4Te_7$ ternary compounds were studied to some extent with respect to physical properties.[179, 183, 186, 194] $SnBi_2Te_4$ was first reported as a *p*-type semiconductor with a maximum Seebeck coefficient around 40 $\mu V \cdot K^{-1}$ (200 K) which becomes negative around 350 K;[194] later it was found to be *p*-type semiconducting reaching a maximum Seebeck around 75 $\mu V \cdot K^{-1}$ (~275 K) and becoming negative near 550 K.[183] The deviations are likely due to non-stoichiometric $Sn_{1\pm x}Bi_{2\mp x}Te_4$. Its thermal conductivity was found to deviate from linearity around 140 K with around 1.67 $W \cdot m^{-1}K^{-1}$ which may be due to both *n*- and *p*-type carriers – this was not observed for the linear $SnBi_4Te_7$ curve (~2.51 $W \cdot m^{-1}K^{-1}$).[194] Studies performed on $SnBi_4Te_7$ yielded different results for the hypothetically stoichiometric ternary ($\mu V \cdot K^{-1}$ at room temperature): $\mathcal{S}$ = -45;[194] $\mathcal{S}$ = -105;[183] $\mathcal{S}$ = -92;[186] $\mathcal{S}$ = +100[205] $\mu V \cdot K^{-1}$. This is likely due to a very sensitive carrier concentration: For example $Sn_{0.995}Bi_4Te_7$ exhibited $\mathcal{S}$ = -30 $\mu V \cdot K^{-1}$, whilst $Sn_{0.99}Bi_4Te_7$ was found to possess $\mathcal{S}$ = +88 $\mu V \cdot K^{-1}$ also at room temperature.[186] The same studies showed a room temperature σ value between 200 and 500 $\Omega^{-1}cm^{-1}$.

Those compounds determined to be pure phase via XRD were examined for thermoelectric properties via the ZEM instrument and in certain cases, the Anter thermal conductivity setup. Pellets of dimensions 10×2×2 mm^3 (ZEM) and cylinders of 8 mm diameter and 1 mm length (Anter) were pressed and annealed at 723 K for 12 hours, yielding densities around 85 % of the theoretical densities. Measurements followed for temperatures up to 673 K.

Upon examination of the annealed ternary samples, it can be seen that all samples are *p*-type semiconductors from their positive Seebeck values. This is a somewhat unexpected occurrence as essentially all preceding literature reports *n*-type conductance at some temperature however, it can be rationalized as potential Te-loss (i.e. $SnBi_2Te_{4-x}$) due to the higher vapour pressure of Te; like all elemental samples sealed in a low-pressure tube, the heat from the torch is capable of causing elements to volatize during sealing. Reproducibility was still reliable with repeat measurements on the same pellets and occasionally, different reaction trials with identical stoichiometry. $SnBi_4Te_7$ and $SnBi_6Te_{10}$ show a maximum Seebeck coefficient of ~116 – 125 $\mu V \cdot K^{-1}$ at 325 K, as seen below in **Figure 7.5**. $SnBi_2Te_4$ shows its maximum at a higher temperature, 441 K, (112 $\mu V \cdot K^{-1}$), while $Sn_2Bi_2Te_5$ shows the Seebeck coefficient increasing until 609 K, where it reaches a maximum of 76 $\mu V \cdot K^{-1}$.

The electrical conductivity values range from 1780 – 335 $\Omega^{-1}cm^{-1}$ as one moves from $Sn_2Bi_2Te_5$ to $SnBi_2Te_4$ to $SnBi_4Te_7$ to $SnBi_6Te_{10}$. All compounds show a turn-around point in the electrical conductivity, where the slope of the curve becomes positive which occurs at the same temperature as the maximum Seebeck coefficient, after which all ternaries show a gradual increase in conductivity. Though it is not obvious in $Sn_2Bi_2Te_5$ due to the range of the measurement, one can observe a reduction of its slope in the last two measured points that is consistent with the other three compounds. A decreasing electrical conductivity is evidence of a constant or even decreasing quantity of charge carriers, as would be observed in a metallic substance. The increasing slope of electrical conductivity may be recognizable in the thermal conductivity measurements as well. In order to further validate the likely change from extrinsic to intrinsic behaviours, an extended σ measurement was performed on $SnBi_4Te_7$. The pellet was measured on the home-made setup from 320 K to 5 K and back with $\pm$V measurements, all averaged. The result was a straight line from 600 $\Omega^{-1}cm^{-1}$ (7 K) to 292 $\Omega^{-1}cm^{-1}$ (320 K) which showed that both σ measurements on this compound overlapped precisely. This linearly decreasing behaviour is typical of metallic charge carriers and if the line is extended, the intrinsic carriers dominate around the 352 K point (third marker from the left in this plot). This corresponds quite nicely to S_{max}, also found at 352 K. Electrical conductivity values are represented on the right axis of Figure 7.5 as dashed lines.

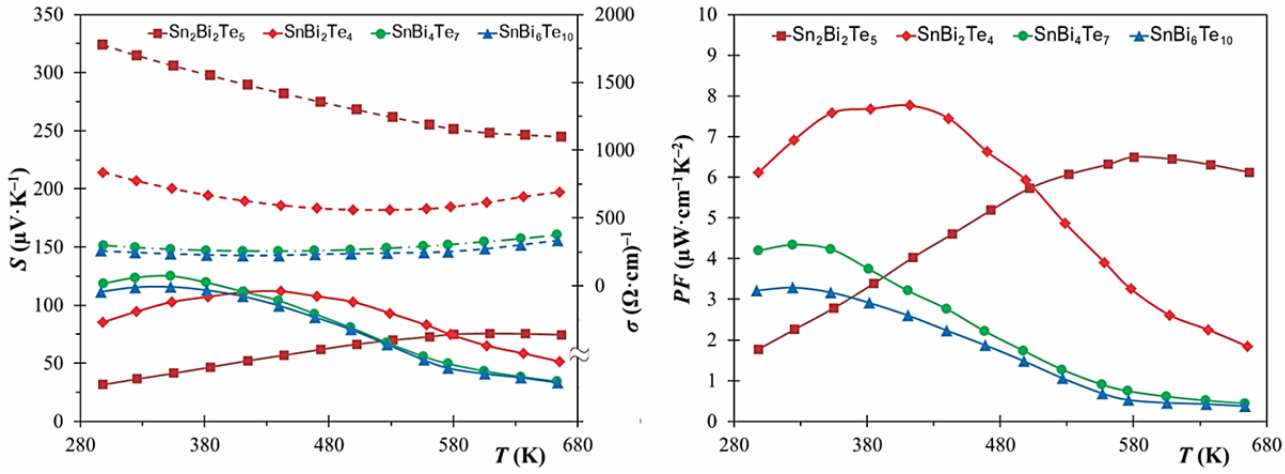

Figure 7.5 Seebeck coefficient (solid), electrical conductivity (dashed), and power factor (right) for $(SnTe)_x(Bi_2Te_3)_y$ compounds.

Upon examination of the power factor, $S^2\sigma$, one observes the same shape as the Seebeck coefficient with maxima at similar temperatures. $SnBi_4Te_7$ and $SnBi_6Te_{10}$ show nearly the same power factor, with $SnBi_4Te_7$ slightly larger as it displays a greater S_{max} and slightly higher σ; respectively their maximum power factors are 4.3 and 3.3 $\mu W \cdot cm^{-1}K^{-2}$. The largest power factor is found for $SnBi_2Te_4$ with 7.7 $\mu W \cdot cm^{-1}K^{-2}$ and with its lower, more gradual increase in S, $Sn_2Bi_2Te_5$ also shows a good power factor (6.5 $\mu W \cdot cm^{-1}K^{-2}$) at the highest temperature of the lot. For reference, the maximum power factor measured for $Pb_{0.9}Bi_{2.1}Te_4$ by Mu[189] was about 5.5 $\mu W \cdot cm^{-1}K^{-2}$, only with *n*-type conductance.

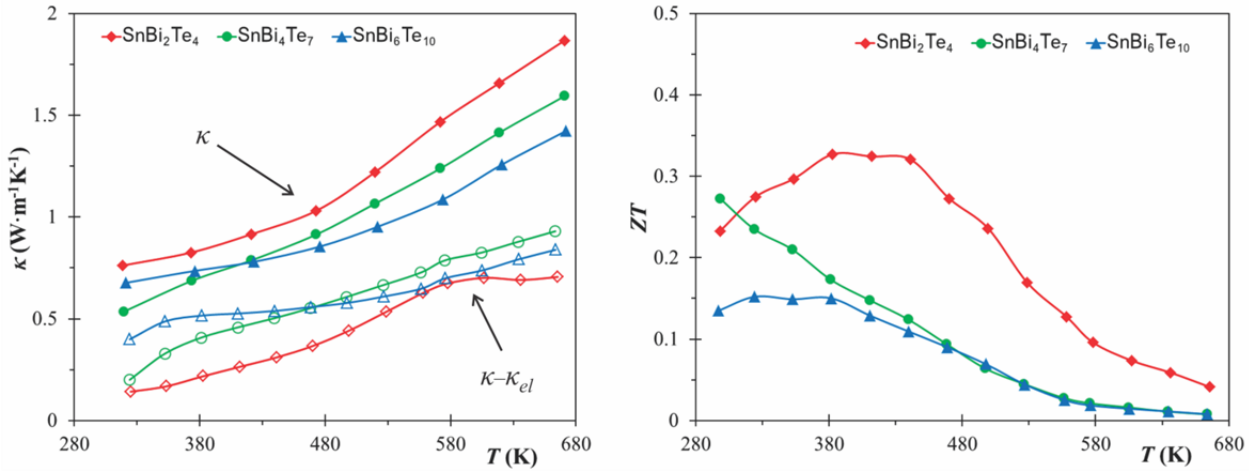

Figure 7.6 Thermal conductivity and ZT for $(SnTe)_x(Bi_2Te_3)_y$ compounds.

Thermal conductivity, measured on three of the ternary compounds, begins at room temperature below 1 $W \cdot m^{-1}K^{-1}$ and after measuring at 480 K, the conductivity quickly increases reaching 1.86 $W \cdot m^{-1}K^{-1}$ for $SnBi_2Te_4$. These results are depicted in Figure 7.6 as solid points. Thermal conductivity trends are the same as the electrical conductivity: $SnBi_2Te_4$ is the largest value, followed by $SnBi_4Te_7$, and closely followed by $SnBi_6Te_{10}$. The hollow points on the chart depict "κ_{ph}" $= (\kappa - \kappa_{el})$, by utilizing Wiedemann-Franz law(1.2.3): $\kappa_{el} = L\sigma T$, with $L = 2.45 \cdot 10^{-8}$ $W\Omega K^{-2}$ – the original value,[29] not an unreasonable estimate though doped PbTe was determined to have $L = 2.07 \cdot 10^{-8}$ $W\Omega K^{-2}$[30] at the lower 250 K. Not depicted on the above figure, the electrical contribution will be of identical shape to σ in Figure 7.5, though this is implied by the nature of the Wiedemann-Franz law. In this particular case, "κ_{ph}" is shown in quotation marks because it is unrealistic to yield phonon contributions that continually increase over the full range of this measurement – for a more accurate statement, one might consider $(\kappa_{ph} + \kappa_{bipolar})$ for the true "left-over" thermal contributions. Many bismuth telluride derivatives

show movement from both *n*- and *p*-type carriers when heated past a certain point[28] – in this case, likely ~480 K – which causes a faster drop in ZT (tail end of Figure 7.6's right-hand plot). Nano-scale alterations on Bi_2Te_3 (hot-pressed ball-milled samples) for example,[122] are being utilized as an approach to suppress the bipolar effect and increase ZT. After engagement of the bipolar contributions (or potentially Te-deficiencies), one notices a large increase in thermal conductivity and presumably a greater rate of change for S moving from positive towards negative values. At this point however, the bipolar contributions cannot be separated from each other, though experimental setups have been derived to specifically measure κ_{ph} – a logical future approach.

Using a 6th order polynomial fit to merge thermal data with power factors at the same temperatures, ZT can be calculated for the three major ternary compounds of interest. As can be seen from Figure 7.6, the figure of merit curves show very similar shape and ordering to that of the experimental Seebeck coefficients. $SnBi_2Te_4$ shows the largest ZT at 383 K with 0.33. $SnBi_4Te_7$ shows its greatest value at 298 K with 0.27, and $SnBi_6Te_{10}$ shows the smallest ZT at 324 K with a value of 0.15.

7.4. Summary and Conclusions

With the full ZT values for three ternary layered tin tellurides, it can be seen that $SnBi_2Te_4$ shows the greatest ZT = 0.33 at 383 K. The measured $SnBi_4Te_7$ and $SnBi_6Te_{10}$ compounds show maximum values closer to room temperature, making them potentially more valuable towards thermoelectric cooling applications as opposed to moderate-temperature automotive applications or high-temperature space exploration applications. With these three compounds it appears some potential disadvantages arise – likely due to Te-loss during sample preparation (i.e. $SnBi_2Te_{4-x}$) – which would make the associated thermoelectric properties drop much faster than expected, either outright lowering ZT or pushing its maximum value towards lower temperatures. Success could be better achieved by taking steps to suppress the evident bipolar conductivity in $SnTe-(Bi_2Te_3)_y$ samples. All compounds are narrow-gap *p*-type semiconductors with variations on the Bi_2Te_3-type layering schemes and plate-like crystals. The simple layered compounds can be easily made pure phase from the raw elements, but as the layering along the c-axis becomes more complex the likelihood of finding pure phase samples greatly decreases; twinning of crystalline samples then made single crystal XRD attempts largely unsuccessful.

$Sn_2Bi_2Te_5$ was eventually found pure phase and is comprised of a nine-layer trigonal structure stacked with alternating layers of *metal*-Te-*metal*-etc forming a ccp arrangement by means of all atom types.[198] By examining the observed data for Seebeck and electrical conductivity, this compound may be an interesting target for future work. With the ternary Seebeck coefficient having a maximum value at 609 K, the coefficient increases for the entire range of this measurement and may show good potential for automotive applications as it has the highest temperature range of the known layered tin ternaries. Likewise, this compound does not show an increase in electrical conductivity at the maximum range of the ZEM measurement. This may imply that the extra bipolar contributions expected for the other three compounds are either non-existent or occurring at a higher temperature then currently explored. Further investigations including *p*-type doping with Ga or Tl, for example, or encapsulation of SnTe/$Sn_2Bi_2Te_5$ nanoparticles in a bulk $Sn_2Bi_2Te_5$ matrix may provide beneficial contributions to the thermoelectric industry.

Chapter 8. Tuning of the Physical Properties for $SnBi_2Te_4$

Zhukova *et al.*[193] discovered the crystal structure of $SnBi_2Te_4$ in 1971, solved in $R\bar{3}m$ having a unit cell of 4.41×4.41×41.51 $Å^3$. This structure is a layered variant of the Bi_2Te_3-type crystal structure, shown previously. Placing the Sn atoms on the 0 0 0 Wyckoff position (3*a*) yields the diagram below (Figure 8.1). Bi sits on the 0 0 0.4278 (6*c*) site and Te occupies two sites: 0 0 0.136 and 0 0 0.29, both 6*c*. As can be seen, the unit cell is comprised of covalently bonded sections separated by van der Waals gaps ($d_{Te–Te}$ = 3.6 Å) with Sn atoms in the centre of each block. Due to each block occurring as alternating cis then trans, each unit cell is comprised of three blocks. While several models propose a mixed occupancy between Sn and Bi, data has been solved in both for example $PbBi_2Te_4$ where indistinguishable Pb, is usually fixed on the 3*a* position. Shown in Figure 8.1 below is a representation of a triple unit cell along *a*:

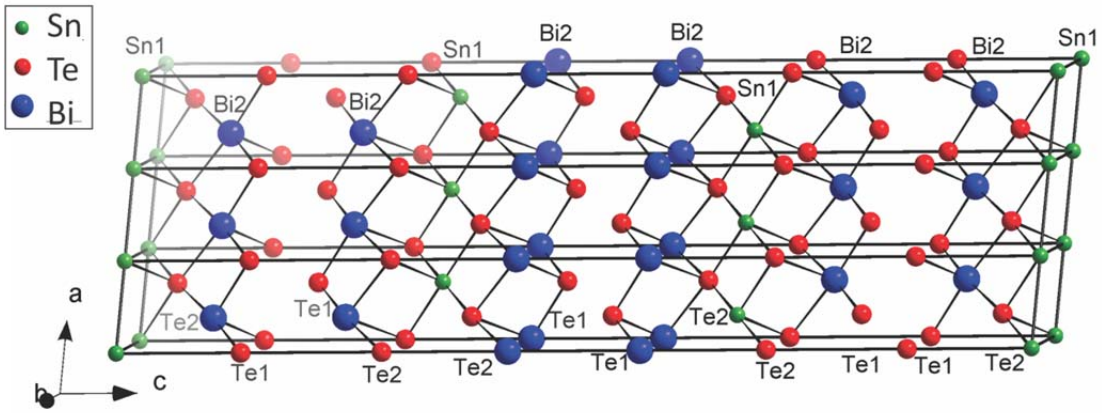

Figure 8.1 Triple unit cell of $SnBi_2Te_4$ along *a*.

Both crystal structure and physical properties of $SnBi_2Te_4$ have been studied to certain extents by a variety of research groups. Most recently, detailed melting studies predict $SnBi_2Te_4$ melts eutectically at 840 K at composition of approximately 45 % SnTe : 55 % Bi_2Te_3.[181] Additionally, studies have explored the phase diagram of the system with attempts at indexing and unit cell size;[178, 180, 193] thermoelectric properties of the stoichiometric ternary were discussed in **Chapter 7**;[179, 183, 188, 194] and electron microscope studies on alloying, solubility, and precipitates within the SnTe/PbTe-Bi_2Te_3 system have been undertaken.[192, 206]

From the understanding of this compound gained in the literature as well as the known benefits of heavy-element layered structures, one is left with numerous queries including structure and improvement of its properties. In 2010, similar studies were also investigated in the Kleinke group[189] on the sister compound $PbBi_2Te_4$ with information regarding the phase range, XRD studies, and thermoelectric properties. Such studies as understanding the compound's phase range and attempts at doping to optimize charge carrier concentrations will greatly aid in a thorough understanding of $SnBi_2Te_4$. Through the gathering of crystallographic and DFT information on this system, one aims to understand the effects of tuning via additional elements on the cation sites. Doping and substitution experiments will ideally reflect some of these behaviours through cumulative physical property studies.

8.1. Synthesis and Structural Analysis

Compounds were synthesized according to 7.2 and were weighed to a minimum of ±0.0005 g. While it was necessary to optimize the heating conditions for this system to avoid primarily Bi_2Te_3 or $SnBi_4Te_7$, reactions were heated slowly to 923 K where they were left for 12 or 24 hours. The samples were then quickly cooled to 843 K and left for 1 to 2 weeks before cooling to room temperature. Thus, a typical heating scheme for this system can be depicted as:

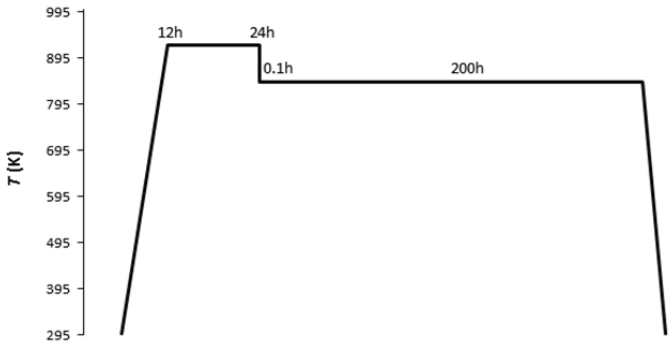

Mixed phases were returned to 843 K in sealed tubes for approximately 2 weeks. Powdered samples of pure phase were typically cold-pressed into 10×2×2 mm^3 bars, annealed for 12 hours in sealed tubes at 723 K and measured by the ZEM instrument.

Attempts throughout this work to obtain a single crystal of $SnBi_2Te_4$ were generally in vain despite numerous strategic attempts including cooling rates of 1 °/hr near its melting point, various salt fluxes, or transport reactions involving $TeCl_4/I_2$; the fine plate-like crystals turned out to be powder when cut and twinning made any obtainable data near-impossible to properly analyze. One exception

however was successfully analyzed from an exploratory synthesis attempt. The data collections were carried out on a BRUKER SMART APEX CCD at room temperature utilizing Mo-K_α radiation. The crystal was picked from a reaction of attempted $TlSnBi_3Te_6$ stoichiometry. Data was collected by scans of 0.3° in ω in at least two blocks of 900 frames at ϕ = 0° and ϕ = 120°, with exposure times of 40 seconds per frame yielding 1893 used reflections between 5.9 and 59.8 2θ. The data was corrected for Lorentz and polarization effects.

Structure refinements were performed with the SHELXTL package [130] and completed using the atomic positions published for $SnBi_2Te_4$ [193] assuming mixed Tl/Sn/Bi occupancies on the 3*a* site and 6*c* site, with Tl:Bi based on EDX data due to their indistinguishable scattering. Attempts to fix Sn on the 3*a* site of the crystal resulted in a negative occupancy factor for Sn, such that the site (Table 8.4) was assumed to include heavier atoms. Refinements converged smoothly without showing any abnormalities.

Using powder data and Rietveld refinements modeled from the early reports of $SnBi_2Te_4$[193] where identical quantities of Sn and Bi were mixed on both the 3*a* (i.e. "Sn site") and 6*c* (i.e. "Bi site") evenly such that [Sn] = 33.3 % and [Bi] = 66.7 % on both sites. Three different refinement scenarios (in Table 8.1) converged successfully with $R_P \backslash R_B$ values between 0.066\0.064 and 0.0492\0.0461 with both Te sites fixed at 100% occupancy, assuming no deficiencies on any site. In some cases, the current model caused the U_{eq} values to converge to negative values – namely *M*(2) and Te(1) – but to fix only these values would result in a negative U_{eq} for *M*(1) and in some cases also for Te(2). Thus, for the sake of this comparison, all U_{eq} were fixed at 0.025 Å; this action still yielded similar and acceptable R values. Fixing *M*(1) as Sn and *M*(2) as Bi yielded reasonable ~6.5 % R values, but better R values were obtained by allowing the originally published quantity of mixing (i.e. 33.3 % Sn on both *M* sites) and onward to higher quantities of Sn on the *M*(1) site. The best R values were not surprisingly found after allowing the occupancies of both *M* sites to refine, but serves as a thought exercise since the stoichiometry is far beyond 1 Sn : 2 Bi.

Table 8.1 Rietveld refinements on $SnBi_2Te_4$ ($R\bar{3}m$ H, 298 K, λ = 1.5406 Å).

Refinement Type	Ordered	Fixed ⅓:⅔ Mixing	Partial Mixing	*M* Sites Free
Formula	$SnBi_2Te_4$	$SnBi_2Te_4$	$SnBi_2Te_4$	$Sn_{1.4}Bi_{1.6}Te_4$
***a* (Å)**	4.40374(6)	4.40369(5)	4.40372(5)	4.40371(4)
***c* (Å)**	41.6042(8)	41.6047(6)	41.6043(6)	41.6044(6)
***V* (Å^3)**	698.730(13)	698.73(1)	698.73(1)	698.727(9)
R_P[c] \ R_B[d]	**0.066 \ 0.064**	**0.0516 \ 0.0483**	**0.0509 \ 0.0542**	**0.0492 \ 0.0461**
% Sn – *M*(1)	1.000	0.333	0.800	0.74(2)
(00*z*) – *M*(2)	0.4303(1)	0.43093(8)	0.4295(1)	0.42941(8)
% Sn	0.000	0.333	0.100	0.32(2)
(00*z*) – Te(1)	0.13886(8)	0.13719(7)	0.13813(7)	0.13683(9)
(00*z*) – Te(2)	0.2908(1)	0.2842(1)	0.2903(1)	0.2891(2)

[c] $R_P = \Sigma|y_o - y_c| / \Sigma|Y_o|$ [d] $R_B = \Sigma|I_o - I_c| / \Sigma|I_o|$

This demonstrates that these *M* sites exhibit preferences for Sn on the *M*(1) site and Bi on the *M*(2) site, but are not likely ordered entirely as such. Nevertheless, with the current model one can only use these observations to speculate; $Sn_{1.4}Bi_{1.6}Te_4$ is impractically off-stoichiometry (namely due to problems with the *M*(1) U_{eq} upon attempted refinement) for a $SnBi_2Te_4$ refinement. Utilizing the "ordered" model above, one yields bond distances of: Sn(1)–Te(2) = 3.098(3) Å; Bi(2)–Te(1) = 3.083(3) Å; Bi(2)–Te(2) = 3.404(4) Å. It is therefore likely that the ternary compound, despite problems with the current model, of hosting quantities of either Sn or Bi on both *M* sites.

8.2. Phase Range Studies on $SnBi_2Te_4$ via $(Sn,Bi)_3Te_4$

The phase range for $SnBi_2Te_4$ was studied in order to determine not only the flexibility of the structure's stoichiometry but to verify the additional phases in the system, including possible secondary phases and any potential unknown compounds in the Sn-Bi-Te phase diagram. The studies thusly aim to understand whether or not an off-stoichiometry version is more easily formed or thermoelectrically more viable. The initial $SnBi_2Te_4$ ternary was first synthesized followed by general formulae $Sn_xBi_{3-x}Te_4$ with $0 < x < 2.2$ in order to push the stoichiometry beyond its limits through *x* increments of 0.1:

Table 8.2 Selected phase range entries for $Sn_xBi_{3-x}Te_4$ in *x* increments of 0.2.

Target	*x*	Primary XRD Phase	Additional Phases
$Sn_0Bi_3Te_4$	0	Bi_2Te_3	Bi_4Te_5
$Sn_{0.2}Bi_{2.8}Te_4$	0.2	$SnBi_6Te_{10}$	–
$Sn_{0.4}Bi_{2.6}Te_4$	0.4	$SnBi_4Te_7$	–
$Sn_{0.6}Bi_{2.4}Te_4$	0.6	$SnBi_4Te_7$	**$SnBi_2Te_4$**
$Sn_{0.8}Bi_{2.2}Te_4$	0.8	**$SnBi_2Te_4$**	$SnBi_4Te_7$ + $SnBi_6Te_{10}$
$Sn_1Bi_2Te_4$	1.0	**$SnBi_2Te_4$**	–
$Sn_{1.2}Bi_{1.8}Te_4$	1.2	**$SnBi_2Te_4$**	–
$Sn_{1.4}Bi_{1.6}Te_4$	1.4	$Sn_2Bi_2Te_5$	**$SnBi_2Te_4$**
$Sn_{1.6}Bi_{1.4}Te_4$	1.6	$Sn_2Bi_2Te_5$	–
$Sn_{1.8}Bi_{1.2}Te_4$	1.8	$Sn_2Bi_2Te_5$	$SnBi_3Te_4$ + Sn_3BiTe_4
$Sn_2Bi_1Te_4$	2.0	$Sn_2Bi_2Te_5$	Sn_3BiTe_4
$Sn_{2.2}Bi_{0.8}Te_4$	2.2	Sn_3BiTe_4	$Sn_2Bi_2Te_5$

The phase range studies show that the $SnBi_2Te_4$ phase is single between $0.90 < x < 1.2$; upon reduction of the Sn : Bi ratio below $x = 0.90$, one yields the additional $SnBi_4Te_7$ phase. Increasing the ratio of Sn : Bi is slightly more resilient however, as up to $Sn_{1.2}Bi_{1.8}Te_4$ can be achieved pure phase, demonstrating the potential for Sn mixing on the Bi site. Crystal data from the nominal composition "$TlSnBi_3Te_6$" led to the discovery of a single crystal, refined to $Tl_{0.35}Sn_{0.66}Bi_{1.99}Te_4$, where unit cell information can be viewed in Table 8.3. The refined crystal data highlights Sn-site changes with additional Tl on the Sn site (3*b*), as is revealed in Table 8.4:

Table 8.3 Crystallographic data for $Tl_{0.36}Sn_{0.65}Bi_{1.99}Te_4$.

Formula Weight [g/mol]	1077.29
T of measurement [K]	293(2)
λ [Å]	0.71073
space group	$R\bar{3}m$
a = *b* [Å]	4.4166(3)
c [Å]	41.504(6)
V [Å^3]	701.13(12)
Z	3
μ [mm^{-1}]	57.48
ρ_{calcd} [g/cm^3]	7.654
$R(F_o)^a \setminus R_w(F_o^2)^b$	0.0278 \ 0.0635

$^a R(F_o) = ||F_o|-|F_c||/|F_o|$ $^b R_w(F_o^2) = [\,\Sigma[w(F_o^2 - F_c^2)^2]/\Sigma[w(F_o^2)^2]\,]^{1/2}$

Although there is evidence here of Tl/Bi mixing on the Sn site and vice-versa, there is still a preference towards heavy atoms on the 6c site (comprising …Bi_2… in the original model) which was found to be only 10 % Sn in this case. The 3*b* site (Sn) was set to 46 % which is less Sn than expected and in the case of the ternary, was Rietveld-refined to as low as ~74 % Sn on 3*b*. Thus, if the phase range studies were to lead to any major conclusions, it would be that $SnBi_2Te_4$ is stable with minimal ordering of Sn-Bi, allowing for flexibility between metal atoms – in this case, Tl. This additional information as well as the aforementioned several refinement iterations (i.e. no mixing, all mixing, some mixing, etc.) on $SnBi_2Te_4$ leads one to believe there is still order in the system, illustrated by Figure 8.1. The structure should not be thought of as the random $(Sn,Bi)_3Te_4$.

Table 8.4 Occupancy factors of $Tl_{0.36}Sn_{0.65}Bi_{1.99}Te_4$.

Atom	Site	*x*	*y*	*z*	U_{eq} [Å^2]	Occ.
Tl1	3*b*	0.3333	0.6667	0.1667	0.0230(2)	0.11
Sn1		0.3333	0.6667	0.1667	0.0230(2)	0.46
Bi1		0.3333	0.6667	0.1667	0.0230(2)	0.43
Tl2	6*c*	0	0	0.07168(5)	0.0234(10)	0.12
Sn2		0	0	0.07168(5)	0.0234(10)	0.1
Bi2		0	0	0.07168(5)	0.0234(10)	0.78
Te1	6*c*	0.3333	0.6667	0.03095(2)	0.0172(2)	1
Te2	6*c*	0.6667	0.3333	0.121827(17)	0.0159(2)	1

It should again be quickly noted that with the addition of three atoms on each of the *M* sites forces one to speculate on the respective ratios. Thusly, one must take advantage of the Rietveld results above as well as supporting EDX data to support the occupancies displayed in the above table. The obtained R-values for the crystal however, demonstrate that this model is also agreeable with the single crystal's obtained reflections.

For phase-pure samples of varying Sn : Bi ratios *x* = 0.8; 0.9; 1.0, ZEM measurements were taken to observe changes in S and σ values. As can be seen from Figure 8.2, the original $SnBi_2Te_4$ and $Sn_{1.1}Bi_{1.9}Te_4$ show Seebeck coefficient values that are nearly identical except for the slight shift in S_{max} towards higher temperatures. The stoichiometry $Sn_{1.2}Bi_{1.8}Te_4$ however, shows a significantly lower Seebeck coefficient with an S_{max} value approximately 100 K further than its counterparts. This, like Figure 7.5, shows similar behaviour to that of $Sn_2Bi_2Te_5$, which happens to be the phase that follows

$SnBi_2Te_4$ in the phase range studies. Based on this observation, it becomes apparent that "$Sn_{1.2}Bi_{1.8}Te_4$" behaves as a Bi-poor variant of "$Sn_{1.5}Bi_{2.5}Te_5$" – which is the same structure as $Sn_2Bi_2Te_5$ – though the observed experimental XRD pattern shows a slightly right-shifted $SnBi_2Te_4$ pattern with ~1% intensity where the $Sn_2Bi_2Te_5$ peak would be expected (Figure 7.3). The $Sn_{1.5}Bi_{2.5}Te_5$ structure-type was adapted by $Ge_{1.5}Bi_{2.5}Te_5$.[207]

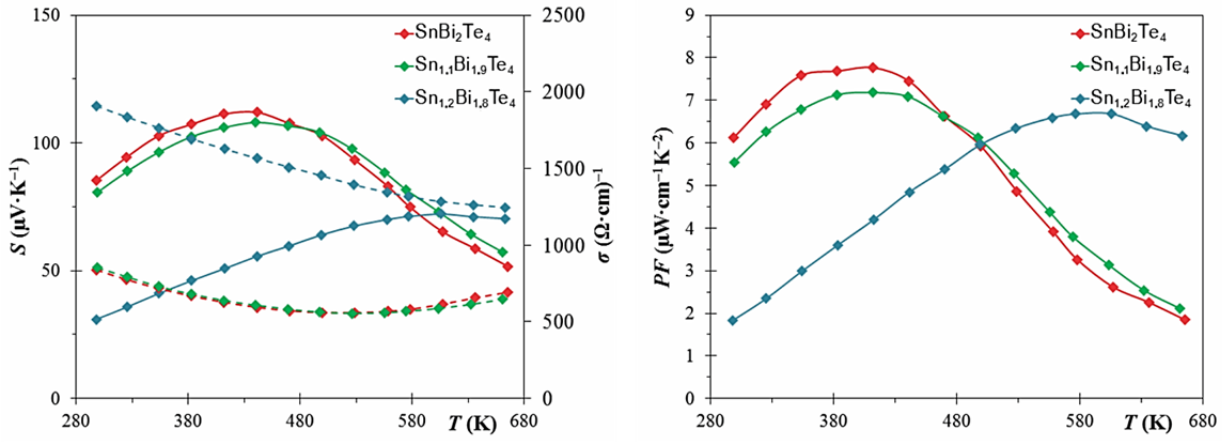

Figure 8.2 Seebeck coefficients (solid), electrical conductivities (dashed) and power factor (right) for $Sn_xBi_{3-x}Te_4$.

Upon examination of the electrical conductivity data, again the two compounds of lesser Sn content show essentially the same properties as one another, with the third behaving similarly to $Sn_2Bi_2Te_5$. Based on these results, it can be concluded that $Sn_{1.1}Bi_{1.9}Te_4$ is essentially the border of this particular phase with minimal changes to its properties.

To further probe the understanding of this system, a series of calculations were performed to model $SnBi_2Te_4$. In this case, the standard LMTO method, used in most of the work herein, was run in parallel to WIEN2k, in a series of comparisons. One is thusly able to observe the differences not only between the muffin tin approximation and full augmented plane wave approximation, but additionally the effects of spin-orbit coupling, an effect considered for structures with very large atoms, as with $SnBi_2Te_4$. The various calculations are paralleled in Figure 8.3:

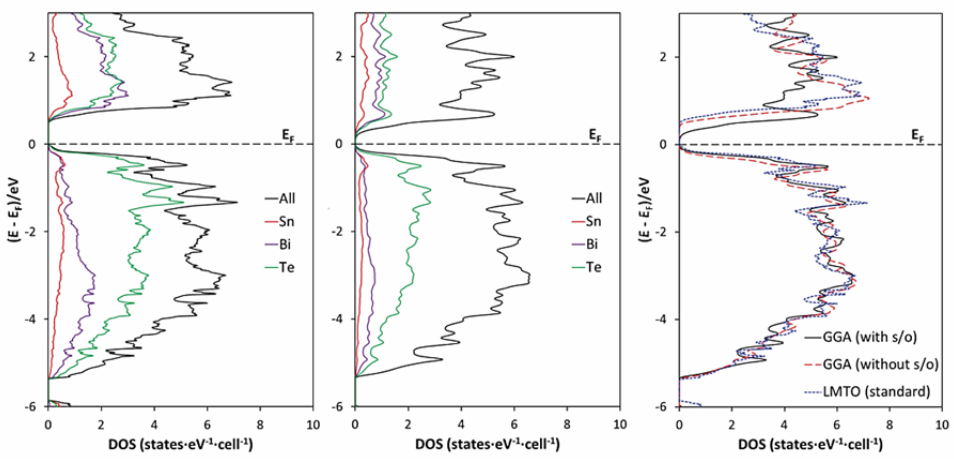

Figure 8.3 *DOS* calculation comparisons for $SnBi_2Te_4$.
Standard LMTO software (left), WIEN2k software with spin-orbit coupling (centre), and three-way comparison (right).

Based on the modifications, it is observed that LMTO overestimates the band gap at 0.48 eV whilst the basic GGA predicts 0.45 eV and spin-orbit coupled GGA predicts 0.27 eV – a significant reduction in band gap energy. All three cases were quite similar when predicting the conduction band of $SnBi_2Te_4$, though a lesser contribution from Bi orbitals (mostly *s*) is reduced in the spin-orbit coupled GGA (centre plot of Figure 8.3). More intense changes are observed in the magnitude of the orbital contributions within the valence band immediately after the Fermi level, where GGA (with SOC) predicts a sharp *DOS* and the others assume a broad *DOS*. The added information from spin-orbit coupling further improves the representation of this structure.

8.3. Doping and Substitution Experiments on $SnBi_2Te_4$

For thermoelectric applications, one would expect a compound to show an ability to improve its properties via an optimization process. In this sense, a traditional solid state approach can be utilized to in order to determine whether or not $SnBi_2Te_4$ has more to gain as a thermoelectric material. Doping experiments can therefore be employed to adjust its physical properties and figure of merit. Based on studies in **Chapter 7**, $SnBi_2Te_4$ with its narrow band gap, reasonable Seebeck magnitude and heavy atoms is in good standing for optimization. Likewise, the phase range experiments support the material's ability to host atoms of varying concentrations. Little is known with respect to the doping potential of $SnBi_2Te_4$ with the possible exception of a study on Te-doped $PbSb_2Te_4$, showing a marginal increase in S and decrease of σ.[208]

Studies done by, for example, Heremans *et al.*[104] and Gelbstein *et al.*[190] show the unique potential of the triel (*Tr*) elements generating impurity states in the band gap and Fermi level pinning – since triel elements are often Tr^{3+}, their introduction to the Sn^{2+} site should lead to a one-electron difference in counting. It should also be noted the tendency for Tl^{+} and in certain cases, In^{+} as a possibility.

8.3.1. Synthesis and Structural Analysis

As expected, all samples in this system can be synthesized from the elements and doped samples were no exception. The dopants utilized were as follows: Ga: 99.999 %, ingot (metals basis), ALFA AESAR; In: 99.999 %, ingot (metals basis), ALFA AESAR. Substituents have a wider range of elements for the Bi site including Ga and In, but also the following: Tl: 99.99 %, granules 1-5mm, ALDRICH; Nb: 99.8 %, powder -325 mesh, ALFA AESAR; Ta: 99.98 %, powder -100 mesh, ALFA AESAR. Upon their removal from the furnaces, many samples were inhomogeneous and required grindings followed by sintering at 843 K for approximately ten days up to a maximum of three reheats. Utilizing either dopant, samples were synthesized according to $Tr_xSn_{1-x}Bi_2Te_4$ with increments of x = 0.01 until x = 0.05 and additional x = 0.07, 0.10, 0.12, and 0.15 to identify the primary impurity phases from excess dopant. The substituents ($V/Tr_xSnBi_{2-x}Te_4$) followed the same increments with additional x = 0.20, and 0.25 to identify primary impurity phases and determine the maximum amount of impurity. XRD yielded, eventually, phase-pure samples up to x = 0.07 for doping and x = 0.15 for substitution. EDX was run on selected phase-pure samples, yielding acceptable atomic ratios.

In order to better determine if the elements were successfully incorporated, refinements were attempted on a series of compounds and their respective LeBail findings are displayed, in Table 8.5. All refinements on doped samples were performed with the proposed single crystal model[193] and followed a similar refinement "recipe" for consistency.

Table 8.5 Summary of LeBail refinements for $Tr_xSn_{1-x}Bi_2Te_4$ and $Tr/V_xSnBi_{2-x}Te_4$.

Target Compound	Space Group	a (Å) = b	c (Å)	V (Å^3)	Z	R_P[a] \ R_B[b] (%)
$SnBi_2Te_4$ (cif)[193]	$R\bar{3}m$	**4.411**	**41.51099**	**699.47**	**3**	\
———	———	———	———	———	———	———
$Ga_{0.02}Sn_{0.98}Bi_2Te_4$	$R\bar{3}m$	4.402(1)	41.66(1)	699.1(5)	3	4.40 \ 7.73
$Ga_{0.07}Sn_{0.93}Bi_2Te_4$	$R\bar{3}m$	4.395(2)	41.77(2)	698.7(9)	3	7.85 \ 8.05
$In_{0.02}Sn_{0.98}Bi_2Te_4$	$R\bar{3}m$	4.394(2)	41.62(2)	696.1(7)	3	5.42 \ 6.89
$In_{0.07}Sn_{0.93}Bi_2Te_4$	$R\bar{3}m$	4.4041(8)	41.590(7)	698.6(3)	3	5.16 \ 7.67
———	———	———	———	———	———	———
Target Compound	**Space Group**	**a (Å) = b**	**c (Å)**	**V (Å^3)**	**Z**	**R_P[a] \ R_B[b] (%)**
$Ga_{0.02}SnBi_{1.98}Te_4$	$R\bar{3}m$	4.3961(3)	41.644(2)	696.99(9)	3	3.98 \ 6.59
$Ga_{0.05}SnBi_{1.95}Te_4$	$R\bar{3}m$	4.37259(8)	41.3911(8)	685.35(2)	3	4.00 \ 5.61
$In_{0.05}SnBi_{1.95}Te_4$	$R\bar{3}m$	4.375(1)	41.39(1)	686.0(6)	3	6.08 \ 7.45
$In_{0.07}SnBi_{1.93}Te_4$	$R\bar{3}m$	4.3966(2)	41.584(1)	696.12(5)	3	3.70 \ 4.18
$In_{0.15}SnBi_{1.85}Te_4$	$R\bar{3}m$	4.37380(7)	41.4294(7)	686.37(2)	3	3.48 \ 5.21
$Tl_{0.05}SnBi_{1.95}Te_4$	$R\bar{3}m$	4.39009(6)	41.5146(7)	692.91(1)	3	3.81 \ 4.73
$Nb_{0.05}SnBi_{1.95}Te_4$	$R\bar{3}m$	4.4012(2)	41.627(2)	698.29(8)	3	4.29 \ 7.81
$Ta_{0.05}SnBi_{1.95}Te_4$	$R\bar{3}m$	4.387(1)	41.56(1)	693.0(6)	3	6.08 \ 6.81

[a] $R_P = \Sigma|y_o - y_c| \,/\, \Sigma|y_o|$ [b] $R_B = \Sigma|I_o - I_c| \,/\, \Sigma|I_o|$

It is apparent from the structural refinements that clear changes to the cell size and volume have occurred with several different impurity elements. With all refinement showing R-values below 10 %, impurity inclusions should be considered successful. As intended, it can also be said that the Bi-site replacements generally produced smaller unit cell sizes than their Sn counterparts.

8.3.2. Electronic Structure Calculations

Via the standard LMTO software, predictions of the quaternary $SnBi_2Te_4$ samples could be performed and compared to one another. Of these calculations, several were selected and presented below in Figure 8.4 including a comparison of three triel elements on the Bi site, followed by increasing [Ga] on the Sn site and Bi site respectively. Calculations were run on a basis of 1000 evenly dispersed k points in the following symmetries: $R\bar{3}m$, $R3m$, and $C2/m$ depending on the size of the supercell used.

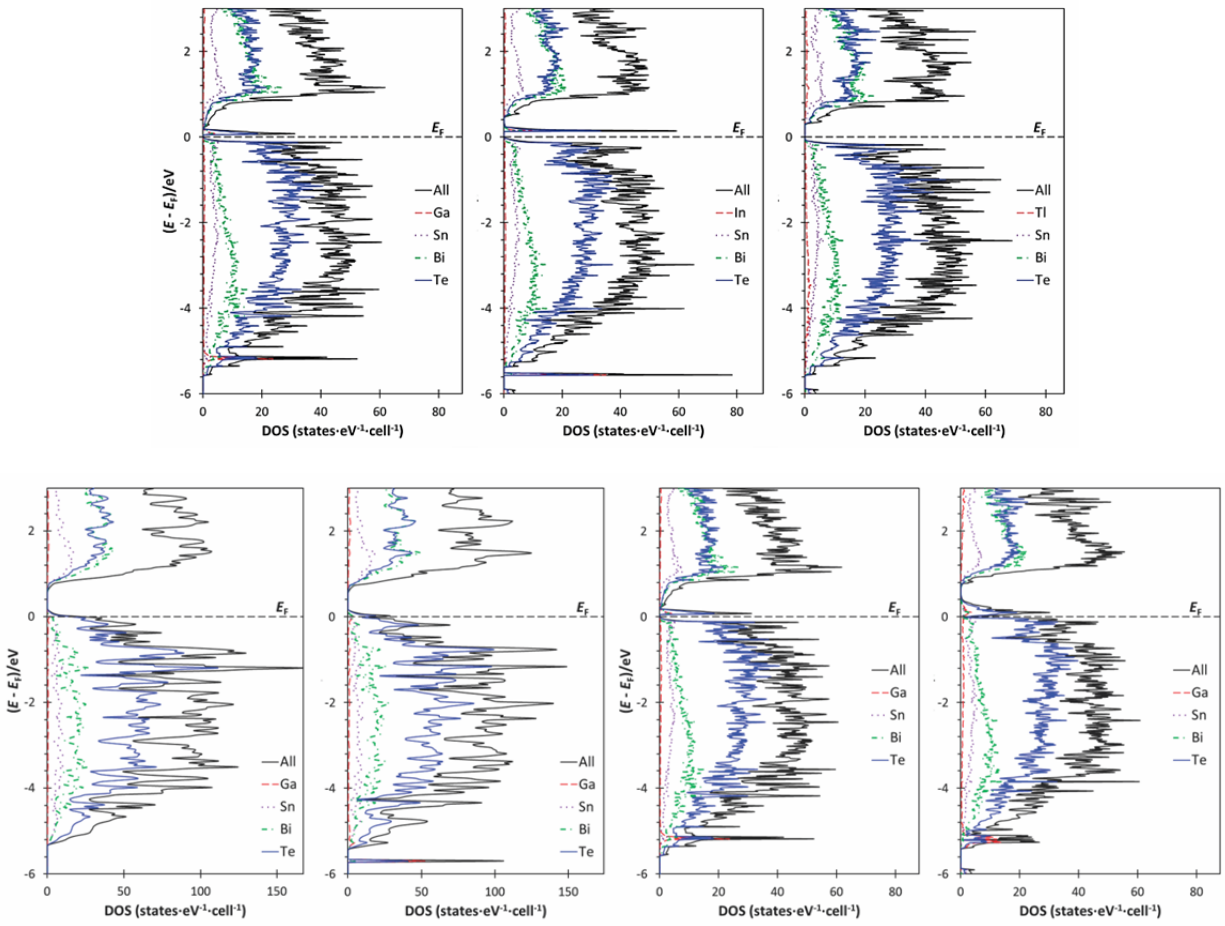

Figure 8.4 Selected *DOS* calculations for $SnBi_2Te_4$.
Top: $[Tr]_{0.625}SnBi_{1.875}Te_4$; Bottom left: $Ga_xSn_{1-x}Bi_2Te_4$, x = 0.0625, 0.125; Bottom right: $Ga_xSnBi_{2-x}Te_4$, x = 0.0625, 0.125

As can be seen in the top half of Figure 8.4, the inclusion of triel elements generates some extra impurity states, displaying a very sharp *DOS* in the case of Ga and In, though Tl inclusions show broader impurity states, having the most intense energy near -5 and 1 eV. The Ga impurity states here effectively replace the band gap, whilst the In states occur at the bottom end of the conduction band with a significant reduction in the band gap – one might expect improved electrical conductivity from this type of calculation. All triels also show impurity states around -5 eV, representing the *Tr-s* orbitals. Through examination of the Ga-inclusion on the Sn site, one notices little-to-no change in the band gap, though impurity states can clearly be seen near -5.6 eV when x = 0.125 (bottom left). The *DOS* graph changes however in the bottom right, where Ga is placed on the Bi site. Now it shows impurity states filling the band gap, increasing in intensity with increasing Ga. It would appear as if the addition of impurity states – especially in this case to the Bi site ought to increase the electrical conductivity as the band gap is driven smaller.

8.3.3. Physical Property Measurements

Samples were pressed into 10×2×2 mm^3 pellets, annealed under vacuum at 723 K and measured up to 673 K on the ZEM instrument with pellet densities of ~85 %. Samples were measured for reproducibility by taking 2 – 5 points on the same pellets with occasional second or third measurements. It should be noted that, simply measuring cold-pressed samples led to very erratic results including *n*-type conductivity. Due to the extremely large quantity of samples, only selected measurements on annealed samples will be shown or discussed.

8.3.3.1. Doping Samples

Since each *Tr* element in $[Tr]_xSn_{1-x}Bi_2Te_4$ is assumed to have one less valence electron than Sn, the initial hypothesis is that the Seebeck coefficient should become more positive with increasing [*Tr*]. The electrical conductivity is then expected to decrease. Examining Figure 8.5, Ga shows a negligible change in S and still minimal changes for In samples. Though they are all of the same shaped curve, there is no observable trend from one sample to another (right of Figure 8.5); at 380 K, 0.05 In appears to be the smallest S followed by 0.07, 0, 0.03, and 0.01. With the Ga-doped series, if 0.01 Ga is treated as an outlier then one can observe the electrical conductivity – and thus, the number of charge carriers – dropping with increasing Ga content, 0.07 Ga then reaches the lowest value of 416 $\Omega^{-1}cm^{-1}$ at 526 K. The electrical conductivity of the In-based samples do not show any trends in the first half of the temperature range, but consistently shows lower conductivity. In the last 100 degrees of the measurement however, one notices that again with the exception of 0.01 In, the trend here shows 0 > 0.05 > 0.07 which is consistent with the measurements taken on Ga. Solid lines below depict Seebeck coefficient curves, whilst dashed lines depict σ.

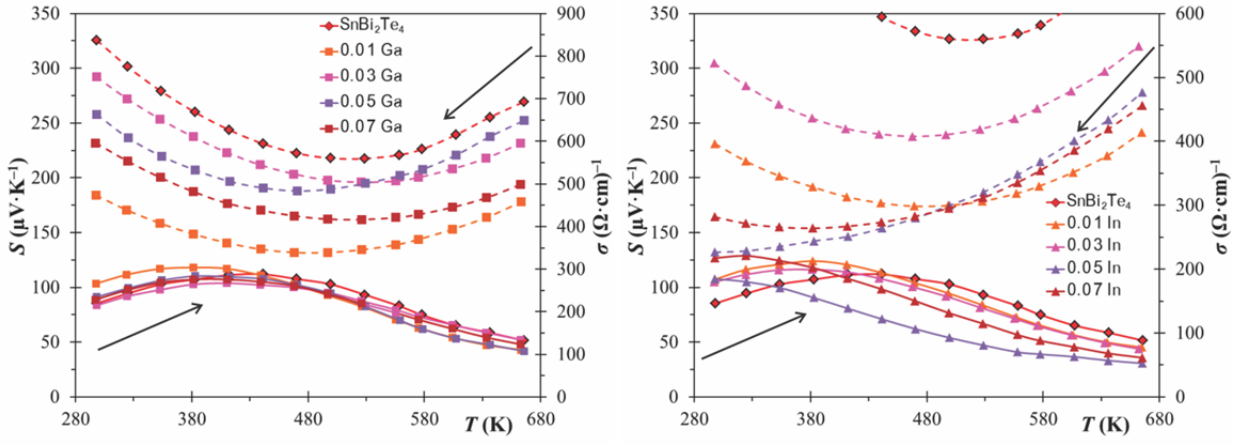

Figure 8.5 ZEM measurements on Ga-doped (left) and In-doped (right) samples for $[Tr]_xSn_{1-x}Bi_2Te_4$.

The power factor (PF) measurements for both doped trials can be examined in the following diagram. The first noticeable trait of the plots is that the largest power factor in both cases belongs to $SnBi_2Te_4$; a maximum value of 7.8 $\mu W \cdot cm^{-1}K^{-2}$ is obtained at 412 K. Any form of doping attempted lowers the magnitude of the PF similarly for both Ga and In trials. The doped magnitudes display no logical order. Though the Ga trials show no additional trends, one notices that the In trials shift their S_{max} towards lower temperatures with increasing [In]. With x = 0.01, a maximum value is reached around 380 K (5.05 $\mu W \cdot cm^{-1}K^{-2}$), but x = 0.05, 0.07 reach maxima around 300 K (263/453 $\mu W \cdot cm^{-1}K^{-2}$ respectively).

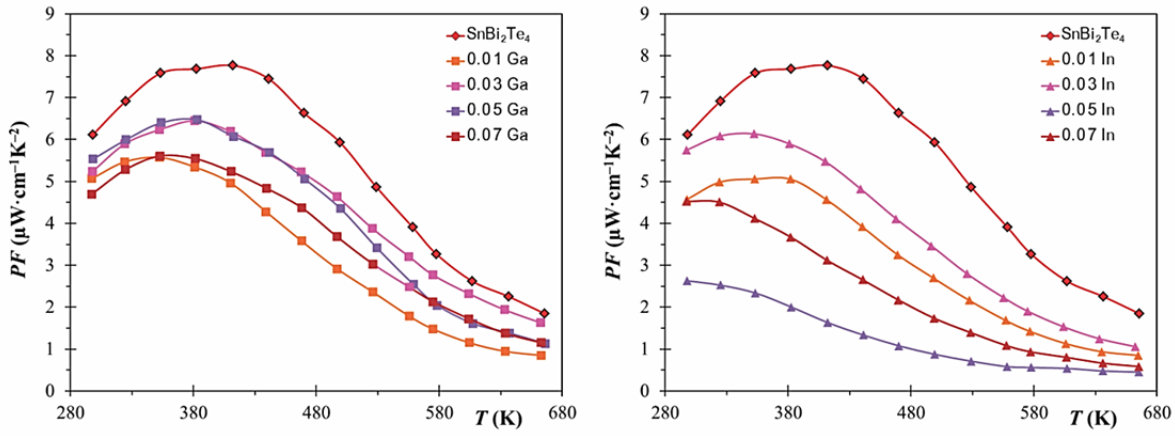

Figure 8.6 Power factor data for Ga-doped (left) and In-doped (right) samples of $[Tr]_xSn_{1-x}Bi_2Te_4$.

Measurements on selected thermal conductivity pellets reveal that there is little change in the behaviour of the doped samples. The magnitudes of the measurements, slopes of the curves and initiation of the bipolar conductivity are all seemingly unaffected by Ga- or In-doping. The one exception to this evidence is $In_{0.07}Sn_{0.93}Bi_2Te_4$ which shows κ values between 0.5 and 1 $W \cdot m^{-1}K^{-1}$. This abnormality is found in three out of eighteen similar measurements on $SnBi_2Te_4$ and is likely experimental error due to a malfunction in the IR detector.

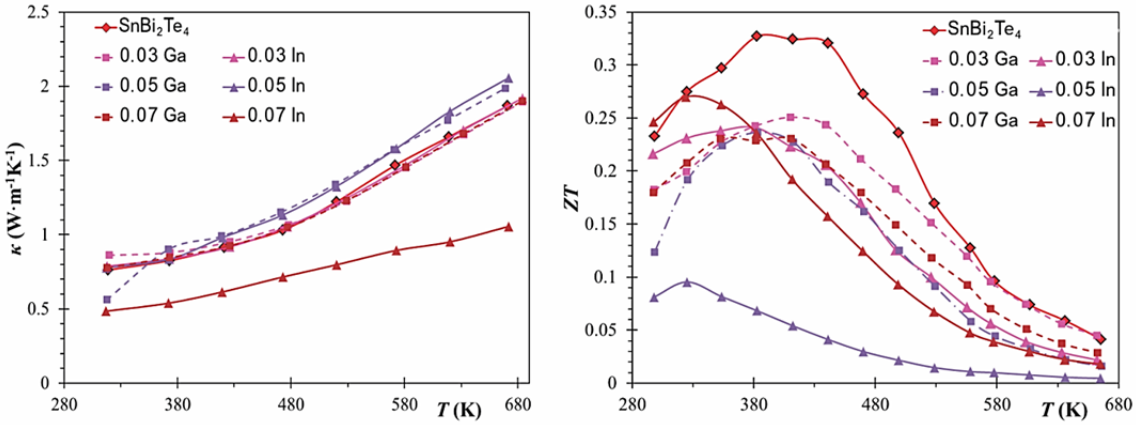

Figure 8.7 Thermal conductivity (left) and dimensionless ZT (right) for $[Tr]_xSn_{1-x}Bi_2Te_4$.

The highest ZT value belongs to the initial ternary compound, $SnBi_2Te_4$. Its maximum value of ~0.34 is found around 420 K, which is also the ZT_{max} temperature for all the doped samples. With the minute changes observed in the DOS (bottom left of Figure 8.3) however, these physical property results are not entirely unexpected – the extra states from Ga for example, blend with the other orbitals and the band gap remains similar to that of the ternary. Ignoring 0.07 In which possess abnormally low thermal conductivity, the Ga-based samples display a better ZT on average than the In samples; these maximum ZT values can be as low as 0.1 in the case of 0.05 In.

8.3.3.2. Substitution Samples

Substitution reactions were also synthesized according to $[Tr]_xSnBi_{2-x}Te_4$, *Tr* = Ga, In, Tl and $[V]_xSnBi_{2-x}Te_4$, *V* = Nb, Ta. Samples were prepared as the reactions above. Substitution of the Bi atoms allows for potential atom size differences whist maintaining the compound's initial electron counts. Ideally, the procedure would lower the thermal conductivity properties whilst keeping the power factor reasonably high.

The ZEM results for selected sample measurements are contained below in Figure 8.8 with the heavy elements displayed in separate graphs for ease of data-interpretation. The lighter substitution elements Ga and In are displayed in the bottom half of the figure with $SnBi_2Te_4$ for comparison. Unlike the previously discussed doped materials, almost all Seebeck coefficients were measured as smaller than $SnBi_2Te_4$. The lowest S values are found with *x* = 0.05 *Tr*, each of which has essentially the same magnitude at room temperature: ~65 $\mu V \cdot K^{-1}$. It is quite clear from the diagrams that all measurements show very similar shapes and that there is no logical order in the Seebeck coefficients for any of the trials. The same can be said for σ values which also show the same curve shape as the ternary, albeit a

slightly larger dispersion than the S coefficients. Samples were tested for reproducibility. Legends depict samples in order of decreasing magnitude.

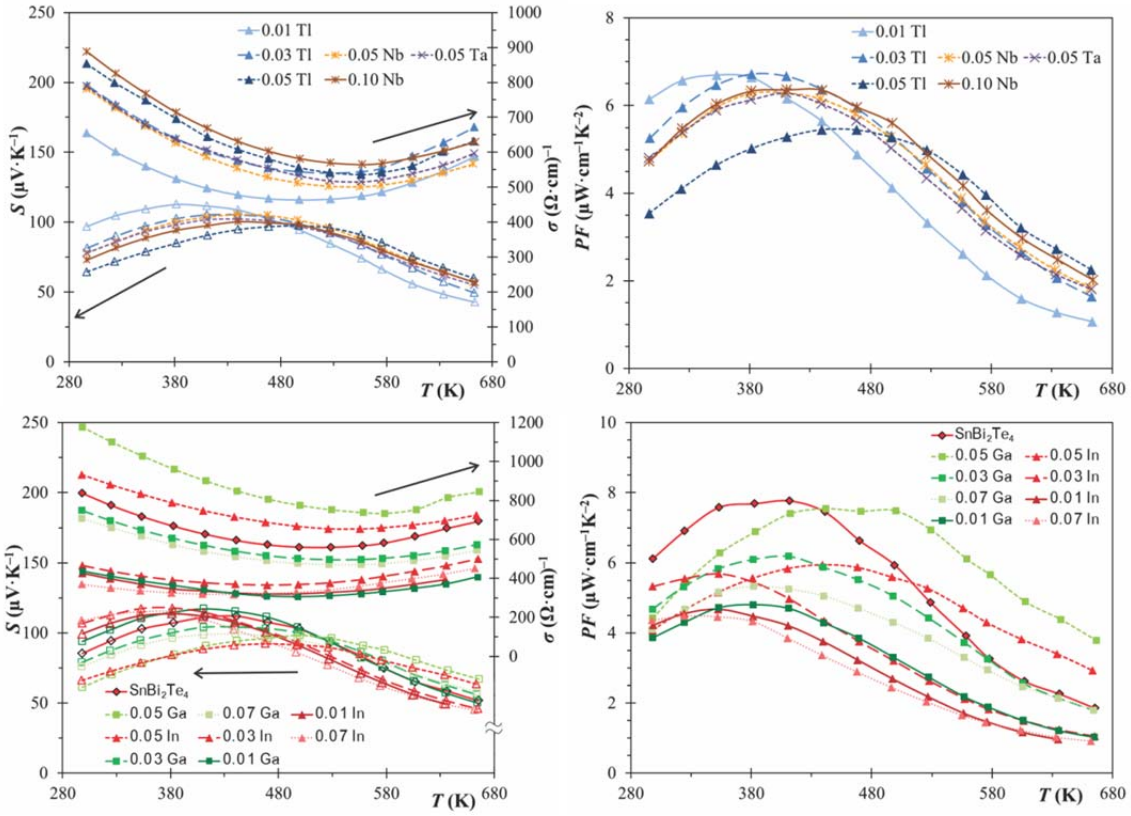

Figure 8.8 ZEM measurements on $[Tr]_xSnBi_{2-x}Te_4$: heavy element substitution (top), light element substitution (bottom).

Since there is no understandable order in either the Seebeck or electrical conductivity from these plots, one is pigeonholed into observing only the magnitude of the power factors shown above. In short, the ternary compound is still the highest magnitude measured, with a maximum power factor of ~8 $\mu W \cdot cm^{-1}K^{-2}$ (380 K) with $Ga_{0.05}SnBi_{1.95}Te_4$ following closely with ~7.5 $\mu W \cdot cm^{-1}K^{-2}$ (440 K) due to the suspiciously high $\sigma = 1180\ \Omega^{-1}cm^{-1}$ at room temperature. Nevertheless, it can be seen that the general trend for additional triel/V elements leads to a reduction of the compound's performance.

Displayed below is the thermal conductivity data obtained for the lighter substituents. Due to the underwhelming similarity of the values and potentially difficult graphic interpretation, Tl, Nb, and Ta data are omitted from Figure 8.9. The vast majority of the measurements yielded the same κ magnitude as $SnBi_2Te_4$, though $Tl_{0.05}SnBi_{1.95}Te_4$, $Nb_{0.05}SnBi_{1.95}Te_4$, and $Ga_{0.05}SnBi_{1.95}Te_4$ were all above 1 $W \cdot m^{-1}K^{-1}$, the largest of which is displayed at the top of the thermal conductivity graph below. The intense increase in

the thermal conductivity slope that can be seen in all cases below is the same as the curve shapes for the doping samples; these also share virtually identical magnitudes.

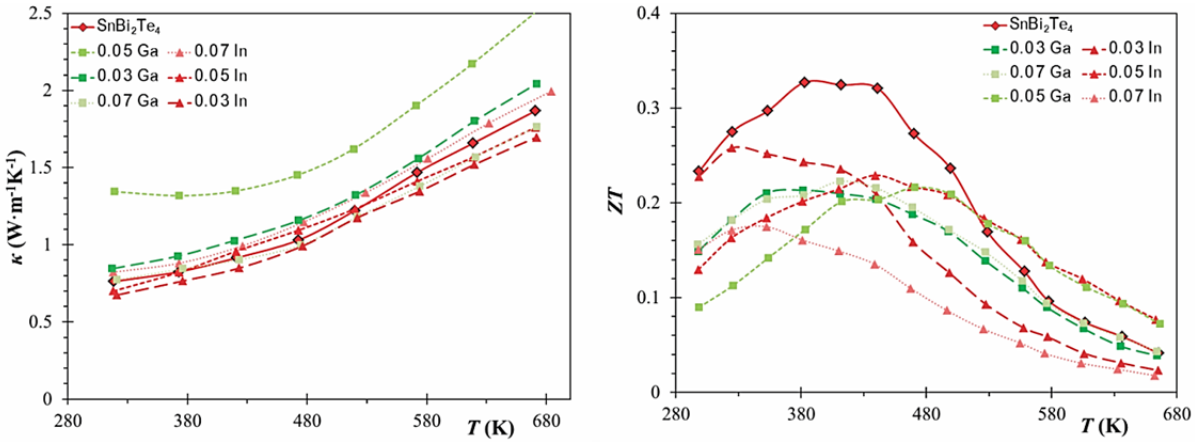

Figure 8.9 Physical properties of $[Tr]_xSnBi_{2-x}Te_4$: thermal conductivity (left) and figure of merit (right).

The figures of merit from this study show a decrease with any attempted substituent in the structure. The large increase in κ in the case of $Ga_{0.05}SnBi_{1.95}Te_4$ for example, demonstrates how the extra 0.5 $W{\cdot}m^{-1}K^{-1}$ can decrease the figure of merit by ~40 % of the ternary (~0.34 at 380 K) value. Likewise, the other reactions measured also appear to have a maximum around 0.2 with the exception of $In_{0.03}SnBi_{1.95}Te_4$ (about 0.26) – still significantly smaller than the original compound.

8.3.3.3. *Overall Comparisons and Discussions*

All physical property measurements of the $SnBi_2Te_4$ reactions were of the same shape, magnitude, and temperature range. Though systematically increasing increments of impurity elements were attempted several times, it is clear that no trend – either good or bad – can be observed for any of the thermoelectric properties. It can however, be concluded that the thermoelectric figure of merit in both doping and substitution cases suffered with the addition of these extra elements. Though the shapes of the curves help tell the story of $SnBi_2Te_4$'s internal workings, few additional conclusions can be brought forward through the incorporation of these elements.

Due to the lack of changes in the physical properties via movement from Ga to In to Tl, it may be quite probable that the impurity elements as well as Sn/Bi are mixed randomly throughout the compound. This could be thought of as, for example, $(Tl, Sn, Bi)_3Te_4$ which is similar to the suggested mixing of the single crystal results. Should the elements be evenly dispersed amongst all crystallographic sties, one would expect little change in the thermal conductivity because the smaller Sn atoms are already mixing on the larger Bi atoms' sites and vice-versa; thus, the inclusion of an additional

Sn-size atom such as In should have negligible size effects. Likewise, if a doped In^{3+} atom migrates to a Bi^{3+} site instead, no carrier difference will be realized. This is seen as a lack of impact on S and σ. This could be studied, provided an investigation has accurately-prepared samples (of systematic *x* values), a reproducible high-temperature Hall Effect setup, and good quality hot-pressed pellets.

8.3.4. DFT Calculations via WIEN2k Software

The true benefit to utilizing the WIEN2k software and the BoltzTraP program – both mentioned in 6.4 – is that one gains access to predictions of the Seebeck coefficient and its variations based on the number of charge carriers. The following calculations therefore help gain insight into the quantity of charge carriers driving the S magnitude – or in other words, what S might look like if the bipolar contributions were completely supressed. As mentioned earlier, spin-orbit coupling is employed with the GGA for a more realistic calculation.

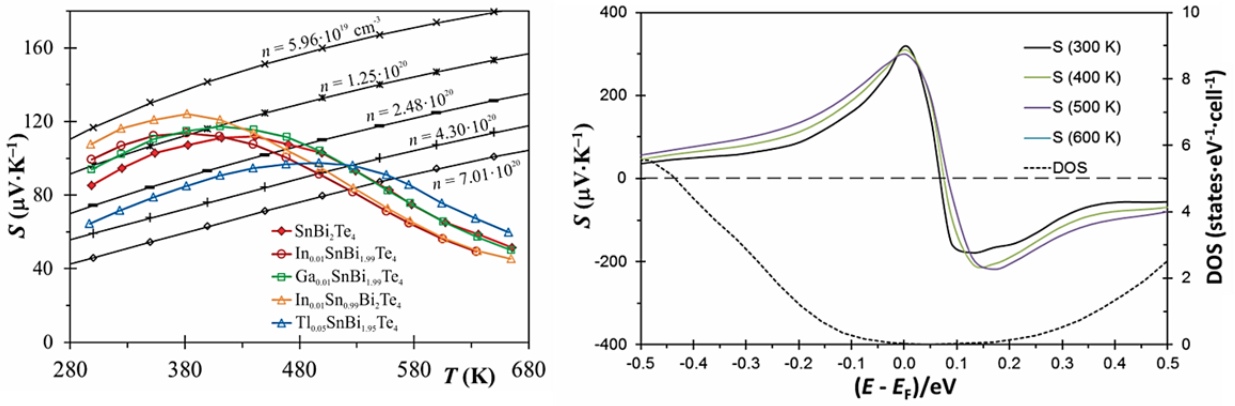

Figure 8.10 Theoretical S at varying n for $SnBi_2Te_4$ (left), S magnitude at varying Fermi levels near the band gap (right).

Shown on the leftmost of Figure 8.10 are different Seebeck coefficients calculated at five different charge carrier concentrations (n). It can be seen that the first portion of the measurement before S loses its magnitude, shares a similar slope to the calculated $SnBi_2Te_4$ data, indicating between $5.96 \cdot 10^{19}$ and $4.30 \cdot 10^{20}$ carriers/cm^3. Since the formula for $SnBi_2Te_4$ is charge-balanced, the theoretical number of free carriers is initially zero (at 0 K). However if one were to, for example, produce "$SnBi_2Te_{3.9855}$" than a simple calculation (i.e. $n = {}^{Z}/_{V} \cdot h^{+}$) where h^+ are the vacancies, one would also find $1.25 \cdot 10^{20}$ carriers/cm^3. With this knowledge, one can also predict from the rightmost image that the Fermi level in the experiment's DOS should lay near -0.25 eV as a slightly deficient conduction band. Thus, the inclusions of I-doping on the Te site, as performed on PbTe-type samples,[209] may help to explain the lack of trend in the measurements by initiating *n*-type trends at constant [*Tr*]s.

8.4. Conclusions and Future Work

A thorough investigation on the ternary compound $SnBi_2Te_4$ has been initiated. The phase range of $Sn_xBi_{2-x}Te_4$ can easily be produced single phase between $0.90 < x < 1.2$, but properties of the original ternary compound appear the best. Single crystal studies on $Tl_{0.36}Sn_{0.65}Bi_{1.99}Te_4$ reveal that both metal sites have mixing although the modelled Bi site (6*c*) still has a strong preference for heavy atoms showing 78 % Bi AND 12 % Tl – this study gives strong indication that its elusive structure is not fully ordered. Electronic structure calculations led to band gap sizes for the ternary compound between 0.48 eV (LMTO) and 0.27 eV (GGA + s/o), proving that this compound is a narrow band gap semiconductor that shows *p*-type physical properties. Though attempts to include Ga and In on the Sn site and triel/*V* elements on the Bi site were successful – as indicated by the LeBail data, the properties showed no logical trend though the figure of merit in each case was reduced below that of the original ternary. This is largely due to a general reduction in σ with a simultaneous increase in κ – namely, κ_{el}. Calculation of the Seebeck effect from the BoltzTraP software indicates that the number of mobile charge carriers before the bipolar effect dominates, are on the order of $0.6 – 5 \cdot 10^{20}$ carriers/cm^3.

With the majority of the information gathered on $SnBi_2Te_4$ regarding the bulk properties, studies can continue towards the improvement of the material through alternate venues. Since this compound is stable and easily annealed at 843 K, it is a good candidate for hot pressing to further improve pellet density and therefore thermoelectric properties. Likewise, a key observation with the current pellets is a dominant bipolar effect taking place beyond 380 K which if supressed, could result in a drastic improvement of the properties. This would involve studies aimed not only at pellet anisotropy, but what charge carriers originate from what crystallographic site. I-doping on the Te site for example has begun in parallel to this work in attempt to explain the lack of trends. It is also known that grain size reduction via ball-milling can potentially make great improvements to the properties, granted the material is hot-pressed afterwards. Studies via TEM microscopy may also reveal nanodomains that could be potentially manipulated (or artificially created via carbon nanotubes for example).

Chapter 9. Complex Layered Materials $SnBi_4Te_7$ and $SnBi_6Te_{10}$

Much like their $SnBi_2Te_4$ counterpart, $SnBi_4Te_7$ and $SnBi_6Te_{10}$ have aroused interest in the thermoelectric field for their likeness to Bi_2Te_3 and complex layering motifs. Whist the point was made in **Chapter 7**, their mysterious formation scheme makes the syntheses challenging – hence the available literature only pertains to phase ranges and diagrams. Nevertheless it was shown that both of these compounds could be produced phase-pure and each had measureable properties comparable to each other. With respect to the individual compounds, do their more complex layering arrangements benefit more suitably from doping/substitution experiments than $SnBi_2Te_4$?

9.1. Synthesis and Structural Analysis

Compounds were synthesized according to **7.2** and were weighed to a minimum precision of ±0.0005 g. While it was necessary to optimize the heating conditions for these systems, the smaller phase ranges make stability and pure phase samples difficult to achieve. All layered compounds were heated to 923 K to ensure a homogeneous melt followed by their respective optimizations: $SnBi_4Te_7$ was cooled to 823 K quickly followed by annealing for 100 hours, then it was cooled to room temperature, crushed, and returned to 823 K for another 100 hours – this strategy produced approximately 75 % pure phase samples with an additional anneal often required; $SnBi_6Te_{10}$ was cooled from 843 K to 823 K over 100 hours for elemental syntheses, while mixed-phase samples were crushed and heated at 798 K for again ~100 hours – these attempts produced pure-phase samples for ~33 % of the cases. Doping reactions on the Sn site were tried using Ga and In with $0.01 \leq x \leq 0.15$. Substitution of some Bi atoms was also tried with Ga, In, Tl, Nb, and Ta with $0.00 \leq x \leq 0.25$ in increments of 0.05, including additional reactions 0.01, 0.02, …, 0.04.

If designated pure phase via XRD, selected samples were examined by DSC/TG and EDX. For example the following data over several crystalline spots were collected: $Ga_{0.05}Sn_{0.95}Bi_4Te_7$ (0.5, 8.9, 32.9, 57.7 at-%). It was found in several cases that Ga was over-estimated by 3 or 4 at-% likely due to integration errors (i.e. small Ga-Ka with Bi-Ll and augmented background). In the case of the attempted substitution with [*V*] elements Nb and Ta, the corresponding binaries $NbTe_2$ and $TaTe_2$ were found in most reactions. As such no further discussion regarding $[V]_x…Bi_{n-x}…$ will ensue.

Attempts at growing suitable single crystal samples for examination via CCD were unsuccessful for both the $SnBi_4Te_7$ and $SnBi_6Te_{10}$ compounds due to the excessive twinning of the plate-like crystals and the poor quality of the plates emerging from the reaction vessels. Though every strategy explained

in **Chapter 3** (except Arc Melting) was endeavoured, single crystal studies would likely require an advanced setup such as the Czochralski[ix] technique.

9.2. Optimization Trials Based on the Layered Compound $SnBi_4Te_7$

The crystal structure of $SnBi_4Te_7$[200] is represented below in Figure 9.1 where Bi atoms are blue, Sn atoms are green, and Te atoms are red; to better visualize the metal–Te bonding, the unit cell is represented threefold along the a direction. The Te–Te distance separating the layers is 3.26 Å which occurs twice in the unit cell, separating the Bi_2Te_3-type layer from the seven atom layers containing Sn. As mentioned in **Chapter 7**, the unit cell is comprised of two $SnBi_2Te_4$ blocks sandwiching one Bi_2Te_3 block.

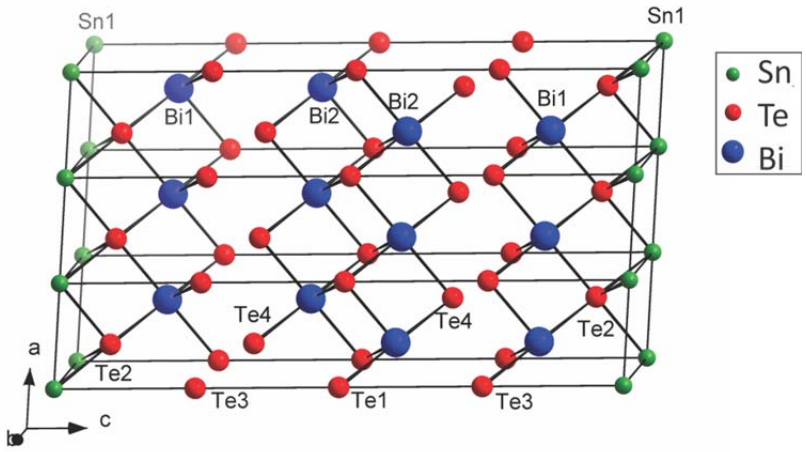

Figure 9.1 Unit cell of $SnBi_4Te_7$ tripled in the *a* direction

$GeBi_4Te_7$[210] was reported in 1968 with dimensions 4.36×4.36×24.11 $Å^3$ in $P\bar{3}m1$ and solved with no mixed occupancies having Ge on the origin, two unique Bi sites (Wyckoff site 2*d*) and four unique Te positions (2*d*, 2*d*, 2*c*, and 1*a*). Subsequent refinements on the $SnBi_4Te_7$ structure are discussed below with Table 9.1. In this model (i.e. "Ordered" below), adjusted for Sn, Sn–Te bonds are 3.20 Å and the Bi–Te bonds are 3.22 Å. This ordering, which was proposed above with the motif discussion (7.1) is also suggested during the Mößbauer studies on both $SnBi_2Te_4$ and $SnBi_4Te_7$, albeit with less certainty in the latter case.[211]

[ix] A rotating seed-based growth technique: Czochralski, J., *Z. Phys. Chem.* **1918**, 92, 219-221.

Table 9.1 Rietveld refinements on $SnBi_4Te_7$ ($P\bar{3}m1$, 298 K, λ = 1.5406 Å).

Refinement Type	Ordered	Even Mixing	Partial Mixing	*M* Sites Free
Formula	$SnBi_4Te_7$	$SnBi_4Te_7$	$SnBi_4Te_7$	$Sn_{0.93}Bi_{4.07}Te_7$
***a* (Å)**	4.402(1)	4.402(1)	4.402(1)	4.402(1)
***c* (Å)**	24.066(5)	24.066(5)	24.066(5)	24.066(5)
***V* (Å^3)**	403.8(3)	403.8(2)	403.8(2)	403.8(2)
R_P[c] \ R_B[d]	**0.0841 \ 0.1042**	**0.0819 \ 0.1005**	**0.0820 \ 0.1005**	**0.0814 \ 0.1000**
% Sn – *M*(1)	1.0000	0.3333	0.800	0.65(9)
(00*z*) – *M*(2)	0.8329(6)	0.8282(3)	0.8332(4)	0.8330(5)
% Sn	0.0000	0.1665	0.100	0.35(9)
(00*z*) – *M*(3)	0.5873(7)	0.5862(4)	0.5873(4)	0.5877(4)
% Sn	0.0000	0.1665	0.00	0.14(7)
(00*z*) – Te(1)	0.5	0.5	0.5	0.5
(00*z*) – Te(2)	0.0725(7)	0.0851(5)	0.0742(5)	0.0761(8)
(00*z*) – Te(3)	0.2435(5)	0.2502(6)	0.2423(4)	0.2417(6)
(00*z*) – Te(4)	0.334(1)	0.3433(4)	0.3340(6)	0.3335(8)

[c] $R_P = \Sigma|y_o - y_c| / \Sigma|Y_o|$ [d] $R_B = \Sigma|I_o - I_c| / \Sigma|I_o|$

Refining the Sn/Bi occupancies, as described previously for the $SnBi_2Te_4$ case, yielded considerable mixing for the *M*(1) and *M*(2) sites of the "$SnBi_2Te_4$ block", and in many cases, exclusively Bi for the "Bi_2Te_3 block"; this was often indicated by a lack of change in *M*(3) site Bi concentrations – especially when U_{eq} parameters were allowed to refine. Though freeing all sites in the above table, the R values from any mixed trial in this case were nearly comparable. The "partial mixing" scenario was devised based on elemental fractions encountered when U_{eq} parameters were allowed to refine and is similar in principle to the equivalent trial with $SnBi_2Te_4$. The "ordered" model was utilized to determine bond lengths as follows: Bi(3)–Te(1) = 3.30(1) Å; Bi(3)–Te(4) = 3.16(2) Å; Bi(2)–Te(3) = 3.14(1); Bi(2)–Te(3) = 3.41(2) Å; Sn(1)–Te(2) = 3.08(1) Å, comparable to that depicted in Figure 9.1.

9.2.1. Structural Studies towards Triel Inclusions

Overnight measurements taken on variants of $SnBi_4Te_7$ were performed to prove that the additive elements were successfully incorporated into the crystal structure. Selected LeBail refinements on various Ga and In based reactions are tabulated below in Table 9.2 utilizing the cif generated by GSAS in 7.2 from $SnBi_4Te_7$. Shown below are three selected refinements highlighting either different triel elements or different sites altered.

Table 9.2 LeBail refinements on various $SnBi_4Te_7$ compounds.

Target Compound	Space Group	a (Å) = b	c (Å)	V (Å^3)	Z	R_P[a] \ R_B[b]
$SnBi_4Te_7$*	$P\bar{3}m1$	4.4037(1)	24.0671(4)	404.19(2)	1	3.57 \ 4.16
$Ga_{0.02}Sn_{0.98}Bi_4Te_7$	"	4.402(1)	24.065(5)	403.8(2)	"	6.64 \ 9.32
$Ga_{0.10}SnBi_{3.90}Te_7$	"	4.38944(8)	24.0236(5)	400.853(9)	"	4.65 \ 7.97
$In_{0.05}SnBi_{3.95}Te_7$	"	4.3918(8)	24.013(5)	401.1(2)	"	3.77 \ 5.42

[a] $R_P = \Sigma|y_o - y_c| / \Sigma|y_o|$ [b] $R_B = \Sigma|I_o - I_c| / \Sigma|I_o|$

Utilizing the initial LeBail refinement on the ternary $SnBi_4Te_7$, unit cell refinements were performed on several compounds showing no impurities after overnight refinements and acceptably flat backgrounds. Three selected refinements on different sites and elements highlight the differences in unit cell sizes found and prove the successful incorporation of elements into the crystal structure. One can most easily notice the differences by looking at the volumes of each crystal structure. Every LeBail refinement performed was executed on an overnight X-ray scan, following a similar refinement recipe including order of refined parameters, background and profile functions, etc.

9.2.2. Electronic Structure Calculations

To better understand its physical properties and potential charge carrier movements, electronic structure calculations – namely DOS calculations were performed utilizing the LMTO method on quaternary variants of $SnBi_4Te_7$. Due to generation of the super-lattice with lmscell.run, the quaternary structures were best simulated with either $Sn_2Bi_8Te_{14}$ or $Sn_4Bi_{16}Te_{28}$, leaving the option for ~12 % or ~6 % [*Tr*] on the Bi site respectively. Though larger than experimentally attempted, this also allowed for 25 % [*Tr*] to be calculated on the Sn site. Though the original ternary was refined in $P\bar{3}m1$, the process of generating the supercells required a symmetry reduction to Pm for $Sn_2Bi_8Te_{14}$ and $P3m1$ for $Sn_4Bi_{16}Te_{28}$ structures. Band structures were also calculated, but due to the very flat, unchanging nature of these bands, little if any new information can be gained from their observation or subsequent discussion.

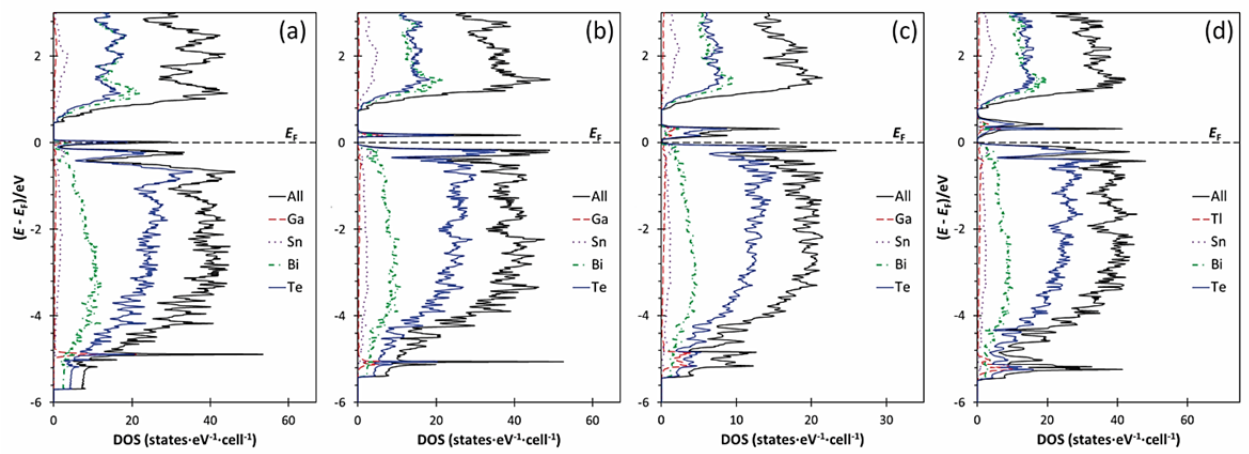

Figure 9.2 Selected *DOS* calculations for [*Tr*]$SnBi_4Te_7$.
From the left: (a) $Ga_{0.25}Sn_{0.75}Bi_4Te_7$, (b) $Ga_{0.25}SnBi_{3.75}Te_7$, (c) $Ga_{0.5}SnBi_{3.5}Te_7$, (d) $Tl_{0.5}SnBi_{3.5}Te_7$.

Like those of the layered $SnBi_2Te_4$ and other layered Bi_2Te_3 compounds, these calculations show large contributions from the Te-*p* orbitals as well as the empty Bi-*p* states in the conduction band and a narrow band gap of approximately 0.4 eV (left) to upwards of 0.8 eV (right) with extra states inside it. The calculations here imply that the addition of triel elements into this structure should generate extra localized impurity states in the band gap. Ga generates a very sharp *DOS* quite near the valence band while In generates visually similar states, but very near the conduction band. Tl, as can be seen on the far right of Figure 9.2, shows lower energy states than In because of relativistic effects.[103, 104] Through the increase of Ga on the Bi site, one observes an additional state per Ga inclusion which can be seen above, moving from $Ga_{0.25}SnBi_{3.75}Te_7$ to $Ga_{0.5}SnBi_{3.5}Te_7$ and observing the energies immediately above the Fermi level. Based on the *DOS* calculations here, one perceives what can be called deep defect states (DDS)[103] in the band gap from hybridized *Tr-s* and Te-*p* orbitals (whose counterparts are found around -5 eV as another localized DDS) which pin these states near the Fermi level and imply thermoelectric enhancement through maintaining high Seebeck values and potentially supressing the bipolar heat conduction.[190]

9.2.3. Physical Property Measurements

As in the previous chapter, studies were carried out on the ZEM and Anter instruments to study the effects of different elements on the Sn site (doping) and Bi site (substitution). Element choices were kept the same as in the $SnBi_2Te_4$ case, utilizing triel elements Ga and In, and in the case of the Bi site, the extra Tl reactions.

9.2.3.1. Doping Trials: $[Tr]_xSn_{1-x}Bi_4Te_7$

Utilizing similar experiments to those attempted in **8.3**, the doping of $SnBi_4Te_7$ was carried out with both Ga and In trials on the Sn site. The attempted doping was intended to increase the electrical conductivity by producing more "holes" in this *p*-type compound. For example $(h^+)_{0.5}(Ga^{3+})_{0.5}(Sn^{2+})_{0.5}(Bi^{3+})_4(Te^{2-})_7$ from its presumed charge-balanced ternary state.

Though quaternary trials were effective in the sense that the dopant was successfully incorporated, results of the ZEM measurements – often taken either twice or thrice per trial – yielded seemingly illogical trends. Seebeck coefficients range from 96 to 124 $\mu V \cdot K^{-1}$ at room temperature which in most trials represents a marginal decrease in value, from 120 $\mu V \cdot K^{-1}$. Seebeck results for select trials including the original ternary are shown in **Figure 9.3** with solid lines. As was the case with most In trials, the values were generally lower than their Ga counterparts which may imply the aforementioned Fermi level pinning in effect. The electrical conductivity values displayed as dashed lines below show essentially the same behaviour as the Seebeck coefficient in terms of the ordering of the compounds. Based on the majority of the results obtained, one can conclude that a systematic increase in dopant content lowers the conductivity suggesting that $SnBi_4Te_7$ is near its maximum *p*-type charge carriers. Several outliers in each case (Ga versus In) were found to counteract this conclusion; typically three of ten potential measurements would not follow this trend however, 0.03 In was the largest of any outliers. The largest value in this study was $In_{0.03}Sn_{0.97}Bi_4Te_7$ reaching 491 $\Omega^{-1}cm^{-1}$ at 664 K.

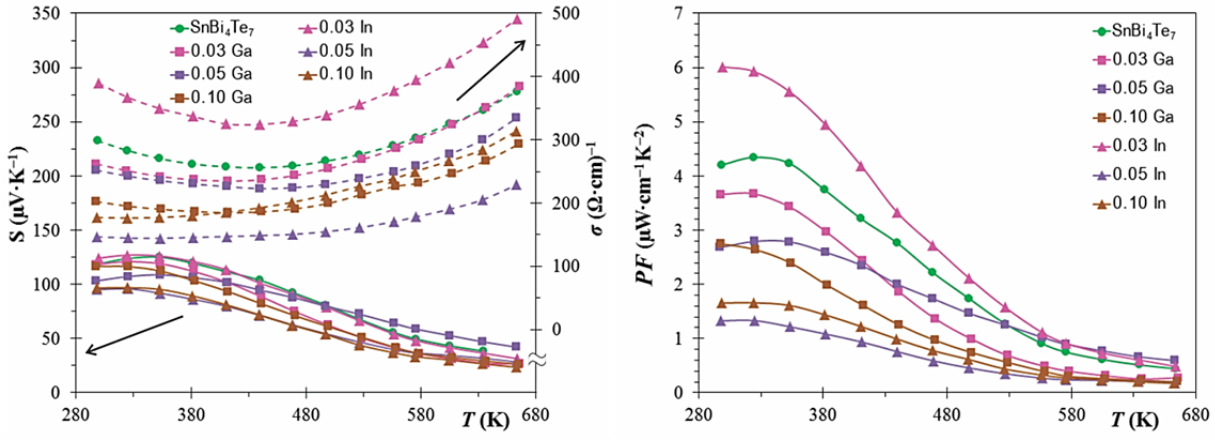

Figure 9.3 Doping trials via $[Tr]_xSn_{1-x}Bi_4Te_7$, *Tr* = Ga, In: Seebeck coefficients/electrical conductivity (left), power factor (right).

The power factors calculated show the same ordering as the Seebeck coefficients with larger quantities of dopants dropping the power factor by over half of the original (4.3 $\mu W \cdot cm^{-1}K^{-2}$ at 324 K). As discussed, these compounds also reach a maximum value around 325 K, then quickly decrease below 1

$\mu W \cdot cm^{-1}K^{-2}$, where decreasing values appear to taper. In this case, the largest power factor, found for 0.03 In, was 6.0 $\mu W \cdot cm^{-1}K^{-2}$ at 300 K.

With respect to thermal conductivity of the system (Figure 9.4), one can see that improvements are observed in almost every case though Ga trials, specifically 0.05 Ga, show the most promising decrease in κ. With a room temperature value of 0.31 $W \cdot m^{-1}K^{-1}$, this trial displays a thermal conductivity reduction of 40 % from the ternary compound. Like the other layered materials, the doped trials display a continuously increasing κ with a slope change occurring around 470 K where the bipolar conductivity, that is mobile positive and negative charge carriers, begins to control the properties. To reiterate, this behaviour can also be observed as the change in direction for the electrical conductivities above. A significant suppression of the bipolar heat conduction cannot be observed with In or Ga unfortunately, though the overall κ has been lowered in addition to the slopes' reduced incline at higher temperatures.

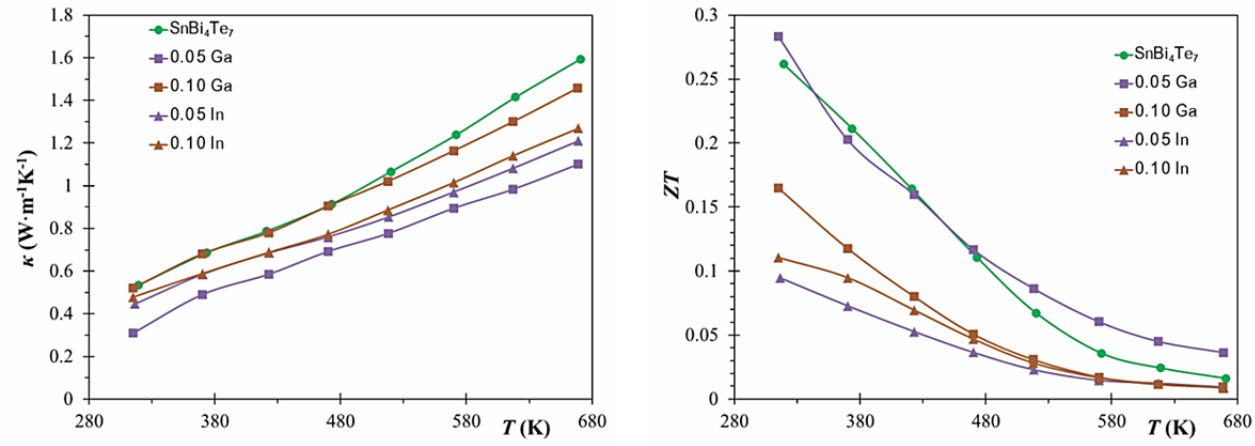

Figure 9.4 Thermal conductivity (left) and ZT (right) for doped $[Tr]_xSn_{1-x}Bi_4Te_7$, Tr = Ga, In.

The dimensionless figures of merit for the doped $SnBi_4Te_7$ compound show a decrease in magnitude from 0.26 ($SnBi_4Te_7$) to below 0.16 (0.10 Ga). The values were calculated by fitting the power factors with a sixth-order polynomial and combining it with the κ data as per the ZT formula. Ga trials indicate that more gallium further decreases the figure of merit and In trials, while less indicative systematic reduction, still prove that added dopants have a hampering effect on ZT. It is noteworthy to observe that due to its significantly lower thermal conductivity combined with a relatively trivial decrease in power factor, small quantities of Ga in this structure actually lead to an overall enhancement in ZT beyond 470 K – a more significant temperature range for power-generation thermoelectrics. $Ga_{0.05}Sn_{0.95}Bi_4Te_7$ shows a fourfold increase from 0.009 at 670 K to 0.036.

9.2.3.2. Substitution Trials: $[Tr]_xSnBi_{4-x}Te_7$, Tr = Ga, In, Tl

Procedurally identical, measurements were also performed on the samples incorporating *x* triel element on the Bi site. Assuming the triel elements are more stable in their Tr^{3+} form, replacement of Bi^{3+} atoms would leave the compound ideally in a charge-balanced state.

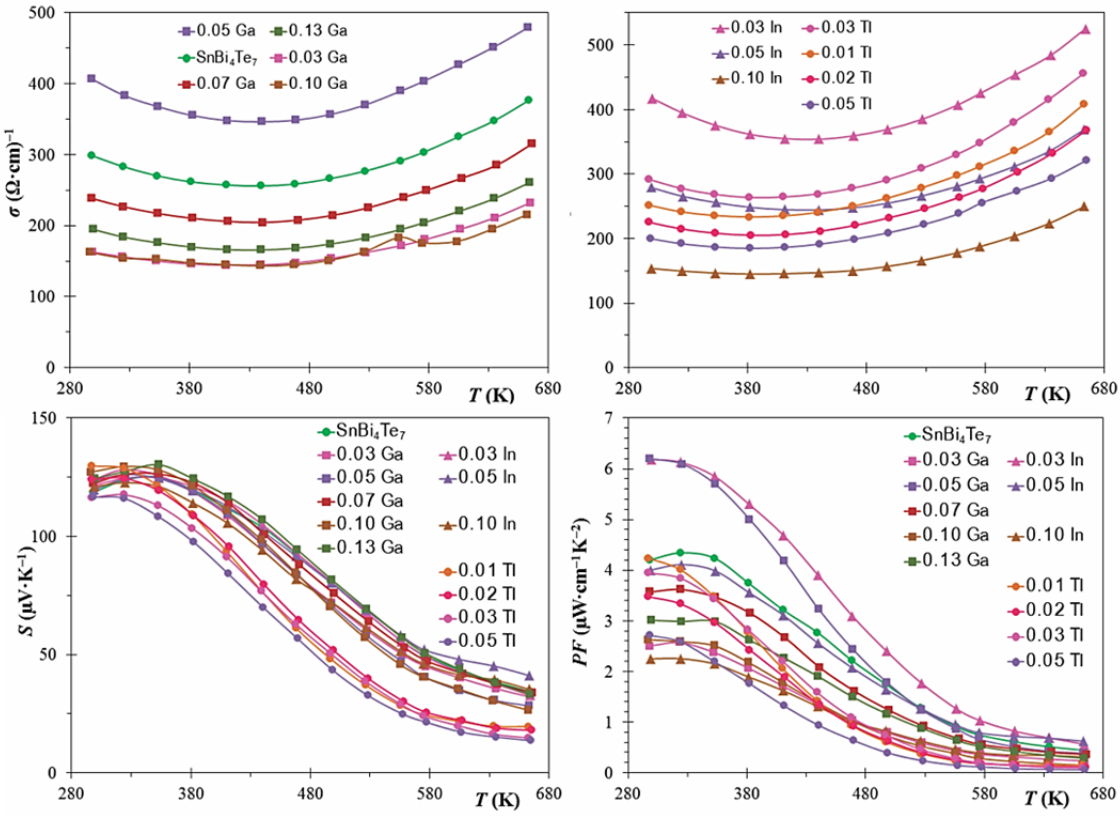

Figure 9.5 Substitution results (ZEM) for $[Tr]_xSnBi_{4-x}Te_7$.

Substitution experiments paint a picture of charge carriers randomly distributed across Sn, Bi, and maybe Te sites displaying the same bipolar conductivity discussed in **Chapter 7**. Searching for trends in the electrical conductivity, shown above in the top left and right of Figure 9.5, shows little evidence for logical changes – though the majority of samples indicate that additional triel elements lower the electrical conductivity beyond that of the ternary (~300 $\Omega^{-1}cm^{-1}$ at room temperature). Should the *DOS* calculations serve correct, one may be observing near-similar *n* with oppression of the mobility factor, μ; if additional Tr^+ is found, this may simultaneously cause a change in *n*. Furthermore, *n* possibly changes based on a Te-loss hypothesis (i.e. …Te_{7-y}), should Te vaporize out of the structure. The legends in this case are displayed in order of decreasing σ. While Ga shows no order whatsoever, the heavier elements again suggest that additional substituents further lower σ. 0.03 Tl, breaking the hypothesized trend, likely had traces of impurity compounds (i.e. $TlBiTe_2$) which were not apparent in the p-XRD data.

Most Seebeck coefficients measured are essentially the same with values around 125 $\mu V \cdot K^{-1}$, but it should be noted that all thallium-based trials reduce S, likely due to its larger relativistic effects and/or preferential Tl^{+} as opposed to Ga^{3+}/In^{3+}. The observation thusly results in power factors below 4.34 $\mu W \cdot cm^{-1}K^{-2}$ ($SnBi_4Te_7$) for the majority with two outlier compounds displaying 6.2 $\mu W \cdot cm^{-1}K^{-2}$. Though not performed here, it can be presumed κ and ZT values on the same order of magnitude as ***9.2.3.1***.

9.2.4. Towards Nanoscopic Improvement of *ZT*

The first study towards nanoscopic improvements was performed on a quaternary ZEM pellet via an extended SEM/EDX scanning period to verify homogeneity and therefore determine if any sections of the pellet's surface showed non-uniform elemental distributions (i.e. matrix encapsulation). Such a study can determine if Ga is concentrating on various portions of the surface, such as the impurity clustering[212] found to significantly impact the figure of merit in LAST materials and the like. The particular study was performed at 1000x magnification and 25,000x magnification. The additional EDX results show that the pellets surface was quite uniform. The data collected at this point was 0.5, 8.9, 32.9, and 57.7 % respectively based on the $Ga_{0.05}Sn_{0.95}Bi_4Te_7$ stoichiometry over six spots. Though uniform appearance in the pellet bodes well for homogeneity and property reproducibility, there is little indication of unusual behaviour – be it good or bad.

TEM studies were also carried out at McMaster University to further probe compounds' potential nanodomains and provide an understanding of the grain boundaries or defects that may contribute towards its behaviour during measurements. The results for the ternary $SnBi_4Te_7$ are thus displayed below in Figure 9.6 and Figure 9.7:

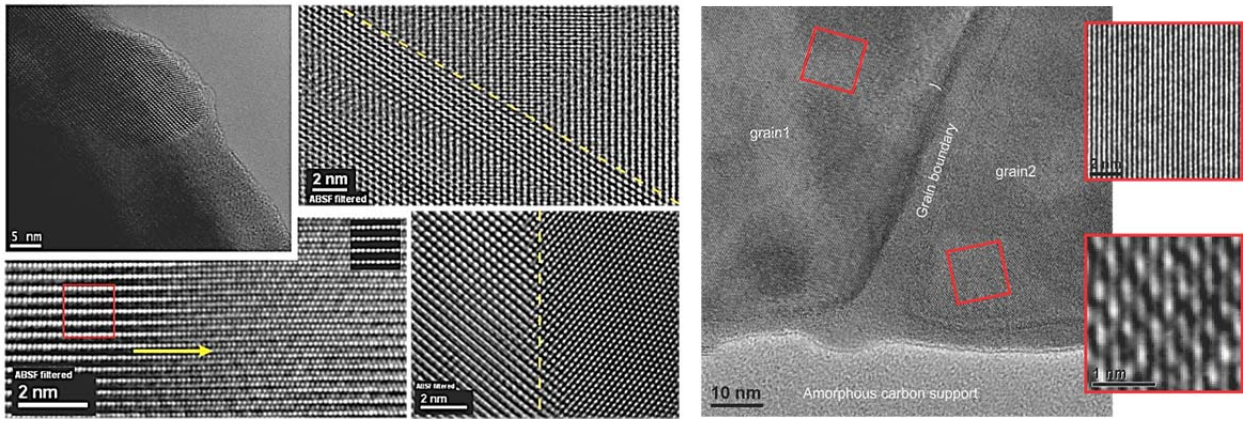

Figure 9.6 TEM grain boundary observations.

One can observe a variety of grain boundaries on the left of Figure 9.6 all on the nanoscopic scale. The very top left shows the inclusion of a nanodomain of approximately 20 nm × 20 nm which occurs on the end of the studied material, as the carbon support can be seen in the top right corner of the image. The bottom left image seems to imply thickening of the layers which ought to affect heat transport in the material, should enough of these domains exist. The other pictures show standard grain boundries in the samples. The rightmost capture in Figure 9.6 shows two distinct regions separated by a boundary of approximately 7 nm – grain 1 shows tightly packed ordered rows (6 per 2 nm), whilst grain 2 shows more disordered growth (~4.5 'rows' in 1 nm). Figure 9.7 below also shows a different kind of defect where it is noticed there is a potential missing atom in the network (top right of the figure) while potentially similar to a Schöttky defect, the feature was not readily observed in any sample trials that were attempted.

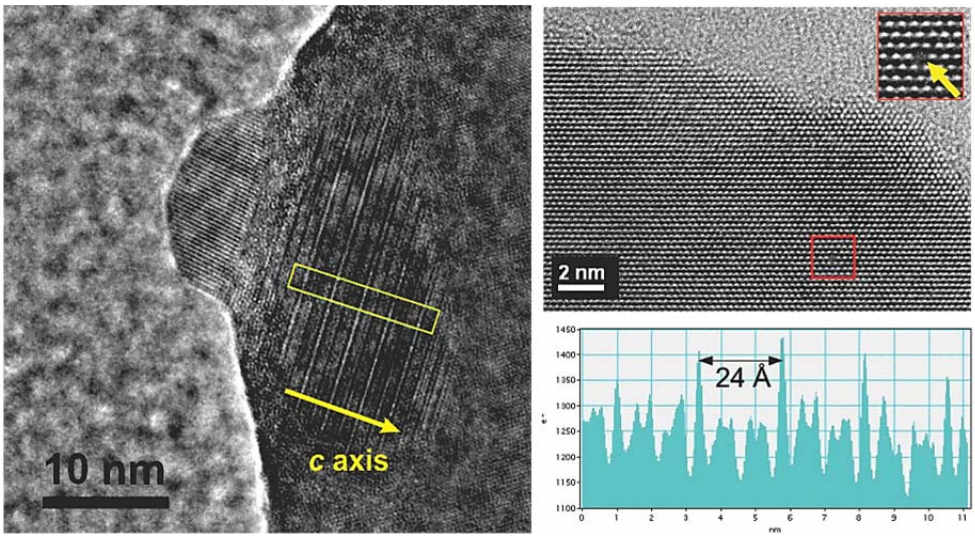

Figure 9.7 TEM interval studies and atomic defects.

The final image attempts to explain the nature of the rows in a particular nanodomain. Measurements of distance were taken on the rows, which can be seen as periodically light and dark. Coincidentally, the difference between repeating "light" rows is approximately 24 Å which is the same length as the c axis of the proposed unit cell. Thus, if light rows are ordered Sn atoms, this observation supports the proposed high degree of ordering of Sn in the unit cell. This measurement is in the lower right of the figure corresponding to the capture on the left.

Considering ball-milling experiments on the layered Bi_2Te_3 compound which not only led to an increase in ZT by 30 %, but a significant reduction in κ_{lat} and the bipolar effect,[122] preliminary studies have been initiated for other layered compounds. The experiments entail a physical mixture of $SnBi_4Te_7$

powder and nanoscopic SnTe – though any material of similar size, structure, and properties to the host material can be attempted. SnTe was synthesized from the elements, verified for pure phase under p-XRD, and ball-milled in 5 minute intervals at least thrice to reduce the powder size from bulk to nano. Debye-Scherrer estimations ($\tau = \frac{K\lambda}{\beta \cos\theta}$, where K is a dimensionless shape factor of 0.9, λ is the X-ray wavelength, β is the FWHM broadening, and θ is the peak position) put the size of the particles around 60 – 70 nm. The powders were weighed to $\pm$0.0001 g and were physically mixed together, pressed into 10×2×2 mm^3 pellets, and annealed at 723 K for 12 hours. The data in Figure 9.8 was collected with the same ZEM settings as the bulk studies.

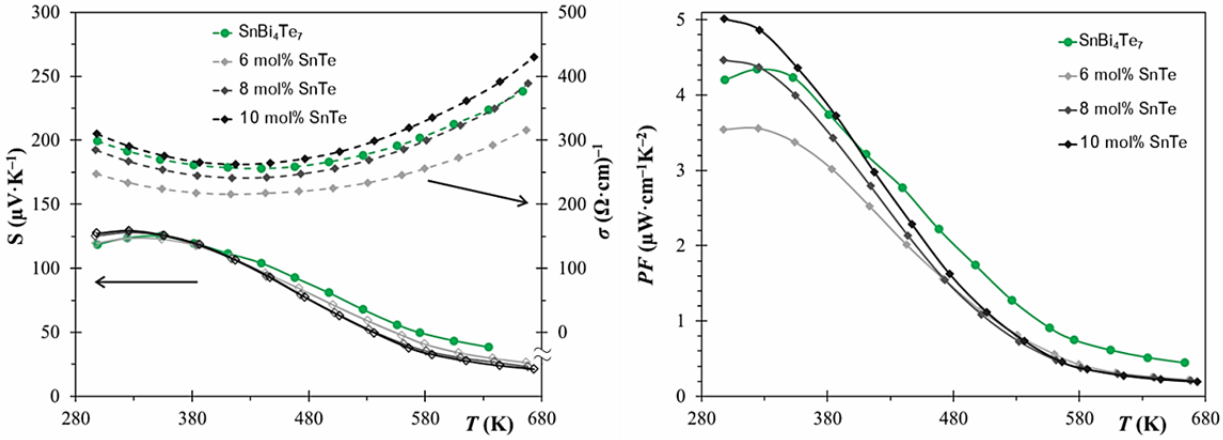

Figure 9.8 Physical properties of $SnBi_4Te_7$–*x*SnTe: $\mathcal{S}$ and σ (left), power factor (right).

The preliminary data of the ball-milling studies give some promising results. One can see that variation of [SnTe] has little effect on $\mathcal{S}$, but makes a significant change in σ from 247 to 310 $\Omega^{-1}cm^{-1}$ at room temperature by increasing the mol % of SnTe through to 10 %. Though apparently not a large jump (4 to 5 $\mu W \cdot cm^{-1}K^{-2}$), if combined with a drop in κ, significant improvements to ZT could be realized and considering the extra grain boundaries and phonon interference, this is a reasonable hypothesis. Should an acceptably low κ be discovered, hot-pressing would be an advisable step. It is likely that the host materials' properties would improve and the stability of nanoparticulate SnTe, at any of $SnBi_4Te_7$'s temperatures of study, is excellent; with the current annealing scheme, no evidence of impurity phase $Sn_2Bi_2Te_5$ or other unwanted side-products have been detected. Thus, some preliminary results regarding the incorporation of nanoscale compounds into a larger host matrix. This should be more successful in this case due to the similarities these structures share, SnTe being of NaCl-type structure as with the overall layering of $SnBi_4Te_7$ (i.e. *M* sites = Na, Te sites = Cl). Future work is this regard requires the crucial κ measurements before suitable conclusions can be reached.

9.2.5. Conclusions Drawn from $SnBi_4Te_7$ Studies

A broad study on the $SnBi_4Te_7$ compound has suggested in favour of ordering in the unit cell as initially predicted. The compound behaves as a degenerate semiconductor until intrinsic charge carriers are activated around 400 K where a strong bipolar contribution begins to dominate its properties. The electronic structure calculations predict a band gap of 0.35 eV for the ternary compound and suggest Fermi level pinning for any triel element added into the structure, creating isolated impurity states in the band gap for potential improvement of its figure of merit. The physical properties of triel-doped and -substituted reactions show no logical trends for each of Ga, In, or Tl inclusions and generally decrease the initial figure of merit due to a reduction in σ, with S and κ changing significantly less. The systematic reduction in σ via In addition however, may support the claim of Fermi level pinning but the strong bipolar contributions to κ make this difficult to quantify or further pursue. Proof of nanodomains forming in the structure have been found, and their existence may explain why κ values are far below 1 $W \cdot m^{-1}K^{-1}$ (room temperature) as was reported for LAST-like compounds. Improvement in this area has excellent potential. The inclusion of ball-milled SnTe to this structure also shows improved power factor measurements with increasing concentration of SnTe, of which should warrant more thorough investigations including proper thermal conductivity and hot-pressing measurements.

9.3. Tuning the Layered Compound $SnBi_6Te_{10}$

In principle, $SnBi_6Te_{10}$ should show excellent thermoelectric potential with its heavy atoms driving down thermal conductivity and more complex layering than either $SnBi_2Te_4$ or $SnBi_4Te_7$. Unfortunately much about $SnBi_6Te_{10}$ still remains a mystery due to its narrow phase range, poor-quality plate-like crystals, and subsequent difficulties with structural refinements and DOS calculations from the anticipated 102 Å *c* axis. LeBail refinements give $SnBi_6Te_{10}$ dimensions of 4.38×4.38×102.4 $Å^3$ in $R\bar{3}m$ which may be comprised of three segments of Bi_2Te_3-$SnBi_2Te_4$-$SnBi_2Te_4$-Bi_2Te_3 repeating along the *c* axis.

9.3.1. Heating, XRD, and Structural Studies

Though the strategies between $SnBi_4Te_7$ and $SnBi_6Te_{10}$ have generally been the same, significantly more effort was required to optimize the heating profiles of compounds with the $SnBi_6Te_{10}$ formula. This includes reactions with Ga and In on both Sn and Bi sites as well as some additional Tl and Nb experiments on the Bi site. Though optimization of heating profiles led to a pure-phase ternary compound, only 13 % of the additional samples were useable beyond XRD studies. This is due to the presence of $SnBi_4Te_7$, $SnBi_8Te_{13}$, and Bi_2Te_3 as common additional phases. The original optimized heating

scheme involving a homogeneous melt at 923 K, slow cooling between 873 and 773 K, followed by crushing and annealing at 798 K for ten days was only successful for the original ternary compound. Further optimization experiments on substitution samples, namely x = 0.1, 0.15, 0.20 in $Ga_xSn_{1-x}Bi_6Te_{10}$, led to nearly pure phase results in a shaker furnace with a homogeneous melt at 923 K followed by four days at 843 K, then four days at 798 K. Those samples with fewer than 5% additional phases were also examined via EDX. All spots were found to contain all expected elements within acceptable elemental percentages, supporting the hypothesis of a uniform and homogeneous composition. $In_{0.15}SnBi_{5.85}Te_{10}$, for example averaged 3, 6, 35, and 56 % respectively over eight crystals.

9.3.2. Electronic Structure Calculations

Standard calculations with the LMTO software were performed with $SnBi_6Te_{10}$ on select variations. Unlike the other compounds however, supercells were restricted by the fact that calculating with c = 102 Å was on the limit of the program's capabilities. Attempts to double the unit cell along the a or b axis were nevertheless successful yielding calculations in $C2/m$ or Cm symmetries for even or odd number of triel atoms added respectively. Calculations were performed on a basis of 1000 evenly dispersed k-points with *Tr* = Ga, In, and Tl. Selected calculation results are shown below:

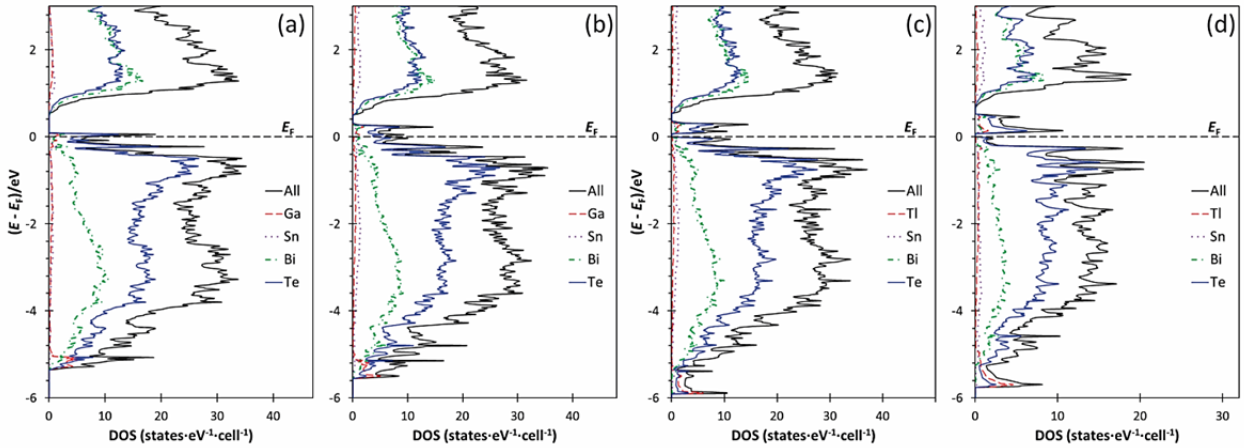

Figure 9.9 *DOS* **calculations on $SnBi_6Te_{10}$ variants: (a) $Ga_{0.5}Sn_{0.5}Bi_6Te_{10}$, (b) $Ga_{0.5}SnBi_{5.5}Te_{10}$, (c) $Tl_{0.5}SnBi_{5.5}Te_{10}$, (d) $TlSnBi_5Te_{10}$.**

While similar in nature to $SnBi_6Te_{10}$, all quaternary compounds calculated show extra states at the top of the valence band from the added triel elements while little changes occur in the conduction band. Ga doping and substitution respectively show extra orbital states in the valence band shrinking the band gap and predicting a more *p*-type material. Tl – the large extreme of the triel elements – shows the extra states occurring inside the band gap, displaying increasing breadth as the Tl content increases. This again implies the added impurity states for the heavier triels appear broad compared to

$SnBi_4Te_7$, but suggest similar albeit more mild behaviours from these calculations. From the observed LMTO calculations, one would expect improved conductivity with a band gap shrinking from 0.44 eV to ~0.2 eV in $Ga_{0.5}SnBi_{5.5}Te_{10}$ for example. Based on the shape of the calculations, one would still expect very similar nature to $SnBi_4Te_7$ trials.

9.3.3. Physical Property Measurements

For compounds deemed pure phase via powder XRD, ZEM measurements were again utilized to measure physical properties. In the case of the $SnBi_6Te_{10}$ compound, only the gallium-based trials (both doping and substitution) were found to be pure phase and measureable. Of the attempted sets, only three (and the aforementioned ternary) reactions were of appropriate quality: $Ga_{0.05}Sn_{0.95}Bi_6Te_{10}$, $Ga_{0.07}Sn_{0.93}Bi_6Te_{10}$, and $Ga_{0.15}SnBi_{5.85}Te_{10}$. The reactions with the ternary $SnBi_6Te_{10}$ for comparison are displayed below in Figure 9.10. As is custom with all of the layered trials mentioned, these were pressed into rectangular pellets, annealed at 723 K, and measured on the ZEM instrument from room temperature up to 673 K. Repeat measurements were taken for consistency. Seebeck measurements on the left-hand side of the figure are the typical expected shape for these layered compounds and on the same order of magnitude as $SnBi_4Te_7$ trials as well as the original $SnBi_6Te_{10}$ included in the diagram. The trial with x = 0.05 Ga is notably lower than the other measurement values but also contains evidence for additional XRD peaks which would be on the order of 2 % of the pattern's major peak. The maximum value for all of the Seebeck coefficients is also on the same temperature order, all of which fall before 380 K. The electrical conductivity values, like the $SnBi_4Te_7$ experiments, show a change of character around the 430 K mark and show virtually the same order of magnitude as their counterparts as well. One can see that the final σ values in Figure 9.3 and Figure 9.10 all fall in the 300 to 400 $\Omega^{-1}cm^{-1}$ range. It is noteworthy to highlight the increase in σ, albeit minor, as Ga is added into the system which can be seen in all cases including $Ga_{0.05}Sn_{0.95}Bi_6Te_{10}$ in the temperature ranges greater than 530 K.

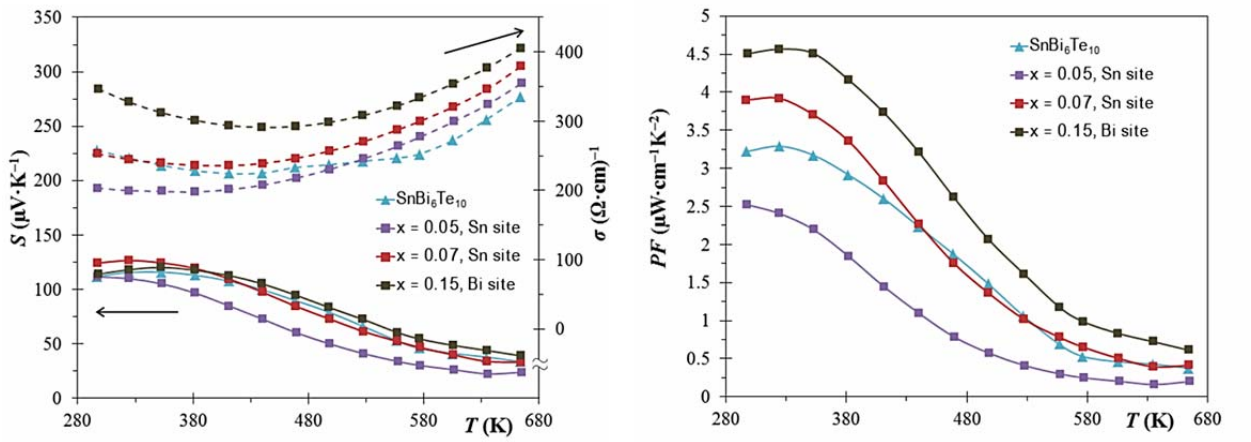

Figure 9.10 Physical properties of Ga-inclusions in $SnBi_6Te_{10}$: Seebeck and electrical conductivity (left), power factor (right).

When power factors are calculated from the S (solid lines) and σ (dashed lines) values, one can see an approximate trend of larger power factors for increasing [Ga] content. From the ternary compound, to the additional 0.07 Ga on the Sn site displayed in burgundy, to the extra 0.15 Ga intended for the Bi atom, one notices increasing maximum power factors at 330 K increasing from approximately 3.25 to 4 to 4.5 $\mu W \cdot cm^{-1}K^{-2}$ and logically one would expect the 0.05 Ga trial to display a power factor at approximately 3.75 $\mu W \cdot cm^{-1}K^{-2}$ if this trial behaved as expected. Though no kappa measurements were taken on the compound, it can be assumed that the results would be nearly identical to those displayed in Figure 9.4 with $SnBi_4Te_7$ albeit, $SnBi_6Te_{10}$ compounds run a greater risk of pellet blistering and deforming at higher temperatures as portions of the material decompose into $SnBi_4Te_7$ and Bi_2Te_3.

9.3.4. Conclusions Drawn from Studies on $SnBi_6Te_{10}$

A proper study on the $SnBi_6Te_{10}$ compound was attempted from both structural and physical perspectives. Heating scheme optimizations were attempted and were successful to a certain extent, despite the fact that additions from triel elements and group V elements made pure phase samples an extremely rare occurrence. Crystallographic studies to elaborate on the true unit cell size and ordering of the atomic positions – particularly Sn – were unsuccessful due to poor crystal quality despite the various attempted growth techniques. Electronic structure calculations predict similar Fermi level pinning with the triel elements and a reduction in the band gap size – especially with the Ga trials, whilst the physical property measurements generally support the claim that Ga addition shrinks the band gap, therefore improving the conductivity of the material. As a result, two of the three successful quaternary trials show significant improvements of the power factor for $SnBi_6Te_{10}$.

9.4. Project Summary and Future Work

Both $SnBi_4Te_7$ and $SnBi_6Te_{10}$ compounds received an in-depth study that extended beyond reports of phase diagrams and phase range. While heating schemes were optimized for ternary and quaternary trials alike, single crystal studies – while preferable – were unsuccessful and therefore direct evidence for atomic ordering within the crystal was unavailable. In the case of $SnBi_4Te_7$ however, TEM studies and powder refinements support the evidence for atomic site ordering. Like the other layered materials, bipolar behaviour was clearly evident, especially with respect to the increasing κ magnitudes with increasing temperature. Power factors and ZT for $SnBi_4Te_7$ trials generally showed an unfavourable reduction in magnitude, while current power factor evidence for the $SnBi_6Te_{10}$ compound suggests a marginal overall improvement.

A thorough study of the charge carriers involved in these two compounds would be a prudent addition including but not limited to Hall measurements. This would allow one to begin to understand all of the charge carrier contributions towards the electrical and thermal conductivity including the potential Te defines upon heating. Likewise, it is still difficult to prove whether the "dopants" are exclusively occupying the target atomic site or whether they are mixing with several in the compound – a significant question to aid in the understanding of the power factor results. Though nanoscopic studies have preliminary results, these compounds do not appear dominated by these effects as LAST materials do, but the larger bipolar effects take priority. Though hot-pressing typically improves the thermoelectric properties, in this case tuning the pressing temperature could prove to be challenging due to the phases' tendencies to decompose during heating.

Section IV – Tl-Based Main Group Tellurides

Improvement of ZT via Inclusion of Tt-Elements

Chapter 10. Introduction to Tl_5Te_3

As mentioned in Section II of this work, many of the leading strategies and materials for improving thermoelectrics stem from materials with heavy atoms, defects, and impurities introduced. Thallium-based materials have become a point of interest due to their fulfilling several of the aforementioned criteria: They form complex crystal structures with heavy atoms (often including heavy *p*-block elements such as Tl, Te, Sb, Pb, etc.), the materials often display exceptionally low thermal conductivity, and are frequently studied for their tendencies to form defects on the nanoscale and DDSs in their DOS plots, such as Tl-doped PbTe.[104] Paired with the fact that the compounds are easily synthesized from the elements, show good thermal stability in and around automotive operating temperatures, and are capable of quick growth of large crystals, it is no surprise that they are favourites of the thermoelectric research field.

10.1. The Binary Material Tl_5Te_3

The binary compounds, namely Tl_2Te,[213] Tl_2Te_3[214] ($C2/c$); TlTe[215] ($I4/mcm$) and of course Tl_5Te_3, have all been studied for their thermal conductivities and have shown κ readings for the monoclinic variants as low as 0.5 $W{\cdot}m^{-1}K^{-1}$ while the mixed valent variants – including Tl_5Te_3 – showed κ values on the order of 4 $W{\cdot}m^{-1}K^{-1}$.[216] To find a κ value such as 0.5 $W{\cdot}m^{-1}K^{-1}$, is to display values already ⅓ to ¼ of that of "standard materials", say, Bi_2Te_3[28] or PbTe. The physical properties of Tl_5Te_3 itself depict metallic behaviour, which can be confirmed through electronic structure calculations,[217] complete with a linearly decreasing σ (~2000 $\Omega^{-1}cm^{-1}$ at room temperature) and an underwhelming $S \approx$ 30 $\mu V{\cdot}K^{-1}$ at room temperature. Combine this with κ = 4 $W{\cdot}m^{-1}K^{-1}$, the overall ZT is only ~0.01 at 325 K.[216] The material still shows promise however, in the sense that its $\kappa_{lat} \approx$ 1 $W{\cdot}m^{-1}K^{-1}$. This means that the lattice thermal conductivity is indeed quite low. This warrants further study and subsequent improvement – namely additional atomic disorder.

Tl_5Te_3 is of the Cr_5B_3 structure-type, belonging to the $I4/mcm$ space group though controversy leading up to this conclusion yielded solutions in $I\bar{4}$[218] and $I4/m$[219] most likely due to Tl disorder camouflaging the *c*-glide's systematic absences.[220] Its unit cell dimensions are 8.93×8.93×12.59 $Å^3$ and is comprised of a 32-atom unit cell displayed in Figure 10.1:

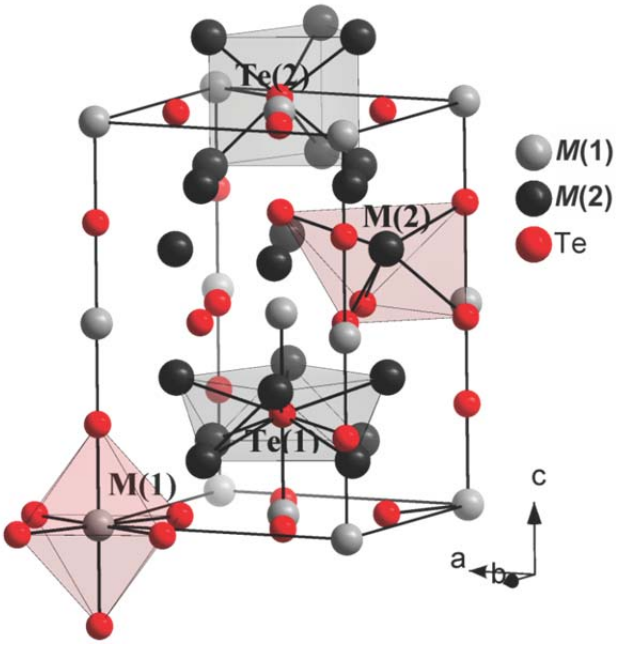

Figure 10.1 Unit cell of Tl_5Te_3 in $I4/mcm$[221, 222]

Atoms sit on four different crystallographic sites: *M*(1), 4*c*; *M*(2), 16*l*; Te(1), 4*a*; Te(2), 8*h*; since Tl is the only *M* in this particular description of Figure 10.1, then Tl fully occupies 4*c*/16*l*. Due to the fact that there are no Te–Te bonds in this structure, one can consider all tellurium as Te^{2-} which means the five Tl atoms are required to balance a total charge of 6-. This is achieved through Tl disorder on the *M*(1) site: It is comprised of 50 % Tl^{+} and 50 % Tl^{3+} (Tl^{2+} on average) thusly for $Tl_{10}Te_6$, the charge breakdown is $(Tl^{3+})_1(Tl^{+})_9(Te^{2-})_6$ yielding a fully charge-balanced compound.[222] The *M*(1) sites form an infinite chain of octahedra travelling along the *c*-direction. This octahedron is also compressed lengthwise along the *c*-axis (*M*(1)–Te(1) = 3.15 Å (×2); *M*(1)–Te(2) = 3.36 Å (×4)). *M*(2) is coordinated to five Te atoms: 1×3.16 Å, 2×3.39 Å, 2×3.60 Å. The tellurium coordination environment is best described as centered in an S_8-type crown for Te(1)–*M*(2), and centred in a triangular prism for Te(2)–*M*(2). There are also weak *M*(2)–*M*(2) bonds in the structure on the order of 1×3.46 Å and 2×3.50 Å respectively.[221]

Electronic structure calculations have been performed on Tl_5Te_3 from a few sources[217, 223, 224] confirming that it is indeed a metallic compound as the Fermi level appears below the top of the valence band, as depicted by the upper image in Figure 10.2:

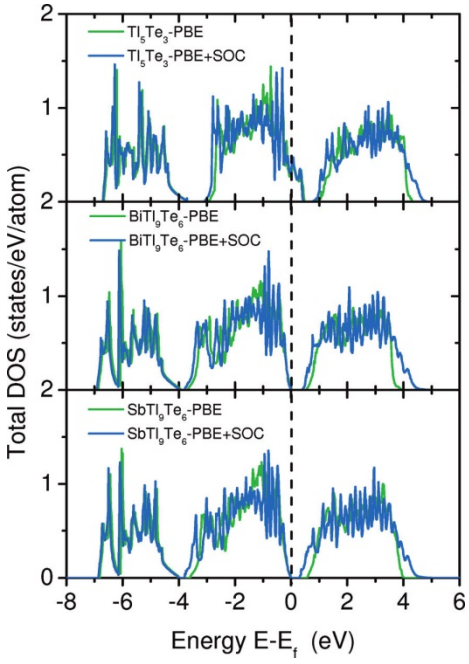

Figure 10.2 ***DOS*** **calculations for Tl_5Te_3 and ternary analogs Tl_9BiTe_6 and Tl_9SbTe_6**[223]

Though Tl_5Te_3 is a 3-dimensionally conducting material, most of the states at the Fermi level are attributed to the *M*(1)–Te(1) bonds along the *c*-direction that comprise the axially-compressed peaks of the $TlTe_6$ octahedra. The more reduced *M*(2) atoms (Tl^+) comprise most of the states between -12 and -5 eV and do not contribute much to the valence states.[217] Also shown above are the addition of Pn^{3+} to the structure, which shows how the extra two electrons provided can change this material from metal to semiconducting, with band gaps of 0.26 eV and 0.37 eV for Tl_9BiTe_6 and Tl_9SbTe_6 respectively. This image also serves to verify that the additional spin-orbit coupling (SOC), while altering the calculation slightly, will not drastically affect the predictions even though SOC does help reduce the over-estimation of the band gaps (without: 0.58 eV and 0.54 eV respectively).[223] The evidence shown in these predictions thusly alludes to a narrow-gap semiconductor influenced by the aforementioned 4*c* site, which controls at least the positioning of the Fermi level if not the steepness of the valence bands.

10.2. Modifications of Tl_5Te_3

There are several ternary compounds derived from the Tl_5Te_3 compound. Similarly the selenide variants of these compounds are known well (i.e. Tl_5Se_3[225]), though not traditionally for thermoelectric applications. The modifications of thermoelectric interest with the tellurides are focussed around the oxidized Tl on the 4*c* site: If one were to "replace" all the Tl^{3+} with a similar element possessing a 3+ charge, one would observe a new ternary compound. In this case Tl_9PnTe_6, *Pn* = Sb, Bi. **Figure 10.3**

depicts the generic Tl_5Te_3 structure and how recent structural changes produce a family of new materials:

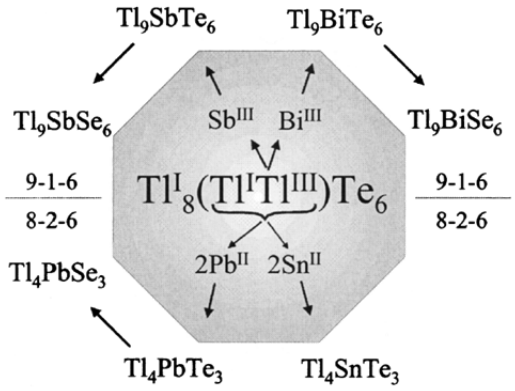

Figure 10.3 Schematic of Tl_5Te_3 ternary variants[222]

Currently, Tl_9BiTe_6 is the best-known and characterized of the Tl_5Te_3 variants.[222] Likewise, it has also been shown that Tl_9ZTe_6 can be further extended to include *Z* = Sn, Pb, La, and *Ln* (including but not limited to Ce, Sm, Gd, Nd[226-228] and others studied in the Kleinke group parallel to the work in this thesis). Since the 4*c*-site defect can also be discussed as an averaged Tl^{2+}, entirely replacing the 4*c* site with an element of 2+ charge is viable and leads to Tl_4SnTe_3 (i.e. $Tl_8Sn_2Te_6$ or $(Tl^+)_8(Tt^{2+})_2(Te^{2-})_6$), Tl_4PbTe_3,[229] Tl_4SnSe_3,[230] and Tl_4PbSe_3.[231] Both the Tl_9BiTe_6-type structures and Tl_4PbTe_3-type structures form with the same space group and crystal structure as Tl_5Te_3, though, Tl_9SbTe_6 has been solved in $I4/m$.[232]

Part of being the best-known and characterized, Tl_9BiTe_6 is understood as a compound with promising thermoelectric properties. Though measurements on this type of compound were taken as early as 1988 with alloyed Tl_4PbSe_3-Tl_4PbTe_3,[233] recognition of the thermoelectric potential with these ternary compounds did not emerge until about 2001.[234] Subsequently, numerous studies have emerged covering thermoelectric properties of the ternary compounds, additional phase range pieces, and papers attempting to advance knowledge of the electronic and atomic structure. Tl_9BiTe_6 achieves ZT = 1.2 at 500 K;[222] its counterpart Tl_9SbTe_6, achieves ZT = 0.42 at 591 K.[235] The other ternaries have in part shown similar promise with Tl_9LaTe_6 (ZT = 0.21 at 580 K),[236] Tl_4SnTe_3 (ZT = 0.74 at 673 K) and Tl_4PbTe_3 (ZT = 0.71 at 673 K).[237]

Thallium-based chalcogenides clearly show good potential for thermoelectric materials with their uniquely low lattice thermal conductivity values which lead to the excellent overall κ values of ~1 $W \cdot m^{-1}K^{-1}$ with Tl_9BiTe_6. With this exceptionally low thermal conductivity and a simple system to synthesize in the laboratory, research on the thermoelectric properties has already expanded into alternate directions with numerous ternary thallium chalcogenide compounds, usually this involves other heavy *p*-block elements, but late-transition-metal inclusions have also shown promising results. Studies on Tl_2GeTe_3,[238] Tl_2SnTe_3 (ZT = 0.6 at 300 K),[239] AgTlTe (ZT = 0.61 at 580 K),[240] $TlSbTe_2$ (ZT = 0.87 at 715 K),[241] $TlBiTe_2$ (ZT = 0.15 at 760 K),[242] and the current rival to Tl_9BiTe_6, $AgTl_9Te_5$ with ZT = 1.23 at 700 K[243] are all being worked on in past and recent years due to the high expectations for thallium tellurides.

The aim of this work herein is to further expand the research in the field of thallium tellurides through phase ranges and doping experiments. Sample sizes in this section (Section IV) range from ~0.75 g to ~1 g to ensure sufficient quantities for physical property measurements. Taking into consideration the strong thermoelectric properties of Tl_9BiTe_6, questions arise about other heavy *p*-block elements such as Pb, Sn, or Sb. Through the use of traditional solid state techniques several systems including modifications of Tl_9BiTe_6, Tl_9SbTe_6, and Tl_4SnTe_3 will be investigated with additional elements or site deficiencies in attempt to further optimize the thermoelectric properties for power generation. Since the structures are so similar in nature the alloying of structures may benefit the properties as well.

Chapter 11. $Tl_{10-x}Sn_xTe_6$

11.1. Introduction

Knowing the magnitude of the figure of merit for the Tl_4SnTe_3 compound mentioned above (ZT = 0.74 at 673 K),[237] this material shows great promise and thermoelectric potential. With the compound's charge balance as $(Tl^+)_8(Sn^{2+})_2(Te^{2-})_6$, this in theory is a neutral compound with no extra carriers. Adjustments to the Tl/Sn ratio in this material can add or remove positive charges depending on whether more Tl or more Sn alters the Tl_4SnTe_3 parent stoichiometry. This yields the general formula $Tl_{10-x}Sn_xTe_6$ and a phase range study in attempt to learn how far the stoichiometry can be pushed before this compound loses its single phase XRD pattern. Subsequently, the thermoelectric properties will be measured in order to find the key stoichiometries achieving the highest figure of merit. To our knowledge the system $Tl_{10-x}Sn_xTe_6$ has been studied here for the first time, with investigations on its phase range and corresponding physical properties.

11.2. Experimental Section

11.2.1.1. Synthesis

All reactions were prepared from the elements (Tl: 99.99 %, granules 1-5mm, ALDRICH; Sn: 99.8 %, powder -325 mesh, ALDRICH; Te: 99.999 %, ingot, ALDRICH), with total sample masses between 500 mg and 1000 mg. The $Tl_{10-x}Sn_xTe_6$ system was explored by heating the elements Tl, Sn and Te in their respective stoichiometric molar ratios inside evacuated (approx. 10^{-3} mbar) silica tubes. Fused silica tubes were sealed under a hydrogen-oxygen flame, and samples were heated in resistance furnaces to 923 K, followed by slow cooling to 743 K within five days. Those typically mixed-phase samples were crushed into fine powder, resealed in silica tubes and annealed at 723 K for fifteen days. In order to explore the full phase range of this system, x was increased in increments of 0.2 such that $0 < x < 3.4$.

11.2.1.2. Analysis

Phase identifications were carried out by powder X-ray diffractometry (4.1) from well-ground products in all cases. Selected crystals were analyzed by means of standardless energy dispersive spectroscopy (6.2) using an acceleration voltage of 25 kV, a procedure that verified the existence of the desired elements within the products, and most importantly provided further evidence for increasing Sn content in the $Tl_{10-x}Sn_xTe_6$ series with increasing x until x = 2.2. For example, averaged over several crystals, the at-% in case of nominal "$Tl_{9.6}Sn_{0.4}Te_6$" were Tl : Sn : Te = 61.1 : 3.9 : 35.0 (expected: 60.0 : 2.5 : 37.5), for the x = 1 case 56.6 : 6.4 : 37.0 (expected: 56.3 : 6.3 : 37.5), and for the x = 2.2 case 53.2 : 10.5

: 36.3 (expected: 48.8 : 13.8 : 37.5). When $x > 2.2$, the side product SnTe was detected both in the EDX analyses as well as in the powder diffractogram.

11.2.2. Crystal Structure Studies

The data collections were carried out as discussed in 4.2. The crystals were picked from two different reactions with different nominal x values (Sn contents), namely from $x = 1$ (crystal 1), and $x = 1.8$ (crystal 2). Data was collected by scans of 0.3° in ω in at least two blocks of 600 frames at $\phi = 0°$ and $\phi = 120°$, with exposure times of 40 seconds per frame for all three cases. The data was corrected for Lorentz and polarization effects.

Structure refinements were performed with the SHELXTL package.[130] The crystal refinements were completed using the atomic positions published for Tl_9BiTe_6[244] assuming mixed Tl/Sn occupancies on the 4*c* (*M*(1)) site and 16*l* (*M*(2)) site, as was observed for Tl_4SnTe_3.[229] This described structure is analogous to that depicted in Figure 10.1. Attempts to include Sn on the 16*l* site of crystal 1 resulted in a negative occupancy factor for Sn within its standard deviation, so that the occupancy was assumed to be 100 % Tl. Refinements converged smoothly without showing any abnormalities. In the case of nominal Tl_9SnTe_6 (crystal 1), the refined x value of 0.95(8) equals the nominal stoichiometry within one standard deviation. For crystal 2, the refined $x = 1.63(9)$ is within two standard deviations of the nominal $x = 1.8$.

As no suitable single crystals were obtained, we performed Rietveld refinements using the samples with nominal $x = 2.0$ and $x = 2.2$. Data were collected on the above-mentioned INEL diffractometer for 16 hours in each case. The refined formulas are $Tl_{8.0}Sn_{2.0(3)}Te_6$ and $Tl_{7.5}Sn_{2.5(3)}Te_6$, respectively. Crystallographic details are summarized in Table 11.1. The atomic positions, isotropic displacement parameters and Sn occupancies of $Tl_{10-x}Sn_xTe_6$ can be found by Kuropatwa *et al.*[245] displayed in Table A.1 and Table A.2. Further details of the crystal structure investigations can be obtained from the Fachinformationszentrum Karlsruhe, 76344 Eggenstein-Leopoldshafen, Germany (fax: +49 7247 808 666; e-mail: crysdata@fiz-karlsruhe.de) on quoting the depository numbers CSD-422128 (nominal $x = 1.0$) and 422129 (nominal $x = 1.8$).

Table 11.1 Crystallographic information for $Tl_{10-x}Sn_xTe_6$.

Chemical formula	$Tl_{9.05}Sn_{0.95(8)}Te_6$	$Tl_{8.37}Sn_{1.63(9)}Te_6$	$Tl_{8.0}Sn_{2.0(3)}Te_6$	$Tl_{7.5}Sn_{2.5(3)}Te_6$
M [g/mol]	2727.90	2669.64	2639.4	2599.08
T [K]	296(2)	296(2)	296(2)	296(2)
λ [Å]	0.71073	0.71073	1.5406	1.5406
space group	$I4/mcm$	$I4/mcm$	$I4/mcm$	$I4/mcm$
a [Å] = *b*	8.8416(6)	8.850(1)	8.8384(4)	8.8375(1)
c [Å]	13.0114(9)	13.059(2)	13.0525(6)	13.0585(3)
V [Å^3]	1017.2(1)	1022.9(2)	1019.6(1)	1019.88(2)
Z	2	2	2	2
$R(F_o)^a$ \ $R_w(F_o^2)^b$	0.064 \ 0.154	0.024 \ 0.057		
$R_P{}^c$ \ $R_B{}^d$			0.052 \ 0.097	0.060 \ 0.112

$^a R(F_o) = ||F_o|-|F_c||/|F_o|$ $^b R_w(F_o^2) = [\Sigma[w(F_o^2 - F_c^2)^2]/\Sigma[w(F_o^2)^2]]^{1/2}$

$^c R_P = \Sigma|y_o - y_c| / \Sigma|y_o|$ $^d R_B = \Sigma|I_o - I_c| / \Sigma|I_o|$

11.2.3. Electronic Structure Calculations

Self-consistent tight-binding *first principles* LMTO calculations (LMTO = linear muffin tin orbitals) were performed using the atomic spheres approximation (ASA) [153, 154] to study the impact of Sn addition on the band gaps. In the LMTO approach, the density functional theory is used with the local density approximation (LDA) for the exchange correlation energy.[161] Three different models were calculated. The initial binary compound, $Tl_{10}Te_6$ ($I4/mcm$), was first calculated and then compared to the two ternary tellurides Tl_9SnTe_6 ($I4/m$) and $Tl_8Sn_2Te_6$ ($I4/mcm$). The wavefunctions used in the calculations are as follows: For Tl *6s*, *6p*, *6d* and *5f*; for Sn *5s*, *5p*, and *5d* and *4f*, and for Te *5s*, *5p*, and *5d* and *4f*. The eigenvalue problems were solved on the basis of 512 *k* points within the irreproducible wedge of the first Brillouin zone, respectively, selected with an improved tetrahedron method.[203]

11.2.4. Physical Property Measurements

Part of the ground phase-pure samples were cold-pressed into bar-shaped pellets of the dimensions 13×2×2 mm^3 for Seebeck coefficient (S) and electrical conductivity (σ) measurements, simultaneously determined utilizing the ULVAC-RIKO ZEM-3 under helium between room temperature and 550 K. Cold-pressed pellet densities ranged between 80 – 85% of the theoretical (calculated) densities of Tl_9SnTe_6 or $Tl_8Sn_2Te_6$ structures depending on the quantity of *x*. The pellets were annealed at 653 K over a period of 24 hours in evacuated fused silica tubes. The densities slightly increased upon

sintering of these pellets. A cold-pressed bar with dimensions of 6×1×1 mm^3 was utilized for Tl_5Te_3 after applying silver paint (Ted Pella) to create the electric contacts. The MMR Technologies device (5.4) was used, measuring the Seebeck coefficient (S) under dynamic vacuum in the temperature range of 300 K - 550 K with constantan as an internal standard, to determine the temperature difference.

11.3. Results and Discussion

11.3.1. Crystal Structure

The crystal structure of $Tl_{9.05}Sn_{0.95}Te_6$ is shown in Figure 10.1, with a 1:1 ratio of Tl : Sn sitting in the 4*c* Wyckoff site (*M*(1)), whilst the second Tl site (*M*(2), 16*l*) contains no Sn. There are no Te–Te bonds in this system. The Tl(1)/Sn(1) atoms are coordinated to four Te(1) (3.25 Å) and two Te(2) atoms (3.31 Å) via an octahedral coordination elongated along the *c* direction. The *M*(2) atoms are surrounded by five Te atoms with bond lengths between 3.16 Å and 3.58 Å. The structures contain weak Tl–Tl bonds between 3.5 Å and 3.7 Å forming two Tl_8 clusters per unit cell, analogous to elemental S_8 crowns. Tl–Tl bonds are formed only with *M*(2), not with *M*(1) – which contains a higher quantity of Sn in all cases.

11.3.2. Electronic Structure Calculations

In the cases of Tl_5Te_3 and $Tl_8Sn_2Te_6$, the space group was set to $I4/mcm$ corresponding to the most accurate crystallographic data.[246] Tl_9SnTe_6 was calculated in $I4/m$. Due to the lack of Te–Te bonds in the system, the Te atoms are formally fully reduced and all anion charges are then balanced by cation charges in the $x = 2$ case via $(Tl^+)_8(Sn^{2+})_2(Te^{2-})_6$.

The density of states (DOS) calculated for the $Tl_{10}Te_6$ model predicts metallic properties with the Fermi level approximately 0.7 eV significantly below the band gap (Figure 11.1). The partially empty valence band is predominantly occupied by Te-*p* states. As the Sn content is increased to 1 (Tl_9SnTe_6), the structure remains metallic with the Fermi level now approximately 0.3 eV below the band gap. The $Tl_8Sn_2Te_6$ model has its Fermi level directly at the band gap, in accord with the results of an earlier Extended Hückel calculation.[217]

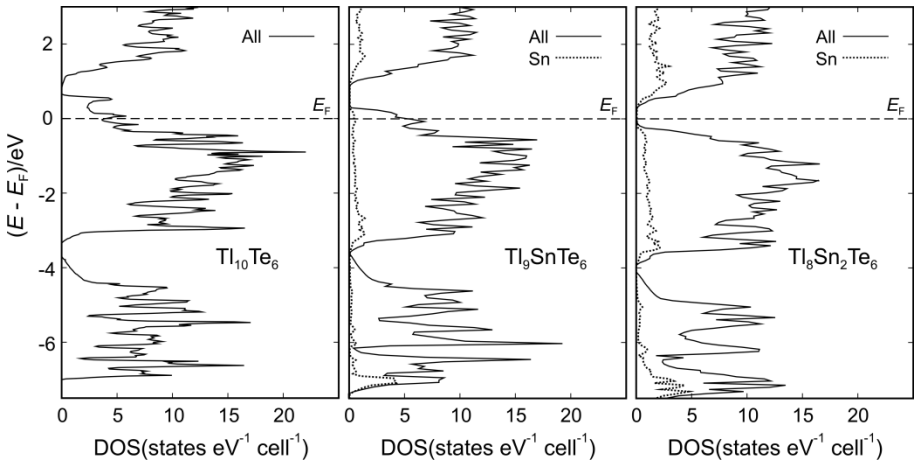

Figure 11.1 Densities of states (*DOS*) of $Tl_{10}Te_6$ (left), Tl_9SnTe_6 (center) and $Tl_8Sn_2Te_6$ (right). The dashed horizontal lines indicate the Fermi energy, E_F.

11.3.3. Physical Property Measurements

The positive Seebeck coefficient, S, increases smoothly with increasing temperature for the $Tl_{10-x}Sn_xTe_6$ samples with $x < 2.1$, typical for *p*-type semiconductors having high charge carrier concentration (top left of Figure 11.2). The Seebeck curve of the sample with $x = 2.2$ exhibits a clear maximum of $S = +190\ \mu V \cdot K^{-1}$ around 555 K. Increasing the Sn content, *x*, leads to an increase in S, e.g. around room temperature from $S = +10\ \mu V \cdot K^{-1}$ for $x = 0$ to $S = +80\ \mu V \cdot K^{-1}$ for $x = 2.2$. The only exception is the sample with x = 2.05, whose S values are slightly larger than those of the $x = 2.1$ case, e.g. around room temperature 70 $\mu V \cdot K^{-1}$ vs. 67 $\mu V \cdot K^{-1}$. This small difference is within experimental error.

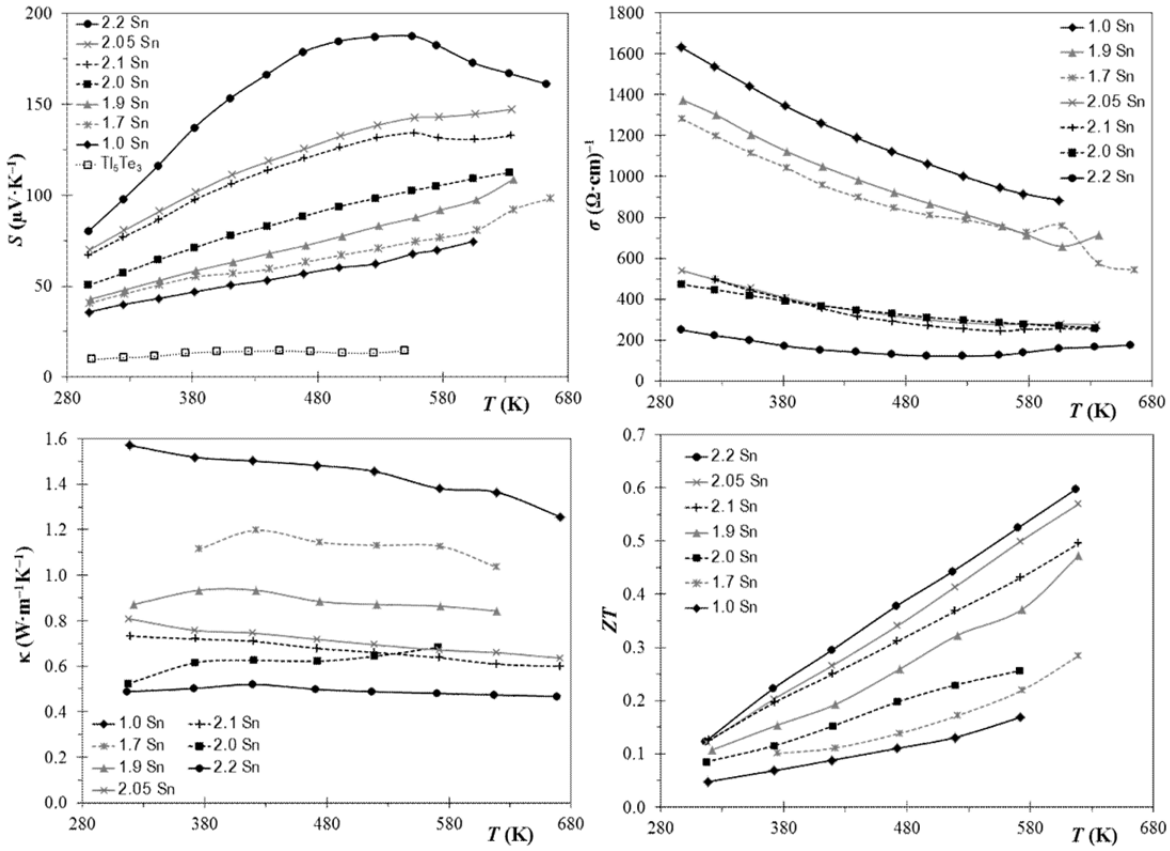

Figure 11.2 Thermoelectric properties of $Tl_{10-x}Sn_xTe_6$: Seebeck coefficient (upper left), electrical conductivity (upper right), thermal conductivity (lower left), dimensionless figure of merit (lower right).

The different temperature behaviour as *x* is varied can be attributed to the relationship between Seebeck coefficient and temperature and charge carrier concentration mentioned in Equation 1.3. Hence the samples with high, and thus temperature independent *n* (small *x*), will exhibit a linearly increasing Seebeck coefficient with temperature; those with small *n* (large *x*) that increases with temperature, show a decrease in S, once sufficient charge carriers are able to cross the gap. Using $E_{\mathrm{gap}} = 2eS_{\max}T_{\max}$,[247] a gap of 0.2 eV results for $Tl_{7.8}Sn_{2.2}Te_6$. Following the aforementioned logic, *x* = 2.2 would yield $(Tl^{+})_{7.8}(Sn^{2+})_{2.2}(Te^{2-})_6(e^{-})_{0.2}$ leaving an overall electron excess of 0.2 in the proposed formula and hence *n*-type conduction, in contrast to the experimentally observed *p*-type conduction. It is noted that we also observed *p*-type carrier in the isostructural $Tl_{8.85}La_{1.15}Te_6$ that also formally contained excess electrons.[236] Some side products may be present below the detection limit of diffraction studies; for attempted *x* > 2.2, this entails one additional phase – SnTe, which is present between 3 – 6 % for "$Tl_{7.6}Sn_{2.4}Te_6$" as found in its diffraction pattern. Moreover, there may be some vacancies in the structure that change the details of the band structure and the charge carrier concentration that may cause the experimentally observed *p*-type conduction.

The 300 K S value of +50 $\mu V \cdot K^{-1}$ obtained from the sintered pellet of $Tl_8Sn_2Te_6$ is significantly below the 80 $\mu V \cdot K^{-1}$ obtained from (low temperature measurements on) a polycrystalline ingot[248] and the 126 $\mu V \cdot K^{-1}$ obtained at 323 K from a hot-pressed pellet of 91 % density.[237] The Seebeck coefficient of the latter continues to increase until 673 K (the end of the measurement), exceeding +200 $\mu V \cdot K^{-1}$. The differences at room temperature may be due to slight variations in the exact Tl:Sn ratio and hence the charge carrier concentration, implying that the sample investigated here had higher charge carrier concentration while nominally the same formula. Interestingly, the polycrystalline ingot with an experimentally determined carrier concentration of $2.22 \cdot 10^{19}$ cm^{-3} has the same room temperature Seebeck coefficient as $Tl_{7.8}Sn_{2.2}Te_6$.

The electrical conductivity, σ, for the $Tl_{10-x}Sn_xTe_6$ samples with $x < 2.1$ decreases with increasing temperature (top right of Figure 3), again evidence of a relatively high carrier concentration. $Tl_{7.8}Sn_{2.2}Te_6$ is again the exception, its σ value reaching a minimum of 121 $\Omega^{-1}cm^{-1}$ at 526 K. Thereafter, its increasing number of intrinsic, thermally activated carriers reverses the trend, causing increasing electrical conductivity. This change was not observed by Kosuga *et al.* in case of the hot-pressed pellet of $Tl_8Sn_2Te_6$.[237] Increasing x causes a decrease in σ, in accord with our expectations and the opposite trend in S. Tl_9SnTe_6 displays the highest value (1630 $\Omega^{-1}cm^{-1}$) at room temperature, and $Tl_{7.8}Sn_{2.2}Te_6$ the lowest with 250 $\Omega^{-1}cm^{-1}$, and the samples with x = 2.05 and 2.1 have almost identical values of 540 $\Omega^{-1}cm^{-1}$and 532 $\Omega^{-1}cm^{-1}$, respectively. For comparison, the corresponding values for the $Tl_8Sn_2Te_6$ ingot and hot-pressed pellet are 275 $\Omega^{-1}cm^{-1}$ and 272 $\Omega^{-1}cm^{-1}$ (at 323 K), respectively.

The thermal conductivity curves (bottom left of Figure 11.2) roughly follow the same trend as the electrical conductivity, with Tl_9SnTe_6 displaying the highest and $Tl_{7.8}Sn_{2.2}Te_6$ the lowest values. The values around 317 K, range from 1.57 $W \cdot m^{-1}K^{-1}$ to 0.49 $W \cdot m^{-1}K^{-1}$ which over the range of measurement, decreases slightly (for the most part) as the temperature increases. The thermal conductivity of the hot-pressed pellet was determined to be basically temperature independent around 0.5 $W \cdot m^{-1}K^{-1}$,[237] while the one of the polycrystalline ingot was not measured.

The thermoelectric (dimensionless) figure-of-merit, ZT, was calculated from the above-mentioned S, σ, and κ data, by computing polynomial fits for $S^2\sigma$, because κ was measured at different temperatures. In order to avoid extrapolation, only the data points that were both within the temperature range of $S^2\sigma$ and κ were considered. Overall, the ZT trends display a gradual increase with increasing temperature (bottom right of Figure 3). Tl_9SnTe_6 exhibits the lowest figure-of-merit ZT = 0.05

at 319 K, increasing smoothly to 0.17 at 572 K. For the most part, ZT gradually increases with increasing *x* such that $Tl_{7.8}Sn_{2.2}Te_6$ attains 0.12 at 316 K and 0.60 at 617 K. Hot-pressed $Tl_8Sn_2Te_6$ exhibited ZT = 0.28 at 323 K, which increased to 0.67 at 623 K and culminated in 0.74 at 673 K.[237]

11.4. Conclusion

Various members of the $Tl_{10-x}Sn_xTe_6$ series were successfully synthesized, analyzed and their physical properties measured for *x* = 1.0, 1.7, 1.9, 2.0, 2.05, 2.1 and 2.2. The materials are isostructural with the binary telluride Tl_5Te_3, and the crystal structure of Tl_9SnTe_6 was determined with the experimental formula $Tl_{9.05}Sn_{0.95}Te_6$, possessing the same space group ($I4/mcm$) as Tl_5Te_3 and $Tl_8Sn_2Te_6$, in contrast to Tl_9SbTe_6 that adopts the space group $I4/m$.

The band structure calculations for Tl_9SnTe_6 and $Tl_8Sn_2Te_6$ suggest that Tl_9SnTe_6 is a heavily doped *p*-type semiconductor with a partially empty valence band, while the Fermi level in $Tl_8Sn_2Te_6$ is located in the band gap. In accord with these calculations, both thermal and electrical conductivity measurements indicate that increasing Sn results in lower values, as determined on sintered polycrystalline samples. The opposite trend is visible with respect to the Seebeck coefficient, as increasing *x* will result in higher values.

The figure-of-merit reaches a maximum at the Sn-rich end of the phase width: $Tl_{7.8}Sn_{2.2}Te_6$ reaches its maximum ZT = 0.60 at 617 K (end of measurement), significantly larger than ZT of $Tl_8Sn_2Te_6$ prepared and treated analogously, which remains under 50 % of the ZT values of $Tl_{7.8}Sn_{2.2}Te_6$ at elevated temperatures. The fact that hot-pressed $Tl_8Sn_2Te_6$ was reported to reach 0.67 at 623 K,[237] implies that hot-pressing of $Tl_{7.8}Sn_{2.2}Te_6$ should ultimately result in higher values.

Chapter 12. Modifications of Tl_9BiTe_6 via the addition of Tt^{2+}

12.1. Introduction

Wölfing *et al.*[222] popularized Tl_9BiTe_6 as an extremely promising thermoelectric material with a ZT = 1.2 at 500 K. Likewise, the recent discovery of *p*-doped Tl_9SnTe_6 in **Chapter 11** with a ZT = 0.17 at 572 K (cold-pressed) can lead to additional Tl_9BiTe_6-based studies. Since both materials share a common crystal structure, experiments will be carried out combining Sn and Bi in the same structure such as $Tl_9Sn_{1-x}Bi_xTe_6$. These alloying experiments should establish a relationship between the two compounds and determine if an excess of *p*-type carriers show desirable changes in the materials' physical properties. Since the inclusions of disorders in well-performing materials have improved their physical properties in other systems, the same strategy may exhibit a favourable change in this system as well. By further altering the general formula to $Tl_{10-x-y}Sn_xBi_yTe_6$, the Tl^+ located on the 16*l* Wyckoff site can be allowed to mix with Sn^{2+} or even Bi^{3+}. Since this also involves charge imbalance, a phase range study should be initiated. The altering of the Sn/Bi ratios in these compounds will be examined at three fixed Tl concentrations: Tl_9…, $Tl_{8.67}$…, and $Tl_{8.33}$… followed by systematic adjustments of the Sn : Bi ratio. Following pure phase samples are physical property measurements.

12.2. Experimental Section

12.2.1.1. Synthesis

All reactions were prepared from the elements (Tl: 99.99 %, granules 1-5mm, ALDRICH; Sn: 99.999 %, powder -100 mesh, ALFA AESAR; Bi: 99.5 %, powder -100 mesh, ALFA AESAR; Te: 99.999 %, ingot, ALDRICH), with total sample masses between 500 mg and 1000 mg for in-lab samples. The $Tl_{10-x-y}Sn_xBi_yTe_6$ system was explored by heating the elements Tl, Sn, Bi and Te in their respective stoichiometric molar ratios inside glassy carbon crucibles and evacuated (approx. 10^{-3} mbar) inside silica tubes. The silica tubes were sealed under a hydrogen-oxygen flame, and samples were heated in resistance furnaces to 923 K to encourage a homogeneous melt, followed by slow cooling from 873 to 723 K within five days. Those samples showing mixed-phases were crushed into fine powder, resealed in silica tubes and annealed at 723 K for between five and ten days. Thallium was studied within three different stoichiometries including the standard ternary composition of 9 Tl as well as deficient trials 8.67 Tl and 8.33 Tl. Variations on the Sn : Bi ratio were then explored in increments for each of the aforementioned Tl concentrations that explore the spectrum: Sn-rich (i.e. 3 Sn : 1 Bi), Bi-heavy (i.e. 1 Sn : 3 Bi), and to approximately equal parts. Samples of $Tl_9Sn_{1-x}Bi_xTe_6$ type were found to be of $\geq$ 95 %

purity upon the first heating with a range of $0 \leq x \leq 0.8$. Studies on the $Tl_{8.67}$…Te_6 compositions yielded pure samples between $0.33 \leq x \leq 1.00$ but with $x \leq 0.5$, minor presence of what was likely $TlBiTe_2$ was encountered and upon reheating was reduced to < 5 % via XRD scans. The largest Tl deficiency, $Tl_{8.33}Sn_{1.67-y}Bi_yTe_6$, yielded pure-phase samples for $0.55 \leq y \leq 0.83$ (or [Sn] > [Bi]) and ~10 % $TlBiTe_2$ along with minor contributions (<4 %) from an unidentified phase for those samples with [Bi] > [Sn]. This shorter range of composition can be attributed to the capability of Sn-heavy samples to form the phase Tl_4SnTe_3 (≡ $Tl_8Sn_2Te_6$).

12.2.1.2. Analysis

Phase identifications were carried out by powder X-ray diffractometry (using an INEL diffractometer with position-sensitive detector and Cu-$K_{\alpha 1}$ radiation) from well-ground products in all cases. When samples are found to be inhomogeneous, a common side-product is either TlTe or $TlBiTe_2$. Since both phases have overlapping major peaks, one would require concentrations of >10 % to distinguish between them; additional phases, if present, were typically on the order of 3 – 6 % and easily removed during annealing. Powdered samples were analyzed by means of standardless energy dispersive spectroscopy (EDX) using an acceleration voltage of 25 kV – a qualitative procedure that verified the existence of the desired elements within the products, such as proving both Sn and Bi are present in the proposed quaternary structure with comparable stoichiometries to the nominal weighings.

12.2.1.3. Single Crystal Structure

The data collections were carried out on a BRUKER Smart Apex CCD at room temperature utilizing Mo-K_α radiation. The crystal in this article was grown from a sample with $x = 0.63$ and $y = 0.70$: slightly more Bi than Sn. Due to the plate-like shape of the crystals, many attempts were necessary to find a proper single crystal. Data was collected by scans of 0.3° in ω in at least two blocks of 600 frames at $\phi = 0°$ and $\phi = 120°$, with exposure times of 40 seconds per frame. The data was corrected for Lorentz and polarization effects.

Structure refinements were performed with the SHELXTL package.[130] The crystal refinements were completed using the atomic positions published for Tl_9BiTe_6[222] attempting mixed Tl/Sn/Bi occupancies on the 4*c* (*M*(1)) site and 16*l* (*M*(2)) site. Attempts to mix Sn on the 16*l* site of $Tl_{8.67}Sn_{0.63}Bi_{0.70}Te_6$ resulted in slightly larger values for the U_{11} displacement parameter and negligibly smaller (i.e. < 0.3 %) $R(F_o) \setminus R_w(F_o^2)$ values, but yielded an impractically small Tl : Sn ratio – the scattering

factor of Bi is comparable to Tl so even with its inclusion, the suggested quantity of Sn in the crystal was unreasonable. Thus, mixing on the 4*c* (*M*(1)) site was comprised of Tl, Sn and Bi based on anisotropic displacement parameter values as well as previous data from Tl_9BiTe_6[244] or $Tl_{9.05}Sn_{0.95}Te_6$[245] or $Tl_{10-x}La_xTe_6$[236] were treated whilst the *M*(2) site was left fully occupied with Tl. Refinements converged smoothly without showing any abnormalities. Due to the difficulty of differentiating Tl from Bi scattering, EDX data taken on the crystal allowed us to fix Bi as ⅓ of the 4*c* site. The formula $Tl_{8.67}Sn_{0.63}Bi_{0.70}Te_6$ was refined to $Tl_{8.66}Sn_{0.67}Bi_{0.67}Te_6$, which leaves the atomic sites within 5 % of the nominal composition.

In order to monitor the unit cell parameters of a wider range of samples, Rietveld refinements were performed on the samples with nominal $x = 0.60$, $y = 0.40$; $x = 0.50$, $y = 0.50$; and $x = 1.00$, $y = 0.33$. Data were collected on the aforementioned INEL diffractometer for approximately 12 hours in each case; all powders showed no additional phases in the resulting diffractograms.

Crystallographic details of the data collections are summarized in Table 12.1, the atomic positions, isotropic displacement parameters, and occupancies of $Tl_{10-x-y}Sn_xBi_yTe_6$ in Table A.3, and the bond ranges in Table A.4.

12.2.1.4. Electronic Structure Calculations

Self-consistent tight-binding *first principles* LMTO calculations, as previously discussed were implemented here. Three different models were calculated in $P4/m$ including the Sn-Bi equivalent compound, $Tl_9Sn_{0.5}Bi_{0.5}Te_6$, the Sn-heavy $Tl_{8.5}Sn_1Bi_{0.5}Te_6$ and the Bi-rich $Tl_9Sn_{0.5}Bi_1Te_6$. All compounds are originally of space group $I4/mcm$. The wavefunctions used in the calculations are as follows: for Tl *6s*, *6p*, *6d* and *5f*; for Sn *5s*, *5p*, and *5d* and *4f*; for Bi *6s*, *6p*, *6d* and *5f*; and for Te *5s*, *5p*, and *5d* and *4f*. The eigenvalue problems were solved on the basis of 1728 evenly-dispersed *k* points within the irreproducible wedge of the first Brillouin zone, respectively, selected with an improved tetrahedron method.[203]

12.3. Results and Discussion

12.3.1. Crystal Structure

A crystal of nominal composition $Tl_{8.67}Sn_{0.63}Bi_{0.70}Te_6$ was selected for single crystal diffraction in order to determine the lattice parameters and verify the atomic site positions and occupancies. This crystal structure was refined to $Tl_{8.66}Sn_{0.67}Bi_{0.67}Te_6$ and is analogous to Figure 10.1, with equal parts

Tl/Sn/Bi present in the 4*c* Wyckoff site (*M*(1)), whilst the second Tl site (*M*(2), 16*l*) contains only Tl. There are no Te–Te bonds in this system. The *M*(1) atoms are coordinated to four Te1 (3.25 Å) and two Te2 atoms (3.32 Å) via an octahedral coordination elongated along the *c* direction. The *M*(2) atoms are surrounded by five Te atoms with bond lengths between 3.16 Å and 3.59 Å. The structures contain weak Tl–Tl bonds between 3.50 Å and 3.67 Å forming two Tl_8 clusters per unit cell, analogous to elemental S_8 crowns. Tl–Tl bonds are formed only with *M*(2), not with *M*(1).

Rietveld refinements on three additional samples were utilized to monitor changes in the unit cell parameters from stoichiometry to stoichiometry. While the unit cell parameters such as dimensions and volume could be refined, the same problem with respect to three atoms – Tl/Sn/Bi – on the same Wyckoff position (4*a*) meant that in each case, the atoms were fixed at their nominal compositions while U values for each site could be refined from the "conventional" 0.025 during the Rietveld procedure. Subsequent EDX measurements on each of these samples yielded acceptable matches. With a volume of 1019.87 $Å^3$, the single crystal data on $Tl_{8.66}Sn_{0.67}Bi_{0.67}Te_6$ is the largest of the measured unit cells. According to the refined powder data, the next largest unit cell has a volume of 1015.9 $Å^3$ for "$Tl_9Sn_{0.50}Bi_{0.50}Te_6$" followed by "$Tl_9Sn_{0.60}Bi_{0.40}Te_6$" with 1012.5 $Å^3$. The final measured cell was "$Tl_{8.67}Sn_{1.00}Bi_{0.33}Te_6$" yielding the smallest volume of 998.2 $Å^3$.

Table 12.1 Crystallographic information for $Tl_{10-x-y}Sn_xBi_yTe_6$.

Chemical formula	$Tl_9Sn_{0.60}Bi_{0.40}Te_6$	$Tl_9Sn_{0.50}Bi_{0.50}Te_6$	$Tl_{8.67}Sn_{1.00}Bi_{0.33}Te_6$	$Tl_{8.66}Sn_{0.67}Bi_{0.67}Te_6$
M [g/mol]	2759.74	2768.76	2725.14	2754.37
T [K]	296(2)	296(2)	296(2)	296(2)
λ [Å]	1.5406	1.5406	1.5406	0.71073
space group	$I4/mcm$	$I4/mcm$	$I4/mcm$	$I4/mcm$
a [Å] = *b*	8.8709(5)	8.8698(4)	8.789(6)	8.8549(3)
c [Å]	12.8661(8)	12.9132(7)	12.922(9)	13.0069(9)
V [$Å^3$]	1012.47(16)	1015.93(15)	998.2(22)	1019.86(9)
Z	2	2	2	2
$R(F_o)^a \setminus R_w(F_o^2)^b$				0.041 \ 0.0927
$R_P{}^c \setminus R_B{}^d$	0.0639 \ 0.0742	0.0762 \ 0.0864	0.0828 \ 0.0905	

$^a R(F_o) = ||F_o|-|F_c||/|F_o|$ $^b R_w(F_o^2) = [\ \Sigma[w(F_o^2 - F_c^2)^2]/\Sigma[w(F_o^2)^2]\ ]^{1/2}$

$^c R_P = \Sigma|y_o - y_c| / \Sigma|y_o|$ $^d R_B = \Sigma|I_o - I_c| / \Sigma|I_o|$

Additional tables including Wyckoff positions and bond distances for the four samples are stored in the appendix of this document (Table A.3).

12.3.2. Electronic Structure Calculations

In all studied cases, the space group was set to $P4/m$ corresponding to the closest space group to $I4/mcm$ where no further symmetry is lost by substituting Sn and Bi atoms on Tl sites. Due to the lack of Te–Te bonds in the system, the Te atoms can be considered Te^{2-}, while the other atoms can be treated as the typical Tl^{+}, Sn^{2+} and Bi^{3+}. This is the same approach taken with literature calculations as well as those found previously in this section. The calculations in $Tl_{10-x}La_xTe_6$[236] utilized a similar strategy to these calculations and also resulted in *p*-type and metallic results.

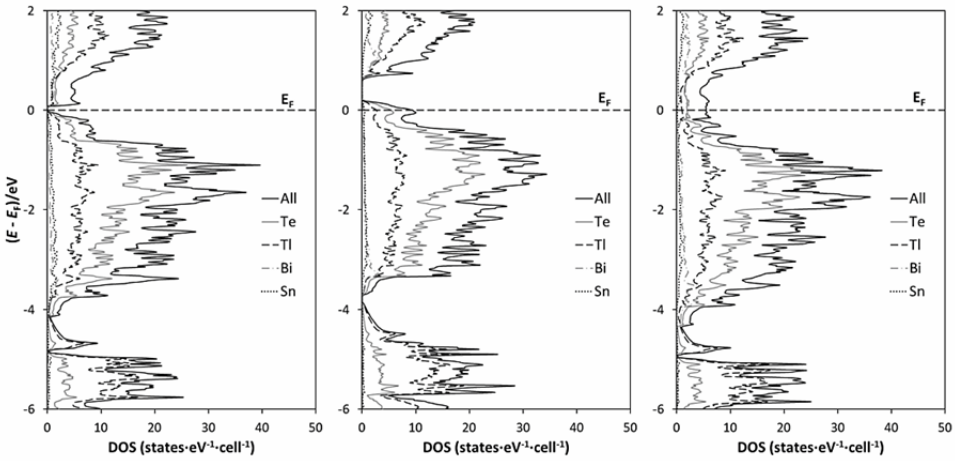

Figure 12.1 *DOS* calculations for $Tl_9Sn_{1-x}Bi_xTe_6$: $Tl_{8.5}SnBi_{0.5}Te_6$ (left), $Tl_9Sn_{0.5}Bi_{0.5}Te_6$ (centre), $Tl_{8.5}Sn_{0.5}BiTe_6$ (right)

The Sn-heavy model was calculated by replacing one more Tl site with a Sn atom wielding $Tl_{8.5}Sn_1Bi_{0.5}Te_6$, an intrinsic semiconductor with a band gap on the order of 0.2 eV with a similar appearance to the ternary itself, shown in Figure 10.2; the density of states (*DOS*) calculated for $x = 0.5$, $y = 0.5$ predicts *p*-type extrinsic semiconductor behaviour with an electron deficiency of ~ 0.15 eV below the band gap, which is then predicted to be on the order of 0.3 eV; the Bi-rich model, $Tl_{8.5}Sn_{0.5}Bi_1Te_6$, is predicted to show metallic behaviour as it has no gap between valence and conduction bands. The valence band is predominantly occupied by Te-*p* states.

12.3.3. Physical Property Measurements

12.3.3.1. $Tl_9Sn_{1-x}Bi_xTe_6$

The Seebeck coefficient for $Tl_9Sn_{1-x}Bi_xTe_6$ displays behaviour typical of *p*-type semiconductors with a reasonably high charge carrier concentration. Seebeck coefficient values increase steadily across the full range of temperature measurement in a constant and linear fashion. The lowest Seebeck coefficient values correspond to $Tl_9Sn_{0.8}Bi_{0.2}Te_6$ with 41 $\mu V \cdot K^{-1}$ at room temperature and increases to 77

$\mu V \cdot K^{-1}$ at 592 K. As the bismuth content increases, so does the Seebeck coefficient, which by nominal composition $Tl_9Sn_{0.2}Bi_{0.8}Te_6$, displays values of 89 $\mu V \cdot K^{-1}$ at room temperature and 151 $\mu V \cdot K^{-1}$ at 587 K. This general trend can be seen in Figure 12.2 increasing with increasing Bi-content. For ease of reference, Tl_9SnTe_6 from the previous chapter has been included in the plot. As expected it appears as the lowest magnitude, showing 39 $\mu V \cdot K^{-1}$ at room temperature – a mere 5 $\mu V \cdot K^{-1}$ below $Tl_9Sn_{0.8}Bi_{0.2}Te_6$. Hot-pressed measurements published on Tl_9BiTe_6 state that it has S = ~150 $\mu V \cdot K^{-1}$ at room temperature[249] showing not only does this data follow an appropriate trend, but is nestled between the two extreme cases: Tl_9SnTe_6 and Tl_9BiTe_6.

The electrical conductivity, σ, for all trials shows a gentle decrease in the slope values from room temperature (~295 K) to the higher temperatures measured herein (Figure 12.2 (dashed)). The straight decreasing line is reminiscent to that of heavily-doped semiconductors. With an excess of carriers, increasing T disrupts μ and decreases σ. The trend is appropriately inversed to that of the Seebeck coefficient due to their (more-or-less) inverse relationship. In the case of $Tl_9Sn_{1-x}Bi_xTe_6$, the smallest σ can be found in $Tl_9Sn_{0.2}Bi_{0.8}Te_6$ with 530 $\Omega^{-1}cm^{-1}$ at room temperature to 357 $\Omega^{-1}cm^{-1}$ at 587 K. The highest of this system can be found in $Tl_9Sn_{0.8}Bi_{0.2}Te_6$ with 1224 $\Omega^{-1}cm^{-1}$ at room temperature to 821 $\Omega^{-1}cm^{-1}$ at 592 K. The intermediate compositions of x = 0.6 and x = 0.4 also follow this trend. σ of Tl_9BiTe_6 is reported to be almost one quarter of $Tl_9Sn_{0.2}Bi_{0.8}Te_6$ showing ~125 $\Omega^{-1}cm^{-1}$ for zone-refined[222] and ~200 $\Omega^{-1}cm^{-1}$ for hot-pressed[249] (~300 K).

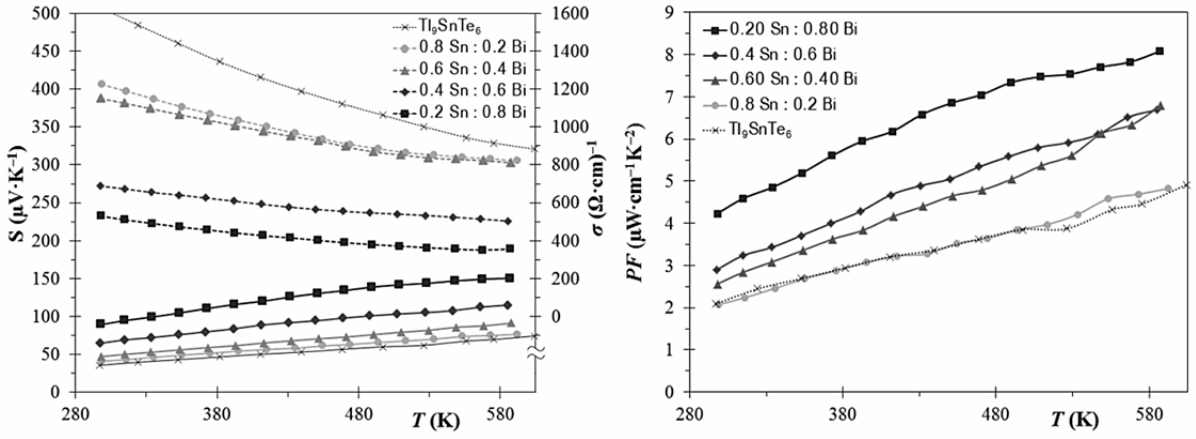

Figure 12.2 ZEM measurements for $Tl_9Sn_{1-x}Bi_xTe_6$: solid Seebeck coefficient and dashed electrical conductivity (left), and power factor (right).

The power factor for these compounds is displayed on the right side of Figure 12.2. All measured power factors rise in a similar fashion to the Seebeck coefficients with Bi-heavy compounds typically achieving the higher values which is exemplified by $Tl_9Sn_{0.2}Bi_{0.8}Te_6$ with a room temperature PF of 4.23 $\mu W \cdot cm^{-1}K^{-2}$ which increases to 8.08 $\mu W \cdot cm^{-1}K^{-2}$ at 587 K. Since $PF = S^2\sigma$, increases in S can be quite significant, as is the case here. With $Tl_9Sn_{0.2}Bi_{0.8}Te_6$ having S = ~80 $\mu W \cdot cm^{-1}K^{-2}$ at room temperature – double the value of $Tl_9Sn_{0.8}Bi_{0.2}Te_6$ – S^2 therefore overpowers its lower σ value.

12.3.3.2. $Tl_{10-x-y}Sn_xBi_yTe_6$

The Seebeck coefficient values of compounds with composition $Tl_{8.67}Sn_{1.33-y}Bi_yTe_6$ increase in a similar fashion as the previous set of *p*-type semiconductors. Like its counterparts, these gently increasing Seebeck coefficient values have the lowest coefficient encountered with a larger [Sn] – in this case 68 $\mu V \cdot K^{-1}$ at room temperature increasing to 116 $\mu V \cdot K^{-1}$ at 563 K – and, following the pattern of increasing [Bi], leads to 113 $\mu V \cdot K^{-1}$ at room temperature to 175 $\mu V \cdot K^{-1}$ at 614 K for $Tl_{8.67}Sn_{0.50}Bi_{0.83}Te_6$. With the exception of the slightly higher-than-expected numbers for $Tl_{8.67}Sn_{0.70}Bi_{0.63}Te_6$, (based on the earlier-mentioned single crystal and EDX study of this composition leading to "$Tl_{8.67}Sn_{0.67}Bi_{0.66}Te_6$", this slight break in the trend can be attributed to synthetic errors leaving both samples with near-identical compositions,) the same behaviour trends are observed in this case – and displayed in Figure 12.3 (left). Upon studying the $Tl_{8.33}Sn_{1.67-y}Bi_yTe_6$ phase, the same observations can be made as this sample contains a larger quantity of Sn versus Bi and therefore sits at a similar magnitude to the lower *y* values in $Tl_{8.67}Sn_{1.33-y}Bi_yTe_6$. For reference, $Tl_8Sn_2Te_6$ from the previous chapter is shown here as this series has a lower Tl:Sn ratio than Tl_9SnTe_6: The higher quantity of Sn (versus Tl or Bi) places this value at the bottom of the figure with 50 $\mu V \cdot K^{-1}$ (300 K), following the general trend in this graph.

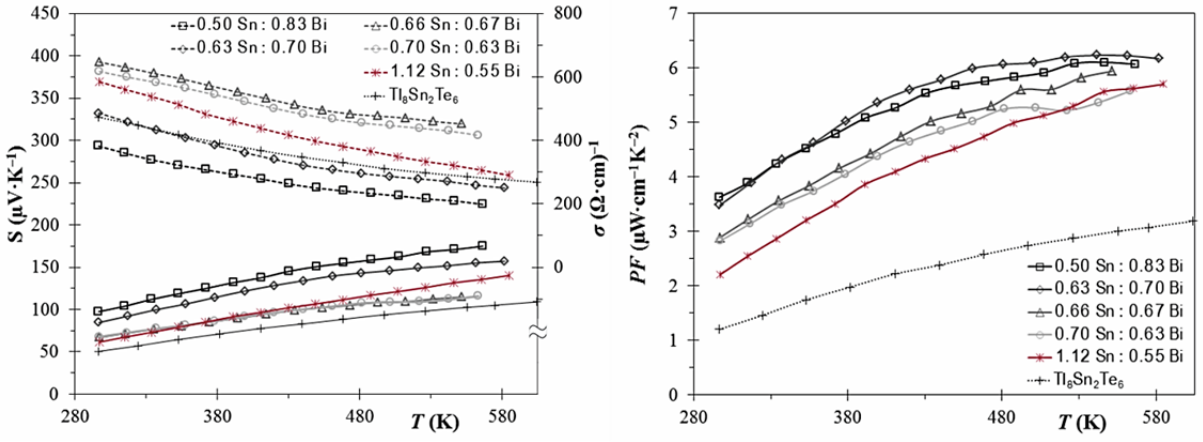

Figure 12.3 ZEM measurements for $Tl_{10-x-y}Sn_xBi_yTe_6$:
solid Seebeck coefficient and dashed electrical conductivity (left), and power factor (right).

Electrical conductivity values are again inversely proportional to their Seebeck counterparts with $Tl_{8.67}Sn_{0.66}Bi_{0.67}Te_6$ showing the highest conductivity with 647 $\Omega^{-1}cm^{-1}$ at room temperature. Apparently as the stoichiometries diverge from ~50:50 Sn/Bi, one notices a loss in conductivity as displayed by $Tl_{8.33}Sn_{1.12}Bi_{0.55}Te_6$ as well as $Tl_{8.67}Sn_{0.50}Bi_{0.83}Te_6$, which has almost 100 fewer $\Omega^{-1}cm^{-1}$ than $Tl_8Sn_2Te_6$ shown as a reference (473 $\Omega^{-1}cm^{-1}$ at room temperature). Power factors for this series therefore range between 2 and 4 $\mu W \cdot cm^{-1}K^{-2}$ at room temperature with higher Bi compounds close to 4 $\mu W \cdot cm^{-1}K^{-2}$. When Tl is further lessened ($Tl_{8.33}Sn_{1.67-y}Bi_yTe_6$), the power factor appears to decrease.

12.3.3.3. Projected Outlook and ZT

Overall, the power factor appears lower with lighter elements. For example, $Tl_9Sn_{1-x}Bi_xTe_6$ displays power factors of ~8 $\mu W \cdot cm^{-1}K^{-2}$, $Tl_{8.67}Sn_{1.33-y}Bi_yTe_6$ shows power factors of ~4 $\mu W \cdot cm^{-1}K^{-2}$, and $Tl_{8.33}Sn_{1.67-y}Bi_yTe_6$ shows values of ~2 $\mu W \cdot cm^{-1}K^{-2}$ so it appears systematic reduction of Tl in these series has a negative impact on the power factor due to a significant reduction in electrical conductivity with lowered values of Tl. In the first study (Figure 12.2), values were between 400 and 800 $\Omega^{-1}cm^{-1}$ and the second study (Figure 12.3) yielded values between 200 and 400 $\Omega^{-1}cm^{-1}$. The significant reduction in electrical conductivity however, leads to the question of what the impact on the thermal conductivity will be: If the added disorder in a case such as $Tl_{8.33}Sn_{1.67-y}Bi_yTe_6$ has a pronounced effect on κ, the power factor loss may be supplemented and ZT may still be reasonable. Unfortunately, mechanical problems with the Anter instrument prevented further measurements from taking place. As such only an "educated guess" can be provided based on the current κ values in the literature and those found in **Chapter 11**. For simplicity's sake, κ_{ph} will be treated as constant across the temperature range, based on literature values – given in $W \cdot m^{-1}K^{-1}$: Tl_4SnTe_3 – 0.29,[237] Tl_9BiTe_6 – 0.25[249] and based on values calculated based on the bottom left of Figure 11.2 via κ - κ_{el}: Tl_9SnTe_6 – 0.27, $Tl_8Sn_2Te_6$ – 0.26, $Tl_{7.8}Sn_{2.2}Te_6$ – 0.32. As the literature value for Tl_4SnTe_3 lies directly in the middle of the two studied in this work ($Tl_{10-x}Sn_xTe_6$), κ_{ph} can be estimated with three values: 0.25, 0.27, and 0.29 $W \cdot m^{-1}K^{-1}$. Through the use of the Wiedemann-Franz law (Equation 1.5), κ_{el} can be estimated with the standard L value. κ is then estimated by adding this value at each T to the three κ_{ph} estimates. With the availability of κ estimates, ZT can be calculated from each of the values.

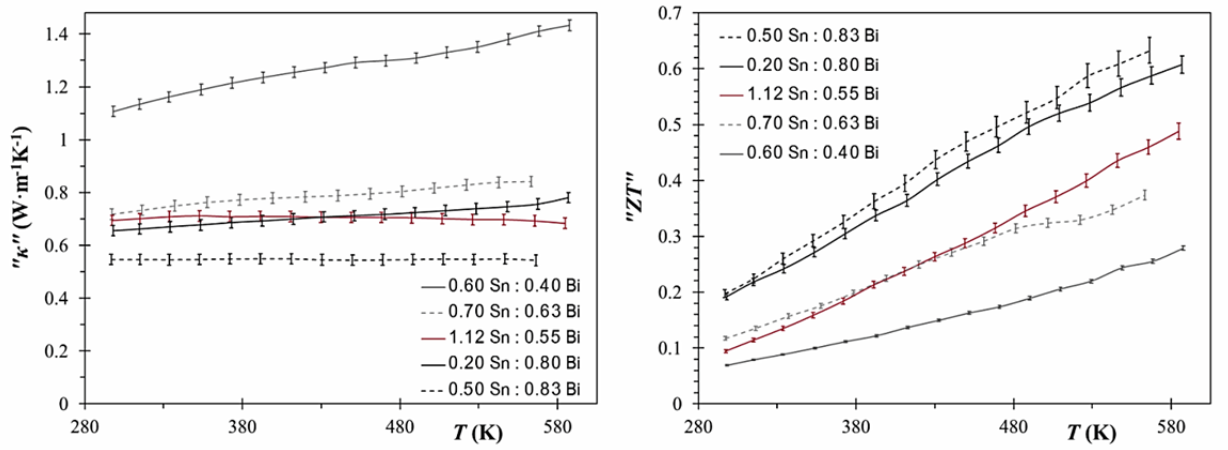

Figure 12.4 Projected thermal conductivity (left) and dimensionless figure of merit (right) for $Tl_{10-x-y}Sn_xBi_yTe_6$.

The projected values of κ depicted as vertical ranged bars above, are in good measure with the other materials – $Tl_8Sn_2Te_6$, for example was measured at ~0.6 $W{\cdot}m^{-1}K^{-1}$ at 372K and Tl_9SnTe_6 measured ~1.5 $W{\cdot}m^{-1}K^{-1}$ at 372 K. With the close values of the available lattice thermal conductivities, the difference between estimated values is only $\pm$0.02 $W{\cdot}m^{-1}K^{-1}$. The calculation of ZT leads to a potential cold-pressed sintered value of 0.6 for $Tl_9Sn_{0.2}Bi_{0.8}Te_6$ and $Tl_{8.67}Sn_{0.50}Bi_{0.83}Te_6$ towards 580 K. This is on the same order of magnitude as $Tl_{7.8}Sn_{2.2}Te_6$ measured in **11.3.3** to reach a maximum value of 0.6 at 617 K.

12.4. Conclusion

Various members of the $Tl_{10-x-y}Sn_xBi_yTe_6$ series were successfully synthesized, analyzed, and their physical properties measured. Rietveld refinements were performed on three pure-phase samples displaying acceptable unit cell parameters, bond distances, and R-values that fall in line with the single crystal data collected for $Tl_{8.66}Sn_{0.67}Bi_{0.67}Te_6$. The near-metallic behaviour of several samples was supported with LMTO calculations which also showed strong potential metallic properties for the hypothetical $Tl_{8.5}Sn_{0.5}Bi_1Te_6$ – which, rationally speaking was also beyond the natural phase range. Though κ measurements are not yet available to the system, reasonable predictions based on literature values of lattice thermal conductivity reveal a strong potential for this series to reach the same magnitude as $Tl_{7.8}Sn_{2.2}Te_6$, if not surpass it. Naturally, hot-pressing of select Bi-rich samples ought to further improve these properties making this series potentially competitive with Tl_9BiTe_6 and other leading materials.

Chapter 13. Modifications of Tl_9SbTe_6 via the addition of Tt^{2+}

13.1. Introduction

Like the preceding chapters, interest in Tl_9SbTe_6 led to the investigation of its thermoelectric properties[232, 250] as well as interest in the subsequent optimization of the properties. Measurements on the Seebeck coefficient at room temperature for Tl_9SbTe_6 was initially reported at 90 $\mu V \cdot K^{-1}$.[250] The ZT was first measured as 0.27 at room temperature.[251] The forthcoming investigations can then be split into two series: Those with Sn-inclusions and those with Pb-inclusions, leading to the $Tl_9Sn_xSb_{1-x}Te_6$ and the $Tl_9Pb_xSb_{1-x}Te_6$ formulae respectively. As with the original Bi-study, one would expect the production of a *p*-type semiconductor with values of *x* approaching values of 0.1 and beyond. As such, improvements to the system should be feasible. With the similarities between Tl_9SbTe_6/Tl_9SnTe_6/Tl_4SnTe_3, the possibility of alloying with mid-range values of *x* could produce different behaviours altogether so studies will involve both large and small values of *x*.

13.2. Experimental Section

13.2.1.1. Synthesis

All reactions were prepared from the elements (Tl: 99.99 %, granules 1-5mm, ALDRICH; Sn: 99.999 %, powder -100 mesh, ALFA AESAR; Pb: 99.9 %, granules 3 mm, ALFA AESAR; Sb: 99.5 %, powder -100 mesh, ALFA AESAR; Te: 99.999 %, ingot, ALDRICH), with total sample masses between 500 mg and 1000 mg for in-lab samples. The systems were again explored by heating the elements their respective stoichiometric molar ratios inside glassy carbon crucibles and evacuated (approx. 10^{-3} mbar) inside silica tubes. The silica tubes were sealed under a hydrogen-oxygen flame, and samples were heated in resistance furnaces to 923 K, followed by slow cooling from 873 to 723 K within five days. Mixed-phases were crushed into powder, resealed and annealed at 723 K for between five and ten days; the melting point of 753 K for Tl_9SbTe_6[252] should ensure a suitable annealing temperature. A wide range of *x* was initially chosen for the series in order to gain an overall understanding of the phase range as well as the properties. Therefore $0.0 \leq x \leq 0.7$ in increments of 0.05 was initially studied followed by increments of 0.025 between $0.0 \leq x \leq 0.2$ for each series.

13.2.1.2. Analysis

Phase identifications were carried out by powder X-ray diffractometry from well-ground products in all cases. Purity could be achieved up to x = 0.6, at which point the binary Tl_5Te_3 phase could be seen in the patterns in addition to an unknown phase. When samples were found to be inhomogeneous, TlTe was again found, often with Tl_5Te_3 or $TlSbTe_2$. Powdered samples were analyzed by means of standardless EDX spectroscopy, leading to quite reasonable results on several polycrystalline samples. The ternary phase for example yielded the following results (at-%): 59.4 Tl, 5.8 Sb, and 34.8 Te. On the samples of nominal compositions $Tl_9Sn_{0.4}Sb_{0.6}Te_6$ and $Tl_9Pb_{0.4}Sb_{0.6}Te_6$ respectively, the following results were obtained(at-%): 58.1 Tl, 2.7 Sn, 4.1 Sb, 35.2 Te; 56.5 Tl, 2.5 Pb, 4.2 Sb, 32.7 Te.

13.2.1.3. Electronic Structure Calculations

Self-consistent tight-binding *first principles* LMTO calculations, as previously discussed were implemented here. Three different models were calculated. In $I4/m$ Tl_9SbTe_6 could be calculated, while two supercells of each Tt^{2+} atom would be calculated in $P4/m$: $Tl_9Sn_{0.5}Sb_{0.5}Te_6$ and $Tl_9Pb_{0.5}Sb_{0.5}Te_6$. All compounds are originally of space group $I4/mcm$. The wavefunctions used in the calculations are as follows: For Tl/Pb *6s*, *6p*, *6d* and *5f*; and for Sn/Sb/Te *5s*, *5p*, and *5d* and *4f*. The eigenvalue problems were solved on the basis of 1728 evenly-dispersed *k* points within the irreproducible wedge of the first Brillouin zone, respectively, selected with an improved tetrahedron method.[203]

13.3. Results and Discussion

13.3.1. Crystal Structure

Since the crystal structure of Tl_9SbTe_6 is already well-known and characterized, no single crystal studies were initiated. However in order to study the change in unit cell parameters and likely differences in atomic sites and occupancy factors, Rietveld refinements were performed on some of the reactions. These were run overnight on phase-pure powdered samples with a model based on the crystallographic data published by Voroshilov *et al.*[253] as it was solved in the higher setting, $I4/mcm$. Due to the presence of three atoms on the *M*(1) site, these parameters could not be freed such that the occupancies were fixed according to the proposed target and the U_{eq} parameters were set to 0.02. The U_{eq} parameters for the other atoms were allowed to refine and were calculated around similar magnitudes to the fixed values. The unit cell data and R-values are displayed in Table 13.1:

Table 13.1 Rietveld refinements for Tl_9SbTe_6-type compounds.

Target Compound	Space Group	a (Å) = b	c (Å)	V (Å^3)	Z	$R_P{}^a \setminus R_B{}^b$
Tl_9SbTe_6[253]	$I4/mcm$	8.847(2)	13.024(5)	1019.38	2	–
$Tl_9Sn_{0.1}Sb_{0.9}Te_6$	"	8.842(4)	13.023(5)	1018.1(12)	"	4.23 \ 4.42
$Tl_9Sn_{0.5}Sb_{0.5}Te_6$	"	8.8420(33)	12.919(5)	1010.0(11)	"	4.66 \ 5.14
$Tl_9Pb_{0.5}Sb_{0.5}Te_6$	"	8.8793(32)	12.973(5)	1022.8(11)	"	5.03 \ 5.27

$^a R_P = \Sigma|y_o - y_c| / \Sigma|y_o|$ $^b R_B = \Sigma|I_o - I_c| / \Sigma|I_o|$

The R-values produced in the Rietveld refinement are excellent and show that the patterns are a good fit with the reference material. All peaks are accounted for in the pattern with near-identical intensities. Likewise, the unit cell volumes show acceptable shifts based on the elements input. The unit cells of Sn-compounds show a slight decrease with respect to the ternary, and the Pb-based sample shows a slight increase in volume. These results are in good agreement with the intended outcome of the reactions.

13.3.2. Electronic Structure Calculations

Due to the lack of Te–Te bonds in the system, the Te atoms can be considered Te^{2-}, while the other atoms can be treated as the typical Tl^+, Pb^{2+}/Sn^{2+} and Sb^{3+}. The calculation of Tl_9SbTe_6 is in good agreement with the literature calculations mentioned in the introductory chapter with respect to shape and elemental contributions despite the slightly different band gap size from their accounting for SOC in the literature cases.

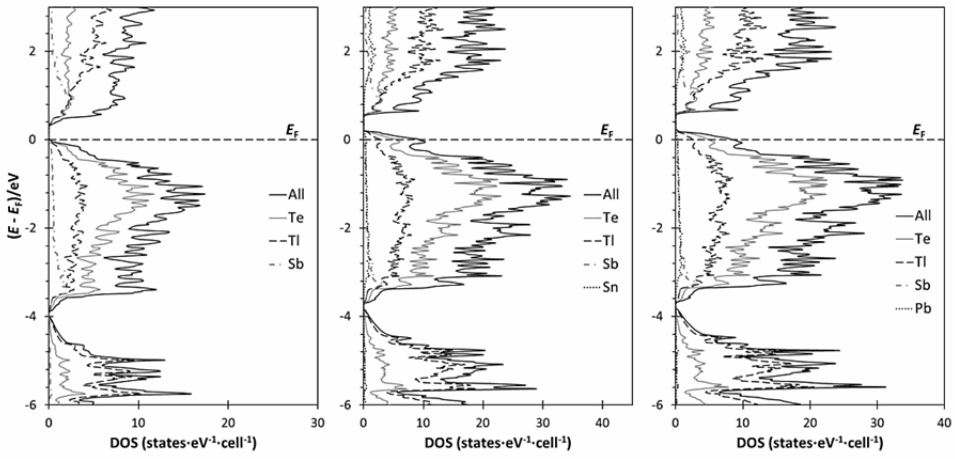

Figure 13.1 *DOS* calculations for Tl_9SbTe_6 (left), $Tl_9Sn_{0.5}Sb_{0.5}Te_6$ (centre), $Tl_9Pb_{0.5}Sb_{0.5}Te_6$ (right).

With the loss of "half" an electron from the chemical formula as the Tt^{2+} atoms are included, one can see that the calculations result in a *p*-type semiconductor with minor vacancies (~0.2 eV) in the valence band. This particular case is analogous to the $Tl_{9.5}La_{0.5}Te_6$ previously studied[236] which did experimentally behave as a heavily-doped p-type semiconductor with room temperature values of S = ~20 $\mu V \cdot K^{-1}$ and σ = ~1500 $\Omega^{-1}cm^{-1}$. The empty *Tt-p* orbitals are most pronounced above 1 eV in the conduction band, while their *Tt-s* orbitals contribute most near -2 eV as expected with *M*(1) elements.

13.3.3. Physical Property Measurements

Physical properties were originally measured as with the $Tl_{10-x-y}Sn_xBi_yTe_6$ study having cold-pressed pellets (having density of approximately 85 %) being sealed in evacuated Si tubes and annealed to 653 K for 12 hours. In order to produce ZT values, this was followed by subsequent ZEM and κ measurements.

13.3.3.1. High-Temperature Physical Properties of $Tl_9Tt_{1-x}Sb_xTe_6$

The initial data, displayed in the form of σ in Figure 13.2 below, shows Sn-data on the left and Pb-data on the right in order of decreasing magnitudes. While the overall gentle decrease in electrical conductivity slope is as expected for this family of compounds, there is no apparent trend is this case. Likewise the observed Seebeck coefficients (not shown) gradually increase with increasing temperature with samples in all cases (Sn and Pb) having room temperature values between 40 and 80 $\mu V \cdot K^{-1}$ which got as high as 141 $\mu V \cdot K^{-1}$ at 573 K for $Tl_9Sn_{0.15}Sb_{0.85}Te_6$ and 118 $\mu V \cdot K^{-1}$ at 573 K for $Tl_9Pb_{0.025}Sb_{0.975}Te_6$.

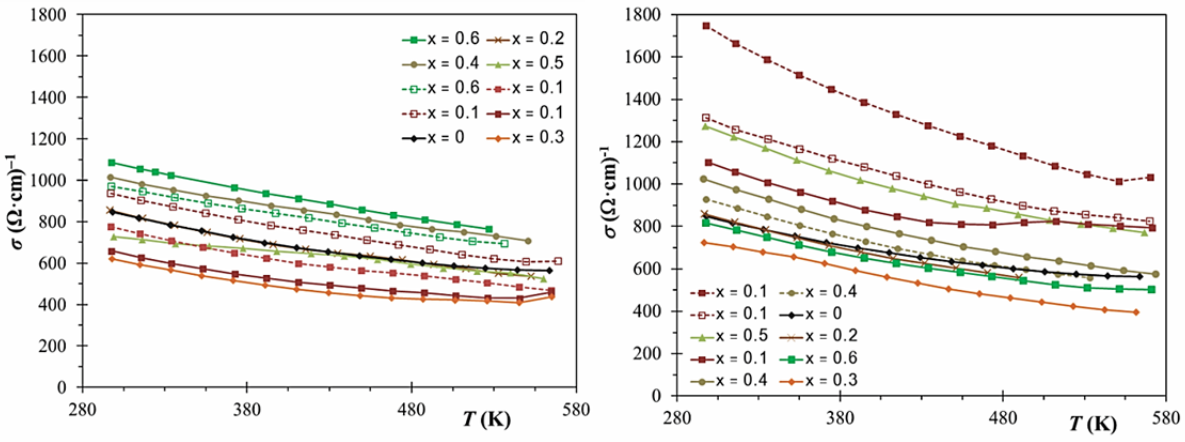

Figure 13.2 Original σ measurements for $Tl_9Tt_xSb_{1-x}Te_6$: $Tl_9Sn_xSb_{1-x}Te_6$ (left) and $Tl_9Pb_xSb_{1-x}Te_6$ (right)

It is apparent through observation of repeat measurements on the same pellet (dashed line) and repeat measurements on a different pellet from the same reaction (hollow marker) that the reproducibility is also very poor with these reactions. In either case, examination of the various magnitudes does not

make an observable trend despite the systematic change in electron-concentration from alteration of compound stoichiometry. Likewise the XRD patterns of pellets before and after measurements appear to be single phase. Close examination of certain pellets under an optical microscope after the measurement however, revealed the typically-expected smooth metallic lustre of these types of compounds was no longer present; upon their initial pressing, pellets appeared as a smooth sheet of graphite might appear though this observation was of a very dull pellet showing bumps and blisters on the surface. The pellets, unlike their Bi analogs would also have a tendency to deform under heat and pressure - a feature neither desirable for reproducibility or practical applications.

13.3.3.2. Thermal Analysis of Tl_9SbTe_6

With the reproducibility problems above, a fresh reaction of Tl_9SbTe_6 was synthesized pure phase for the intention of thermal analysis. DSC measurements were run from room temperature to 673 K with the slower measurement rate of 2 °/min (as opposed to the typical 10 °/min used) in attempt to observe any abnormalities to the compound with increasing temperature.

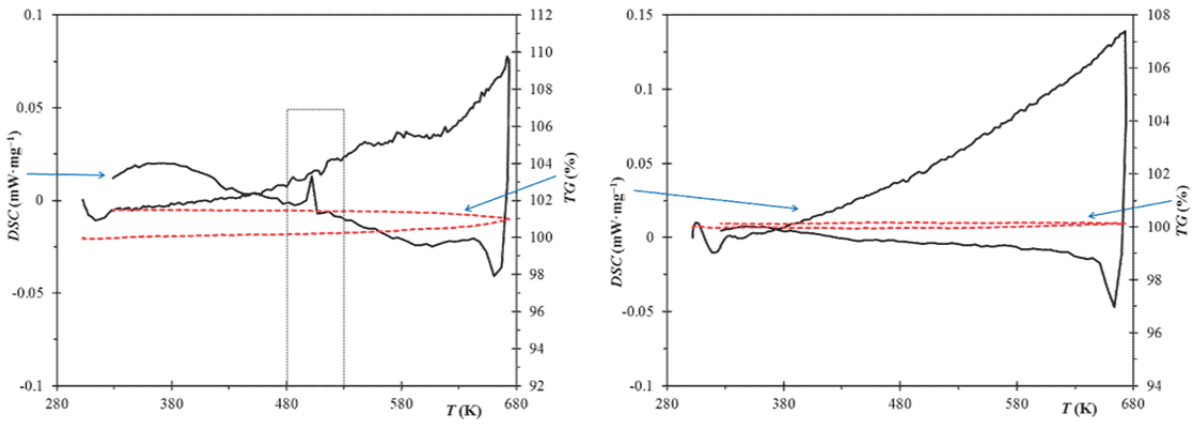

Figure 13.3 Thermal analysis of Tl_9SbTe_6 and Tl_9BiTe_6 for comparison.

As is apparent from the DSC of Tl_9SbTe_6, there is a large exothermic peak at 500 K which implies the presence of a solid-solid phase transition that is either negligible or not found in the bismuth analog (Figure 13.3 (right)). The change appears fully reversible, as the peak is found in both heating and cooling cycles (it appears in the heating cycle at ¼ intensity at 510 K) with no obvious change in mass (see TG curve above). It should be noted that in most studies involving Tl_9BiTe_6-type compounds in the Kleinke group, a very small peak was observed in DSC studies that could not be identified. For example, $Tl_8Sn_{0.5}Bi_{1.5}Te_6$ displays an exothermic peak at 533 K less than 10 % intensity to that of its melting peak, and Tl_9BiTe_6 shows a minor fluctuation around 593 K with similar oddities occurring in certain Tl_9LaTe_6 experiments as well. A solid-solid phase transition is a reasonable hypothesis as it has previously been

reported that another ternary in this system, $TlSbTe_2$, also undergoes a phase transition – albeit at low temperatures.[254] Several unsuccessful attempts involving high-temperature XRD were also endeavoured to further pursue this issue, but due to sample oxidation and additional noise from the furnace, no reliable data could be produced. Quenching experiments in attempt to freeze the sample's state above this temperature are currently underway to learn if there is an identifiable high-temperature phase for the Sb compounds.

13.3.3.3. Low-Temperature Physical Properties of $Tl_9Tt_xSb_{1-x}Te_6$

Due to the phase transition's effect on the pellet quality and stability, samples were required to be reproduced and annealed up to 473 K instead. Unfortunately, this lowers the functional temperature for this material, therefore projecting that it may not be as useful as Tl_9BiTe_6 due to the temperature ranges; lower annealing temperature also drops the magnitude of σ. Take for example $Tl_9Sn_{0.5}Sb_{0.5}Te_6$ which initially showed a value of 727 $\Omega^{-1}cm^{-1}$, dropping to 575 $\Omega^{-1}cm^{-1}$ at room temperature. Likewise, measurements on Tl_9SbTe_6 initially showed 874 $\Omega^{-1}cm^{-1}$ to 429 $\Omega^{-1}cm^{-1}$ at room temperature –a loss of 50 %. The systems however, show a more realistic trend in this lower temperature range, as depicted in Figure 13.4. With both of the measured series, one observes the generic increase of S with increasing temperature as expected for this family of compounds. All samples now show an overall increase in S with decreasing *x* values, from 42 $\mu V \cdot K^{-1}$ at room temperature with $Tl_9Pb_{0.5}Sb_{0.5}Te_6$ to 86 $\mu V \cdot K^{-1}$ at room temperature with $Tl_9Sn_{0.1}Sb_{0.9}Te_6$. It can be seen in the image that both series fall between the Seebeck values of the respective ternaries. Though values can be slightly more erratic due to the low annealing temperatures, this case demonstrates the system's ability to form the expected trend through modifications in *x*.

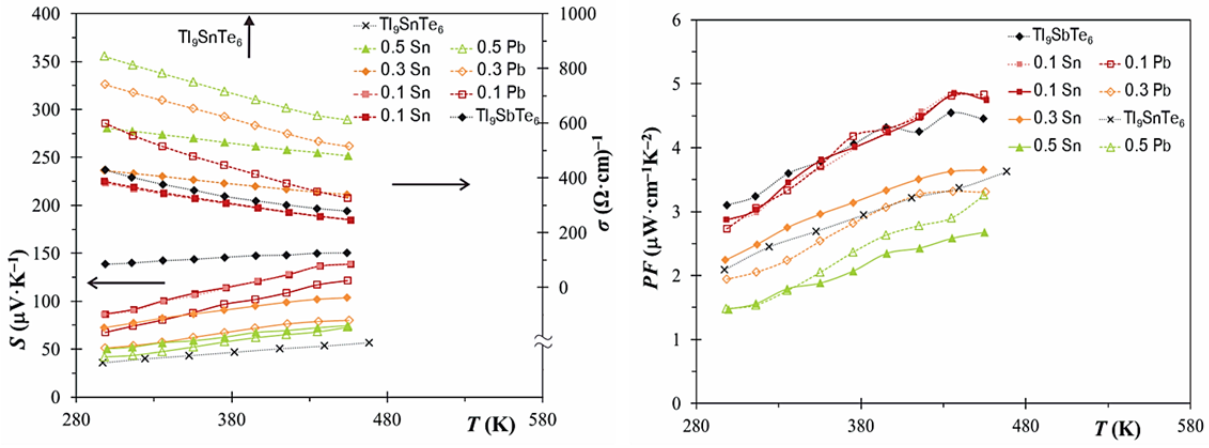

Figure 13.4 Low-temperature ZEM measurements for $Tl_9Tt_xSb_{1-x}Te_6$: Seebeck coefficient and electrical conductivity (left) and power factor (right)

The electrical conductivity values again show a linear decrease with increasing temperature as predicted by the LMTO calculations. Both the Sn- and Pb-based series show a general increase with *x*, opposite to the S trend. The reproducibility is now quite good as can be seen with the dark red and pink variations of $Tl_9Sn_{0.1}Sb_{0.9}Te_6$. Looking at the power factor results on the right of Figure 13.4 show a general decrease in magnitude for both series from the original ternary to 1.5 $\mu W \cdot cm^{-1}K^{-2}$ at room temperature for both *x* = 0.5 samples. Though it would be expected that Tl_9SnTe_6 sit around 1 $\mu W \cdot cm^{-1}K^{-2}$ at room temperature, the greater annealing temperatures increase its magnitude with respect to the others in this diagram.

Thermal conductivity measurements were taken on this system, but were taken with the high-temperature conditions mentioned in the first half of the physical properties discussion. Though these pellets were carefully examined for any blisters and loss of lustre, the measurements were still found to be somewhat erratic. The magnitudes of κ measurements were still around the 1 $W \cdot m^{-1}K^{-1}$ region which is in agreement with the previous chapters in this section and the reproducibility was more successful than that of the high-temperature σ measurements. Therefore useful information can still be extracted from the plots (Figure 13.5 (left)) despite the marginal breaking of the expected trend in some cases. With $Tl_9Pb_xSb_{1-x}Te_6$, four measurements were useful (in addition to that of the reference Tl_9SbTe_6 values) all of which were between 0.95 (*x* = 0.3) and 1.21 (*x* = 0.10) $W \cdot m^{-1}K^{-1}$ and all displayed a reasonably flat κ curve that in essence plateaus with increasing temperature. $Tl_9Sn_xSb_{1-x}Te_6$ yielded seven realistic measurements over a broader scale – both in stoichiometry and magnitude – than $Tl_9Pb_xSb_{1-x}Te_6$. These ranged from 1.03 (*x* = 0) to 0.43 (*x* = 0.6) $W \cdot m^{-1}K^{-1}$. Interestingly enough, this implies, like the κ data shown in Figure 11.2, that larger quantities of Sn (as opposed to Tl or Pb) greatly reduce the overall thermal conductivity. This data largely points towards an overall reduction of κ with decreasing *x*.

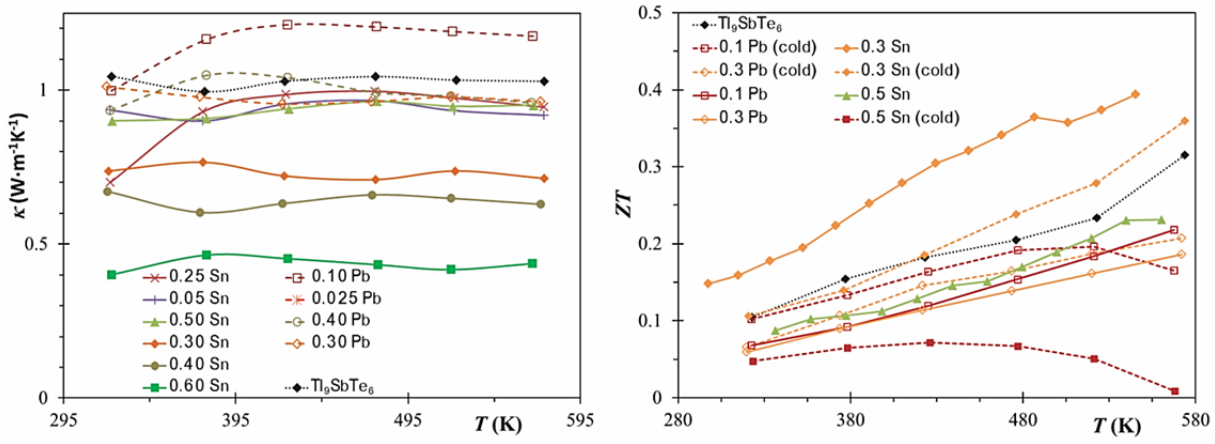

Figure 13.5 Selected preliminary κ (left) and ZT (right) for $Tl_9Tt_xSb_{1-x}Te_6$ in order of decreasing magnitude.

ZT values can be calculated by combining the low-temperature power factor results with the preliminary κ data to produce the dashed curves shown on the right of Figure 13.5. For comparative purposes, the higher temperature results were also added to the figure (solid lines). In this particular study, the highest ZT factor belongs to $Tl_9Sn_{0.3}Sb_{0.7}Te_6$, which reaches ~0.35 or ~0.40 near 560 K depending on the annealing attempt. With the results being more erratic in this study, it is not prudent to assign a trend but comparatively, $Tl_9Sn_{1-x}Bi_xTe_6$ is almost twice as large at similar temperatures.

13.4. Conclusion

Various members of the $Tl_9Sn_xSb_{1-x}Te_6$ and $Tl_9Pb_xSb_{1-x}Te_6$ series were successfully synthesized and analyzed, structural parameters were predicted with Rietveld refinements, electronic structure calculations were provided, and their physical properties measured. Despite the existence of an unknown phase transition at 500 K, the $Tl_9Sn_xSb_{1-x}Te_6$ and $Tl_9Pb_xSb_{1-x}Te_6$ series were able to be characterized, albeit to lower temperatures than other Tl_5Te_3-type compounds. Of these compounds, $Tl_9Sn_{0.3}Sb_{0.7}Te_6$ shows the best results, achieving a ZT of ~0.35 at 560 K with cold-pressed and sintered pellets. Pb-based samples generally had lower ZT values due to the fact that the initial κ data collected for them was higher than the corresponding Sn data. Though hot-pressing would be tempting, it is likely that their instability at higher temperatures as well as the instrument's great pressure would lead to further problems. Though additional studies regarding the material and its mysterious transition are in pursuit, it is likely that this material will not be appealing for thermoelectric applications. Comparative phase range studies for $Tl_{10-x}Sb_xTe_6$ and $Tl_{10-x}Bi_xTe_6$ have been undertaken in lieu of these results but may help to further explain the oddity and why it is not observed with the heavier Bi atom. Studies on the $Tl_9Pb_xBi_{1-x}Te_6$ system have also ensued to make the phase-property studies in this section even more complete.

Section V – Ba Late-Transition-Metal Chalcogenides

Discovery of new crystal structures and corresponding physical properties in the Ba-Cg-Q system.

Chapter 14. Introduction to Barium Coinage-Metal Tellurides

Chalcogenides and polychalcogenides attract the attention of solid state chemists, researchers, engineers, and materials scientists alike. Their practical semiconducting-based applications including electronics,[255] rechargeable batteries,[256] data storage,[257-259] and thermoelectric energy conversion[16, 69, 78] give chalcogenides a functional place in today's society. In addition to doping strategies previously employed in this thesis, it is prudent to discover new types of compounds for potential thermoelectric studies. As mentioned in Section I, it is important to choose compounds with heavy elements, a complicated structure, and semiconducting properties. Barium and tellurium are both heavy elements and as will be discussed, Te can show unique bonding properties if it is forced to exhibit Te–Te (or Te–*Q*) bonds. With the large size and ionic nature of Ba, contributing few-to-no bonds, as well as the known d^{10}-d^{10} interactions found with the group [11] (*Cg*) elements – namely Cu/Ag – a system involving Ba-*Cg*-*Q* is ripe with potential for new thermoelectric materials.

The Zintl concept, briefly introduced in **1.3**, explores the ability of atoms near the Zintl line in the periodic table to form homonuclear bonds to fulfill the octet rule, that could not otherwise be satisfied with the layout of the atoms.[50] The typical Zintl-Klemm concept deals with binary phase AZ_n where *A* = [1],[2] and *Z* = [*Tr*],[*Tt*],[*Pn*],[*Q*] such that the Alkali and Alkaline Earth metals donate their valence electrons to a late main group element of more moderate electronegativity; strongly electronegative elements such as Cl would not apply to the Zintl concept. A good example of a Zintl phase is the binary Cs_2Te_5 where the usual valence rules would yield an unbalanced $2(Cs^+) + 5(Te^{2-}) = 8-$. Nature instead forms a continuous covalent chain of (Te_5^{2-}) planes (analogous to square planar PtH_4) in alternating high plane and low plane order, where each Te-centered planar square completes its octet with covalent Te–Te bonds and the remaining two Cs electrons.[50] This concept allows for the formation of numerous unique *Z*–*Z* covalent bonds, as demonstrated in **Figure 14.1** where two examples on the left demonstrate selenium's isolated segments – respectiviely dumbbell and bent Q_3^{2-} – and two examples of tellurium square planar chains (infinite length) in both *cis*- and *trans*- formations.[260]

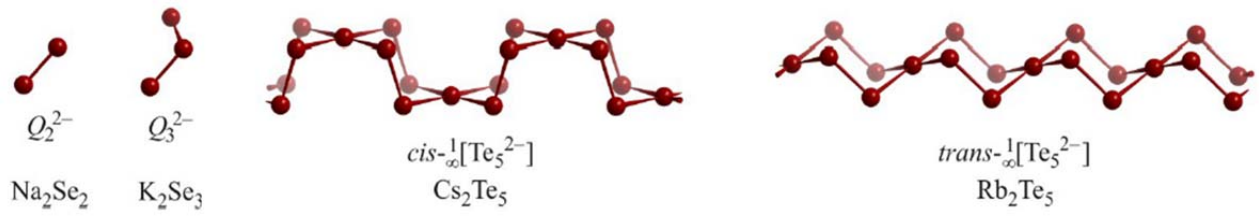

Figure 14.1 Various *Q*–*Q* bonds in Zintl compounds.[260]

Obviously, compounds possessing the extra feature of *Z*–*Z* bonds strike an interest in the thermoelectric field due to the added structural complexity and the ability for researchers to vary *Z* from compound-to-compound, tuning the semiconducting band structure to their desired shape and gap size. As discussed in **Chapter 1.2**, structural complexity is a necessary component of low thermal conductivity, κ; discussed in **Chapter 2.3**, is the variation of charge carriers (n) and its effects on the band gap and subsequently, the thermoelectric properties. Together, they form support for the thermoelectric promise of these polychalcogenide structures.

The unique bonding of polychalcogenides led us to investigate a series of materials based on stoichiometric variations of Ba(Cu,Ag)(Se,Te) following the discovery of $BaCu_2Te_2$[261] and the reports that followed regarding its thermoelectric properties.[13, 262, 263] Soon thereafter the compound $A_2BaCu_8Te_{10}$ (*A* = K, Rb, Cs) was discovered by Patschke *et al.*[264] Investigation into this family of compounds led to the discovery of several new ternary and quaternary compounds, the first of which having the formula $Ba_3Cu_{14-x}Te_{12}$. This structure, displayed in **Figure 14.2 (a)**, features Te_2^{2-} dumbbells and $CuTe_4$ tetrahedral components likely leading to its low thermal conductivity values on the order of 1.08 $W \cdot m^{-1}K^{-1}$ at 300 K.[265] The structures discovered after the first were $Ba_{6.76}Cu_{2.42}Te_{14}$[69] (**Figure 14.2 (b)**) and $Ba_2Ag_4Se_5$[265] (**Figure 14.2 (c)**). These feature bent Te_3^{2-}/$CuTe_4$-tetrahedra and $Ag_4Se_5^{4-}$ layers respectively.

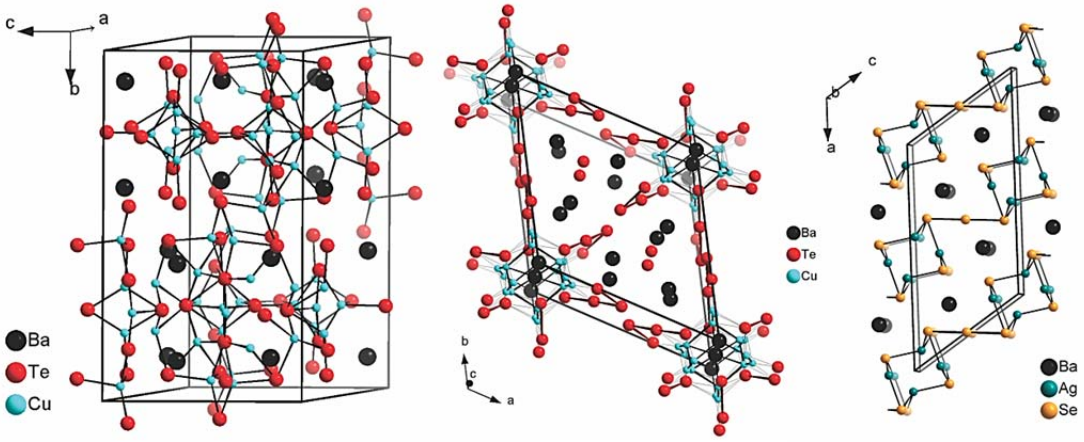

Figure 14.2 Unit cells of (a) $Ba_3Cu_{14-x}Te_{12}$[266] (b) $Ba_{6.76}Cu_{2.42}Te_{14}$[267] (c) $Ba_2Ag_4Se_5$[265]

This intriguing family of polychalcogenides became a great interest of the Kleinke group, with further discoveries expanding to include: $Ba_2Cu_{3.3}Te_5$[268] – chains of $CuTe_4$ tetrahedra, with Cu and Te linear chains; $Ba_2Cu_{6-x}STe_4$[269] – Cu–Te chains bridged by S atoms; $BaCu_{6-x}(S,Se)Te_6$[270] – cubic Cu-clusters centered by *Q*, with Te_2^{2-} dumbbells; and $BaAg_{2-x}Te_2$[271] – a 3-D network of $AgTe_4$ tetrahedra, with zigzag Ag–Ag chains.[271]

Our ongoing investigation into barium copper chalcogenides and barium silver chalcogenides were originally motivated by thermoelectric energy conversion[13, 262, 263] as well as the unique Q–Q bonds discussed. Examples include $HfTe_5$[272] and the phase-change material $Ag_{10}Te_4Br_3$.[273] Earlier reports about thermoelectric properties of such materials were on the tellurides $BaCu_2Te_2$[261] and $A_2BaCu_8Te_{10}$ (*A* = K, Rb, Cs).[264] The aforementioned newly discovered materials mostly form a new structure type with various Cu/Ag–Cu/Ag d^{10}–d^{10} interactions. Our first example of a new structure type in this family with this feature was $Ba_3Cu_2Sn_3Se_{10}$ with a [3+1] coordination of the Cu atoms and a Cu–Cu bond of 2.65 Å,[274] followed by those mentioned above in **Figure 14.2**.

On further pursuit of this system, we uncovered the chalcogenides that would only form upon mixing two different *Q* atoms on the same site – a concept known as *differential fractional site occupancy* (DFSO), further mentioned in **15.1**. Such compounds as $Ba_2Cu_{6-x}STe_4$ and $Ba_2Cu_{6-x}Se_yTe_{5-y}$,[269] $BaCu_{6-x}S_{1-y}Te_{6+y}$ and $BaCu_{6-x}Se_{1-y}Te_{6+y}$,[270] and $Ba_2Cu_{4-x}Se_yTe_{5-y}$,[268] only form when using two different chalcogen atoms (the ternary telluride $Ba_2Cu_{4-x}Te_5$ adopts a structure type different to $Ba_2Cu_{4-x}Se_yTe_{5-y}$). This further motivates one to not only experiment with tellurides in this family, but expand into the sulfide-tellurides and selenide-tellurides. Therein, many of the compounds discovered were Cu- or Ag-deficient and therefore *p*-type semiconductors featuring low thermal conductivity values.

A convenient summary of some of the recently discovered Ba-*Cg*-*Q* materials is summarized in a recent review[275] by Mayasree *et al.* This table summarizes the motifs of *Cg*–*Cg* and *Q*–*Q* bonding, and measured physical properties of known compounds in this system:

Table 14.1 Known Ba-*Cg*-*Q* compounds:[275] Bonding motifs and physical properties[a].

Formula	*Q* unit	Cu/Ag motifs	E_{gap} [b] (eV)	σ ($\Omega^{-1}cm^{-1}$)	S ($\mu V \cdot K^{-1}$)
$Ba_3Cu_{13.9}Te_{12}$[266]	Te_2^{2-} pairs	3-D network	0.1	190	+30
$BaCu_{5.7}Se_{0.6}Te_{6.4}$[270]	Te_2^{2-} pairs	(deficient) cubes	0.05	20	+100
$Ba_{6.76}Cu_{2.42}Te_{14}$[267]	bent Te_3^{2-}	-	1.0	$7 \cdot 10^{-5}$	-
$Ba_2CuAg_3Se_5$[265]	linear Se_3^{4-}	1-D ribbon	0.9	$3 \cdot 10^{-5}$	-
$Ba_2Cu_{3.3}Te_5$[268]	linear Te chain	cis/trans chain	-	1.5	+440
$Ba_2Cu_{3.3}SeTe_4$[268]	linear Te chain	cis/trans chain	-	0.2	+310
$Ba_3Cu_{14.4}Se_{8.5}Te_{2.5}$[276]	-	3-D network	0.02	125	+50
$Ba_3Cu_{16.6}S_4Te_{7.5}$[277]	-	3-D network	-	310	+40
$Ba_2Cu_{5.53}SeTe_4$[269]	-	1-D ribbon	0.05	7	+35
$BaCu_2Te_2$[261]	-	zigzag chain	0.6	125	+90
$BaCuAgTe_2$[271]	-	zigzag chain		2.5	+325
$BaAg_2Te_2$[271]	-	zigzag chain	0.5	0.1	+995

[a] Obtained around 300 K on pressed pellets of microcrystalline samples.

[b] Calculated for the electron-precise (not Cu-deficient) model.

These materials are able to be created from the elements or from binaries such as BaTe – depending on the availability of materials. Sample masses (Section V) were generally kept between 0.5 g and 0.8 g due to the exploratory nature of the experiments. The elements were loaded into silica tubes in stoichiometric ratios and in the case of Ba, the oxidized surface material was scraped off the blocks. Once synthesized, the compounds were stable in air and could be analyzed via XRD, though many of the patterns were quite complicated due to the presence of numerous peaks. Crystals were generally simple to grow by slow-cooling around 873 K, which was usually preceded by a 1073 K temperature for melting and homogeneity. In all cases, the powders were fine and black yielding block-like crystals.

Chapter 15. $Ba_3Cu_{17-x}(Se,Te)_{11}$

15.1. Introduction

Currently we are expanding the chalcogenides under investigation by using two different chalcogen atoms, e.g. selenium and tellurium. Thereby we are applying the concept of anionic DFSO materials, which led to the discovery of several new materials in this decade. Originally, the concept of differential fractional site occupancies, DFSO, was utilized to create new structure types by mixing similar transition metal atoms, e.g. niobium and tantalum, on one crystallographic site.[278, 279] The DFSO concept thus led to the formation of the new materials $Nb_{1.72}Ta_{3.28}S_2$,[280] $Nb_{0.95}Ta_{1.05}S$,[281] $Nb_{4.92}Ta_{6.08}S_4$[282] and $Nb_{6.74}Ta_{5.26}S_4$.[283] This concept was then successfully expanded to include mixtures on the anionic sites.[284, 285] Recent examples of selenide-tellurides that exist only when both Se and Te are incorporated include $Ta_{15}Si_2Se_yTe_{10-y}$[286] and *Ln*SeTe$_2$ with *Ln* = lanthanoid.[287] Partial replacement of Te with Se in tellurides[288] or vice versa, Se with Te in selenides,[289] may have a profound impact on the physical properties. Herein reports on the first barium copper selenide-tellurides,[276] which are stabilized by – and evidently requires – mixed Se/Te occupancies.

15.2. Experimental Section

15.2.1.1. Synthesis

All reactions commenced from the elements (Ba: 99 % nominal purity, pieces, Aldrich; Cu: 99.5 %, powder -150 mesh; Alfa Aesar; Se: 99.99 %, pellets < 4 mm, Aldrich; Te: 99.8 %, powder -200 mesh, Aldrich), with sample masses of approximately 600 mg. Reactions were prepared per the usual method in 3.1. The tubes were heated in a resistance furnace at 1023 K for twelve hours. Thereafter, the furnace was slowly cooled down to 723 K over a period of 200 hours to allow for crystallization. Lastly, the furnace was switched off prompting fast cooling.

The black title compound was first encountered in a reaction with the Ba : Cu : Se : Te ratio of 2 : 3 : 2 : 1, and identified as $Ba_3Cu_{14.4}Se_{8.6}Te_{2.4}$ via the single crystal structure determination described below. Since its structure contained Cu deficient sites and mixed Se/Te occupancies, several reactions were loaded to analyze the phase range of $Ba_3Cu_{17-x}Se_{11-y}Te_y$, with x = 0, 0.5, 1.0, 1.6, 2.0, 2.5, 2.7, 3 and y = 0, 1, 2, 2.5, 3, 4, 5, 6.

All samples were analyzed by means of powder X-ray diffraction, utilizing the INEL diffractometer with Cu-$K_{\alpha 1}$ radiation. Apparently phase pure samples were obtained only with $2 \leq x \leq 2.7$ and $1 \leq y \leq 3$. In the other cases, the identified side products were mostly Cu chalcogenides. A DSC measurement (**5.3**) revealed the melting point of $Ba_3Cu_{14.4}Se_{8.5}Te_{3.5}$ to be around 968 K.

15.2.1.2. Analysis

To further prove in principle the existence of a phase width, as well as the absence of heteroelements such as silicon stemming from the reaction container, several samples of different starting compositions were analyzed via EDX (**6.2**). No heteroelements were detected in any case. While the Cu content did not change significantly from one sample to another, the Se:Te ratio of different samples varied from approximately 14 : 1 to 3 : 1. This corresponds to $0.8 < y < 3.7$ in $Ba_3Cu_{17-x}Se_{11-y}Te_y$, which is comparable to the range of y deduced from the X-ray powder diagrams, $1 \leq y \leq 3$. Although the EDX analysis is known to be only semi-quantitative, this large range indicates a significant phase width.

15.2.1.3. Structure Determination

The first X-ray single crystal structure study (I) was performed on a plate-like single crystal of the reaction with the starting ratio of 2 Ba : 3 Cu : 2 Se : 1 Te. The Bruker diffractometer (**4.2**) was used for the data collection, performed by scans of 0.3° in ω in two groups of 606 frames (each with an exposure time of 60 seconds) at $\phi = 0°$ and 90°. The data were corrected for Lorentz and polarization effects. Absorption corrections were based on fitting a function to the empirical transmission surface as sampled by multiple equivalent measurements using SADABS incorporated into the package SAINT.[128]

The structure solution and refinements were carried out with the SHELXTL program package.[130] The lattice parameters indicated rhombohedral symmetry. No systematic absences were identified, leaving $R\bar{3}m$ as the space group of highest symmetry. Using the "Direct Methods" of SHELXS gave 12 atomic sites, to which one Ba, two Te, three Se and six Cu atoms were assigned based on their interatomic distances and relative heights. Subsequent refinements revealed large thermal expansion parameters in case of one Te and two Cu sites, pointing towards Se/Te mixtures and Cu deficiencies, respectively. As a consequence, the occupancies of all Cu sites were refined, yielding occupancies between 0.55 and 0.96. Similarly, all chalcogen sites (*Q*) were refined as being mixed albeit fully occupied by Se and Te, allowing the Se:Te ratio to vary freely. Of the five *Q* sites, one was occupied solely by Te (i.e. within its standard deviation of 2 %), denoted Te1, two by Se (Se3 and Se5), one (*Q*2)

was clearly mixed occupied (54 % Se, 46 % Te), and the fifth (*Q*4) appeared to be a Se site with a small amount of Te, namely 7 %. In the final refinement, Te1 was fixed as a Te site and Se3 and Se5 as Se sites. This refinement yielded the formula of $Ba_3Cu_{14.4(2)}Se_{8.6(1)}Te_{2.4}$. To investigate the possibility of additional long range Se/Te or Cu ordering, additional refinements were performed at lower symmetry in accord with the allowed space groups, i.e. $R3m$, $R32$, and $R\bar{3}$. Because none of the latter models constituted an improvement in the residual values or showed tendency to additional ordering, the space group of highest symmetry, $R\bar{3}m$, was selected as the final model.

To prove the existence of a phase range, three more crystals were analyzed using the Smart APEX CCD diffractometer. Their nominal compositions were "$Ba_3Cu_{15}Se_7Te_4$" (II), "$Ba_3Cu_{14.5}Se_8Te_3$" (III) and "$Ba_3Cu_{15}Se_{10}Te$" (IV), i.e. the first more Se-poor and the last more Se-rich. In case II, the formula was refined to $Ba_3Cu_{15.0(1)}Se_{7.75(6)}Te_{3.25}$, with more Te on the *Q*2 site (74 %) and comparable Cu occupancies between 56 % and 96 %. Case II has the highest Te content, and thus the largest unit cell volume of 3665.8(2) Å^3, which constitutes an increase of 1.3 % from I. Case III is intermediate in Te content with *V* = 3629.9(3) Å^3, the refined formula being $Ba_3Cu_{14.4(2)}Se_{8.30(8)}Te_{2.70}$. In case IV, the crystal quality was not sufficient to refine the occupancies, but the 3.1 % decrease in the unit cell volume from 3617.8(3) Å^3 (I) to 3504.8(2) Å^3 (IV) implies a significantly higher Se content. The crystallographic data are summarized in Table B.1, and the atomic parameters including the occupancy factors can be found in the appendices Table B.2.

15.2.1.4. Ion Exchange Reactions

Motivated by the three-dimensional network of deficient Cu atom sites, we attempted to replace part of the Cu atoms with Ag at room temperature. Finely crushed microcrystalline samples of nominal composition $Ba_3Cu_{14.4}Se_{8.5}Te_{2.5}$ and $Ba_3Cu_{15}Se_{10}Te$ were placed in glass vials in respective masses of 45 mg and 40 mg. To each vial, approximately ten drops of 2N $AgNO_3$ solution were added via a glass pipette. The vials were capped and placed in a cool, dark enclosure for approximately 2 – 3 weeks, while the vials were lightly stirred on a day-to-day basis. The mixtures began to turn blue after a few hours, indicating the presence of Cu^{2+} ions in the solutions. The chalcogenides did not dissolve into the solution. Afterwards, the powders were filtered and dried in an evaporating dish overnight. EDX analyses revealed significant presence of Ag in the crystals of both samples, of about 7-10 % of the Cu content. Also, the powder diagrams revealed a slight shift towards smaller angles, indicative of a unit cell increase caused by partial substitution of small Cu atoms by larger Ag atoms. An additional single

crystal structure study of the Se-rich sample revealed a volume increase of 2 % (from a = 12.0096(3) Å, c = 28.059(2) Å, V = 3504.8(2) Å^3 to a = 12.0952(2) Å, c = 28.2032(9) Å, V = 3573.2(1) Å^3).

15.2.1.5. Electronic Structure Calculations

As discussed in 6.4, the LMTO method was utilized. The following wavefunctions were used: For Ba *6s*, *6p* (downfolded[202]), *5d* and *4f*; for Cu *4s*, *4p*, and *3d*, for Se *4s*, *4p*, and *4d* (downfolded) and for Te *5s*, *5p*, and *5d* and *4f* (the latter two downfolded). The eigenvalue problem was solved on the basis of 126 *k* points chosen with an improved tetrahedron method.[203] Crystal orbital Hamilton populations[96] were calculated to gain insight into the strength of the Cu–Cu interactions.

The structural parameters were taken from the refinement on $Ba_3Cu_{15.0}Se_{7.75}Te_{3.25}$. The Cu sites with occupancies above 87 % were treated as fully occupied, and one of the two Cu5 (refined occupancy: 56 %) and one of the two Cu6 sites (67 %) per primitive cell was removed. The two mixed Se/Te sites were treated as follows: The six *Q*1 atoms per primitive cell with 74 % Te as four Te and two Se, and *Q*4 with 96 % Se as a Se site. As a result, the model has the formula $Ba_3Cu_{16}Se_8Te_3$ in space group Cm.

15.2.1.6. Physical Property Measurements

A cold-pressed bar of the dimensions 6×1×1 mm^3 of the sample $Ba_3Cu_{14.4}Se_{8.5}Te_{2.5}$ was used for Seebeck coefficient (S) and electrical conductivity (σ) measurements, after applying silver paint (Ted Pella) to create the electric contacts. S was measured under dynamic vacuum in the temperature range between 300 K and 550 K as in 5.4. The specific electrical conductivity (σ) was determined between 320 K and 180 K as in 5.5. The achieved density was around 80 % of the theoretical maximum determined via the single crystal structure study.

15.3. Results and Discussion

15.3.1. Crystal Structure

The crystal structure of $Ba_3Cu_{17-x}(Se,Te)_{11}$ is comprised of a three-dimensional network of corner-, edge- and face-sharing CuQ_4 tetrahedra. Because no short *Q*–*Q* contacts occur in this structure, the oxidation states may be readily assigned to Ba^{+2}, Cu^{+1}, and Q^{-2}. Accordingly, the chalcogenides with x = 1, i.e. $Ba_3Cu_{16}(Se,Te)_{11}$, are electron precise. Figure 15.1 shows the crystal structure with the Cu_{26} clusters in polyhedral representation.

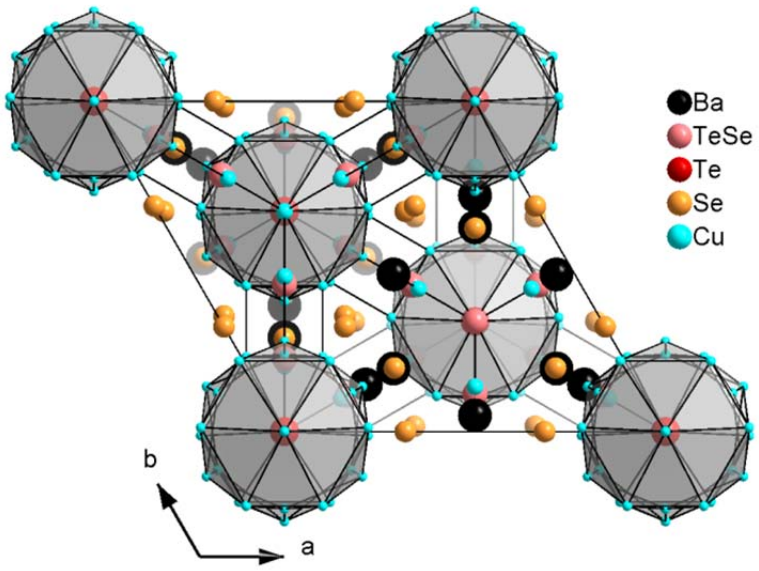

Figure 15.1 Crystal structure of $Ba_3Cu_{17-x}(Se,Te)_{11}$. The Cu_{26} polyhedra are emphasized.

A multitude of Cu–Cu contacts occur between 2.53 Å and 2.94 Å (Table B.2). Similar distances were found in $Ba_3Cu_{14-x}Te_{12}$,[266] noting that these closed-shell (d^{10}–d^{10}) interactions occur regularly in Cu chalcogenides, and are usually bonding as a consequence of the hybridization of the filled *d* states with the nominally empty, energetically higher lying *s* and *p* orbitals.[290-292] The Cu_{26} clusters are comprised of hexagonal Cu_{12} antiprisms formed by the Cu1, Cu3 and Cu4 atoms. One hexagonal face of the antiprisms is capped by the Cu5 atom, and the Cu atoms of the second hexagonal face form bonds with a second symmetry-equivalent Cu_{12} antiprism (Figure 15.2 (a)).

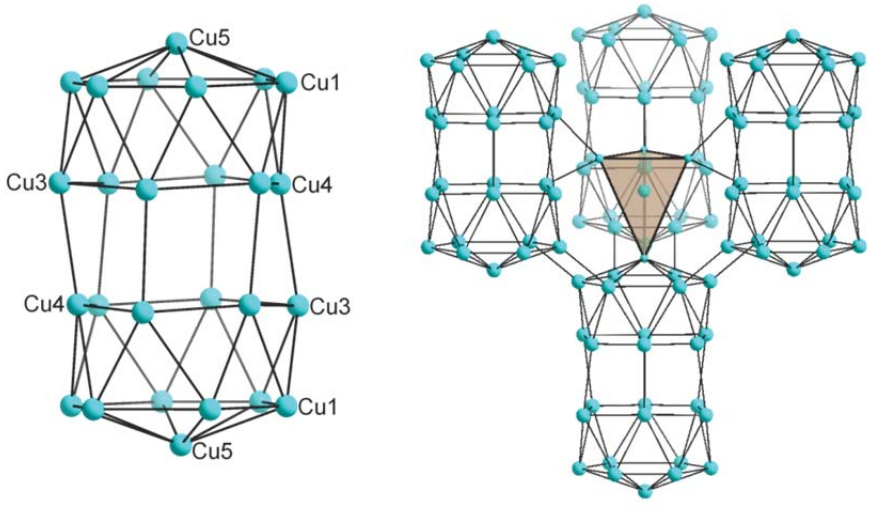

Figure 15.2 (a) The Cu_{26} cluster of $Ba_3Cu_{17-x}(Se,Te)_{11}$. (b) The three-dimensional network of Cu atoms with emphasis on the Cu6-Cu4 tetrahedron connecting the Cu_{26} clusters.

As emphasized in Figure 15.2 (b), the Cu network is three-dimensional, with the Cu_{26} clusters being connected to the surrounding Cu_{26} clusters via additional Cu–Cu contacts smaller than 3 Å of the inter-cluster atoms Cu2 and Cu6. The Cu6 atom, situated in the center of a tetrahedron, is connecting four Cu_{26} clusters together through three inter-cluster atoms (Cu2) and one cluster atom (Cu5). Considering the three-dimensional extension of the Cu–Cu contacts in combination with the Cu deficiencies on all sites (ranging from 4 % to 45 %), the possibility of Cu ion conductivity appears to be high. On the other hand, the anisotropic displacement parameters are mostly (but not completely) inconspicuous, in contrast to the best Cu ion conductors such as $Rb_4Cu_{16}I_7Cl_{13}$[293, 294] and Cu_6PS_5Cl.[295]

To probe the Cu ion mobility, ion exchange reactions were carried out in an $AgNO_3$ solution. Since a few days passed until the blue color - caused by Cu cations in the solution - became evident, the ion conductivity is very slow. For comparison, the process was much slower than the Ag exchange experiment on $Cu_2P_3I_2$.[296] The ion conductivity observed here is however significant, because Ag was able to replace 7 – 10 % of Cu in the solid at ambient conditions without destroying the crystals, as detected via EDX analysis and proven by the unit cell increase.

The Ba cations are incorporated in bicapped trigonal prismatic voids, surrounded by three Se5 atoms in distances of 3.25 Å to 3.34 Å, two Se3 (3.33 Å), one Se4 (3.49 Å), and two *Q*1 (3.57 Å). Therefore, the Te2 site is the only chalcogen site with no direct contact to the Ba atom. The Ba-*Q* polyhedra extend themselves along all directions, like the CuQ_4 tetrahedra that share corners, edges, and faces (Figure 15.3).

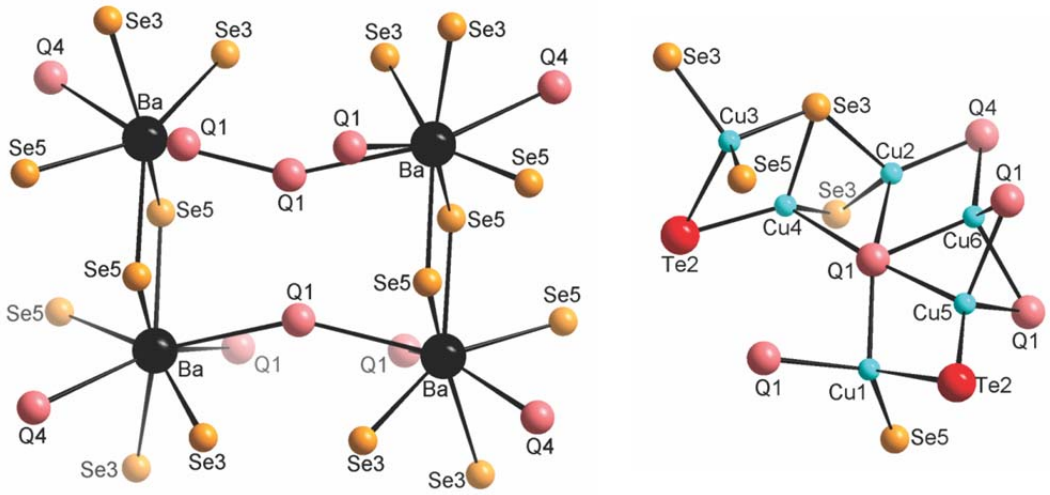

Figure 15.3 (a) A section of Ba-*Q* (b) Cu-*Q* network of $Ba_3Cu_{17-x}(Se,Te)_{11}$.

Concerning the Se/Te distribution, it is noted that of the five chalcogen sites, one is exclusively occupied by Te (Te2), three are almost entirely Se sites (Se3, Se5, and *Q*4 with at least 93 % Se), and one (*Q*1) exhibits a larger range of Te contents, namely between 74 % in case of $Ba_3Cu_{15.0}Se_{7.75}Te_{3.25}$ and 46 % in case of $Ba_3Cu_{14.4}Se_{8.6}Te_{2.4}$. Hence the variations in Te reflect themselves almost exclusively in different Te contents of *Q*1. The Te2 site is the one with the largest coordination sphere, being surrounded by 13 Cu atoms, and it is the only *Q* site without a Ba neighbour. The *Q*1 site is intermediate, surrounded by eight Cu and two Ba sites, whereas the (almost pure) Se sites Se3, *Q*4, and Se5, respectively, are only surrounded by six, four, and three Cu atoms as well as two, two, and three Ba atoms. These vast differences in the coordination environment of the *Q* atoms may be the reason why this structure was not found in either of the ternary systems, Ba/Cu/Se or Ba/Cu/Te.

15.3.2. Electronic Structure Calculations

The densities of states, *DOS*, of the electron precise model $Ba_3Cu_{16}Se_8Te_3$ reveal a very small band gap of the order of 0.02 eV (left part of Figure 5). The area below the Fermi level, E_F, is predominated by Cu 3*d* states with contributions from the Se *4p* and Te *5p* states, and the conduction band consists of Ba-*s*, Cu-*s* and Cu-*p* states. With the phase width being within $Ba_3Cu_{15}(Se,Te)_{11}$ and $Ba_3Cu_{14.4}(Se,Te)_{11}$, all these chalcogenides exhibit a Cu deficiency and are heavily doped *p*-type semiconductors.

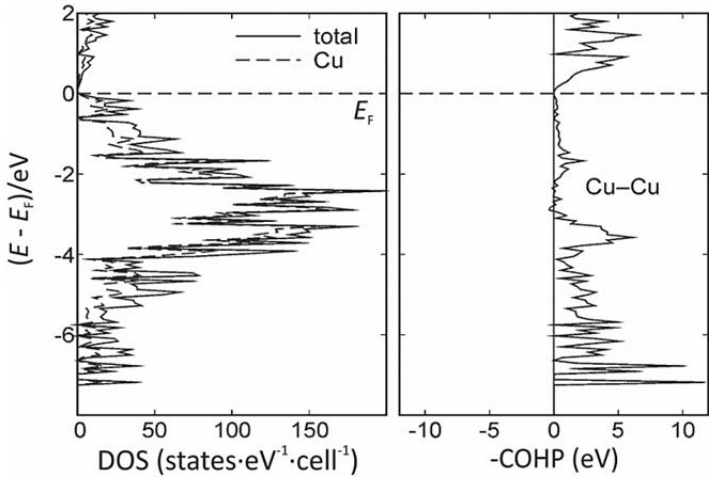

Figure 15.4 (a) *DOS* calculation and (b) cumulated Cu–Cu *COHP* curve of the model $Ba_3Cu_{16}Se_8Te_3$.

The Cu–Cu *COHP* curve, cumulated over all Cu–Cu bonds under 2.8 Å, provides evidence for the significance of these interactions (Figure 15.4 (b)). Their integrated *COHP* values (*ICOHP*)[297-299] vary between -1.00 eV for the 2.46 Å bond and -0.44 eV for the 2.71 Å bond, and even the 2.94 Å bond exhibits the still significant *ICOHP* value of -0.28 eV. The Cu deficiencies observed in all cases thus far have only a minor impact onto the *ICOHP* values, because the Cu–Cu interactions show only minor contributions to the area directly below E_F, similar to the situation in $Ba_3Cu_{14-x}Te_{12}$.[266]

15.3.3. Physical Property Measurements

The electrical transport properties of $Ba_3Cu_{14.4}Se_{8.5}Te_{2.5}$ are depicted in Figure 15.5. Both the Seebeck coefficient and the electrical conductivity are typical for (*p*-type) semiconductors with high charge carrier concentration, as deduced from the electronic structure calculation on the model $Ba_3Cu_{16}Se_8Te_3$: The Seebeck coefficient increases linearly from +50 $\mu V \cdot K^{-1}$ at 300 K to +100 $\mu V \cdot K^{-1}$ at 550 K. Other $Ba_3Cu_{17-x}(Se,Te)_{11}$ samples that we tested showed room temperature Seebeck values between +40 $\mu V \cdot K^{-1}$ and +75 $\mu V \cdot K^{-1}$, which covers a slightly higher range than in case of $Ba_3Cu_{14-x}Te_{12}$ (*S* at 300 K between +35 $\mu V \cdot K^{-1}$ and +50 $\mu V \cdot K^{-1}$).[266] The electrical conductivity of $Ba_3Cu_{14.4}Se_{8.5}Te_{2.5}$ increases from 98 $\Omega^{-1}cm^{-1}$ at 180 K to 130 $\Omega^{-1}cm^{-1}$ at 320 K, indicating that the charge carrier concentration does not significantly increase with increasing temperature. Here it should be noted that the apparently small ionic conductivity contributes to the cross conductivity as well,[300] but its impact should be negligible.

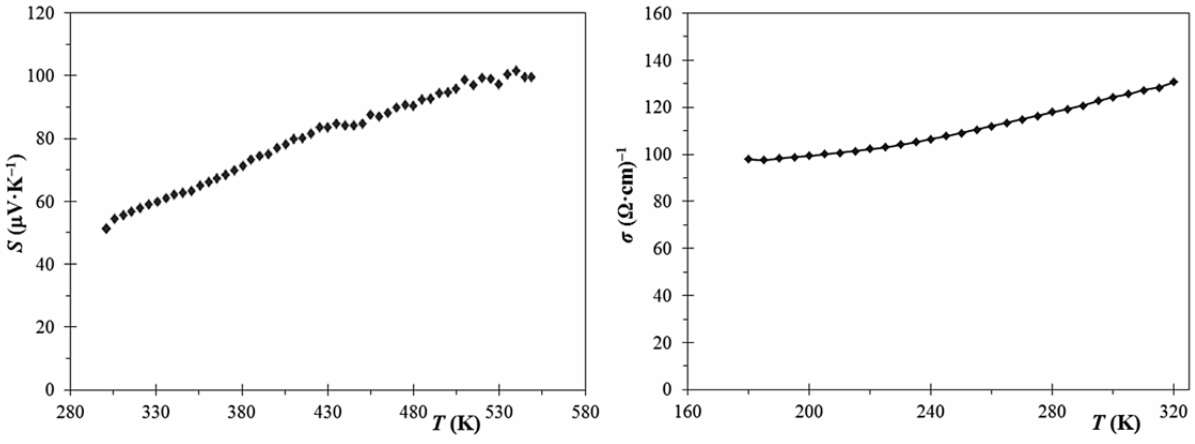

Figure 15.5 (a) Seebeck coefficient (b) Electrical conductivity of $Ba_3Cu_{14.4}Se_{8.5}Te_{2.5}$.

15.4. Conclusions

A new structure type was uncovered, adopted by $Ba_3Cu_{17-x}(Se,Te)_{11}$. This structure apparently exists only when both selenium and tellurium are used. Although the Se:Te ratio may vary as determined via different single crystal structure and EDX studies, one of the five chalcogen sites is always mixed occupied by Se and Te, while a second site is solely occupied by Te, with the remaining sites being almost exclusively Se positions. The large differences in the coordination spheres of the chalcogen sites are concluded to be responsible for the different occupancy ratios.

According to the electronic structure calculations, $Ba_3Cu_{17-x}(Se,Te)_{11}$ would be an intrinsic semiconductor when $x = 1$; however, the experiments indicate that $x > 2$. This is in agreement with $Ba_3Cu_{14.4}Se_{8.5}Te_{2.5}$ being classified as a heavily doped *p*-type semiconductor. The absolute numbers and temperature dependencies of the Seebeck coefficient and electrical conductivity are comparable to those of (also cold-pressed pellets of) $Mo_3Sb_{5.4}Te_{1.6}$[59] and $Re_3Ge_{0.6}As_{6.4}$,[301] which reach ZT values between 0.3 and 1.0 at elevated temperatures.[302] Hypothetically one might expect $Ba_3Cu_{14.4}Se_{8.5}Te_{2.5}$ to have higher ZT values because of its likely lower thermal conductivity, as e.g. a comparison with the related $Ba_3Cu_{14-x}Te_{12}$ implies.[266] However the experimentally proven mobility of the Cu ions militates against a use of $Ba_3Cu_{17-x}(Se,Te)_{11}$ in a thermoelectric device, as such a device would deteriorate within days.

Chapter 16. $Ba_3Cu_{17-x}(S,Te)_{11}$ and $Ba_3Cu_{17-x}(S,Te)_{11.5}$

16.1. Introduction

By again following the concept of *differential fractional site occupancy* (DFSO)[278, 279] with respect to the anionic components[284, 285] – the same approach that also led to the discovery of $Nb_{1.72}Ta_{3.28}S_2$,[280] $Nb_{0.95}Ta_{1.05}S$,[281] $Nb_{4.92}Ta_{6.08}S_4$[282] and $Nb_{6.74}Ta_{5.26}S_4$[283] with fractional occupancies of the cations – we were able to discover another unique structure type in the plentiful Ba-Cu-*Q* system: $Ba_3Cu_{17-x}(Se,Te)_{11}$[276] with $1 < x \leq 2.7$ (discussed in **Chapter 15**). Through replacement of selenium by sulfur, the existence of a new structure type, $Ba_3Cu_{17-x}Q_{11.5}$, not found in the selenide-telluride system is revealed to occur when [S] < [Te] and a structure analogous to $Ba_3Cu_{17-x}(Se,Te)_{11}$ when [Te] < [S]. These two different sulfide-tellurides are henceforth introduced.

16.2. Experimental Section

16.2.1.1. Synthesis

All reactions commenced from the elements (Ba: 99 %, pieces, Aldrich; Cu: 99.5 %, powder -150 mesh; Alfa Aesar; S: 99.98 %, powder, Aldrich; Te: 99.999 %, ingot, Aldrich), with sample masses of approximately 600 mg. The elements were stored and handled in a glove box filled with argon. Inside the box, the elements were placed into silica tubes, which were subsequently sealed under vacuum (10^{-3} mbar). The tubes were then heated in a resistance furnace at 1073 K for six hours. Thereafter, the furnace was slowly cooled down to 873 K and left for a period of 100 hours to allow for homogenization. Lastly, the furnace was switched off prompting fast cooling.

The rhombohedral variant was first encountered in a similar reaction with the Ba : Cu : S : Te ratio of 1 : 4 : 2 : 1, and identified as $Ba_3Cu_{15.1(1)}S_{7.92(2)}Te_{3.08}$ via the single crystal structure determination described below. The cubic variant was discovered in a reaction with the Ba : Cu : S : Te ratio of 1 : 4 : 1 : 2, and subsequently identified as $Ba_3Cu_{16.0(1)}S_{4.45(4)}Te_{7.05}$. Since its formula contained Cu deficient sites and mixed S/Te occupancies, several reactions were carried out to analyze the phase range of $Ba_3Cu_{17-x}S_{11-y}Te_y$. This formula results hypothetically with $x = 0$, when all filled Wyckoff sites are fully occupied. Variations of S/Te were studied with $x = 0$ or 1.0, while varying y between 2 and 9. Holding a constant $y = 4$ allowed for an additional study where $x = 0$, 0.5, 1.0, 1.5, 2. All samples were analyzed by means of X-ray powder diffraction, utilizing the INEL diffractometer with Cu-$K_{\alpha 1}$ radiation. Samples were found pure-phase for $x = 0.5$, 1 or 1.5 with $2 \leq y \leq 5$, producing the rhombohedral variant. For $y = 6$ and 7, respectively, the cubic variant was the primary phase with purity > 95 %, while larger values of y

produced mixtures of both rhombohedral and cubic structures. Having $x < 0.5$, especially with large values of y, additionally produced the binary Cu_2Te, which was also noticed as a side product in the reaction with $x = 1$ and $y = 2$. During this study, the $Ba_3Cu_{17-x}S_{11.5-y}Te_y$ phase was treated as $Ba_3Cu_{17-x}S_{11-y}Te_y$, as the slightly different Ba:*Q* ratio (3 : 11.5 = 0.26 vs. 3 : 11 = 0.27) was not a determining factor. Cu deficiencies are very common among Cu chalcogenides, likely due to the tendency to mixed valent Cu, so that x has to be > 0 is not surprising.

A differential scanning calorimetry, DSC, measurement (**5.3**) performed under argon flow, revealed $Ba_3Cu_{16.5}S_4Te_7$ to be stable until approximately 900 K. There were no additional peaks encountered and the TG revealed that its mass was stable throughout the measurement range.

16.2.1.2. Analysis

To prove the absence of heteroelements such as silicon stemming from the reaction container, two samples of nominal composition $Ba_3Cu_{17}S_8Te_3$ (rhombohedral variant) and $Ba_3Cu_{17}S_5Te_6$ (cubic variant) were analyzed via energy dispersive analysis of X-rays (**6.2**). The scans were performed with an acceleration voltage of 20 kV under high dynamic vacuum. No heteroelements were detected during the examination. The obtained Ba : Cu : S : Te ratios were reasonable with respect to the accuracy of the technique, yielding 9 : 57 : 29 : 6 at-%, as averaged over six crystals, compared to the nominal 9.7 : 54.8 : 25.8 : 9.7 in case of $Ba_3Cu_{17}S_8Te_3$, and 10 : 54 : 18 : 18 averaged over four crystals, compared to the nominal 9.7 : 54.8 : 16.1 : 19.4 in case of $Ba_3Cu_{17}S_5Te_6$.

16.2.1.3. Structure Determination

X-ray single crystal structure studies were performed on black block-like single crystals. The Bruker CCD diffractometer (**4.2**) was used for the data collections, performed by scans of 0.3° in ω in two groups of 600 frames (each with an exposure time of 60 seconds) at ϕ = 0° and 90°. The data were corrected for Lorentz and polarization effects. Absorption corrections were based on fitting a function to the empirical transmission surface as sampled by multiple equivalent measurements using SADABS incorporated into the APEX II package.[127]

The structure solution and refinements were carried out with the SHELXTL program package.[131] The lattice parameters indicated either rhombohedral or cubic symmetry, depending on the S:Te ratio. Using a higher S than Te amount yields rhombohedral symmetry, to which no additional systematic absences were identified, leaving $R\bar{3}m$ as the space group of highest symmetry, as in $Ba_3Cu_{17-x}(Se,Te)_{11}$.[276] Thus, that model was used as a starting point for the refinements. As in case of

the selenide-telluride before, the occupancies of all Cu sites were refined, yielding occupancies between 0.10(2) and 0.96(1). Similarly, all chalcogen sites (*Q*) were refined as being mixed albeit fully occupied by S and Te, allowing the S:Te ratio to vary freely. Of the five *Q* sites, one was occupied solely by Te (i.e. within its standard deviation of 2 %), denoted Te2, three by S (S3, S4 and S5), and one (*Q*1) was clearly mixed occupied (30.5(7) % S, 69.5 % Te). In the final refinement, Te2 was fixed as a Te site and S3, S4 and S5 as S sites. This refinement yielded the formula of $Ba_3Cu_{15.1(1)}S_{7.92(2)}Te_{3.08}$.

When choosing a higher Te than S content, face-centered cubic symmetry was observed, without any (additional) systematic absences. Thus, the space group of highest symmetry is $Fm\bar{3}m$. The direct methods were used, which yielded eight atomic positions, to which one Ba, three Cu, one S, two mixed (S/Te) *Q* sites, and one Te sites were assigned based on interatomic distances and relative heights. Based on their displacement parameters, the Cu sites were treated as deficient, which gave refined occupancies between 50.0(8) % and 98.5(6) %. Refining the occupancies of Te2 and S3 did not show any significant deviations from full occupancy, and the presence of Te on the *Q*1 site may not be significant either. The formula was refined to be $Ba_3Cu_{16.0(1)}S_{4.45(4)}Te_{7.05}$. Standardization of the atomic positions was carried out with the TIDY program included in the PLATON package.[303]

To prove the existence of a phase range and investigate its impact on the *Q* site occupancies, an additional crystal from each of the two structure types was analyzed. Their nominal compositions were $Ba_3Cu_{16}S_6Te_5$ (rhombohedral) and $Ba_3Cu_{17}S_5Te_6$ (cubic). In the first case, the formula was refined to $Ba_3Cu_{15.7(4)}S_{7.051(5)}Te_{3.949}$, with the second case refined to $Ba_3Cu_{15.6(2)}S_{5.33(4)}Te_{6.17}$, now with a significant amount of 14.2(5) % S on *Q*1. No evidence for ordering was found in either case. The crystallographic data are summarized in Table B.3, and the atomic parameters including the occupancy factors in Table B.4 (rhombohedral) and Table B.5 (cubic).

16.2.1.4. Electronic Structure Calculations

We utilized the LMTO (linear muffin tin orbitals) method (6.4) for the electronic structure calculations. The following wavefunctions were used: For Ba *6s*, *6p* (downfolded[202]), *5d* and *4f*; for Cu *4s*, *4p*, and *3d*, for S *3s*, 3*p*, and 3*d* (downfolded) and for Te *5s*, *5p*, and *5d* and *4f* (the latter two downfolded). The eigenvalue problems were solved on the basis of 512 and 1000 irreproducible *k* points spread evenly in all directions for cubic and rhombohedral structures, respectively, chosen with an improved tetrahedron method.[203]

The structural parameters were taken from the refinements on $Ba_3Cu_{15.1}S_{7.92}Te_{3.08}$ and $Ba_3Cu_{16.0}S_{4.45}Te_{7.05}$, respectively. These two structures were selected because the rhombohedral one had no split sites and the *Q*1 site of the cubic one was almost exclusively occupied by Te atoms; thus modeling *Q*1 as Te was most realistic. The sulfur-rich model was calculated with full Cu sites except for the removal of one of each Cu2 and Cu4 positions, while the 2/3 of *Q*1 sites were treated as Te and 1/3 as S, in accord with the experimental S occupancy of 0.31. As a result, this model has the formula $Ba_3Cu_{16}S_8Te_3$ in space group Cm. The second, originally cubic, model was calculated in $I4mm$ by removing half of the eight Cu2 and half of eight Cu3 positions, where *Q*1 was treated as Te and *Q*4 as S, to yield $Ba_3Cu_{16}S_{4.5}Te_7$.

16.2.1.5. Physical Property Measurements

Cold-pressed bars of the dimensions 6×1×1 mm^3 of selected samples from rhombohedral and cubic settings were used for Seebeck coefficient (S) and electrical conductivity (σ) measurements. S and σ were simultaneously measured on a commercial ULVAC-RIKO ZEM-3 instrument from room temperature up to 750 K. The specific electrical conductivity (σ) is determined via the four-point-method (**5.5**), and the Seebeck coefficient via $S = \Delta V/\Delta T$ (**5.4**); thermocouple probe separation was approximately 3 mm for these studies. The achieved density was around 85 % of the theoretical maximum determined via the single crystal structure study.

16.3. Results and Discussion

16.3.1. Crystal Structure

The rhombohedral selenide-telluride was described in 2009 (**Chapter 15**).[276] Like the selenide-telluride, the rhombohedral sulfide-telluride features interconnected Cu_{26} clusters, which are composed of two stacked hexagonal antiprisms capped on both terminal hexagonal faces. The unit cell is comprised of a series of corner-, edge- and face-sharing CuQ_4 tetrahedra. Four of the six Cu sites are essentially fully occupied, with occupancies between 92 % and 98 %, while the occupancies of Cu5 and Cu6 can range anywhere between 50 % and 80 % or 10 % and 60 %, respectively. In the case of tellurium-richer $Ba_3Cu_{15.7(4)}S_{7.051(5)}Te_{3.949}$, however, Cu2 had to be refined as a split site, while the Cu6 site was virtually unoccupied (refined to be 1.3%), in contrast to 10 % in case of $Ba_3Cu_{15.1(1)}S_{7.92(2)}Te_{3.08}$. This can be rationalized as Cu atoms being forced into different sites to compensate for the nearly Te-exclusive *Q*1 site (**Table B.4**) – typically between 46 % and 74 % Te with the selenides, as Cu6 is

surrounded by three *Q*1 atoms. Besides *Q*1, all other *Q* sites (2 through 5) were found to be exclusively occupied by either S or Te atoms.

The crystal structure of the cubic variant, realized in $Ba_3Cu_{16.0(1)}S_{4.45(4)}Te_{7.05}$ and $Ba_3Cu_{15.6(2)}S_{5.33(4)}Te_{6.17}$, is also comprised of a three-dimensional network of corner-, edge- and face-sharing CuQ_4 tetrahedra. For example, the Cu2Q_4 and Cu3Q_4 tetrahedra share a common face formed by three Te1 atoms. The Ba cations are centered in square antiprisms comprised of two $Q1_4$ faces, and the square antiprisms are interconnected via common edges.

Since no short *Q*–*Q* contacts occur in this structure, the oxidation states are therefore assigned to Ba^{2+}, Cu^{+}, and Q^{2-}. Thus, the chalcogenides with $x = 0$, i.e. $Ba_3Cu_{17}(S,Te)_{11.5}$, are electron precise. The Cu_{16} clusters are regular icosioctahedra (emphasized in Figure 1), as sometimes found in intermetallics such as $Na_{35}Cd_{24}Ga_{56}$[304] and $Mg_{35}Cu_{24}Ga_{53}$.[305] To our knowledge, this is the first time that such an icosioctahedron is centered by a chalcogen atom.

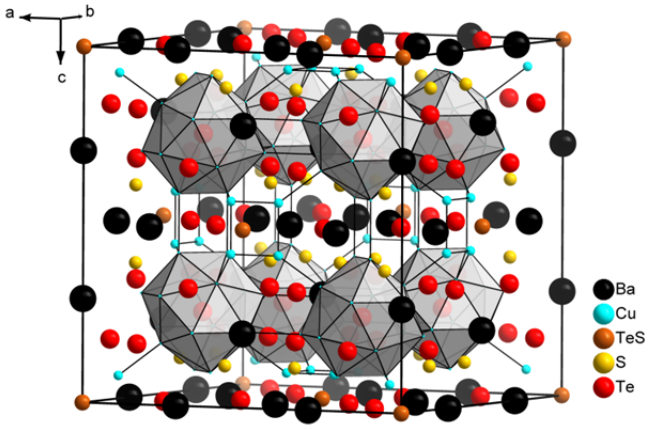

Figure 16.1 Unit cell of $Ba_3Cu_{17-x}(S,Te)_{11.5}$. The icosioctahedra are emphasized.

The Cu_{16} icosioctahedron is centered by a Te2 atom, and its 28 triangular faces are formed by twelve Cu1 atoms and four Cu3 atoms, subsequently of point symmetry *T* (left part of Figure 16.2). While Cu1 is almost fully occupied (refined values were 92 % – 99 %), Cu3 is roughly half occupied, so that the averaged coordination number of Te2 is about 12×1 + 4×2 = 14. Each Cu3 atom is bonded to one Cu2 atom, which in turn forms $Cu2_8$ cubes located between the icosioctahedra. S3 atoms are bonded to three Cu1 atoms on each of the four triangular icosioctahedron faces that are not coordinated to Cu3 (right part of Figure 16.2). The intracluster distances of 2.46 Å - 2.81 Å (Table B.6) are typical Cu–Cu bonds, as found in several other Cu-chalcogenides,[306] including $Ba_3Cu_{14-x}Te_{12}$[266] and $Ba_3Cu_{17-x}(Se,Te)_{11}$,[276]

noting that these formally closed-shell (d^{10}–d^{10}) interactions occur regularly in Cu chalcogenides, and their bonding character arises from mixing of the filled *d* states with the nominally empty, energetically higher lying *s* and *p* orbitals.[290-292]

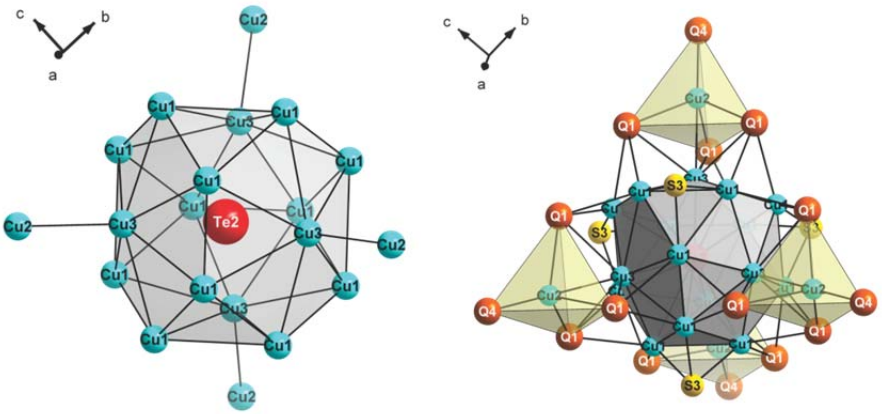

Figure 16.2 The Cu_{16} icosioctahedron with four interconnecting Cu2–Cu3 bonds (left) and its extension with surrounding *Q* atoms (right).

As can be observed in Figure 3, the Cu atom network is three-dimensional, with the icosioctahedra being connected to six other icosioctahedra via twelve intercluster Cu1–Cu1 contacts of around 2.87 Å, of which Figure 3 shows only those connected in one unit cell; each icosioctahedron joins others in three neighboring unit cells along [100], [010], and [001]. Additionally, each icosioctahedron is bonded to four Cu2 atoms from each of the polyhedron's Cu3 sites. The Cu2 atoms form cubes centered by *Q*4 atoms with Cu2–Q4 bonds of 2.20 Å – 2.22 Å, with Cu2–Cu2 distances along the edges of approximately 2.55 Å. With the occupancy of Cu2 between 50 % and 58 %, the averaged coordination number of *Q*4 – dominated by S atoms – is about 8/2 = 4. Similarly, the Cu cubes of $BaCu_{5.9}STe_6$ were centered by S atoms, with Cu–S bonds of 2.33 Å and a Cu occupancy of 74 %, resulting in an average coordination number of 8 × 3/4 = 6 for this S atom.[270] Because of the three-dimensional extension of the Cu–Cu contacts in combination with the Cu deficiencies of Cu2 and Cu3 (each on the order of 50 %), Cu ion conductivity appears to be likely in $Ba_3Cu_{17-x}(Se,Te)_{11.5}$, as previously shown for $Ba_3Cu_{17-x}(Se,Te)_{11}$, though the anisotropic displacement parameters are not as large and distinctly anisotropic as found in the best Cu ion conductors including $Rb_4Cu_{16}I_7Cl_{13}$[293, 294] and Cu_6PS_5Cl.[295]

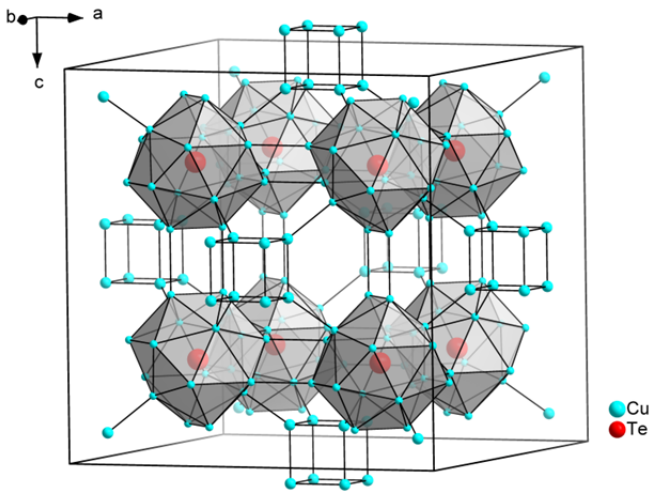

Figure 16.3 The three-dimensional network of Cu atoms with central Te2 atoms centering the icosioctahedra.

While no mixed S/Te occupancies were identified in the sulfide-tellurides $Ba_2Cu_{6-x}STe_4$[270] and Zr_6STe_2,[307] each of the four crystals investigated here has at least one mixed S/Te site, with ratios of up to 30:70 and 80:20, respectively. Other examples for mixed S/Te occupancies, while rare, do exist, including $Ta_6S_{1+x}Te_{3-x}$[308] (with up to 4 % S on Te sites and 7 % Te on S sites) and $Ta_{15}Si_2S_xTe_{10-x}$[286] (with one pure S site and four mixed S/Te sites, albeit with very high standard deviations). It is most probable that, due to the large difference in atom sizes, the S and Te atoms do not occupy the same absolute position. This seems to be not resolvable from the X-ray data, but it is reflected in large displacement parameters of the sites involved, e.g. *Q*4 and its neighboring Cu2 in case of $Ba_3Cu_{17-x}(S,Te)_{11.5}$. In this case, Te on *Q*4 is very likely to be surrounded by more deficient Cu2 cubes and to be placed off-center because of the short averaged Cu2–*Q*4 distance of 2.2 Å.

16.3.2. Electronic Structure Calculations

The density of states, *DOS*, of the electron precise model $Ba_3Cu_{16}S_8Te_3$ reveal a small band gap of the order of 0.12 eV at the Fermi level (left part of Figure 16.4). The area below the Fermi level, E_F, is predominated by Cu 3*d* states with contributions from the S-*3p* and Te-*5p* states, and the conduction band consists of Ba *s*, Cu *s* and Cu *p* states. The $Ba_3Cu_{16}S_{4.5}Te_7$ model (right part of Figure 16.4) possesses no band gap at the Fermi level, but has a very few states immediately above the Fermi level with some minima at approximately 0.5 eV and 0.8 eV; this metal-like *DOS* would suggest a small Seebeck coefficient, which can be verified in the following section. The energy levels below the Fermi level are again predominantly Cu-3*d* states and chalcogen *p* states.

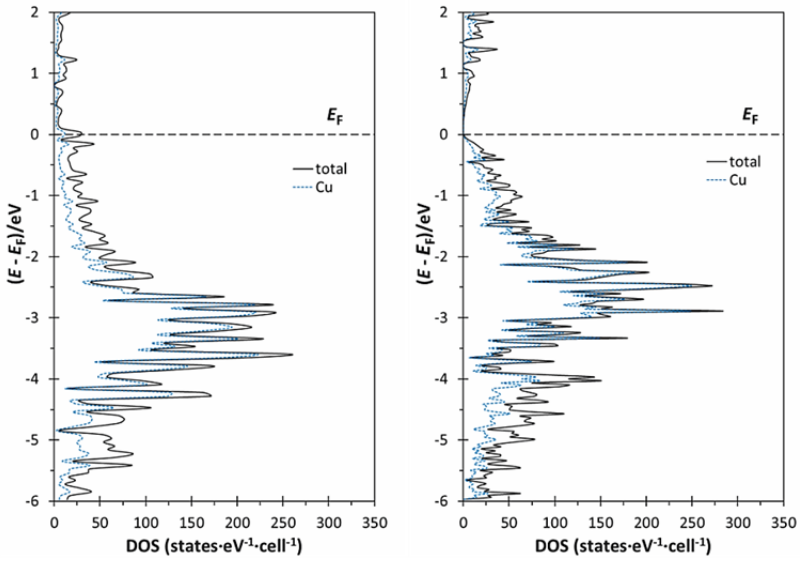

Figure 16.4 *DOS* calculations for $Ba_3Cu_{16}S_8Te_3$ in *Cm* (left) and of $Ba_3Cu_{16}S_{4.5}Te_7$ in *I4mm* (right).

16.3.3. Physical Property Measurements

The rhombohedral sulfide-tellurides showed physical properties that were comparable to that of the previously-studied selenide material published in 2009.[276] Measurements were performed on rhombohedral $Ba_3Cu_{16}S_6Te_5$, $Ba_3Cu_{17}S_8Te_3$ and $Ba_3Cu_{16}S_9Te_2$ (Figure 16.5). Seebeck coefficient values were mostly between S = +150 μV·K^{-1} and +250 μV·K^{-1} for the full range of the measurement. Electrical conductivity values were all below σ = 20 Ω^{-1}cm^{-1} at room temperature and gently increased with the temperature, as is expected of a slightly doped semiconductor, reaching a maximum of 163 Ω^{-1}cm^{-1} at 700 K for $Ba_3Cu_{16}S_9Te_2$. The resulting highest power factor $PF = S^2\sigma$ at room temperature was 0.45 μW·cm^{-1}K^{-2} for $Ba_3Cu_{16}S_9Te_2$, which reached 2.38 μW·cm^{-1}K^{-2} at 700 K.

For the cubic materials of nominal composition "$Ba_3Cu_{16.5}S_4Te_7$" (measured directly after cold-pressing as well as after cold-pressing and sintering at 825 K) and "$Ba_3Cu_{16.6}S_4Te_7$", S – being almost unaffected by the annealing process – rose gradually from about +40 μV·K^{-1} to +100 μV·K^{-1}. The electrical conductivity behaved like a metal or degenerate semiconductor, showing a gradually decreasing slope as temperature rises. The annealed sample exhibited, not surprisingly, the highest value at room temperature, namely 412 Ω^{-1}cm^{-1}, while the cold-pressed samples showed comparable conductivity curves beginning around 465 K. σ of the three cubic samples decreased to about 200 Ω^{-1}cm^{-1} at 750 K. The highest power factor at room temperature was 0.63 μW·cm^{-1}K^{-2} for cubic, annealed "$Ba_3Cu_{16.6}S_4Te_7$", which reached 2.12 μW·cm^{-1}K^{-2} at 750 K.

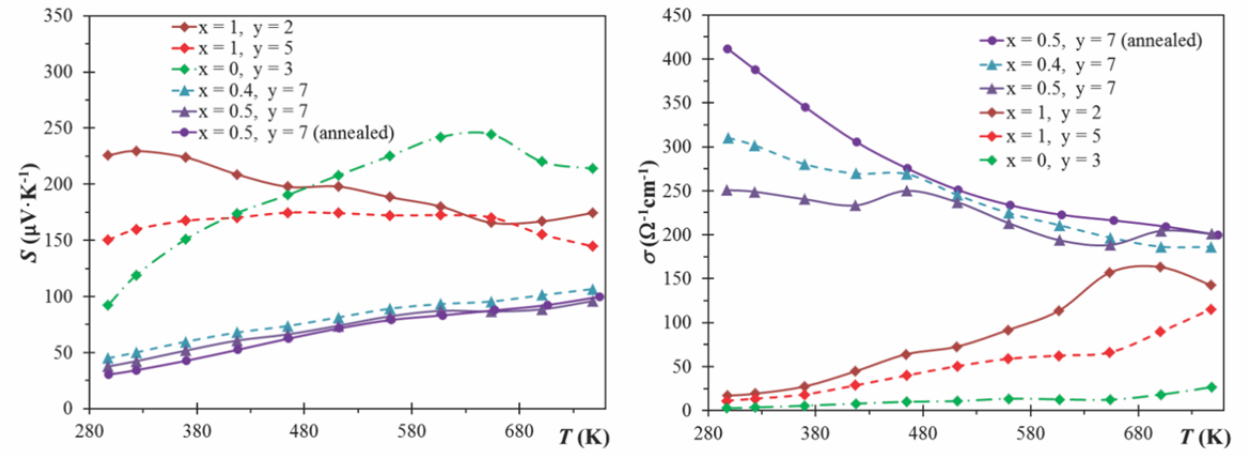

Figure 16.5 Seebeck coefficient (left) and electrical conductivity (right) of $Ba_3Cu_{17-x}S_{11-y}Te_y$ (diamonds) and $Ba_3Cu_{17-x}S_{11.5-y}Te_y$ (triangles/circles).

For comparison, the S values at room temperature of other barium copper chalcogenides were +35 μVK^{-1} for $Ba_3Cu_{13.88}Te_{12}$,[266] +100 μVK^{-1} for $BaCu_{5.7}Se_{0.6}Te_{6.4}$,[270] and +120 μVK^{-1} for $K_2BaCu_8Te_{10}$,[264] with σ (300 K) of these three materials being 190 Ω^{-1}cm^{-1}, 40 Ω^{-1}cm^{-1}, and 70 Ω^{-1}cm^{-1}, respectively. Thus, the last three materials exhibited comparable power factors, ranging from $PF = 0.2$ μW·cm^{-1}K^{-2} to 1.0 μW·cm^{-1}K^{-2} at 300 K.

16.4. Conclusion

Two structure types were discovered for the Ba-Cu-(S,Te) system, which are dependent not only on the crucial mixing of both S and Te atoms but on the S:Te ratio as well. The rhombohedral variant is found when [S] > [Te] and shows mixing on the *Q*1 site, with the Cu5 and Cu6 atoms displaying large deficiencies. The Cu cages are based on Cu_{26} clusters, topologically equivalent to the previously published $Ba_3Cu_{17-x}(Se,Te)_{11}$. Upon introducing [Te] > [S], a new, cubic structure type is found: $Ba_3Cu_{17-x}(S,Te)_{11.5}$, also with mixed S/Te occupancies. Two of three Cu sites have between 50 % and 58 % occupancies and form regular Cu_{16} icosioctahedra of point symmetry *T*, eight of which are found in one unit cell, all interconnected via additional Cu_8 cubes to an infinite Cu atom network. Phase width studies indicate that both structures require a Cu-deficiency, a common observation in many Cu chalcogenides, and like in case of the previously reported rhombohedral selenide-telluride, at least a ~1:4 mixture of the two different chalcogen atoms is required for the formation of these structures. The cubic structure will form as soon as the Te content is higher than the S content, as became evident when comparing the structures of nominal compositions $Ba_3Cu_{16}S_5Te_6$ and $Ba_3Cu_{16}S_6Te_5$.

The electronic structure calculations suggest that $Ba_3Cu_{17-x}(S,Te)_{11}$ would be an intrinsic *p*-type semiconductor when $x = 1$, which is in agreement with the measurement of three stoichiometric variations thereof. The highest power factor was found to be 2.38 $\mu W \cdot cm^{-1}K^{-2}$ at 700 K, but like in case of its Se-counterpart, high Cu ion mobility makes this material a poor choice for thermoelectric materials. The calculations for $Ba_3Cu_{17-x}(S,Te)_{11.5}$ revealed a significant albeit small number of states around the Fermi level, which concurs well with its smaller Seebeck coefficient and larger electrical conductivity. The highest power factor of this series, 2.12 $\mu W \cdot cm^{-1}K^{-2}$ at 750 K, is very comparable to the maximum measured for $Ba_3Cu_{17-x}(S,Te)_{11}$. Here as well, the structure refinements suggest the possibility of a high Cu mobility that makes it unappealing from a thermoelectric perspective.

Chapter 17. $Ba_2Cu_{7-x}Te_6$

17.1. Introduction

All of the compounds we discovered previously discussed in Section V were characterized as Cu-deficient thus *p*-type semiconductors, with only exception thus far, namely the metallic sulphide-telluride $BaCu_{17-x}S_{11.5-y}Te_y$.[277] As a high Ba : Cu ratio proved to be disadvantageous for thermoelectric properties (because of low electrical conductivity), we have increasingly concentrated on smaller Ba : Cu ratios, along with an excess of tellurium in order to obtain polytellurides, expected to cause the desired small band gaps.[24, 309] During this process, we discovered the new telluride $Ba_2Cu_{7-x}Te_6$ with significant Te–Te interactions, which is introduced with this chapter.

17.2. Experimental Section

17.2.1.1. Synthesis

All reactions commenced from the elements (Ba: 99 %, pieces, Aldrich; Cu: 99.5 %, powder -150 mesh; Alfa Aesar; Te: 99.999 %, ingot, Aldrich), with sample masses of approximately 600 mg. The elements were stored and handled in a glove box filled with argon. Within, the elements were placed into glassy carbon crucibles inside silica tubes, which were subsequently sealed under vacuum (10^{-3} mbar). The tubes were then heated in a resistance furnace at 1073 K for six hours. Thereafter, the furnace was slowly cooled down to 923 K and left for a period of 60 hours to allow for homogenization. Lastly, the furnace was switched off prompting fast cooling. Investigations on the phase range of $Ba_2Cu_{7-x}Te_6$ were carried out with $0 \leq x \leq 1$ in increments of 0.2. Therein, the sample with $x = 0.4$ was found pure phase, and the samples with $x = 0.2$ and 0.6 contained less than 5 % side products, hinting towards the existence of a rather small phase range.

17.2.1.2. Analysis

The sample of nominal composition $Ba_2Cu_{6.6}Te_6$ was analyzed via EDX. No heteroelements were detected during the examination. The obtained Ba : Cu : Te ratios were very homogenous, yielding 14 : 45:41 at-%, as averaged over six crystals, compared to the nominal 13.7 : 45.2 : 41.1.

Differential scanning calorimetry was also utilized to study the thermal stability of $Ba_2Cu_{6.6}Te_6$. The compound was heated from room temperature to 1123 K under argon flow against a sapphire reference. Upon heating at a rate of 10 $K \cdot min^{-1}$, the experiment showed a single endothermic peak around 1000 K corresponding to the melting point; upon cooling at a rate of 20 $K \cdot min^{-1}$, the opposite

exothermic crystallization peak was found around 900 K; throughout the measurement, thermogravimetry data remained stable between 99 % and 98 % of the initial starting mass. No phase changes or decompositions were observed in the aforementioned range.

17.2.1.3. Structure Determination

A plate-like single crystal of $Ba_2Cu_{7-x}Te_6$ was selected for the data collection using the SMART APEX CCD. Two sets of 606 frames were collected with an exposure time of 40 seconds per frame. The data were corrected for Lorentz and polarization effects. Using RLATT, incorporated within the APEX II package, revealed that the crystal was a twin, and the twin reflections in the P4P list were separated using the cell_now program and gave the same cell for both components. The second individual is related to the first by a 180° rotation, $a_2 = -a_1$, $b_2 = -b_1$, $c_2 = a_1 + c_1$. The integration and subsequent data reduction of both components was carried out using the APEX II package.[127]

The structure solution and refinements were performed with the SHELXTL program package,[131] and XS found two Ba (*2e* positions), four Cu (three on *4f* and one on *2e*) and four Te (two on *4f* and two on *2e*). As often observed in Cu chalcogenides, not all Cu sites were fully occupied: Minor albeit significant deficiencies were found for Cu2, Cu3 and Cu4 of 2 % – 12 %, while the Cu1 occupancy was refined to 100 % within two standard deviations (99.1(6) %). Allowing for these deficiencies, the refinement's residuals of R1 = 0.0492 and wR2 = 0.1289 improved to 0.0473 and 0.1216, respectively. Ultimately, the formula was refined to $Ba_2Cu_{6.64(4)}Te_6$. Attempts to grow better single crystals using different heating conditions and different fluxes did not lead to any noticeable improvements, and the crystals were always twinned. Crystallographic data for $Ba_2Cu_{6.6}Te_6$ are given below:

Table 17.1 Crystallographic Data for $Ba_2Cu_{6.64(4)}Te_6$.

Refined Formula	$Ba_2Cu_{6.64(4)}Te_6$
Formula Weight [g/mol]	1462.2
T of measurement [K]	298(2)
λ [Å]	0.71073
Space Group	$P21/m$
a [Å]	6.8591(7)
b [Å]	12.1439(12)
c [Å]	9.0198(9)
β	110.7509(14)
V [Å^3]	702.58(12)
Z	2
μ [mm^{-1}]	27.51
ρ_{calcd} [g/cm^3]	6.91
$R(F_o)^a \setminus R_w(F_o^2)^b$	0.0573 \ 0.1220

$^a R(F_o) = ||F_o|-|F_c||/|F_o|$ $^b R_w(F_o^2) = [\,\Sigma[w(F_o^2 - F_c^2)^2]/\Sigma[w(F_o^2)^2]\,]^{1/2}$

17.2.1.4. Electronic Structure Calculations

LMTO with the atomic spheres approximation (ASA) was used here as per the other calculations in this section. The following wavefunctions were used: For Ba *6s*, *6p* (downfolded[202]), *5d* and *4f*; for Cu *4s*, *4p*, and *3d*, for S *3s*, 3*p*, and 3*d* (downfolded) and for Te *5s*, *5p*, and *5d* and *4f* (the latter two downfolded).

The full $Ba_2Cu_7Te_6$ model was calculated in $P2_1/m$ with the unit cell parameters pertaining to the crystal structure analyzed herein and all Cu sites fully occupied (*x* = 0). Removal of one Cu4 atom to yield $Ba_2Cu_{6.5}Te_6$ generates space group $P1$ (*x* = 0.5). The eigenvalue problems were solved on the basis of 798 and 288 irreproducible *k* points, respectively. Points were chosen with an improved tetrahedron method.[203] To better understand the bonding in the structure, crystal orbital Hamiltonian populations (*COHP*s)[96, 297] were calculated for the *x* = 0 case for all Cu–Cu interactions < 3 Å and for the Te–Te contacts < 3.6 Å.

17.2.1.5. Physical Property Measurements

A cold-pressed bar of the dimensions 6×1×1 mm^3 of a $Ba_2Cu_{6.6}Te_6$ sample was used for Seebeck coefficient (S) and electrical conductivity (σ) measurements. S and σ were simultaneously measured on the ZEM instrument from room temperature up to 725 K, with a thermocouple probe separation of approximately 3 mm. The achieved density was around 85 % of the theoretical maximum determined via the single crystal structure study.

17.3. Results and Discussion

17.3.1. Crystal Structure

The new ternary telluride $Ba_2Cu_{6.6}Te_6$ crystallizes in a new structure type in the space group $P2_1/m$. The unit cell (Figure 17.1), contains two crystallographically independent Ba atoms (Ba1 and Ba2), both located on Wyckoff position *2e*, four Cu atoms (Cu1, Cu2, Cu3 and Cu4) located on Wyckoff position *4f*, *2e*, *4f* and *4f* with site deficiencies of 0 %, 8 %, 2 % and 12 %, respectively. The four Te atoms (Te1, Te2, Te3 and Te4) occupy the positions *2e*, *2e*, *4f* and *4f*, respectively (Table 17.2). The refined formula is $Ba_2Cu_{6.64(4)}Te_6$.

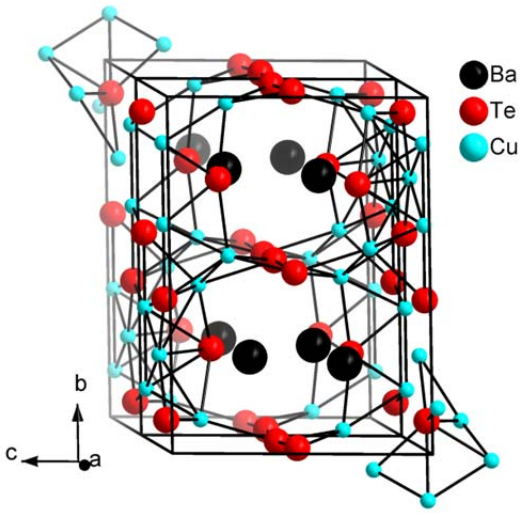

Figure 17.1 Unit cell of $Ba_2Cu_{7-x}Te_6$. Ba–Te bonds are omitted for clarity.

Table 17.2 Atomic coordinates, U_{eq} parameters, and occupancy factors of $Ba_2Cu_{7-x}Te_6$.

Atom	Site	*x*	*y*	*z*	U_{eq} [Å^2]	occ.
Ba1	*2e*	0.59291(13)	¼	0.64891(10)	0.0147(2)	1
Ba2	*2e*	0.93065(14)	¼	0.32531(11)	0.0184(2)	1
Cu1	*4f*	0.1200(2)	0.13572(12)	0.99328(18)	0.0217(3)	1
Cu2	*2e*	0.4853(3)	¼	0.9847(2)	0.0193(7)	0.921(9)
Cu3	*4f*	0.3297(2)	0.06097(12)	0.81129(18)	0.0213(5)	0.978(7)
Cu4	*4f*	0.3728(3)	0.03567(15)	0.2693(2)	0.0234(5)	0.881(7)
Te1	*2e*	0.12575(14)	¼	0.74233(11)	0.0116(2)	1
Te2	*2e*	0.38038(14)	¼	0.23640(11)	0.0131(2)	1
Te3	*4f*	0.25259(9)	0.58055(5)	0.00821(7)	0.01209(18)	1
Te4	*4f*	0.24466(13)	0.50397(7)	0.50881(8)	0.0209(2)	1

Both Ba atoms are centered in a tri-capped trigonal prism, with Ba–Te bonds in the range between 3.45 and 3.9 Å (Table B.7) – similar to those found in many ternary Ba/Cu/Te compounds such $BaCu_2Te_2$ (3.40 – 3.61 Å),[261] $Ba_2Cu_{4-x}Te_5$ (3.44 – 4.02 Å),[268] $Ba_3Cu_{14-x}Te_{12}$ (3.47 – 3.83 Å),[266] and in the binary tellurides BaTe (3.50 Å),[310] $BaTe_2$ (3.57 Å)[311, 312] and $BaTe_3$ (3.59 and 3.63 Å).[313] The [$BaTe_9$] polyhedra share common faces, edges and corners to form a three-dimensional network.

The Cu atoms are in tetrahedral coordination with Cu–Te bonds ranging from 2.62 and 2.77 Å similar to those found in many ternary Ba/Cu/Te compounds, including in $BaCu_2Te_2$ (2.60 – 2.78 Å).[261] The [$CuTe_4$] tetrahedra are distorted with bond angles ranging from 84° to 120°. The [$Cu3Te_4$] and [$Cu4Te_4$] tetrahedra share common edges to form an eight member ring [Cu_4Te_4]. [$Cu1Te_4$] tetrahedra share common edges with each other and common corners with the [$Cu2Te_4$], [$Cu3Te_4$] and [$Cu4Te_4$] tetrahedra. The [$Cu4Te_4$] tetrahedra form layers along the *c*-axis, and these layers are connected to each other via the Te3 atoms. Ba2 atoms fill the space between the layers and Ba1 is located in the center of the eight member ring [Cu_4Te_4].

The Cu–Cu bonds are in the range between 2.67 and 2.89 Å. Similar Cu–Cu bonds were reported in numerous other heavy chalcogenides,[306] including $Ba_3Cu_{14-x}Te_{12}$.[266] The bonding character of these formally closed-shell (d^{10}–d^{10}) interactions is a consequence of the hybridization of the filled *d* states with the nominally empty, energetically higher lying *s* and *p* orbitals.[290-292] Cu1 and Cu2 are coordinated to four Cu neighbors, Cu3 to three Cu neighbors and Cu4 has only two Cu neighbors. Cu1, Cu3 and Cu4 form an almost planar six member ring, which is connected to the next one via Cu2 atoms

and Cu1–Cu1 bonds, ultimately fused into an infinite ribbon along the *b* axis (Figure 17.2). The triangles, each formed by one Cu2 and two Cu1, are almost isosceles.

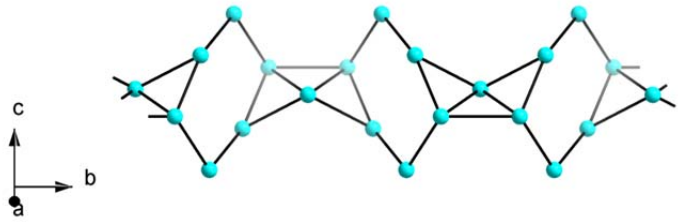

Figure 17.2 Infinite Cu ribbon of $Ba_2Cu_{7-x}Te_6$.

With Ba in the +2 and Cu in the +1 oxidation state, not all Te atoms of $Ba_2Cu_{6.6}Te_6$ can attain the -2 state ($2\times 2 + 6.6 \times 1 = 10.6 < 12 = 6 \times 2$). While Te1, Te2 and Te3 are not bonded to each other and are thus in the -2 oxidation state, the Te4 atoms form an infinite distorted pseudo-linear chain with alternating Te–Te distances of 3.30 and 3.56 Å with a bond angle of 174° (Figure 17.3). A similar Te chain but with shorter Te–Te contacts and with split sites was found in $Ba_2Cu_{4-x}Te_5$, with the shorter distances being around 3.0 Å.[268] The occurrence of a topologically equivalent Sb atom chain in $Zn_{4-\delta}Sb_3$[57] was speculated to be partially responsible for its extraordinarily low thermal conductivity (along with the complex structure and the multitude of different Zn-deficient sites[77]) caused by experimentally found "dumbbell rattling".[314]

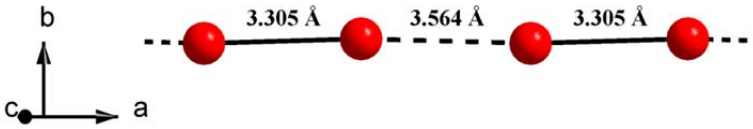

Figure 17.3 Infinite Te chain of $Ba_2Cu_{7-x}Te_6$.

The 3.3 Å distance of $Ba_2Cu_{6.6}Te_6$ are much longer than a Te–Te single bond of approximately 2.7 – 2.8 Å as typically found in $[Te_2]^{2-}$ dumbbells, e.g. in $[N(CH_3)_4]_2Te_2$ (d_{Te-Te} = 2.74 Å)[315] and $[Na(CH_3OH)_3]_2Te_2$.[316] On the other hand, interlayer Te–Te distances < 3.8 Å in layered transition metal tellurides, such as 3.78 Å in $TiTe_2$, can have bonding character and be thus responsible for the metallic character of $TiTe_2$ because of the partially empty Te *5p* states.[317]

17.3.2. Electronic Structure Calculations

The density of states, *DOS*, of both models, $Ba_2Cu_7Te_6$ and $Ba_2Cu_{6.5}Te_6$, exhibit a few numbers of states at the Fermi level, E_F (Figure 17.4). Examining the elemental contributions to the *DOS*, the energy levels below the Fermi level are predominantly Cu-3*d* states and Te-5*p* states. The most significant change to the *DOS* by going from $Ba_2Cu_7Te_6$ to $Ba_2Cu_{6.5}Te_6$ is the lowering of the Fermi level into a region with more filled Cu-3*d* states.

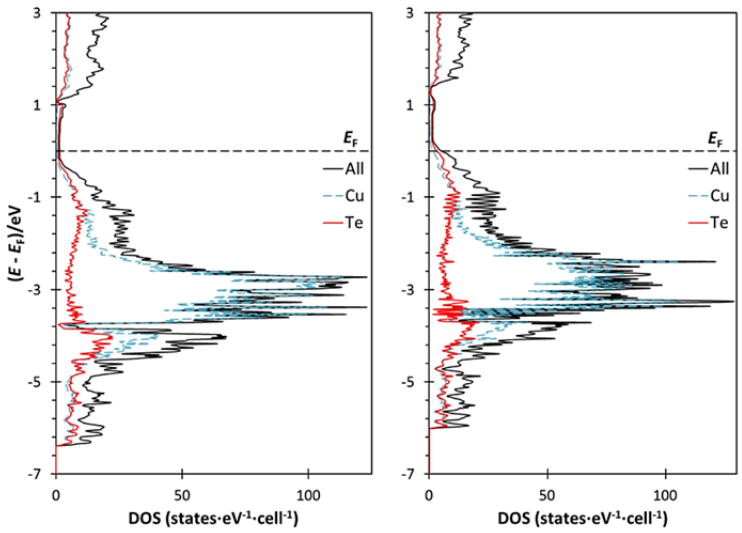

Figure 17.4 *DOS* calculations for $Ba_2Cu_{7-x}Te_6$. Left: $x = 0$, $P2_1/m$; right: $x = 0.5$, $P1$.

Analyzing the band structure is instructive in order to investigate the significance of the small numbers of states occurring at E_F. Therefore, fat band[318] calculations were performed for the $Ba_2Cu_7Te_6$ model (Figure 17.5). The small *DOS* at E_F is evidently a consequence of two bands crossing the Fermi level parallel to *a** (Z-D and B-Γ), while no crossings occur along any other direction, suggesting one-dimensional metallic behaviour. These at E_F rather steep bands have a band width of about 1.8 eV, and the primary contributions to these bands are from the Te4-p_x orbitals, with minor contributions from the Te4-p_z orbitals. This corresponds to the direction of the one-dimensional Te atom chains running along the *a* axis in the crystal structure. With the crystal structure solved for $Ba_2Cu_{6.6}Te_6$, it should also be noted that the Fermi level in this diagram would be slightly lower.

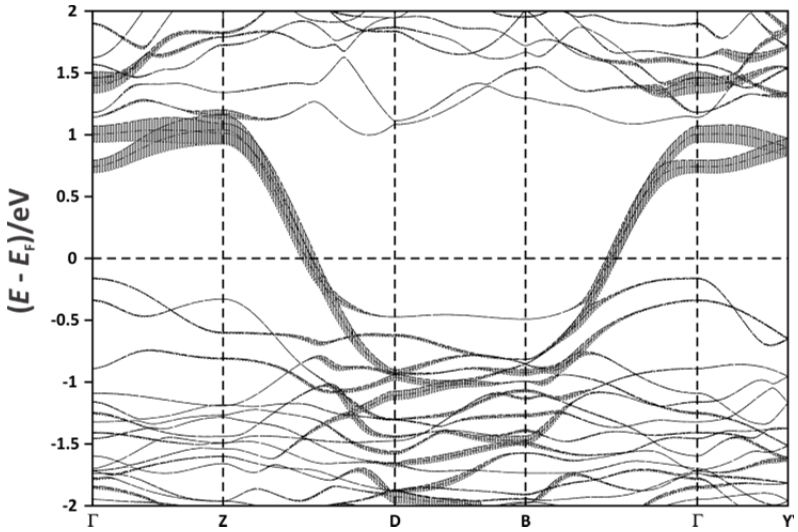

Figure 17.5 Band structure of $Ba_2Cu_7Te_6$ with highlighted Te4 p_x interactions via fat band representation. Fractional coordinates of the special points with respect to the reciprocal unit cell: Γ: (0, 0, 0); Z: (0, 0, ½); D: (½, 0, ½); B: (½, 0, 0); Y: (0, ½, 0).

Crystal orbital Hamiltonian populations (*COHP*s) were calculated for Cu–Cu and Te–Te interactions of the model $Ba_2Cu_7Te_6$ (Figure 17.6). All Cu–Cu bonds (between 2.69 and 2.89 Å) below the Fermi level have bonding character. While there are no Cu–Cu interactions near the Fermi level, the Cu–Cu states above 1 eV have bonding character as well, like many other compounds studied in the Ba/Cu/Te system.[266, 268, 276] Conversely, the Te–Te interactions, separated into 3.30 and 3.56 Å, do not show a strongly bonding character; the integrated *COHP* at the Fermi level indicates that the 3.30 Å interaction is in total of a weakly bonding nature (*ICOHP* = –0.19 eV) whilst the 3.56 Å interaction is weakly antibonding (*ICOHP* = +0.06 eV). As in the case of $TiTe_2$, empty (antibonding) states exist in the Te-*5p* band, as evident from these *COHP* curves. The strongly antibonding character of both Te–Te interactions around the Fermi level combined with the Te4 chain running along the *a* axis is responsible for the steep character of the Te4-p_x–based bands.

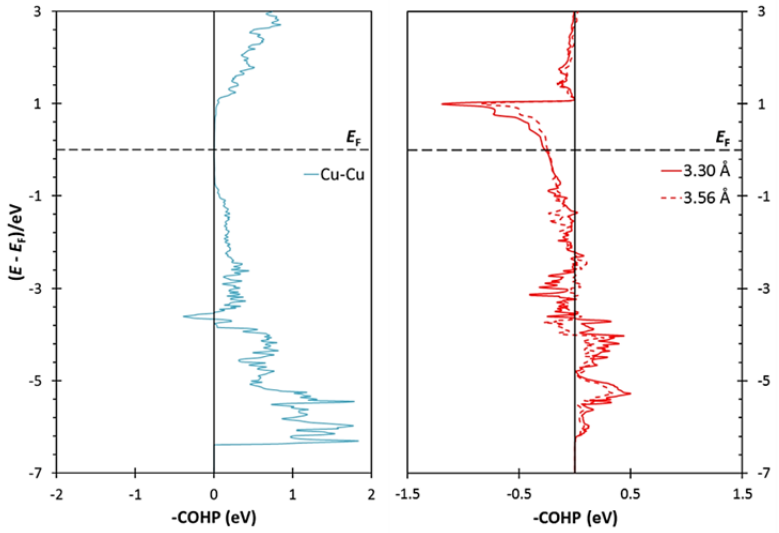

Figure 17.6 Crystal orbital Hamilton population (*COHP*) curves of $Ba_2Cu_7Te_6$. Cu–Cu interactions (left); Te–Te interactions (right).

17.3.3. Physical Property Measurements

In order to determine its suitability for the thermoelectric energy conversion as well as to verify the results of the band structure calculation, physical properties were measured for a polycrystalline bulk sample with nominal composition $Ba_2Cu_{6.6}Te_6$ up to 725 K (Figure 17.7), as no large single crystals could be grown. The previously-studied tellurides exhibit room temperature values of S = 88 $\mu V \cdot K^{-1}$ and σ = 126 $\Omega^{-1}cm^{-1}$ in case of $BaCu_2Te_2$,[261] S = 30 $\mu V \cdot K^{-1}$ and σ = 190 $\Omega^{-1}cm^{-1}$ in case of $Ba_3Cu_{13.88}Te_{12}$.[266] Seebeck coefficient values of $Ba_2Cu_{6.6}Te_6$ fell between +50 and +100 $\mu V \cdot K^{-1}$ for the full range of the measurement, showing a small but steady rise. Electrical conductivity was also reasonably steady with values falling from 180 $\Omega^{-1}cm^{-1}$ at 297 K to 167 $\Omega^{-1}cm^{-1}$ at 725 K, displaying a decreasing slope overall for the full measurement range. The values are thus intermediate between those of $BaCu_2Te_2$ and $Ba_3Cu_{13.88}Te_{12}$. Both physical property measurements are to be expected based on the aforementioned calculations; the band structure calculation predicts the compound's one-dimensional metal-like behaviour such as a gradually decreasing electrical conductivity with increasing temperature and intermediate Seebeck coefficient. The resulting power factor shows a very similar shape to the Seebeck coefficient with a room temperature value of 0.43 $\mu W \cdot cm^{-1}K^{-2}$, which reached 1.45 $\mu W \cdot cm^{-1}K^{-2}$ at 725 K.

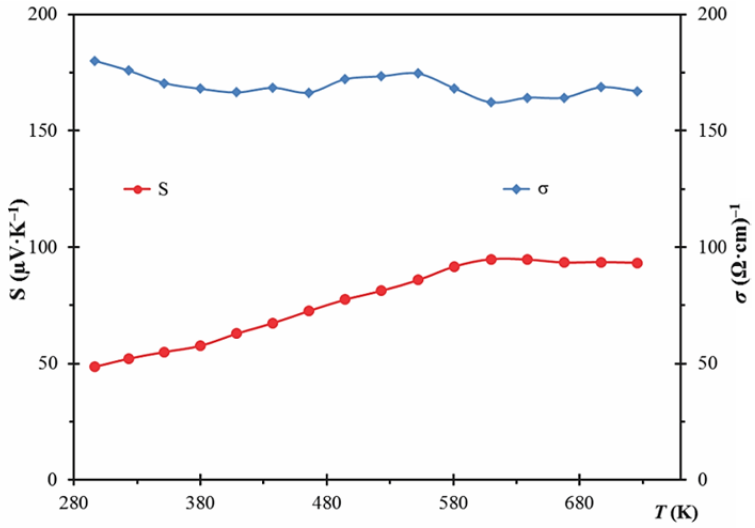

Figure 17.7 Seebeck coefficient (circle) and electrical conductivity (diamond) of $Ba_2Cu_{6.6}Te_6$.

The metallic character, even though persistent in only one direction, stands against using this telluride in the thermoelectric energy conversion, unless one succeeds in preparing a device wherein the metallic direction is exclusively perpendicular to the carrier transport direction, or one produces a more significant distortion into the Te chain leading to a band gap formation. While the latter occurs readily in form of a Peierls distortion[319] in many one-dimensional materials, such as in the Te chain of $RbUSb_{0.33}Te_6$,[320] this case already displays a distorted chain making a further introduction of a gap-opening distortion highly unlikely.

17.4. Conclusion

The new $Ba_2Cu_{7-x}Te_6$ telluride was discovered and characterized. Its crystal structure, determined by an X-ray structure determination, is of a new structure type with infinite zigzag chains of Cu_8-clusters and infinite distorted pseudo-linear chains of Te atoms. The band structure calculations show two steep bands arising from antibonding Te–Te interactions crossing the Fermi level parallel to *a**, pointing to one-dimensional metallic properties. The electrical conductivity and Seebeck measurements yielded values around 180 $\Omega^{-1}cm^{-1}$ and 50 $\mu V \cdot K^{-1}$, respectively, at room temperature. The power factor was found to be 1.45 $\mu W \cdot cm^{-1}K^{-2}$ at 750 K, which is low compared to advanced thermoelectrics. This material could on the other hand become a useful thermoelectric, if large single crystals of defined orientation could be grown, but thus far our attempts to do so failed (or a Peierls distortion be introduced).

Section VI – Supplementary Information

EndNote Bibliography, Tabulated Appendices

Bibliography

[1] Dawson, D., Plant-Covered Roofs Ease Urban Heat. In National Geographic: **2002**.

[2] Winder, E. J.; Ellis, A. B.; Lisensky, G. C., *J. Chem. Educ.* **1996,** 73, 940-946.

[3] Stabler, F. Benefits of Thermoelectric Technology for the Automobile. http://www1.eere.energy.gov/vehiclesandfuels/pdfs/thermoelectrics_app_2011/tuesday/stabler.pdf (Feb. 6),

[4] Rowe, D. M., *CRC Handbook of Thermoelectrics*. CRC Press: Boca Raton, FL, **1995**.

[5] Seebeck, T. J., *Magnetic Polarization of metals and minerals*. Berlin, **1822**.

[6] Slack, G. A., The Thermoelectrics of Bulk Materials: A History. In *30th International Conference on Thermoelectrics*, Traverse City, MI, **2011**.

[7] Peltier, J. C., *Ann. Chem. LVI, 371*: **1834**.

[8] Thomson, W. Proc. Roy. Soc. , Edinburgh, 1851; Edinburgh, **1851**.

[9] Strutt, M. J. O., *Ann. Phys. (Leipzig)* **1927,** 84, 485.

[10] Ioffe, A. F., *Semiconductor Thermoelements and Thermoelectric Cooling*. London, **1957**.

[11] Ioffe, A. F., *Fizika Tverdogo Tele.* **1960,** 2, 781 - 1032.

[12] Slack, G. A., *Solid State Phys.* **1979,** 34, 1-71.

[13] Rowe, D. M., *Thermoelectrics Handbook: Macro to Nano*. CRC Press, Taylor & Francis Group: Boca Raton, FL, USA, **2006**.

[14] Ravich, Y. I.; Efimova, B. A.; Smirnov, I. A., *Semiconducting Lead Chalcogenides*. Plenum Press: New York, **1970**.

[15] Christakudis, G. C.; Plachkova, S. K.; Shelimova, L. E.; Avilov, E. S. Eighth International Conference on Thermoelectric Energy Conversion, Nancy, France, 1989; Nancy, France, **1989**; p 125.

[16] Chung, D.-Y.; Hogan, T. P.; Rocci-Lane, M.; Brazis, P.; Ireland, J. R.; Kannewurf, C. R.; Bastea, M.; Uher, C.; Kanatzidis, M. G., *J. Am. Chem. Soc.* **2004,** 126, 6414-6428.

[17] Saramat, A.; Svensson, G.; Palmqvist, A. E. C.; Stiewe, C.; Mueller, E.; Platzek, D.; Williams, S. G. K.; Rowe, D. M.; Bryan, J. D.; Stucky, G. D., *J. Appl. Phys.* **2006,** 99, 023708/1-023708/5.

[18] Sales, B. C.; Mandrus, D.; Williams, R. K., *Science (Washington, D. C.)* **1996,** 272, 1325-1328.

[19] Quarez, E.; Hsu, K.-F.; Pcionek, R.; Frangis, N.; Polychroniadis, E. K.; Kanatzidis, M. G., *J. Am. Chem. Soc.* **2005,** 127, 9177-9190.

[20] Poudeu, P. F. P.; D'Angelo, J.; Downey, A. D.; Short, J. L.; Hogan, T. P.; Kanatzidis, M. G., *Angew. Chem. Int. Ed.* **2006,** 45, 3835-3839.

[21] Androulakis, J.; Pcionek, R.; Quarez, E.; Do, J.-H.; Kong, H.; Palchik, O.; Uher, C.; D'Angelo, J. J.; Short, J.; Hogan, T.; Kanatzidis, M. G., *Chem. Mater.* **2006,** 18, 4719-4721.

[22] Chitroub, M.; Besse, F.; Scherrer, H., *J. Alloys Compd.* **2008,** 460, 90-93.

[23] Zhu, G. H.; Lee, H.; Lan, Y. C.; Wang, X. W.; Joshi, G.; Wang, D. Z.; Yang, J.; Vashaee, D.; Guilbert, H.; Pillitteri, A.; Dresselhaus, M. S.; Chen, G.; Ren, Z. F., *Phys. Rev. Lett.* **2009,** 102, 196803/1-196803/4.

[24] Xu, J.; Kleinke, H., *J. Comput. Chem.* **2008,** 29, 2134-2143.

[25] Snyder, G. J.; Caillat, T., *Mater. Res. Soc. Symp. Proc.* **2004,** 793, 37-42.

[26] Greig, D., *Electrons in metals and semiconductors*. McGraw-Hill: London, UK, **1969**.

[27] Franz, R.; Wiedemann, G., *Ann. Phys.* **1853,** 165, 497-531.

[28] Tritt, T. M., *Thermal Conductivity: theory, properties, and applications*. Plenum Publishers: New York, **2004**.

[29] Sommerfeld, A., *Naturwissenschaften* **1927,** 15, 825.

[30] Kumar, G. S.; Prasad, G.; Pohl, R. O., *J. Mater. Sci.* **1993,** 28, 4261-4272.

[31] Snyder, G. J.; Toberer, E. S., *Nat. Mater.* **2008,** 7, 105-14.

[32] Yang, J.; Caillat, T., *MRS Bull.* **2006,** 31, 224-229.

[33] Rowe, D. M.; Kuznetsov, V. L.; Kuznetsova, L. A.; Min, G.; Williams, S. G. K.; Tilley, R. J. D.; Jones, R. W., *Adv. Sci. Technol. (Faenza, Italy)* **1999,** 24, 777-784.
[34] Willigan, R. R.; Hautman, D.; Krommenhoek, D.; Martin, P. *Cost-Effective Fabrication Routes for the Production of Quantum Well Structures and Recovery of Waste Heat from Heavy Duty Trucks*; United Technologies Research Center: Washington, D.C., **2006**.
[35] Sales, B. C.; Chakoumakos, B. C.; Jin, R.; Thompson, J. R.; Mandrus, D., *Phys. Rev.* **2001,** B63, 245113/1-245113/8.
[36] Hatzikraniotis, E.; Zorbas, K.; Kyratsi, T.; Paraskevopoulos, K. M., *Mater. Res. Soc. Symp. Proc.* **2009,** 1166, No pp given, Paper #: 1166-N03-14.
[37] LLC, S. The Igloo Online Store. http://www.igloo-store.com/detail/IGL+COOL+CHILL+40
[38] Bell, L. E., *Science* **2008,** 321, 1457-1461.
[39] Gould, C. A.; Shammas, N. Y. A.; Grainger, S.; Taylor, I., *Mater. Sci. Eng., B* **2011,** 176, 316-325.
[40] LaGrandeur, J.; Crane, D.; Ayers, S.; Maranville, C.; Eder, A.; Chiew, L. *High-Efficiency Thermoelectric Waste Energy Recovery System for Passenger Vehicle Applications*; Energy Efficiency and Renewable Energy Office of Vehicle Technologies: Washington, D.C., **2009**.
[41] Meisner, G. P.; Yang, J.; Salvador, J. R.; Reynolds, M. G. *Develop Thermoelectric Technology for Automotive Waste Heat Recovery* Energy Efficiency and Renewable Energy Office of Vehicle Technologies: Washington, D.C., **2009**.
[42] Schock, H.; Case, E. D.; Hogan, T. P.; Sakamoto, J.; Peng, F.; Timm, E.; Ruckle, R.; Winkelman, J. *Thermoelectric Conversion of Waste Heat to Electricity in an Internal Combustion Engine Vehicle*; Energy Efficiency and Renewable Energy Office of Vehicle Technologies: Washington, D.C., **2009**.
[43] Zhao, X. B.; Ji, X. H.; Zhang, Y. H.; Zhu, T. J.; Tu, J. P.; Zhang, X. B., *Appl. Phys. Lett.* **2005,** 86, 062111/1-062111/3.
[44] Skrabek, E. A.; Trimmer, D. S., Properties of the general TAGS system. In *CRC Handbook of Thermoelectrics*, Rowe, D. M., Ed. CRC Press: Boca Raton, FL, **1995**; pp 267-275.
[45] Tritt, T. M.; Nolas, G. S.; Mahan, G. D.; Mandrus, D.; Kanatzidis, M. G.; Editors, Thermoelectric Materials 2000--The Next Generation Materials for Small-Scale Refrigeration and Power Generation Applications. (Symposium held 24-27 April 2000, in San Francisco, California.) [In: Mater. Res. Soc. Symp. Proc., 2001; 626]. In **2001**; p No pp. given.
[46] Sharp, J. W., *Int. Conf. Thermoelectr.* **2003,** 22nd, 267-270.
[47] Chung, D.-Y.; Hogan, T.; Brazis, P.; Rocci-Lane, M.; Kannewurf, C.; Bastea, M.; Uher, C.; Kanatzidis, M. G., *Science* **2000,** 287, 1024-1027.
[48] Hogan, T. P.; Downey, A.; Short, J.; D'Angelo, J.; Wu, C.-I.; Quarez, E.; Androulakis, J.; Poudeu, P. F. P.; Sootsman, J. R.; Chung, D.-Y.; Kanatzidis, M. G.; Mahanti, S. D.; Timm, E. J.; Schock, H.; Ren, F.; Johnson, J.; Case, E. D., *J. Electron. Mater.* **2007,** 36, 704-710.
[49] Giacovazzo, C., *Fundamentals of Crystallography*. Second ed.; Oxford University Press: Oxford, **1992**.
[50] Müller, U., *Inorgainc Structural Chemistry*. Second ed.; Wiley & Sons: West Sussex, **2007**.
[51] Iversen, B. B.; Palmqvist, A. E. C.; Cox, D. E.; Nolas, G. S.; Stucky, G. D.; Blake, N. P.; Metiu, H., *J. Solid State Chem.* **2000,** 149, 455-458.
[52] Kleinke, H., *Chem. Mater.* **2010,** 22, 604-611.
[53] Brown, A., *Nature* **1965,** 206, 502-503.
[54] Brown, S. R.; Kauzlarich, S. M.; Gascoin, F.; Snyder, G. J., *Chem. Mater.* **2006,** 18, 1873-1877.
[55] Dashjav, E.; Szczepenowska, A.; Kleinke, H., *J. Mater. Chem.* **2002,** 12, 345-349.
[56] Braun, D. J.; Jeitschko, W., *J. Less-Common Met.* **1980,** 72, 147-156.
[57] Caillat, T. F., J. P.; Borshchevsky, A., *J. Phys. Chem. Solids* **1997,** 58, 1119-1125.
[58] Koza, M. M.; Johnson, M. R.; Viennois, R.; Mutka, H.; Girard, L.; Ravot, D., *Nat. Mater.* **2008,** 7, 805-810.

[59] Zhang, H.; He, J.; Zhang, B.; Su, Z.; Tritt, T. M.; Soheilnia, N.; Kleinke, H., *J. Electron. Mater.* **2007,** 36, 727-731.
[60] Holgate, T.; Su, Z.; He, J.; Tritt, T. M.; Xu, H.; Kleinke, K. M.; Kleinke, H., *MS&T 08 Conf. Proc.* **2008**, 436-443.
[61] Soheilnia, N.; Dashjav, E.; Kleinke, H., *Can. J. Chem.* **2003,** 81, 1157-1163.
[62] Yao, T., *Appl. Phys. Lett.* **1987,** 51, 1798-800.
[63] Harman, T. C.; Taylor, P. J.; Walsh, M. P.; LaForge, B. E., *Science* **2002,** 297, 2229-2232.
[64] Vineis, C. J.; Shakouri, A.; Majumdar, A.; Kanatzidis, M. G., *Adv. Mater. (Weinheim, Ger.)* **2010,** 22, 3970-3980.
[65] Boukai, A. I.; Bunimovich, Y.; Tahir-Kheli, J.; Yu, J.-K.; Goddard, W. A., III; Heath, J. R., *Nature (London, U. K.)* **2008,** 451, 168-171.
[66] Hochbaum, A. I.; Chen, R.; Delgado, R. D.; Liang, W.; Garnett, E. C.; Najarian, M.; Majumdar, A.; Yang, P., *Nature (London, U. K.)* **2008,** 451, 163-167.
[67] Li, L.; Yang, Y.; Huang, X.; Li, G.; Zhang, L., *Nanotechnology* **2006,** 17, 1706-1712.
[68] Heremans, J. P., *Springer Handb. Nanotechnol. (2nd Ed.)* **2007**, 345-373.
[69] Venkatasubramanian, R.; Slivola, E.; Colpitts, T.; O'Quinn, B., *Nature* **2001,** 413, 597-602.
[70] Venkatasubramanian, R., *Phys. Rev. B Condens. Matter Mater. Phys.* **2000,** 61, 3091-3097.
[71] Zide, J. M. O.; Vashaee, D.; Bian, Z. X.; Zeng, G.; Bowers, J. E.; Shakouri, A.; Gossard, A. C., *Phys. Rev. B Condens. Matter Mater. Phys.* **2006,** 74, 205335/1-205335/5.
[72] Caylor, J. C.; Coonley, K.; Stuart, J.; Colpitts, T.; Venkatasubramanian, R., *Appl. Phys. Lett.* **2005,** 87, 023105/1-023105/3.
[73] Chiritescu, C.; Cahill, D. G.; Nguyen, N.; Johnson, D.; Bodapati, A.; Keblinski, P.; Zschack, P., *Science (Washington, DC, U. S.)* **2007,** 315, 351-353.
[74] Liu, J. L.; Wan, J.; Wang, K. L.; Yu, D. P., *J. Cryst. Growth* **2003,** 251, 666-669.
[75] Wang, W.; Huang, Q.; Jia, F.; Zhu, J., *J. Appl. Phys.* **2004,** 96, 615-618.
[76] Slack, G. A., New Materials and Performance Limits for Thermoelectric Cooling. In *CRC Handbook of Thermoelectrics*, Rowe, D. M., Ed. CRC Press: Boca Raton, FL, **1995**; pp 407-440.
[77] Snyder, G. J.; Christensen, M.; Nishibori, E.; Caillat, T.; Iversen, B. B., *Nat. Mater.* **2004,** 3, 458-463.
[78] Hsu, K. F.; Loo, S.; Guo, F.; Chen, W.; Dyck, J. S.; Uher, C.; Hogan, T.; Polychroniadis, E. K.; Kanatzidis, M. G., *Science* **2004,** 303, 818-821.
[79] Guéguen, A.; Poudeu, P. F. P.; Li, C.-P.; Moses, S.; Uher, C.; He, J.; Dravid, V.; Paraskevopoulos, K. M.; Kanatzidis, M. G., *Chem. Mater.* **2009,** 21, 1683-1694.
[80] Cook, B. A.; Kramer, M. J.; Harringa, J. L.; Han, M.-K.; Chung, D.-Y.; Kanatzidis, M. G., *Adv. Funct. Mater.* **2009,** 19, 1254-1259.
[81] Kanatzidis, M. G., *Chem. Mater.* **2010,** 22, 648-659.
[82] Powell, A. V.; Guinet, F.; Vaqueiro, P.; Wilcock, I. M.; Jones, R. L., *Mater. Res. Soc. Symp. Proc.* **2008,** 1044, No pp given, Paper #: 1044-U08-04.
[83] Stout, G. H.; Jensen, L. H., *X-Ray Structure Determination*. Second ed.; Wiley & Sons: New York, **1989**.
[84] West, A. R., *Solid Sate Chemistry and its Applications*. John Wiley & Sons Ltd.: New York, **1984**.
[85] Tilley, R. J. D., *Defects in Solids*. John Wiley & Sons Inc.: New Jersey, **2008**.
[86] Mizushima, K.; Jones, P. C.; Wiseman, P. J.; Goodenough, J. B., *Ferrites, Proc. ICF, 3rd* **1982**, 425-428.
[87] Wolverton, C.; Zunger, A., *J. Electrochem. Soc.* **1998,** 145, 2424-2431.
[88] He, J.; Sootsman, J. R.; Girard, S. N.; Zheng, J.-C.; Wen, J.; Zhu, Y.; Kanatzidis, M. G.; Dravid, V. P., *J. Am. Chem. Soc.* **2010,** 132, 8669-8675.
[89] Seeger, K., *Semiconductor Physics An Introduction*. 9th ed.; Springer: Berlin, **2004**.

[90] Albright, T. A.; Burdett, J. K.; Whangbo, M. H., *Orbital Interactions in Chemistry*. Wiley and Sons: **1984**.
[91] Hoffman, R., *Solids and Surfaces: a Chemist's View of Bonding in Extended Strctures*. VCH: **1988**.
[92] Huheey, J. E.; Keiter, E. A.; Keiter, R. L., *Inorganic Chemistry: Principles of Structure and Reactivity*. Fourth ed.; HarperCollins College Publishers: New York, **1993**.
[93] Kittel, C., *Introduction to Solid State Physics*. John Wiley & Sons Inc.: New York, **1971**.
[94] Hoffmann, R., *Angew. Chem. Int. Ed. Engl.* **1987,** 26, 846-878.
[95] Williams, J. M., *Adv. Inorg. Chem. Radiochem.* **1983,** 26, 235-68.
[96] Dronskowski, R.; Blöchl, P. E., *J. Phys. Chem.* **1993,** 97, 8617-24.
[97] Institute of Inorganic Chemistry COHP Pages. www.cohp.de
[98] Mott, N. F.; Jones, H., *The Theory of the Properties of Metals and Alloys*. Dover Publications: New York, NY, **1958**; p 310.
[99] Rao, A. M.; Ji, X.; Tritt, T. M., *MRS Bull.* **2006,** 31, 218-223.
[100] Mahan, G. D.; Sofo, J. O., *Proc. Natl. Acad. Sci. U. S. A.* **1996,** 93, 7436-7439.
[101] Ryabova, L. I.; Khokhlov, D. R., *JETP Lett.* **2004,** 80, 133-139.
[102] Lent, C. S.; Bowen, M. A.; Allgaier, R. S.; Dow, J. D.; Sankey, O. F.; Ho, E. S., *Solid State Commun.* **1987,** 61, 83-7.
[103] Ahmad, S.; Hoang, K.; Mahanti, S. D., *Phys. Rev. Lett.* **2006,** 96, 056403/1-056403/4.
[104] Heremans, J. P.; Jovovic, V.; Toberer, E. S.; Saramat, A.; Kurosaki, K.; Charoenphakdee, A.; Yamanaka, S.; Snyder, G. J., *Science* **2008,** 321, 554-557.
[105] Hicks, L. D.; Dresselhaus, M. S., *Phys. Rev. B Condens. Matter* **1993,** 47, 12727-12731.
[106] Szczech, J. R.; Higgins, J. M.; Jin, S., *J. Mater. Chem.* **2011,** 21, 4037-4055.
[107] Vaqueiro, P.; Powell, A. V., *J. Mater. Chem.* **2010,** 20, 9577-9584.
[108] Slack, G. A.; Hussain, M. A., *J. Appl. Phys.* **1991,** 70, 2694-2718.
[109] Kim, W.; Zide, J.; Gossard, A.; Klenov, D.; Stemmer, S.; Shakouri, A.; Majumdar, A., *Phys. Rev. Lett.* **2006,** 96, 045901.
[110] Kim, W.; Singer, S. L.; Majumdar, A.; Vashaee, D.; Bian, Z.; Shakouri, A.; Zeng, G.; Bowers, J. E.; Zide, J. M. O.; Gossard, A. C., *Appl. Phys. Lett.* **2006,** 88, 242107/1-242107/3.
[111] Poudel, B.; Hao, Q.; Ma, Y.; Lan, Y.; Minnich, A.; Yu, B.; Yan, X.; Wang, D.; Muto, A.; Vashaee, D.; Chen, X.; Liu, J.; Dresselhaus, M. S.; Chen, G.; Ren, Z., *Science* **2008,** 320, 634-638.
[112] Bux, S. K.; Blair, R. G.; Gogna, P. K.; Lee, H.; Chen, G.; Dresselhaus, M. S.; Kaner, R. B.; Fleurial, J.-P., *Adv. Funct. Mater.* **2009,** 19, 2445-2452.
[113] Mi, J. L.; Zhao, X. B.; Zhu, T. J.; Tu, J. P., *Appl. Phys. Lett.* **2007,** 91, 172116/1-172116/3.
[114] Sumanasekera, G. U.; Pradhan, B. K.; Romero, H. E.; Adu, K. W.; Eklund, P. C., *Phys. Rev. Lett.* **2002,** 89, 166801/1-166801/4.
[115] Meng, C.; Liu, C.; Fan, S., *Adv. Mater. (Weinheim, Ger.)* **2010,** 22, 535-539.
[116] Yan, X.; Joshi, G.; Liu, W.; Lan, Y.; Wang, H.; Lee, S.; Simonson, J. W.; Poon, S. J.; Tritt, T. M.; Chen, G.; Ren, Z. F., *Nano Lett.* **2011,** 11, 556-560.
[117] Winter, M. WebElements: the periodic table on the web. http://www.webelements.com/
[118] Lam, R.; Mar, A., *Inorg. Chem.* **1996,** 35, 6959-6963.
[119] Lam, R.; Mar, A., *Solid State Sci.* **2001,** 3, 503-512.
[120] Kanatzidis, M. G.; Pöttgen, R.; Jeitschko, W., *Angew. Chem. Int. Ed.* **2005,** 44, 6996-7023.
[121] FTsalt - FACT Salt Phase Diagrams. http://www.crct.polymtl.ca/fact/documentation/FTsalt/FTsalt_Figs.htm
[122] Yu, F.; Zhang, J.; Yu, D.; He, J.; Liu, Z.; Xu, B.; Tian, Y., *J. Appl. Phys.* **2009,** 105, 094303/1-094303/5.
[123] Laue, M. v., *Sitz. math. phys. Klasse Bayer. Akad. Wiss.* **1912**.
[124] Bragg, W. L. Proc. Camb. Phil. Soc., 1913; **1913**; pp 43 - 57.

[125] Pecharsky, V. K.; Zavalij, P. Y., *Fundamentals of Powder Diffraction and Structural Characterization of Materials*. 2nd ed.; Springer: New York, **2009**.
[126] Will, G., *Powder Diffraction: The Rietveld Method and the Two-Stage Method*. Springer: Berlin Heidelberg, **2006**.
[127] Bruker, A. I., *M86-Exx078 APEX2 User Manual*. Madison, WI, **2006**.
[128] *SAINT*. Version 4 ed.; Siemens Analytical X-ray Instruments Inc.: Madison, WI., **1995**.
[129] Patterson, A. L., *Z. Krist.* **1935,** A90, 517.
[130] Sheldrick, G. M., *SHELXTL*. Version 5.12 ed.; Siemens Analytical X-Ray Systems: Madison, WI., **1995**.
[131] Sheldrick, G. M., *Acta Crystallogr.* **2008,** 64, 112 - 122.
[132] Larson, L. C.; von Dreele, R. B. *Generalized Structural Analysis System (GSAS)*; LANSCE, MSH805, Los Alamos National Laboratory, NM 87545, USA: **1995**.
[133] Larson, A. C.; von Dreele, R. B. *GSAS-General Structure Analysis System*; Los Alamos National Laboratory: Los Alamos, NM: **2000**.
[134] Toby, B. H., *J. Appl. Crystallogr.* **2001,** 34, 210-213.
[135] Cranswick, L. Collaborative Computational Project No. 14. www.ccp14.uk/
[136] Shirley, R., *The Crysfire 2002 System of Automatic Powder Indexing: User's Manual*. http://www.ccp14.ac.uk/tutorial/crys/: **2002**.
[137] David, W. I. F.; Shankland, K.; van de Streek, J.; Pidcock, E.; Motherwell, W. D. S.; Cole, J. C., *J. Appl. Cryst.* **2006,** 39, 910 - 915.
[138] Favre-Nicolin, V.; Cerny, R., *J. Appl. Cryst.* **2002,** 35, 734 - 743.
[139] Rietveld, H. M., *Acta Crystallogr.* **1967,** 22, 151-2.
[140] Loopstra, B. O.; Rietveld, H. M., *Acta Crystallogr., Sect. B* **1969,** 25, 787-91.
[141] Malmros, G.; Thomals, J. O., *J. Appl. Crystallogr.* **1977,** 10, 7.
[142] Young, R. A., *The Rietveld Method*. Oxford University Press: Oxford, **2002**.
[143] Cagliotti, G.; Paoletti, A.; Ricci, E. P., *Nucl. Instru. Methods* **1958,** 3, 223 - 228.
[144] Baerlocher, C. 6th International Zeolite Conference, 1984; Butterworth Scientific: **1984**.
[145] Le Bail, A.; Duroy, H.; Fourquet, J. L., *Mater. Res. Bull.* **1988,** 23, 447-52.
[146] Le Bail, A.; Fourquet, J. L., *Mater. Res. Bull.* **1992,** 27, 75-85.
[147] Wang, H.; Porter, W. D.; Böttner, H.; König, J.; Chen, L.; Bai, S.; Tritt, T. M.; Mayolett, A.; Senawiratne, J.; Smith, C.; Harris, F.; Sharp, J.; Lo, J.; Kleinke, H.; Kiss, L. I. *Annex VIII - Thermoelectric Materials For Waste Heat Recovery: An International Collaboration For Transportation Applications*; UT-Battelle: Oak Ridge National Laboratory, TN, **2012 (to be published)**.
[148] Watson, E. S.; O'Neil, M. J. Differential Microcalorimeter. **1962**.
[149] Mackenzie, R. C., *Differential Thermal Analysis*. Academic Press Inc.: London and New York, **1970**; Vol. 1.
[150] Blumm, J. Improving Zirconia Ceramics through Thermoanalytical Characterization. http://www.ceramicindustry.com/Articles/Feature_Article/9ee47442bbac7010VgnVCM100000f932a8c0____
[151] Group, N., *STA 409 PC Luxx User Manual*. Selb, Germany, **1998**.
[152] Höhne, G.; Hemminger, W.; Flammersheim, H.-J., *Differential Scanning Calorimetry: An Introduction for Practitioners*. Springer: Berlin Heidelberg, **1996**.
[153] Andersen, O. K., *Phys. Rev. B* **1975,** 12, 3060-3083.
[154] Skriver, H. L., *The LMTO Method*. Springer: Berlin, Germany, **1984**.
[155] Blaha, P.; Schwarz, K.; Madsen, G. K. H.; Kvasnicka, D.; Luitz, J., *WIEN2k, An Augmented Plane Wave + Local Orbitals Program for Calculating Crystal Properties*. Techn. Universität Wien, Austria, **2001**.

[156] Cottenier, S., Density Functional Theory and the family of (L)APW-methods: a step-by-step introduction. In Instituut voor Kern- en Stralingsfyica: K.U.Leuven, Belgium, **2002**.
[157] Hohenberg, P.; Kohn, W., *Physical Reviews* **1964,** 136, B864.
[158] Kohn, W. S., L. J. , *Phys. Rev.* **1965,** 140, 1133.
[159] Springborg, M., *Methods of Electronic-Structure Calculations*. Wiley: New York, **2000**.
[160] Vosko, S. H.; Wilk, L., *Phys. Rev. B Condens. Matter* **1980,** 22, 3812-15.
[161] Hedin, L.; Lundqvist, B. I., *Journal of Physics Part C Solid State Physics* **1971,** 4, 2064-2083.
[162] Koch, W.; Holthausen, M. C., *A Chemist's Guide to Density Functional Theory*. Wiley-VCH: Weinheim, **2000**.
[163] Schwarz, K., *J. Solid State Chem.* **2003,** 176, 319-328.
[164] Perdew, J. P.; Burke, K.; Ernzerhof, M., *Phys. Rev. Lett.* **1996,** 77, 3865-3868.
[165] Madsen, G. K. H.; Singh, D. J., *Comput. Phys. Commun.* **2006,** 175, 67-71.
[166] Han, M.-K.; Ahn, K.-H.; Kim, H.-J.; Rhyee, J.-S.; Kim, S.-J., *J. Mater. Chem.* **2011,** 21, 11365-11370.
[167] Dresselhaus, M. S.; Chen, G.; Ren, Z. F.; Dresselhaus, G.; Henry, A.; Fleurial, J. P., *JOM* **2009,** 61, 86-90.
[168] Abdullaev, N. A.; Kakhramanov, S. S.; Kerimova, T. G.; Mustafayeva, K. M.; Nemov, S. A., *Semiconductors* **2009,** 43, 145-151.
[169] Feutelais, Y.; Legendre, B.; Rodier, N.; Agafonov, V., *Mater. Res. Bull.* **1993,** 28, 591-596.
[170] Yavorsky, B. Y.; Hinsche, N. F.; Mertig, I.; Zahn, P., *Phys. Rev. B: Condens. Matter Mater. Phys.* **2011,** 84, 165208/1-165208/7.
[171] Hashibon, A.; Elsasser, C., *Phys. Rev. B: Condens. Matter Mater. Phys.* **2011,** 84, 144117/1-144117/9.
[172] Wang, G.; Endicott, L.; Uher, C., *Sci. Adv. Mater.* **2011,** 3, 539-560.
[173] Qiu, B.; Sun, L.; Ruan, X., *Phys. Rev. B Condens. Matter Mater. Phys.* **2011,** 83, 035312/1-035312/7.
[174] Georgobiani, A. N.; Pashaev, A. M.; Tagiev, B. G.; Aleskerov, F. K.; Tagiev, O. B.; Kakhramanov, K. S., *Inorg. Mater.* **2011,** 47, 1319-1323.
[175] Pinisetty, D.; Haldolaarachchige, N.; Young, D. P.; Devireddy, R. V., *J. Nanotechnol. Eng. Med.* **2011,** 2, 011006/1-011006/5.
[176] Tritt, T. M., In *CRC Handbook on Thermoelectrics*, Rowe, D. M., Ed. CRC press: Boca Raton, FL, USA, **2005**.
[177] Zemskov, V. S.; Shelimova, L. E.; Karpinskii, O. G.; Konstantinov, P. P.; Avilov, E. S.; Kretova, M. A., *J. Thermoelectr.* **2010**, 15 - 29.
[178] Karpinskii, O. G.; Shelimova, L. E.; Avilov, E. S.; Kretova, M. A.; Zemskov, V. S., *Inorg. Mater.* **2002,** 38, 17-24.
[179] Shelimova, L. E.; Karpinskii, O. G.; Konstantinov, P. P.; Avilov, E. S.; Kretova, M. A.; Zemskov, V. S., *Inorg. Mater.* **2004,** 40, 451-460.
[180] Karpinskii, O. G.; Shelimova, L. E.; Kretova, M. A.; Avilov, E. S.; Zemskov, V. S., *Inorg. Mater.* **2003,** 39, 240-246.
[181] Abrikosov, N. K.; Elagina, E. I.; Tskhadaya, R. A., *Izv. Akad. Nauk SSSR, Neorg. Mater.* **1975,** 11, 2083-2084.
[182] Kuznetsov, V. L.; Kuznetsova, L. A.; Kaliazin, A. E.; Rowe, D. M., Preparation and thermoelectric properties of $A\text{II}_8B\text{III}_{16}B\text{IV}_{30}$ clathrate compounds. In *Proc. Intern. Conf. Thermoelectrics*, **1999**; Vol. 18th, pp 177-180.
[183] Kuznetsova, L. A.; Kuznetsov, V. L.; Rowe, D. M., *J. Phys. Chem. Solids* **2000,** 61, 1269-1274.
[184] Caillat, T.; Huang, C. K.; Fleurial, J. P.; Snyder, G. J.; Borshchevsky, A. *Synthesis and thermoelectric properties of some materials with the $PbBi_4Te_7$ crystal structure*, Intern. Conf. Thermoel., 2000; **2000**; pp 151-154.

[185] Shelimova, L. E.; Karpinskii, O. G.; Svechnikova, T. E.; Avilov, E. S.; Kretova, M. A.; Zemskov, V. S., *Inorg. Mater.* **2004,** 40, 1264-1270.
[186] Kuznetsov, V. L.; Kuznetsova, L. A.; Rowe, D. M., *J. Phys. D Appl. Phys.* **2001,** 34, 700-703.
[187] Shelimova, L. E.; Karpinskii, O. G.; Konstantinov, P. P.; Kretova, M. A.; Avilov, E. S.; Zemskov, V. S., *Inorg. Mater.* **2002,** 38, 790-794.
[188] Oosawa, Y.; Tateno, Y.; Mukaida, M.; Tsunoda, T.; Imai, Y.; Isoda, Y.; Nishida, I. A. *$PbBi_2Te_4$ and $PbBi_4Te_7$, thermoelectric materials in the system of Pb-Bi-Te*, Intern. Conf. Thermoel., 1999; **1999**; pp 550-553.
[189] Mu, T. Thermoelectric Properties of Ternary Tellurides and Quaternary Derivative of Tl_9BiTe_6. University of Waterloo, Waterloo, Ontario, Canada, **2010**.
[190] Gelbstein, Y.; Dashevsky, Z.; Dariel, M. P., *Physica B* **2005,** 363, 196-205.
[191] Kuznetsov, V. L.; Kuznetsova, L. A.; Rowe, D. M. *Effect of nonstoichiometry on the electrical transport properties of $SnBi_4Te_7$ and $PbBi_4Te_7$*, Intern. Conf. Thermoel., 2000; **2000**; pp 174-177.
[192] Reynolds, R. A., *J. Electrochem. Soc.* **1967,** 114, 526-529.
[193] Zhukova, T. B.; Zaslavskii, A. I., *Kristallografiya* **1971,** 16, 918-922.
[194] Zhukova, T. B.; Kutasov, V. A.; Parfen'eva, L. S.; Smirnov, I. A., *Izv. Akad. Nauk SSSR, Neorg. Mater.* **1974,** 10, 2221-2222.
[195] Petrov, I. I.; Imamov, R. M., *Kristallografiya* **1970,** 15, 168-70.
[196] Goldak, J.; Barrett, C. S.; Innes, D.; Youdelis, W., *J. Chem. Phys.* **1966,** 44, 3323-5.
[197] Zhukova, T. B.; Zaslavskii, A. I., *Kristallografiya* **1967,** 12, 37-41.
[198] Matsunaga, T.; Kojima, R.; Yamada, N.; Kifune, K.; Kubota, Y.; Takata, M., *Acta Crystallogr., Sect. B* **2007,** 63, 346-52.
[199] Wagner, J. W.; Woolley, J. C., *Mater. Res. Bull.* **1967,** 2, 1055-62.
[200] Petrov, I. I.; Imamov, R. M., *Kristallografiya* **1969,** 14, 699-703.
[201] Imai, Y.; Watanabe, A., *Intermet.* **2003,** 11, 451-458.
[202] Lambrecht, W. R. L.; Andersen, O. K., *Phys. Rev. B* **1986,** 34, 2439-2449.
[203] Blöchl, P. E.; Jepsen, O.; Andersen, O. K., *Phys. Rev. B* **1994,** 49, 16223-16233.
[204] Masri, P., *Mod. Phys. Lett. B* **1991,** 5, 95-100.
[205] Shelimova, L. E.; Konstantinov, P. P.; Kretova, M. A.; Avilov, E. S.; Zemskov, V. S., *Inorg. Mater.* **2004,** 40, 461-467.
[206] Ikeda, T.; Toussaint, M. B.; Bergum, K.; Iwanaga, S.; Snyder, J. G., *J. Mater. Sci.* **2011,** 46, 3846-3854.
[207] Karpinskii, O. G.; Shelimova, L. E.; Kretova, M. A., *Inorg. Mater. (Transl. of Neorg. Mater.)* **1997,** 33, 793-797.
[208] Shelimova, L. E.; Karpinskii, O. G.; Svechnikova, T. E.; Nikhezina, I. Y.; Avilov, E. S.; Kretova, M. A.; Zemskov, V. S., *Inorg. Mater.* **2008,** 44, 371-376.
[209] Guch, M.; Sankar, C. R.; Salvador, J. R.; Meisner, G. P.; Kleinke, H., *J. Appl. Phys.* **2012,** 111, 063706.
[210] Agaev, K. A.; Talybov, A. G.; Semiletov, S. A., *Kristallografiya* **1968,** 13, 59-62.
[211] Ledda, F.; Muntoni, C.; Serci, S.; Pellerito, L., *Chem. Phys. Lett.* **1987,** 134, 545-548.
[212] Hoang, K.; Mahanti, S. D.; Kanatzidis, M. G., *Phys. Rev. B Condens. Matter Mater. Phys.* **2010,** 81, 115106/1-115106/15.
[213] Cerny, R.; Joubert, J. M.; Filinchuk, Y.; Feutelais, Y., *Acta Crystallogr. C* **2002,** 58, i63-i65.
[214] Doert, T.; Cardoso Gil, R. H.; Böttcher, P., *Z. Anorg. Allg. Chem.* **1999,** 625, 2160-2163.
[215] Burkhardt, K.; Schubert, K., *J. Less-Common Metals* **1969,** 18, 426-9.
[216] Matsumoto, H.; Kurosaki, K.; Muta, H.; Yamanaka, S., *Mater. Trans.* **2009,** 50, 1582-1585.
[217] Nordell, K. J.; Miller, G. J., *J. Alloys Compd.* **1996,** 241, 51-62.
[218] Man, L. I.; Imamov, R. M.; Pinsker, Z. G., *Kristallografiya* **1971,** 16, 122-6.

[219] Toure, A. A.; Kra, G.; Eholie, R.; Olivier-Fourcade, J.; Jumas, J. C., *J. Solid State Chem.* **1990,** 87, 229-36.
[220] Marsh, R. E., *J. Solid State Chem.* **1991,** 92, 594-5.
[221] Schewe, I.; Böttcher, P.; von Schnering, H. G., *Z. Kristallogr.* **1989,** 188, 287-298.
[222] Wölfing, B.; Kloc, C.; Teubner, J.; Bucher, E., *Phys. Rev. Lett.* **2001,** 86, 4350-4353.
[223] Tao, X.-M.; Jund, P.; Viennois, R.; Tedenac, J.-C., *J. Phys. Chem. A* **2011,** 115, 8761-8766.
[224] Jund, P.; Tao, X.; Viennois, R.; Tedenac, J.-C., *arXiv.org, e-Print Arch., Condens. Matter* **2011**, 1-8, arXiv:1111 0534v1 [cond-mat mtrl-sci].
[225] Stasova, M. M.; Vainshtein, B. K., *Kristallografiya* **1958,** 3, 141-7.
[226] Imamalieva, S. Z.; Sadygov, F. M.; Babanly, M. B., *Inorg. Mater.* **2008,** 44, 935-938.
[227] Babanly, M. B.; Imamalieva, S. Z.; Babanly, D. M.; Sadygov, F. M., *Azerb. Khim. Zh.* **2009**, 122-125.
[228] Babanly, M. B.; Tedenac, J. C.; Imamalieva, S. Z.; Guseynov, F. N.; Dashdieva, G. B., *J. Alloys Compd.* **2009,** 491, 230-236.
[229] Bradtmöller, S.; Böttcher, P., *Z. Anorg. Allg. Chem.* **1993,** 619, 1155-1160.
[230] Bradtmöeller, S.; Kremer, R. K.; Böettcher, P., *Z. Anorg. Allg. Chem.* **1994,** 620, 1073-80.
[231] Bradtmöeller, S.; Böettcher, P., *Z. Anorg. Allg. Chem.* **1993,** 619, 1155-60.
[232] Doert, T.; Böttcher, P., *Z. Kristallogr.* **1994,** 209, 96-96.
[233] Latypov, Z. M.; Faizullina, N. R.; Sagitov, R. N.; Savel'ev, V. P., *Izv. Akad. Nauk SSSR, Neorg. Mater.* **1988,** 24, 1920-1921.
[234] Wölfing, B. Tl_9BiTe_6 A New Thermoelectric Material with Record Efficiencies. Ph.D., Universitat Konstanz, Fachbereich Physik, **2001**.
[235] Kurosaki, K.; Goto, K.; Kosuga, A.; Muta, H.; Yamanaka, S., *Mat. Res. Soc. Symp. Proc.* **2006,** 886, 281-286.
[236] Bangarigadu-Sanasy, S.; Sankar, C. R.; Assoud, A.; Kleinke, H., *Dalton Trans.* **2011,** 40, 862-867.
[237] Kosuga, A.; Kurosaki, K.; Muta, H.; Yamanaka, S., *J. Appl. Phys.* **2006,** 99, 063705/1-063705/4.
[238] Klepp, K. O.; Ecker, P., *J. Solid State Chem.* **1995,** 117, 351-5.
[239] Sharp, J. W.; Sales, B. C.; Mandrus, D. G.; Chakoumakos, B. C., *Appl. Phys. Lett.* **1999,** 74, 3794-3796.
[240] Kurosaki, K.; Goto, K.; Muta, H.; Yamanaka, S., *Mater. Trans.* **2007,** 48, 2083-2087.
[241] Kurosaki, K.; Uneda, H.; Muta, H.; Yamanaka, S., *J. Alloys Compd.* **2004,** 376, 43-48.
[242] Kurosaki, K.; Kosuga, A.; Yamanaka, S., *J. Alloys Compd.* **2003,** 351, 279-282.
[243] Kurosaki, K.; Kosuga, A.; Muta, H.; Uno, M.; Yamanaka, S., *Appl. Phys. Lett.* **2005,** 87, 061919/1-061919/3.
[244] Doert, T.; Böttcher, P., *Z. Kristallogr.* **1994,** 209, 95-95.
[245] Kuropatwa, B. A.; Assoud, A.; Kleinke, H., *J. Alloys Compd.* **2011,** 509, 6768-6772.
[246] Bhan, S.; Schubert, K., *Journal of the Less-Common Metals* **1970,** 20, 229-235.
[247] Goldsmid, H. J.; Sharp, J. W., *J. Electron. Mater.* **1999,** 28, 869-872.
[248] E. Dichi, M. S., G. Kra, *J. Alloys Compd.* **2008,** 458, 109-114.
[249] Yamanaka, S.; Kosuga, A.; Kurosaki, K., *J. Alloys Compd.* **2003,** 352, 275-278.
[250] Wölfing, B.; Kloc, C.; Ramirez, A.; Bucher, E., *Int. Conf. Thermoelectr.* **1999,** 18th, 546-549.
[251] Teubner, J. T. Optimization of High Efficiency Thermoelectrics based on Tl_5Te_3. Universität Konstanz, Fachbereich Physik, **2001**.
[252] Kurosaki, K.; Kosuga, A.; Muta, H.; Yamanaka, S., *Mater. Trans.* **2005,** 46, 1502-1505.
[253] Voroshilov, Y. V.; Gurzan, M. I.; Kish, Z. Z.; Lada, L. V., *Izv. Akad. Nauk SSSR, Neorg. Mater.* **1988,** 24, 1479-84.
[254] Lin, H.; Markiewicz, R. S.; Wray, L. A.; Fu, L.; Hasan, M. Z.; Bansil, A., *Phys. Rev. Lett.* **2010,** 105, 036404/1-036404/4.
[255] Kosbar, L. L.; Murray, C. E.; Copel, M.; Afzali, A.; Mitzi, D. B., *Nature* **2004,** 428, 299-303.

[256] Tarascon, J.-M.; Armand, M., *Nature* **2001,** 414, 359-367.
[257] Atwood, G., *Science* **2008,** 321, 210-211.
[258] Lencer, D.; Salinga, M.; Grabowski, B.; Hickel, T.; Neugebauer, J.; Wuttig, M., *Nat. Mater.* **2008,** 7, 972-977.
[259] Yamada, N.; Wuttig, M., *Nat. Mater.* **2007,** 6, 824-832.
[260] Graf, C.; Assoud, A.; Mayasree, O.; Kleinke, H., *Molecules* **2009,** 14, 3115-3131.
[261] Wang, Y. C.; DiSalvo, F. J., *J. Solid State Chem.* **2001,** 156, 44-50.
[262] Tritt, T. M., *Science* **1995,** 272, 1276-1277.
[263] DiSalvo, F. J., *Science* **1999,** 285, 703-706.
[264] Patschke, R.; Zhang, X.; Singh, D.; Schindler, J.; Kannewurf, C. R.; Lowhorn, N.; Tritt, T.; Nolas, G. S.; Kanatzidis, M. G., *Chem. Mater.* **2001,** 13, 613-621.
[265] Assoud, A.; Xu, J.; Kleinke, H., *Inorg. Chem.* **2007,** 46, 9906-9911.
[266] Assoud, A.; Thomas, S.; Sutherland, B.; Zhang, H.; Tritt, T. M.; Kleinke, H., *Chem. Mater.* **2006,** 18, 3866-3872.
[267] Cui, Y.; Assoud, A.; Xu, J.; Kleinke, H., *Inorg. Chem.* **2007,** 46, 1215 - 1221.
[268] Mayasree, O.; Cui, Y. J.; Assoud, A.; Kleinke, H., *Inorg. Chem.* **2010,** 49, 6518-6524.
[269] Mayasree, O.; Sankar, C. R.; Assoud, A.; Kleinke, H., *Inorg. Chem.* **2011,** 50, 4580-4585.
[270] Mayasree, O.; Sankar, C. R.; Cui, Y.; Assoud, A.; Kleinke, H., *Eur. J. Inorg. Chem.* **2011,** 2011, 4037-4042.
[271] Assoud, A.; Cui, Y.; Thomas, S.; Sutherland, B.; Kleinke, H., *J. Solid State Chem.* **2008,** 181, 2024-2030.
[272] Lowhorn, N. D.; Tritt, T. M.; Abbott, E. E.; Kolis, J. W., *Appl. Phys. Lett.* **2006,** 88, 022101/1-022101/3.
[273] Nilges, T.; Lange, S.; Bawohl, M.; Deckwart, J. M.; Janssen, M.; Wiemhoefer, H.-D.; Decourt, R.; Chevalier, B.; Vannahme, J.; Eckert, H.; Weihrich, R., *Nat. Mater.* **2009,** 8, 101-108.
[274] Assoud, A.; Soheilnia, N.; Kleinke, H., *Chem. Mater.* **2005,** 17, 2255-2261.
[275] Mayasree, O.; Sankar Cheriyedath, R.; Kleinke, K. M.; Kleinke, H., *Coord. Chem. Rev.* **2012,** In press.
[276] Kuropatwa, B.; Cui, Y.; Assoud, A.; Kleinke, H., *Chem. Mater.* **2009,** 21, 88-93.
[277] Kuropatwa, B. A.; Assoud, A.; Kleinke, H., *Inorg. Chem.* **2011,** 50, 7831-7837.
[278] Yao, X.; Marking, G.; Franzen, H. F., *Ber. Bunsenges.* **1992,** 96, 1552-1557.
[279] Köckerling, M.; Franzen, H. F., *Croat. Chem. Acta* **1995,** 68, 709-719.
[280] Yao, X.; Franzen, H. F., *J. Am. Chem. Soc.* **1991,** 113, 1426-1427.
[281] Yao, X.; Miller, G. J.; Franzen, H. F., *J. Alloys Compd.* **1992,** 183, 7-17.
[282] Yao, X.; Franzen, H. F., *J. Solid State Chem.* **1990,** 86, 88-93.
[283] Yao, X.; Franzen, H. F., *Z. Anorg. Allg. Chem.* **1991,** 598-599, 353-362.
[284] Kleinke, H., *Trends Inorg. Chem.* **2001,** 7, 135-149.
[285] Kleinke, H., *J. Alloys Compd.* **2002,** 336, 132-137.
[286] Debus, S.; Harbrecht, B., *Z. Anorg. Allg. Chem.* **2001,** 627, 431-438.
[287] Fokwa Tsinde, B. P.; Doert, T., *Solid State Sci.* **2005,** 7, 573-587.
[288] Huang, Z.; Bensch, W.; Mankovsky, S.; Polesya, S.; Ebert, H.; Kremer, R. K., *J. Solid State Chem.* **2006,** 179, 2067-2078.
[289] Assoud, A.; Soheilnia, N.; Kleinke, H., *Chem. Mater.* **2005,** 17, 4509-4513.
[290] Mehrotra, P. K.; Hoffmann, R., *Inorg. Chem.* **1978,** 17, 2187-2189.
[291] Merz Jr., K. M.; Hoffmann, R., *Inorg. Chem.* **1988,** 27, 2120-2127.
[292] Pyykkö, P., *Chem. Rev. (Washington, DC, U. S.)* **1997,** 97, 597-636.
[293] Owens, B. B., *J. Power Sourc.* **2000,** 90, 2-8.

[294] Kanno, R.; Ohno, K.; Kawamoto, Y.; Takeda, Y.; Yamamoto, O.; Kamiyama, T.; Asano, H.; Izumi, F.; Kondo, S., *J. Solid State Chem.* **1993,** 102, 79-92.
[295] Gagor, A.; Pietraszko, A.; Kaynts, D., *J. Solid State Chem.* **2008,** 181, 777-782.
[296] Möller, M. H.; Jeitschko, W., *J. Solid State Chem.* **1986,** 65, 178-189.
[297] Landrum, G. A.; Dronskowski, R., *Angew. Chem. Int. Ed.* **2000,** 39, 1560-1585.
[298] Dashjav, E.; Kleinke, H., *J. Solid State Chem.* **2003,** 176, 329-337.
[299] Soheilnia, N.; Assoud, A.; Kleinke, H., *Inorg. Chem.* **2003,** 42, 7319-7325.
[300] Ogawa, H.; Kobayashi, M., *Solid State Ion.* **2002,** 148, 211-217.
[301] Soheilnia, N.; Xu, H.; Zhang, H.; Tritt, T. M.; Swainson, I.; Kleinke, H., *Chem. Mater.* **2007,** 19, 4063-4068.
[302] Xu, H.; Soheilnia, N.; Zhang, H.; Alboni, P. N.; Tritt, T. M.; Kleinke, H., *Mater. Res. Soc. Symp. Proc.* **2008,** 1044, 459-467.
[303] Spek, A. L., *J. Appl. Crystallogr.* **2003,** 36, 7-13.
[304] Tillard-Charbonnel, M.; Belin, C., *Mater. Res. Bull.* **1992,** 27, 1277-86.
[305] Lin, Q.; Corbett, J. D., *Inorg. Chem.* **2005,** 44, 512-518.
[306] Jansen, M., *Angew. Chem., Int. Ed. Engl.* **1987,** 26, 1098-1110.
[307] Örlygsson, G.; Conrad, M.; Harbrecht, B., *Z. Anorg. Allg. Chem.* **2001,** 627, 1017-1022.
[308] Debus, S.; Harbrecht, B., *Z. Anorg. Allg. Chem.* **2000,** 626, 173-179.
[309] Assoud, A.; Derakhshan, S.; Soheilnia, N.; Kleinke, H., *Chem. Mater.* **2004,** 16, 4193-4198.
[310] Spangenberg, K., *Naturwissenschaften* **1927,** 15, 266-266.
[311] Li, F.; Franzen, H. F., *J. Alloys Compd.* **1994,** 215, L3-L6.
[312] Li, J.; Guo, H.-Y.; Carey, J. R.; Mulley, S.; Proserpio, D. M.; Sironi, A., *Mater. Res. Bull.* **1994,** 29, 1041 - 1048.
[313] Cordier, G.; Schwidetzky, C.; Schaefer, H., *Z. Naturforsch., B Anorg. Chem., Org. Chem.* **1984,** 39B, 833-834.
[314] Schweika, W.; Hermann, R. P.; Prager, M.; Persson, J.; Keppens, V., *Phys. Rev. Lett.* **2007,** 2007, 125501/1-125501/4.
[315] Batchelor, R. J.; Einstein, F. W. B.; Gay, I. D.; Jones, C. H. W.; Sharma, R. D., *Inorg. Chem.* **1993,** 32, 4378-4383.
[316] Thiele, K.-H.; Steinicke, A.; Dümichen, U.; Neumüller, B., *Z. Anorg. Allg. Chem.* **1996,** 622, 231-234.
[317] Canadell, E.; Jobic, S.; Brec, R.; Rouxel, J.; Whangbo, M. H., *J. Solid State Chem.* **1992,** 99, 189-99.
[318] Jepsen, O.; Andersen, O. K., *Z. Phys.* **1995,** 97, 35-47.
[319] Peierls, R. E., *Quantum Theory of Solids*. Clarendon Press: Oxford, UK, **1955**.
[320] Choi, K.-S.; Kanatzidis, M. G., *J. Solid State Chem.* **2001,** 161, 17-22.

Appendix A. Thallium Telluride Crystal Tables (SECTION IV)

Table A.1 Atomic positions, isotropic displacement parameters, and Sn occupancies for $Tl_{10-x}Sn_xTe_6$.

Formula	Atom	Site	% Sn	x	y	z	U_{eq} [Å^2]
$Tl_{9.05}Sn_{0.95(8)}Te_6$	*M*(1)	4*c*	48.0(4)	0	0	0	0.026(1)
	M(2)	16*l*	0	0.1465(1)	0.6465(1)	0.1593(1)	0.035(1)
	Te(1)	4*a*	-	0	0	0.2500	0.028(1)
	Te(2)	8*h*	-	0.3369(3)	0.8369(3)	0	0.027(1)
$Tl_{8.37}Sn_{1.63(9)}Te_6$	*M*(1)	4*c*	70.6(10)	0	0	0	0.028(3)
	M(2)	16*l*	2.8(9)	0.1463(3)	0.6463(3)	0.1585(3)	0.034(2)
	Te(1)	4*a*	-	0	0	0.2500	0.024(3)
	Te(2)	8*h*	-	0.3368(6)	0.8368(6)	0	0.024(3)
$Tl_{8.0}Sn_{2.0(3)}Te_6$	*M*(1)	4*c*	72(4)	0	0	0	0.011(4)
	M(2)	16*l*	7(3)	0.1471(2)	0.6471(2)	0.1605(3)	0.021(1)
	Te(1)	4*a*	-	0	0	0.2500	0.010(3)
	Te(2)	8*h*	-	0.3361(4)	0.8361(4)	0	0.013(3)
$Tl_{7.5}Sn_{2.5(3)}Te_6$	*M*(1)	4*c*	84(4)	0	0	0	0.014(5)
	M(2)	16*l*	10(3)	0.1469(2)	0.6469(2)	0.1609(4)	0.026(2)
	Te(1)	4*a*	-	0	0	0.2500	0.024(4)
	Te(2)	8*h*	-	0.3376(5)	0.8376(5)	0	0.025(5)

Table A.2 Bond distances [Å] for $Tl_{10-x}Sn_xTe_6$.

Bond	$Tl_{9.05}Sn_{0.95}Te_6$	$Tl_{8.37}Sn_{1.63}Te_6$	$Tl_{8.0}Sn_{2.0}Te_6$	$Tl_{8.5}Sn_{2.5}Te_6$
M(1)–Te(1) ×2	3.2529(2)	3.2647(4)	3.2631(2)	3.26464(7)
M(1)–Te(2) ×4	3.310(1)	3.3122(5)	3.305(2)	3.311(2)
M(2)–Te(2) ×1	3.156(3)	3.1576(7)	3.157(4)	3.177(5)
M(2)–Te(2) ×2	3.436(3)	3.4370(6)	3.459(4)	3.450(5)
M(2)–Te(1) ×2	3.583(1)	3.592(1)	3.576(2)	3.575(2)
M(2)–*M*(2) ×1	3.506(3)	3.5278(9)	3.475(6)	3.473(8)
M(2)–*M*(2) ×2	3.503(4)	3.5230(7)	3.496(6)	3.487(7)
M(2)–*M*(2) ×1	3.664(4)	3.6621(9)	3.677(4)	3.671(5)

Table A.3 Atomic positions and U_{eq} parameters for $Tl_{10-x-y}Sn_xBi_yTe_6$.

Formula	Atom	Site	x	y	z	U_{eq} [Å^2]
$Tl_{8.66}Sn_{0.67}Bi_{0.67}Te_6$	*M*(1)	4*c*	0	0	0	0.02466(6)
	M(2)	16*l*	0.14669(8)	0.64669(8)	0.15914(7)	0.0361(4)
	Te(1)	4*a*	0	0	0.25	0.0262(6)
	Te(2)	8*h*	0.33735(16)	0.83735(16)	0	0.0243(5)
$Tl_{8.67}Sn_{1.00}Bi_{0.33}Te_6$*	*M*(1)	4*c*	0	0	0	0.02
	M(2)	16*l*	0.14613(34)	0.64613(34)	0.1580(6)	0.050(4)
	Te(1)	4*a*	0	0	0.25	0.021(6)
	Te(2)	8*h*	0.3383(8)	0.8383(8)	0	0.030(6)
$Tl_9Sn_{0.60}Bi_{0.40}Te_6$*	*M*(1)	4*c*	0	0	0	0.02373
	M(2)	16*l*	0.1466	0.6466	0.1592	0.0327(16)
	Te(1)	4*a*	0	0	0.25	0.0153(32)
	Te(2)	8*h*	0.33751	0.83751	0	0.0179(24)
$Tl_9Sn_{0.50}Bi_{0.50}Te_6$*	*M*(1)	4*c*	0	0	0	0.014
	M(2)	16*l*	0.14763(23)	0.64763(23)	0.1595(4)	0.0135(17)
	Te(1)	4*a*	0	0	0.25	0.017(4)
	Te(2)	8*h*	0.3371(6)	0.8371(6)	0	0.017(4)

*Rietveld refinement

Table A.4 Bond distances [Å] for $Tl_{10-x-y}Sn_xBi_yTe_6$.

Bond	$Tl_{8.66}Sn_{0.67}Bi_{0.67}Te_6$	$Tl_{8.67}Sn_{1.00}Bi_{0.33}Te_6$*	$Tl_9Sn_{0.60}Bi_{0.40}Te_6$*	$Tl_9Sn_{0.50}Bi_{0.50}Te_6$*
M(1)–Te(1) ×2	3.2517(2)	3.2306(23)	3.21652(19)	3.22829(18)
M(1)–Te(2) ×4	3.3163(7)	3.295(4)	3.32293(17)	3.3209(26)
M(2)–Te(2) ×1	3.1598(17)	3.142(7)	3.15145(12)	3.145(6)
M(2)–Te(2) ×2	3.4363(14)	3.392(8)	3.42540(14)	3.442(6)
M(2)–Te(1) ×2	3.588(1)	3.569(4)	3.58944(17)	3.5844(21)
M(2)–*M*(2) ×1	3.504(2)	3.510(12)	3.49141(14)	3.472(9)
M(2)–*M*(2) ×2	3.5123(16)	3.501(10)	3.49629(14)	3.509(7)
M(2)–*M*(2) ×1	3.674(2)	3.633(9)	3.67829(19)	3.704(6)

*Rietveld refinement

Appendix B. Ba-Cu-*Q* Crystal Tables (SECTION V)

Table B.1 Crystallographic data for $Ba_3Cu_{17-x}(Se,Te)_{11}$.

Refined formula	**$Ba_3Cu_{14.4(2)}Se_{8.6(1)}Te_{2.4}$**	**$Ba_3Cu_{14.4(2)}Se_{8.30(8)}Te_{2.70}$**	**$Ba_3Cu_{15.0(1)}Se_{7.75(6)}Te_{3.25}$**
formula weight [g/mol]	2311.74	2325.38	2396.09
T of measurement [K]	298(2)	298(2)	298(2)
λ [Å]	0.71073	0.71073	0.71073
space group	$R\bar{3}m$	$R\bar{3}m$	$R\bar{3}m$
a [Å]	12.1718(4)	12.1897(3)	12.2339(3)
c [Å]	28.197(2)	28.2087(17)	28.2819(16)
V [Å^3]	3617.8(3)	3629.9(3)	3665.8(2)
Z	6	6	6
μ [mm^{-1}]	32.956	32.786	32.854
ρ_{calcd} [g/cm^3]	6.366	6.383	6.512
$R(F_o)^a$ \ $R_w(F_o^2)^b$	0.064 \ 0.126	0.046 \ 0.091	0.038 \ 0.087

$^a R(F_o) = \Sigma||F_o|-|F_c|| \,/\, \Sigma|F_o|$ $^b R_w(F_o^2) = [\,\Sigma[w(F_o^2 - F_c^2)^2] \,/\, \Sigma[w(F_o^2)^2]\,]^{1/2}$

Table B.2 Selected interatomic distances [Å] of $Ba_3Cu_{17-x}(Se,Te)_{11}$.

Interaction	*d*[Å] [a]	#	*d*[Å] [b]	#
Ba–Se	3.251(2) – 3.337(2)	5	3.233(1) – 3.364(1)	5
Ba–*Q*	3.487(4) – 3.567(3)	3	3.491(2) – 3.595(1)	3
Cu1–Se	2.303(3)	1	2.336(2)	1
Cu1–Cu	2.417(6) – 2.968(8)	6	2.457(3) – 2.912(3)	6
Cu1–*Q*	2.674(3) – 2.684(4)	2	2.701(2) – 2.722(2)	2
Cu1–Te	3.135(4)	1	3.115(2)	1
Cu2–*Q*	2.378(4) – 2.694(4)	2	2.383(2) – 2.742(2)	2
Cu2–Cu	2.527(6) – 2.885(5)	3	2.540(3) – 2.866(3)	3
Cu2–Se	2.559(2)	2	2.561(1)	2
Cu3–Se	2.412(3) – 2.497(2)	3	2.428(2) – 2.505(1)	3
Cu3–Cu	2.690(2) – 2.914(5)	5	2.706(1) – 2.935(3)	5
Cu3–Te	2.960(3)	1	2.980(2)	1
Cu4–Se	2.535(3)	2	2.545(2)	2
Cu4–Te	2.613(4)	1	2.624(2)	1
Cu4–*Q*	2.870(6)	1	2.880(3)	1
Cu4–Cu	2.645(5) – 2.914(5)	6	2.663(3) – 2.935(3)	6
Cu5–Cu	2.662(14) – 2.864(6)	7	2.763(7) – 2.846(2)	7
Cu5–*Q*	2.718(6)	3	2.757(3)	3
Cu5–Te	2.559(12)		2.510(6)	
Cu6–Cu	2.527(6) – 2.662(14)	4	2.540(3) – 2.763(7)	4
Cu6–*Q*	2.605(8) – 2.629(4)	4	2.575(4) – 2.668(2)	4

[a] $Ba_3Cu_{14.4(2)}Se_{8.6(1)}Te_{2.4}$

[b] $Ba_3Cu_{15.0(1)}Se_{7.75(6)}Te_{3.25}$

Table B.3 Crystallographic Data for $Ba_3Cu_{17-x}(S,Te)_{11}$ and $Ba_3Cu_{17-x}(S,Te)_{11.5}$.

Refined formula	$Ba_3Cu_{15.1(1)}S_{7.92(2)}Te_{3.08}$	$Ba_3Cu_{15.7(4)}S_{7.051(5)}Te_{3.949}$	$Ba_3Cu_{15.6(2)}S_{5.33(4)}Te_{6.17}$	$Ba_3Cu_{16.0(1)}S_{4.45(4)}Te_{7.05}$
M [g/mol]	2018.13	2139.96	2362.97	2473.81
T [K]	298(2)	298(2)	296(2)	293(2)
λ [Å]	0.71073	0.71073	0.71073	0.71073
space group	$R\bar{3}m$	$R\bar{3}m$	$R\bar{3}m$	$R\bar{3}m$
a [Å] = b	11.9371(3)	12.009(1)	17.2095(8)	17.2364(4)
c [Å]	27.522(2)	27.764(2)		
V [Å^3]	3396.3(2)	3467.6(5)	5096.9(4)	5120.8(2)
Z	6	6	8	8
μ [mm^{-1}]	23.601	24.628	24.625	25.763
ρ_{calcd} [g/cm^3]	5.927	6.149	6.159	6.417
$R(F_o)^a \setminus R_w(F_o^2)^b$	0.0579, 0.1045	0.0199, 0.0283	0.0277, 0.0737	0.0287, 0.0544

$^a R(F_o) = \Sigma||F_o|-|F_c|| \,/\, \Sigma|F_o|$ $^b R_w(F_o^2) = [\,\Sigma[w(F_o^2 - F_c^2)^2] \,/\, \Sigma[w(F_o^2)^2]\,]^{1/2}$

Table B.4 Atomic coordinates and U_{eq} parameters of $Ba_3Cu_{15.7(4)}S_{7.051(5)}Te_{3.949}$, and occupancy factors of $Ba_3Cu_{15.7(4)}S_{7.051(5)}Te_{3.949}$ and $Ba_3Cu_{15.1(1)}S_{7.92(2)}Te_{3.08}$.

Atom	Site	*x*	*y*	*z*	U_{eq}[Å^2]	Occ.[a]	Occ.[b]
Ba	18h	0.47016(1)	0.52984(1)	0.086879(9)	0.01327(7)	1	1
Cu1	36i	0.22846(5)	0.01116(4)	0.13437(2)	0.0246(2)	0.987(2)	0.915(7)
Cu2	18h	0.4274(6)	0.5726(6)	0.3480(3)	0.027(3)	0.49(6)	0.94(1)
Cu2B[c]	36i	0.446(2)	0.610(2)	0.3507(3)	0.026(1)	0.24(3)	--
Cu3	18h	0.52308(3)	0.47692(3)	0.28218(2)	0.0221(2)	0.987(3)	1
Cu4	18h	0.54696(3)	0.45304(3)	0.37877(2)	0.0233(2)	0.979(3)	0.96(1)
Cu5	6c	0	0	0.16634(4)	0.0217(4)	0.954(5)	0.78(2)
Cu6	6c	⅓	⅔	0.399(3)	0.02(3)	0.013(4)	0.10(2)
*Q*1 (S, Te)	18h	0.77510(1)	0.22490(1)	0.110205(9)	0.01059(9)	0.017(2), 0.983	0.305(7), 0.695
Te2	6c	0	0	0.07441 (2)	0.0122(1)	1	1
S3	18f	0.31968(9)	0	0	0.0116(2)	1	1
S4	6c	0	0	0.36128(6)	0.0115(3)	1	1
S5	18h	0.47630(5)	0.52370(5)	0.20644(3)	0.0112(2)	1	1

[a] Occupancies of $Ba_3Cu_{15.7(4)}S_{7.051(5)}Te_{3.949}$
[b] Occupancies of $Ba_3Cu_{15.1(1)}S_{7.92(2)}Te_{3.08}$
[c] Only present in $Ba_3Cu_{15.7(4)}S_{7.051(5)}Te_{3.949}$

Table B.5 Atomic coordinates and U_{eq} parameters of $Ba_3Cu_{16.0(1)}S_{4.45(4)}Te_{7.05}$, and occupancy factors of $Ba_3Cu_{16.0(1)}S_{4.45(4)}Te_{7.05}$ and $Ba_3Cu_{15.6(2)}S_{5.33(4)}Te_{6.17}$.

Atom	Site	*x*	*y*	*z*	U_{eq} [Å^2]	*Occ.*[a]	*Occ.*[b]
Ba	24*e*	0.29213(5)	0	0	0.0134(2)	1	1
Cu1	96*k*	0.19950(4)	0.19950(4)	0.41664(8)	0.0327(4)	0.985(6)	0.923(7)
Cu2	32*f*	0.0745(1)	0.0745(1)	0.0745(1)	0.026(1)	0.500(8)	0.58(1)
Cu3	32*f*	0.1630(1)	0.1630(1)	0.1630(1)	0.026(1)	0.556(9)	0.55(1)
*Q*1 (S, Te)	48*h*	0	0.16969(3)	0.16969(3)	0.0140(2)	0.007(5),0.993	0.142(5),0.858
Te2	8*c*	¼	¼	¼	0.0268(5)	1	1
S3	32*f*	0.3906(1)	0.3906(1)	0.3906(1)	0.0115(5)	1	1
*Q*4 (S, Te)	4*a*	0	0	0	0.038(3)	0.80(1),0.20	0.95(2),0.05

[a] Occupancies of $Ba_3Cu_{16.0(1)}S_{4.45(4)}Te_{7.05}$

[b] Occupancies of $Ba_3Cu_{15.6(2)}S_{5.33(4)}Te_{6.17}$

Table B.6 Selected interatomic distances [Å] of $Ba_3Cu_{17-x}(S,Te)_{11}$ and $Ba_3Cu_{17-x}(S,Te)_{11.5}$.

$Ba_3Cu_{17-x}(S,Te)_{11}$			*distance range*				*distance range*
Ba	*Q*1	2x	3.5662(8) - 3.6047(4)	Cu1	Cu1	3x	2.458(3) - 2.894(4)
	S3	2x	3.268(2) - 3.3004(7)		Cu3	1x	2.811(2) - 2.8171(7)
	S4	1x	3.2829(9) - 3.298(3)		Cu4	1x	2.746(3) - 2.7645(7)
	S5	3x	3.1169(7) - 3.322(1)		Cu5	1x	2.8224(6) - 2.830(3)
					*Q*1	2x	2.666(2) - 2.7605(5)
Cu2	Cu2B	3x	'0.40(2)', 3.06(3)		Te2	1x	3.126(2) - 3.154(2)
	Cu3	1x	2.70(1) - 2.800(4)		S5	1x	2.213(3) - 2.2365(9)
	Cu4	1x	2.63(1) - 2.663(4)				
	Cu6	1x	2.42(4) - 2.90(4)	Cu3	Cu1	2x	2.811(2) - 2.8171(7)
	*Q*1	1x	2.585(3) - 2.669(8)		Cu2B	2x	2.92(2)
	S3	2x	2.565(8) - 2.613(2)		Cu4	3x	2.712(3) - 2.7764(5)
	S4	1x	2.228(4) - 2.29(1)		Te2	1x	3.039(2) - 3.0556(7)
					S3	2x	2.395(2) - 2.4116(7)
Cu2B	Cu2	1x	3.06(2)		S5	1x	2.306(4) - 2.317(1)
	Cu2B	2x	'0.68(4)', 2.71(4)				
	Cu6	1x	2.24(5)	Cu4	Cu1	2x	2.746(3) - 2.7645(7)
	*Q*1	1x	2.645(8)		Cu2	1x	2.63(1) - 2.663(4)
	S3	1x	2.48(2)		Cu2B	2x	2.81(2)
	S4	1x	2.19(1)		Cu3	3x	2.712(3) - 2.7764(5)
					*Q*1	1x	2.812(3) - 2.8323(7)
Cu5	Cu1	6x	2.8224(6) - 2.830(3)		Te2	1x	2.615(2) - 2.6167(7)
	Cu6	1x	1.84(5) - 2.81(7)		S3	2x	2.429(3) - 2.4439(8)
	*Q*1	3x	2.701(3) - 2.7520(7)				
	Te2	1x	2.523(6) - 2.552(1)	Cu6	Cu2	3x	2.42(4) - 2.90(4)
					Cu2B	5x	2.24(5)
					Cu5	1x	1.84(5) - 2.81(7)
					*Q*1	3x	2.268(7) - 2.57(4)
					S4	1x	3.43(5) - 2.60(8)
$Ba_3Cu_{17-x}(S,Te)_{11.5}$			*distance range*				*distance range*
Ba	*Q*1	4x	3.5932(6) - 3.6067(5)	Cu1	Cu1	4x	2.461(2) - 2.874(3)
	S3	4x	3.161(1) - 3.167(1)		Cu3	2x	2.810(1) - 2.819(2)
					*Q*1	2x	2.714(1) - 2.7224(9)
Cu2	Cu2	3x	2.543(5) - 2.567(4)		S3	1x	2.233(2) - 2.242(2)
	Cu3	1x	2.640(6) - 2.642(5)		Te2	1x	3.125(1) - 3.134(2)
	*Q*1	3x	2.652(2) - 2.653(2)				
	*Q*4	1x	2.202(4) - 2.223(4)	Cu3	Cu1	6x	2.810(2) - 2.819(2)
					*Q*1	3x	2.801(2) - 2.814(2)
					Te2	1x	2.598(3) - 2.610(4)

Table B.7 Selected interatomic distances [Å] of $Ba_2Cu_{7-x}Te_6$.

Ba1	Te1	1x	3.4475(13)	Cu4	Te3	1x	2.617(2)
	Te2	1x	3.4822(13)		Te2	1x	2.6223(18)
	Te3	2x	3.551(1)		Te4	1x	2.649(2)
	Te1	1x	3.5904(13)		Te4	1x	2.705(2)
	Te4	2x	3.649(1)				
	Te4	2x	3.831(1)				
				Cu1	Cu3	1x	2.695(2)
					Cu4	1x	2.761(2)
Ba2	Te2	1x	3.451(1)		Cu1	1x	2.776(3)
	Te3	2x	3.489(1)		Cu2	1x	2.890(2)
	Te1	1x	3.517(1)				
	Te2	1x	3.570(1)	Cu2	Cu3	2x	2.770(2)
	Te4	2x	3.7263(11)		Cu1	2x	2.890(2)
	Te4	2x	3.790(1)				
Cu1	Te3	1x	2.638(1)	Cu3	Cu4	1x	2.668(2)
	Te1	1x	2.667(2)		Cu1	1x	2.695(2)
	Te2	1x	2.674(2)		Cu2	1x	2.770(2)
	Te3	1x	2.767(2)				
				Cu4	Cu3	1x	2.668(2)
					Cu1	1x	2.761(2)
Cu2	Te2	1x	2.613(2)				
	Te1	1x	2.654(2)	Te4	Te4	1x	3.305(2)
	Te3	2x	2.7178(14)		Te4	1x	3.564(2)
Cu3	Te1	1x	2.6454(16)				
	Te3	1x	2.6547(16)				
	Te4	1x	2.6978(17)				
	Te3	1x	2.759(2)				

Appendix C. Experimental Synthesis Information

Table C.1 Physical Properties of Commonly-Used Elements[117]

Element	Melting Point (K)	Liquid Range (K)	Crucible Recommended
Antimony (Sb)	903.78	956.22	Yes
Barium (Ba)	1000.00	1143.00	No
Bismuth (Bi)	544.40	1292.6	No
Copper (Cu)	1357.77	1842.23	No
Gallium (Ga)	302.91	2174.09	Yes
Indium (In)	429.75	1915.25	Yes
Lead (Pb)	600.61	1421.39	Yes
Selenium (Se)	494.00	464.00	Yes
Sulfur (S)	388.36	329.51	Yes
Tellurium (Te)	722.66	538.34	No
Thallium (Tl)	577.00	1169.00	No
Tin (Sn)	505.08	2369.92	No

Table C.2 Synthesis Conditions for Commonly-Used Compounds

Compound	DSC Melting Point (K)	Upper Reaction Temperature (K)	Annealing Temperature (K)	Cooling Rate (°/hr)* \ Time (hr)
Bi_2Te_3	860	923	843	0 \ 200
$SnBi_2Te_4$	868	"	"	0 \ 336
$SnBi_4Te_7$	852	"	823	"
$SnBi_6Te_{10}$	~843	"	803	"
$Sn_2Bi_2Te_5$	–	"	798	"
Tl_5Te_3	725	923	698	0 \ 120
$Tl_8Sn_2Te_6$	~823	"	923	1.5 \ 180
Tl_9SnTe_6	~787	"	"	"
$Tl_8Pb_2Te_6$	~850	"	–	–
Tl_9SbTe_6	783	"	873	1.25 \ 150
Tl_9BiTe_6	811	"	"	"
$Ba_3Cu_{17-x}(Se,Te)_{11}$	968	1023	1023	1.5 \ 200
$Ba_3Cu_{17-x}(S,Te)_{11}$	~930	1073	873	0 \ 100
$Ba_3Cu_{17-x}(S,Te)_{11.5}$	900	"	"	"
$Ba_2Cu_{7-x}Te_6$	970	"	923	0 \ 60

*Cooling rate of 0 °/hr implies holding compound at Annealing Temperature